

Contrails

Cleared: March 29th, 1972

Clearing Authority: Air Force Materials Laboratory

CORROSION CRACKING OF METALLIC MATERIALS

Mars G. Fontana

*** Export controls have been removed ***

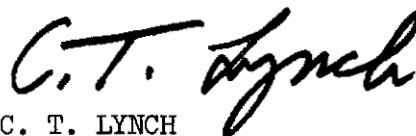
This document is subject to special export controls and each transmittal to foreign governments or foreign nationals may be made only with prior approval of the Metals and Ceramics Division (MAM), Air Force Materials Laboratory, Wright-Patterson AFB, Ohio 45433

FOREWORD

This report was prepared by the Department of Metallurgical Engineering, The Ohio State University, Columbus, Ohio. The principal investigator for this project was Dr. Mars Fontana, under Contract F33(615)-69-C-1258. This contract was initiated under Project No. 7312, "Metal Surface Deterioration and Protection," Task No. 731202, "Metal Surface Deterioration," during the period December 15, 1968 through December 31, 1969. This work was administered by the Advanced Metallurgical Studies Branch of the Metals and Ceramics Division, Air Force Materials Laboratory, Wright-Patterson Air Force Base, Ohio, under the direction of Dr. C. T. Lynch and Dr. H. B. Kirkpatrick.

This manuscript was released by the author in December, 1969, for publication.

This technical report has been reviewed and is approved.



C. T. LYNCH
Chief, Advanced Metallurgical
Studies Branch
Metals and Ceramics Division
Air Force Materials Laboratory

ABSTRACT

Stress corrosion behavior of titanium alloys and high strength steels has been studied.

In titanium alloys the initiation and propagation of cracks in aqueous and methanolic environments is being studied as a function of alloy composition, electrochemical control, and applied stress. Corrosion processes within crevices are being studied. Straining electrode studies are also reported. Crack initiation in Ti-6Al-4V specimens was observed at α - β interfaces and in β grains. Studies of crack velocity show it to depend on applied stress but not on potential. Crevice studies show corrosion to be accelerated when the IR drop is large.

In high strength steels the processes of transient passivity, dissolution of carbides, crack propagation and hydrogen permeation are being studied. The kinetics of transient passivity on iron alloy surfaces shows good agreement with classic models for growth of thin films. Dissolution of iron carbides is shown to depend on pH, potential and anion. The action of cathodic poisons such as arsenic is shown to depend on co-deposition of the poison species.

This document is subject to special export controls and each transmittal to foreign governments or foreign nationals may be made only with prior approval of the Metals and Ceramics Division (MAM), Air Force Materials Laboratory, Wright-Patterson Air Force Base, Ohio 45433

Contrails

TABLE OF CONTENTS

<u>Section</u>		<u>Page</u>
I	INTRODUCTION	1
II	TITANIUM AND TITANIUM-BASE ALLOYS	2
	A. Effect of Applied Potential on Crack Initiation and Growth for Ti-6Al-4V Alloy in Methanol-Water-Sodium Chloride Solutions	2
	1. Introduction	2
	2. Experimental	2
	3. Results	4
	4. Discussion	12
	B. Crevice Effect During Polarization of Ti-8Al-1Mo-1V Alloy in Aqueous and Methanol Environments	20
	1. Introduction	20
	2. Experimental	20
	3. Results	22
	4. Discussion	27
	C. Effects of Strain Rate and Polarization Potential on the Susceptibility of Ti-6Al-4V Alloy to Stress-Corrosion Cracking by Methanol-0.166% Hydrochloric Acid-Water Solutions	31
	1. Introduction	31
	2. Experimental	34
	3. Results	34
	4. Discussion	59
	D. An Electrochemical Investigation of the Factors Affecting the Stress-Corrosion Cracking Behavior of Titanium-Base Alloys in Methanol Environments	63
	E. Effects of Texture and Grain Size on Stress-Corrosion Cracking of Titanium-Base Alloys	64
	F. Effect of State of Stress on the Susceptibility of Titanium-Base Alloys to Stress Corrosion Cracking	64
	1. Material and Experimental Analysis	65
	2. Future Work	67

TABLE OF CONTENTS - (Continued)

<u>Section</u>		<u>Page</u>
III	STRESS CORROSION CRACKING OF STEELS	69
	A. Objectives and Scope	69
	B. Controlled Phenomenological Study of Crack Propagation	69
	1. Objectives and Background	69
	2. Experimental Procedure for Crack Length Determination	69
	3. General Description of Acoustic Emission Techniques	76
	4. Description of Acoustic Detection System	79
	5. Experimental Procedure for Detection of Acoustic Signals	80
	6. Discussion	84
	7. Conclusions	84
	C. Effect of Environmental Additives--Hydrazine	84
	1. Objectives and Background	84
	2. Experimental	86
	3. Discussion	92
	D. Interaction of Hydrogen with Steel	95
	1. Objectives and Background	95
	2. Experimental	95
	3. Discussion	112
	E. Dissolution of Ferrite-Carbide Heterogeneous Structure	114
	1. Objectives	114
	2. Experimental	114
	3. Results	114
	4. Discussion	149
	F. Dissolution Kinetics of Iron Carbide, Graphite	150
	1. Objectives and Background	150
	2. Preparation of Iron Carbide	150
	3. Work on Carbide Dissolution Kinetics	153
	G. Kinetics of Growth of Passive Films	154
	1. Objectives and Background	154

TABLE OF CONTENTS - (Continued)

<u>Section</u>	<u>Page</u>
2. Experimental	154
3. Results and Discussion	154
H. Electrochemical Processes Above 25°C	165
1. Background and Objectives of Current Work	165
2. Thermodynamic Stability	165
3. Kinetic Experiments	169
IV DELAYED FRACTURE OF HIGH STRENGTH STEELS	184
A. Introduction	184
B. Experimental	184
C. Results and Discussion	185
D. Future Work	185
V COORDINATION AND BRIEFING	187
VI MISCELLANEOUS	187
REFERENCES	189

LIST OF ILLUSTRATIONS

<u>Figure No.</u>		<u>Page</u>
1	Experimental Apparatus	3
2	The Effect of Applied Potential upon Crack Initiation Time and Failure Time in Methanol-0.3% Water and Saturated NaCl	5
3	The Effect of Applied Potential upon Crack Velocity in Methanol-0.3% Water and Saturated NaCl	6
4	The Effect of Stress Level upon Crack Initiation Time and Failure Time in Methanol-0.3% Water and Saturated NaCl at 0 mV	8
5	The Effect of Stress Level upon Crack Velocity. Specimen Polarization at 0 mV in Methanol-0.3% Water Saturated NaCl	9
6	The Effect of Water Content upon Crack Initiation Time and Failure Time. Specimens Polarized at 0 mV and Stressed to 80% of the Yield Strength in Methanol-Saturated NaCl	10
7	The Effect of Water Content upon Crack Velocity. Specimen Polarized at 0 mV and Stressed to 80% of the Yield Strength in Methanol-Saturated NaCl.	11
8	The Effect of NaCl Content upon Crack Initiation and Failure Times. Specimens Polarized at 0 mV and Stressed to 80% of the Yield Strength in Methanol-0.3% Water	13
9	The Effect of NaCl Content upon Crack Velocity. Specimens Polarized at 0 mV and Stressed to 80% of the Yield Strength in Methanol-0.3% Water	14
10	Crack Propagation from a Pit. Unetched. Magnification 250X	15
11	Crack Propagation from a Pit. Kroll's Etch. Magnification 500X	15
12	Preferential Corrosion at the α - β Interface and β Phase in Ti6Al-4V. (Note: micro-crack between two small pits) Kroll's Etch. Magnification 2000X	16

LIST OF ILLUSTRATIONS - (Continued)

<u>Figure No.</u>		<u>Page</u>
13	Cracks in a Failed Ti-6Al-4V Specimen. (Note: black areas associated with preferential α - β interface corrosion) Kroll's Etch. Magnification 2000X	16
14	Electron Micrograph of Fracture Surface of Ti-6Al-4V Specimen. (Note: cleavage fracture) Magnification 7000X	17
15	Electron Micrograph of Fracture Surface of Ti-6Al-4V Specimen. (Note: intergranular fracture and quasi-cleavage fracture) Magnification 7000X	17
16	Cell for Crevice Effect on Ti-8Al-1Mo-1V Alloy	21
17	Polarization Potential at Crevice Exterior vs. Potential in Crevice (Ti-8Al-1Mo-1V in 1N H_2SO_4)	23
18	Polarization Potential at Crevice Exterior vs. Potential in Crevice (Ti-8Al-1Mo-1V in 10N H_2SO_4)	24
19	Polarization Potential at Crevice Exterior vs. Potential in Crevice (Ti-8Al-1Mo-1V in 0.6N KBr)	25
20	Polarization Potential at Crevice Exterior vs. Potential in Crevice (Ti-8Al-1Mo-1V in 0.6N KI)	26
21	Polarization Potential at Crevice Exterior vs. Potential in Crevice (Ti-8Al-1Mo-1V in CH_3OH + 0.37% HCl + 0.63% H_2O)	28
22	Polarization Potential at Crevice Exterior vs. Potential in Crevice (Ti-8Al-1Mo-1V in CH_3OH + 2% H_2SO_4)	29
23	Crevice Effect by Anodic and Cathodic Polarization (Ti-8Al-1Mo-1V in 0.6M KI)	30
24	Fracture Load vs. Potential (Bend Specimens) (Ti-8Al-1Mo-1V in 0.6M KBr and 0.6M KI Solutions)	32
25	Failure Time and Cracking Propagation Time vs. Potential (Ti-8Al-1Mo-1V in 0.6M KBr) (Notched tensile specimens, Load = 80.5 lb, $K_1 = 7.15 \sqrt{in}$)	33

LIST OF ILLUSTRATIONS - (Continued)

<u>Figure No.</u>		<u>Page</u>
26	Specimen Configuration: (a) Tensile Specimen for Straining Electrode Tests, (b) Bend Specimen for Static Tests	35
27	Cell for Straining Electrode Tests	36
28	Cell for Stress Corrosion Bend Tests	37
29a	Elongation vs. Water Content. $\text{CH}_3\text{OH} + 0.166\%$ $\text{HCl} + \text{H}_2\text{O}$ (Tensile direction parallel to rolling direction. Strain rate 0.005 cm/min)	38
29b	Elongation vs. Water Content. $\text{CH}_3\text{OH} + 0.166\%$ $\text{HCl} + \text{H}_2\text{O}$ (Tensile direction perpendicular to rolling direction. Strain rate = 0.005 cm/min)	39
30a	Effect of Polarization Potential on Elongation (%)	41
30b	Potential vs. Water Content (%)	42
31a	Corrosion Potential vs. Water Content $\text{CH}_3\text{OH} + 0.166\%$ $\text{HCl} + \text{H}_2\text{O}$ (no applied load)	42
31b	Corrosion Potential vs. Elongation in $\text{CH}_3\text{OH} + 0.166\%$ $\text{HCl} + \text{H}_2\text{O}$	43
32	Effect of Water Content on the Polarization Curves in $\text{CH}_3\text{OH} + 0.166\%$ $\text{HCl} + \text{H}_2\text{O}$ (scanning rate 25mV/min)	44
33a	Effect of Strain Rate on Current vs. Time in $\text{CH}_3\text{OH} + 0.166\%$ $\text{HCl} + 0.42\%$ H_2O at +350 mV(SHE)	46
33b	Effect of Strain Rate on Current vs. Strain at +350 mV(SHE) in $\text{CH}_3\text{OH} + 0.166\%$ $\text{HCl} + 0.42\%$ H_2O	47
33c	Effect of Strain Rate on Specimen Elongation at +350 mV(SHE)	48
34a	Effect of Strain Rate on Current vs. Strain at +200 mV(SHE) in $\text{CH}_3\text{OH} + 0.166\%$ $\text{HCl} + 0.42\%$ H_2O	49
34b	Effect of Strain Rate on Specimen Elongation at +200 mV(SHE) (same environment as 34-a)	50
35a	Effect of Strain Rate on Current vs. Time in $\text{CH}_3\text{OH} + 0.166\%$ $\text{HCl} + 0.42\%$ H_2O at +50 mV(SHE)	51

LIST OF ILLUSTRATIONS - (Continued)

<u>Figure No.</u>		<u>Page</u>
35b	Effect of Strain Rate on Current vs. Strain at +50 mV(SHE) in $\text{CH}_3\text{OH} + 0.166\% \text{HCl} + 0.42 \text{H}_2\text{O}$	52
35c	Effect of Strain Rate on Specimen Elongation at +50 mV(SHE) (same environment as Fig. 35a and b)	53
36a	Effect of Strain Rate on Current vs. Strain at + 550mV(SHE) in $\text{CH}_3\text{OH} + 0.166\% \text{HCl} + 0.80\% \text{H}_2\text{O}$	54
36b	Effect of Strain Rate on Specimen Elongation at +550 mV(SHE) (same environment as Fig. 36a)	55
37a	Effect of Strain Rate on Corrosion Potential vs. Strain in $\text{CH}_3\text{OH} + 0.166\% \text{HCl} + 0.28\% \text{H}_2\text{O}$	56
37b	Effect of Strain Rate on Corrosion Potential vs. Strain in $\text{CH}_3\text{OH} + 0.166\% \text{HCl} + 0.42\% \text{H}_2\text{O}$	57
37c	Effect of Strain Rate on Corrosion Potential vs. Strain in $\text{CH}_3\text{OH} + 0.166\% \text{HCl} + 0.99\% \text{H}_2\text{O}$	58
38	Failure Time vs. Water Content at Corrosion Potential	60
39	Failure Time vs. Polarization Potential in $\text{CH}_3\text{OH} + 0.166\% \text{HCl} + 0.99\% \text{H}_2\text{O}$	61
40	Schematic Diagram of Combined Bending-Torsion Apparatus	66
41	Notched Bend Specimen	68
42	Specimen Size and Relationship Governing Stress Intensity Factor	71
43	Gas Purification System Being Used for Crack Propagation Studies	72
44	Electronic System for Detection of Acoustic Emissions	73
45	Cantilever Beam Apparatus	74
46	Relationship between Crack Length, Load, and Deflection as Determined in Argon Atmosphere for 4335 Steel	75

LIST OF ILLUSTRATIONS - (Continued)

<u>Figure No.</u>		<u>Page</u>
47	Deflection of Beam vs. Displacement for Cantilever Beam Specimen	77
48	Calibration Curve for Pre-Cracked 4335 Cantilever Beam Specimens	78
49	Photographs of Oscillographic Trace Produced by Acoustic Emission During Crack Propagation in 4335 Steel	83
50	Background Count Rate vs. Trigger Level Setting (mV) of Peak Counter for a Specimen of 4335 Steel Loaded but Undergoing no Crack Growth	85
51	4335 Steel Crack Growth in Salt Water and Hydrazine Environments	87
52	Polarization of 1010 Steel in 3.5% NaCl. Scan at 5000 mV/Hr	88
53	Polarization of 1010 Steel in 3.5% NaCl + 0.02 w/o Hydrazine. Scan at 5000 mV/Hr	89
54	Polarization of 1010 Steel in 3.5% NaCl + 0.2 w/o Hydrazine. Scan at 5000 mV/Hr	90
55	Anodic Scans Comparing Effects With and Without Hydrazine for 1010 Steel	91
56	Schematic Arrangement of Apparatus Used for Measuring Hydrogen Permeation	93
57	Permeation of Hydrogen through a 1010 Steel Membrane as Affected by the Presence of Hydrazine in a 3.5% NaCl Solution	94
58	Schematic Model for Permeation of Hydrogen through a Membrane	96
59	Initial Transients for Hydrogen Permeation	99
60	Rise Transients for Experiment Conducted on Subsequent Day	100
61	Effect of Palladium Plating of the Exit Surface on the Hydrogen Permeability in AISI-1010 Steel	102

LIST OF ILLUSTRATIONS - (Continued)

<u>Figure No.</u>		<u>Page</u>
62	Effect of Arsenite Additions to Acetate on Solution pH and Rest Potential of 1010 Steel	104
63	Cathodic Polarization of 1010 Steel in Acetate Buffer with Arsenite Additions	105
64	Rise Transients for Hydrogen Permeation in Palladized AISI 1010 Steel	106
65	Relationship of Permeation Current to Charging Current	108
66	Nonsteady-State Behavior Permeation Transients	109
67	Effect of Deposition Processes on Hydrogen Permeation	111
68	Arsenic Deposits on Steel Substrate 500X	113
69	Arsenic Deposits on Steel Substrate 2000X	113
70	Schematic Potential-pH Diagram for Fe-H ₂ O at 25°C Showing the Potentials at Which Specimens were Examined in the Electron Microscope	115
71	Electron Micrographs of the 1045 Carbon Steel Used in these Investigations (as received)	116
72	Electron Micrographs Showing Various Modes of Attack	117
73	Electron Micrographs of Specimens Exposed at pH 0 in KCl-HCl Buffer	118
74	Electron Micrographs of Specimens Exposed at pH 4 in H ₂ SO ₄	120
75	Electron Micrographs of Specimens Exposed at pH 4 in HCl	121
76	Electron Micrographs of Specimens Exposed at pH 4 in HNO ₃	123
77	Electron Micrographs of Specimens Exposed at pH 4 in H ₃ PO ₄	124

LIST OF ILLUSTRATIONS-(Continued)

<u>Figure No.</u>		<u>Page</u>
78	Electron Micrographs of Specimens Exposed at pH 4 in Acetic Acid	126
79	Electron Micrographs of Specimens Exposed at pH 4 in 0.1N NaOH - 0.1M $\text{KHC}_8\text{H}_4\text{O}_4$ Buffer	127
80	Electron Micrographs of Specimens Exposed at pH 10 in NaOH - 0.1M H_3BO_3 Buffer	128
81	Electron Micrographs of Specimens Exposed at pH 14 in NaOH	130
82	Electron Micrographs of Specimens Exposed at pH 14 in 1N NaOH + 1M Na_2SO_4	131
83	Electron Micrographs of Specimens Exposed at pH 14 in NaOH + 1N NaCl	132
84	Degree of Attack as a Function of Potential and Environment	133
85	Potential-pH Diagram for the Iron-Water System at 25°C	138
86	Potential-pH Diagram for the Carbon-Water System at 25°C	145
87	Potential-pH Diagrams for Fe_3C in H_2O Considering Species Shown	146
88	Potential-pH Diagrams for Cr_7C_3 Considering Species Shown	148
89	Schematic Arrangement of Furnace for Producing Fe_3C Using H_2 - CH_4 Mixtures	151
90	Schematic Arrangement of Furnace Tube	152
91	Photomicrograph of Specimen Containing Fe_3C	153
92	Growth of Passive Film on Fe in Solution of pH 8.41	156
93	Growth of Passive Film on Fe-10Ni in Solution of pH 8.41	157

LIST OF ILLUSTRATIONS - (Continued)

<u>Figure No.</u>		<u>Page</u>
94	Growth of Passive Film on Fe-10 Cr in Solution of pH 8.41	158
95	Growth of Passive Film on Fe-10 Cr in Solution of pH 8.41	159
96	Plot of Reciprocal of Film Thickness vs. Time for Fe in Solution pH 8.41	160
97	Plot of Reciprocal of Film Thickness vs. Log Time for Fe-10 Cr in Solution of pH 8.41.	161
98	Plot of Reciprocal of Film Thickness vs. Log Time for Fe-10 Cr in Solution of pH 8.41.	162
99	Plot of Reciprocal Film Thickness vs. Log Time for Fe-10 Cr-10 Ni in Solution of pH 8.41	163
100	Film Thickness vs. Potential for One Hour Polarization	164
101	A Comparison of the Anodic Curve for Ni 270 at pH 1.3 Determined in a Standard Glass Polarization Cell and the Autoclave Cell at 25°C	171
102	The Cathodic Reduction Curves of Ni 270 at pH 1.3 from 25°C to 300°C	172
103	The Anodic Dissolution Curves for Ni 270 at pH 1.3 from 25°C to 125°C in the Active to Noble Scan Mode	173
104	The Anodic Dissolution Curves for Ni 270 at pH 1.3 from 125°C to 300°C in the Active to Noble Scan Mode	174
105	The Anodic Dissolution Curve for Ni 270 at pH 1.3 from 150°C to 300°C in the Active to Noble Scan Mode	175
106	Cathodic Reduction Curves for Ni 270 at pH 3.4 from 25°C to 125°C	176
107	Cathodic Reduction Curves for Ni 270 at pH 3.4 from 150°C to 300°C	177

LIST OF ILLUSTRATIONS - (Continued)

<u>Figure No.</u>		<u>Page</u>
108	The Anodic Dissolution Curves for Ni 270 at pH 3.4 from 25°C to 125°C in the Noble to Active Scan Mode	178
109	The Anodic Dissolution Curves for Ni 270 at pH 3.4 from 150°C to 300°C in the Noble to Active Scan Mode	179
110	The Anodic Dissolution Curves from Ni 270 at pH 3.4 from 25°C to 125°C in the Noble to Active Scan Mode	180
111	The Anodic Dissolution Curves of Ni 270 at pH 3.4 from 150°C to 300°C in the Active to Noble Scan Mode	181
112	Variation of the Measured Hydrogen Redox Potential, $E(H^+/H_2)$, and the Corrosion Potential, E_{corr} , with Temperature at pH 1.3 and pH 3.4	182
113	Arrhenius Plot of the Minimum Passive Current Density and the Critical Current Density at pH 1.3 and pH 3.4	183

LIST OF TABLES

<u>Table No.</u>		<u>Page</u>
I	Chemical Compositions of Titanium Alloys (0.025" Sheet)	4
II	Stress Intensity Factors, Crack Growth Rates, and Emission Rates for a Hydrogen Level of 3.3%	80
III	Stress Intensity Factors, Crack Growth Rates, and Emission Rates for a Hydrogen Level of 6.9%	81
IV	Stress Intensity Factors, Crack Growth Rates, and Emission Rates for a Hydrogen Level of 7.1%	82
V	Stress Intensity Factors, Crack Growth Rates, and Emission Rates for a Hydrogen Level of 7.7%	82
VI	Effect of Arsenite Additions on the Hydrogen Permeability of Unpalladized AISI-1010 Steel at Room Temperature	101
VII	Effect of Arsenite Additions on the Hydrogen Permeability of Palladized AISI-1010 Steel at Room Temperature	103
VIII	Diffusivity of Hydrogen in Palladized AISI-1010 Steel. Hydrogen Charged from Arsenite-Acetate Solutions. Units: cm^2/sec	110
IX	Diffusivity of Hydrogen in Palladized AISI-1010 Steel for Various Thicknesses	112
X	Current Readings during Tests	134
XI	Free Energy of Formation of Species Considered	136
XII	Reactions and Equilibrium Formulae	139
XIII	Comparison of the Complex Refractive Indices, $\eta(1-ki)$ of Iron and Iron Base Alloys and their Anodic Films for $\lambda = 5461 \text{ \AA}$	155
XIV	Comparison of the Change of Film Thickness of Fe, Fe-10 Ni, Fe-10 Cr, and Fe-Cr-10Ni Alloys for One Hour of Polarization	165
XV	Summary of Entropy Constants for Eq. (6) (in $\text{cal mole}^{-1}\text{deg}^{-1}$)	166

SECTION I

INTRODUCTION

Stress-corrosion cracking is one of the most important, if not the most important, corrosion problem facing this country. Cracking often occurs prematurely with catastrophic results.

The program is aimed at developing fundamental information concerning the nature and control of stress-corrosion cracking including design of alloys and environmental control. Primary emphasis is on titanium alloys and high-strength steels.

Pursuant to the coupling aspects of this program, seven lectures and seminars were held at AFML by our staff, and a postdoctoral fellow was transferred to AFML and is conducting research there.

One Master's degree and one Doctor's degree were awarded during this period based on this research.

SECTION II

TITANIUM AND TITANIUM-BASE ALLOYS (F. H. Beck)

A. EFFECT OF APPLIED POTENTIAL ON CRACK INITIATION AND GROWTH FOR Ti-6Al-4V ALLOY IN METHANOL-WATER- SODIUM CHLORIDE SOLUTIONS (E. J. Timmer)

(This investigation was completed and was the basis of a thesis by
E. J. Timmer who received the M.Sc. degree in March, 1969)

1. Introduction

The purpose of this investigation was to study crack initiation and propagation in Ti-6Al-4V alloy in $\text{CH}_3\text{OH}-\text{H}_2\text{O}-\text{NaCl}$ solutions. Stress corrosion tests were conducted using smooth bend specimens which were observed at a magnification of 60X during the tests. The effects of applied potential, stress level, and environment upon the crack initiation time, failure time, and crack velocity were investigated.

2. Experimental

A schematic diagram of the apparatus used in this investigation appears in Fig. 1. It consists of a pyrex cell (in which the specimen and specimen holder were immersed in the methanol solution), a Luggin probe, a saturated calomel reference electrode, a Bausch and Lomb binocular viewer, and a Wenking potentiostat.

The specimen holder, constructed of fused silica, contained a 2-inch-long slot to receive the stress-corrosion bend specimen. Metal contacts of Ti-6Al-4V at the ends of the slot were used to provide an accurate and constant gage length and to provide an electrical connection from the specimen to the potentiostat. The stress on the outer fibers of the bend specimens was varied by changing the specimen length.

Stress corrosion specimens were made from Ti-6Al-4V alloy sheet of composition No. 1 given in Table I. This sheet was solution-heat-treated and then aged in a vacuum of 5×10^{-5} mmHg at 1100°F for six hours and furnace-cooled (treatment results in high susceptibility to stress-corrosion cracking). All samples were cut so that the longitudinal direction of the specimen corresponded to the rolling direction of the sheet. Specimens were 0.25" wide X 0.025" thick, and of a length predetermined to give the desired stress level when placed in the holder. The specimens were then lightly cleaned on all surfaces with 280-grit paper to remove excessive oxide; and finally, one of the large surfaces was metallographically polished through No. 2 alumina. This polished surface was placed in tension and viewed during the test.

The specimen and holder were then placed into the test cell,

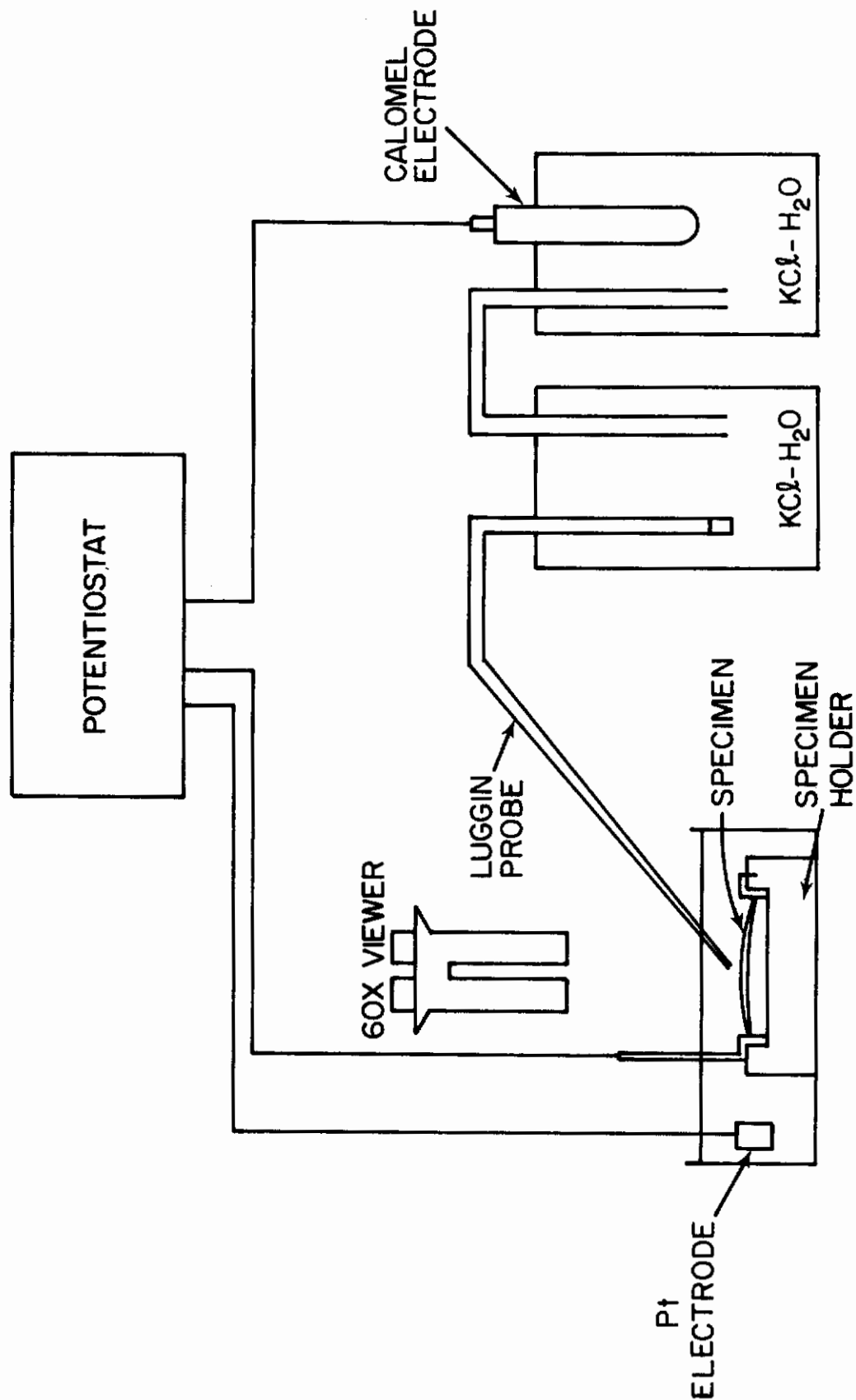


Fig. 1 - Experimental Apparatus

Table I - Chemical Compositions of Titanium Alloys
(0.025" sheet)

Element	Ti-8Al-1Mo-1V w/o	Ti-6Al-4V (w/o)	
		Alloy #1	Alloy #2
Al	7.85	6.30	6.75
V	1.05	4.10	4.00
Fe	0.13	0.19	0.30
Mo	1.1	--	--
C	0.02	0.03	0.10
N	0.008	0.01	0.05
O	0.08	0.106	0.20
H	102 ppm	60 ppm	150 ppm
Ti	balance	balance	balance

electrical connections were made, and the $\text{CH}_3\text{OH}-\text{H}_2\text{O}-\text{NaCl}$ solution was added. The Luggin probe was then positioned adjacent to the surface of the specimen being examined and the desired potential was applied. When the potential was applied a clock was started and continuous observation of the specimen surface was begun. The time for the first crack to be formed (cracks always originated from pits) was recorded as the initiation time, and failure time was recorded when the sample was cracked into two parts. Crack velocity was measured on the tension surface of the specimen. Current measurements were also recorded for some specimens during the tests.

In order to determine the crack path, the failed specimens were examined with the light microscope in the etched and unetched conditions at magnifications up to 2000X. In addition, replicas were made of the fracture surfaces of several specimens to provide electron fractographs. The two-step plastic-carbon replication technique was used.

3. Results

a. Effect of Potential

The effect of applied potential on crack initiation time, total failure time, and crack velocity is shown in Figs. 2 and 3. In these tests, the bend specimens were stressed to 80% of the yield stress in the outer fibers, and were immersed in a $\text{CH}_3\text{OH}-0.3\% \text{H}_2\text{O}$ -saturated NaCl solution. This solution was shown by several investigators^{1,2,3} to be the most effective in causing stress-corrosion cracking of titanium alloys. It is seen from Fig. 2 that Ti-6Al-4V alloy was susceptible to stress-corrosion cracking over a wide range of applied potentials, from approximately -650 mV to +500 mV (SHE). The crack initiation time and total failure time decreased significantly in this range with increasing anodic potential, and were minimum near +150 mV. Crack

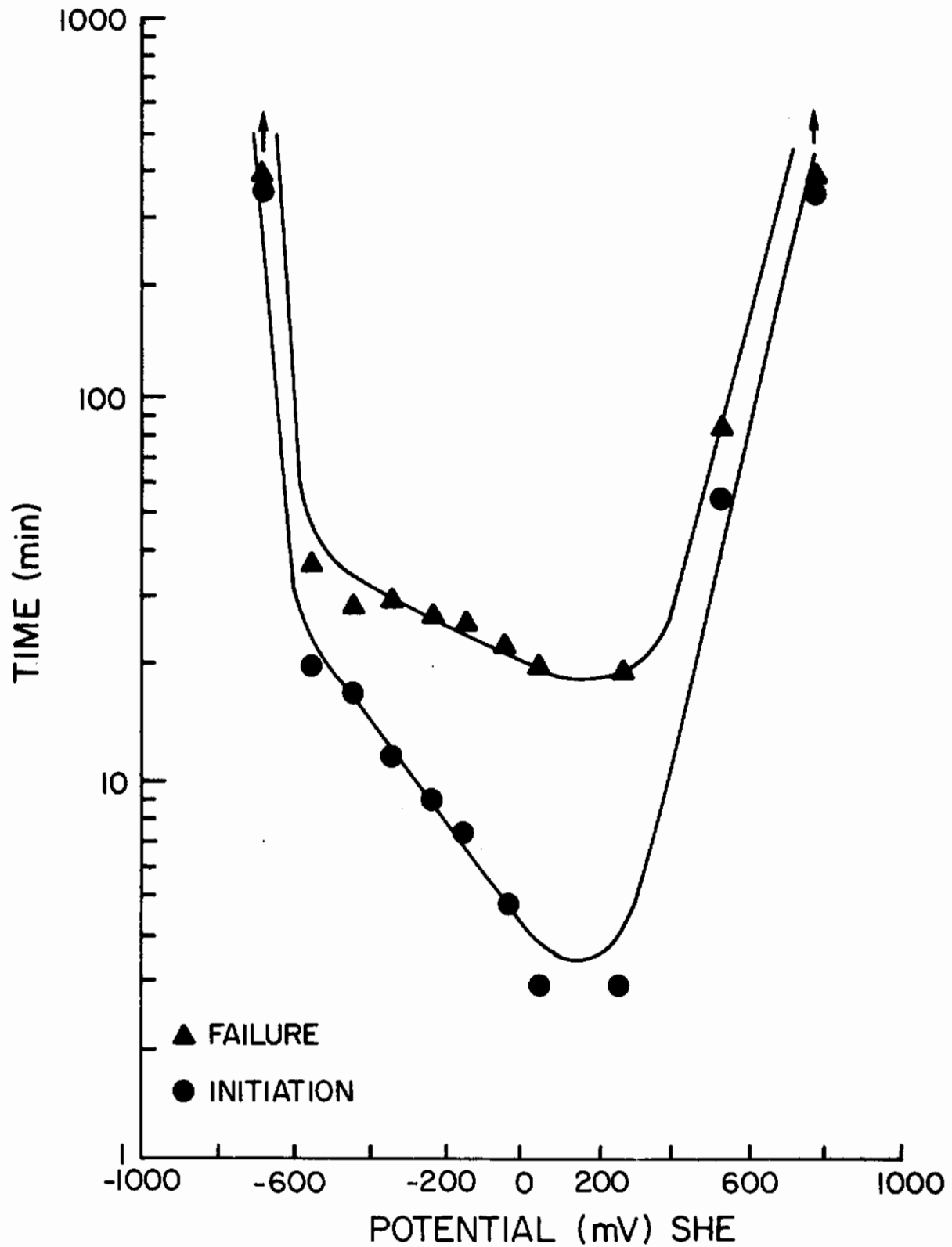


Fig. 2 - The Effect of Applied Potential upon Crack Initiation Time and Failure Time in Methanol-0.3% Water and Saturated NaCl

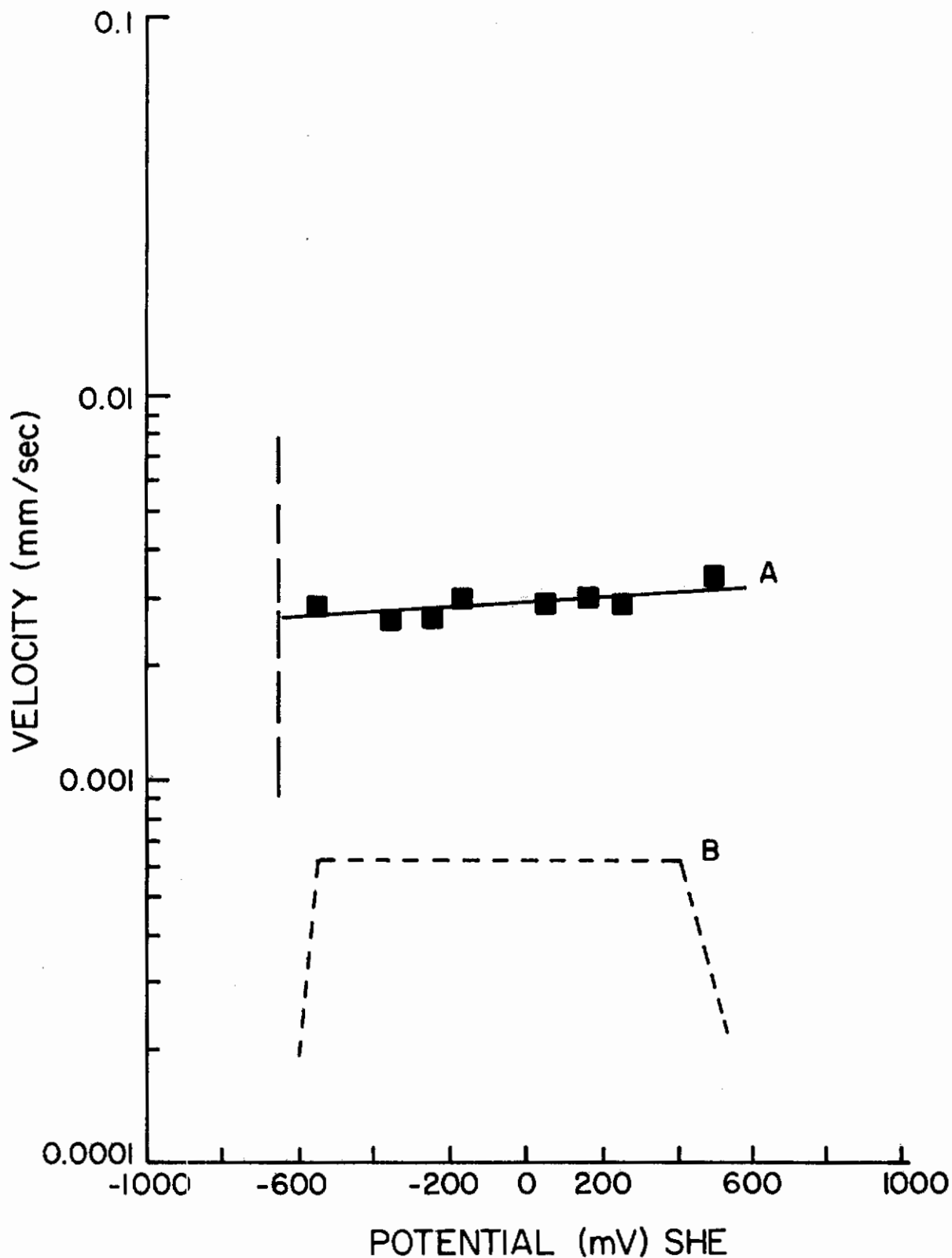


Fig. 3 - The Effect of Applied Potential upon Crack Velocity in Methanol-0.3% Water and Saturated NaCl
(A--measured on tension surface during test)
(B--calculated from total failure time minus initiation time)

velocity measured on the tension surface, however, increased only slightly with increasing potential, and was approximately 0.003 mm/sec in the susceptible potential range (curve A of Fig. 3). Curve B of Fig. 3 shows the crack velocity obtained by subtracting the crack initiation time from the total failure time. Although the crack velocity obtained by the latter method is somewhat lower than that measured on the tension surface, the crack velocity is still constant over a significant part of the susceptible potential range. At the extremes of the potential range investigated the alloy is much more resistant to stress corrosion as indicated by the sharp increase in both crack initiation and total failure times (Fig. 2). Curve B of Fig. 3 shows that crack velocity decreases rapidly with increases in cathodic and anodic potentials in the highly cathodic and highly anodic potential ranges. It appears that the crack initiation time has the predominant effect on the total time-to-failure in the highly susceptible potential region.

Each data point on the figures represents an average of between three and five test results. The data scatter for crack initiation times and failure times were approximately 0.5-1.0 minutes and 2-3 minutes, respectively. Cocks et al.⁴ showed that aging the test solution, methanol-bromine, had a considerable effect on the times-to-failure of Ti-6Al-4V alloy specimens and concluded that this was the cause of data scatter in many reports. Therefore, in all of the tests conducted during this investigation, the $\text{CH}_3\text{OH}-\text{H}_2\text{O}-\text{NaCl}$ solutions were allowed to age for five hours before the tests. In addition, it has been shown⁵ that a mechanically polished surface on a stress-corrosion cracking specimen produced the least data scatter of any surface preparation; and, therefore, this technique was also used.

b. Effect of Stress

Figures 4 and 5 show the relation of stress to crack initiation time, failure time, and crack velocity. Increasing the stress was found to decrease total failure time and to increase crack velocity. In addition, crack initiation time decreased with increasing stress. A threshold stress of about 60% of the yield stress was necessary to initiate stress-corrosion cracking. A potential of 0 mV was applied to the specimens during these tests in order to shorten the testing time. $\text{CH}_3\text{OH}-0.30\% \text{ H}_2\text{O}$ -saturated NaCl solution was used.

c. Effect of Solution Composition

The effects of sodium chloride and water concentrations were determined by holding either the water at 0.3% or the sodium chloride at saturation. The effect of water content on initiation time, failure time, and crack velocity appears in Figs. 6 and 7. When water concentration is varied, both crack initiation time and failure time show a minimum at approximately 0.2% water. Velocity measured on the tension surface was found to be independent of water content (curve A) and to show a maximum at about 0.2% (curve B, total failure time minus initiation time).

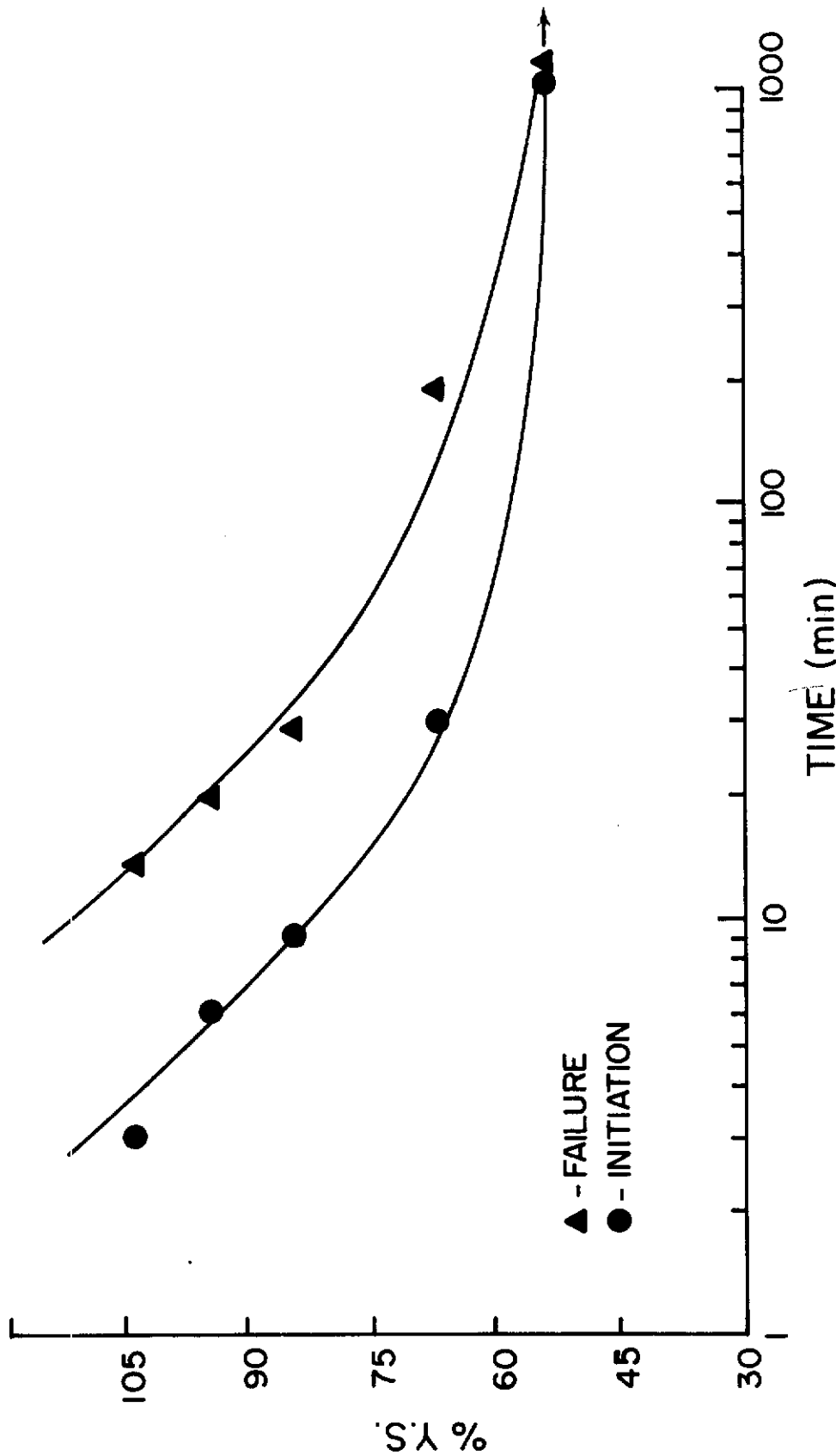


Fig. 4 - The Effect of Stress Level upon Crack Initiation Time and Failure Time in Methanol-0.3% Water and Saturated NaCl at 0 mV

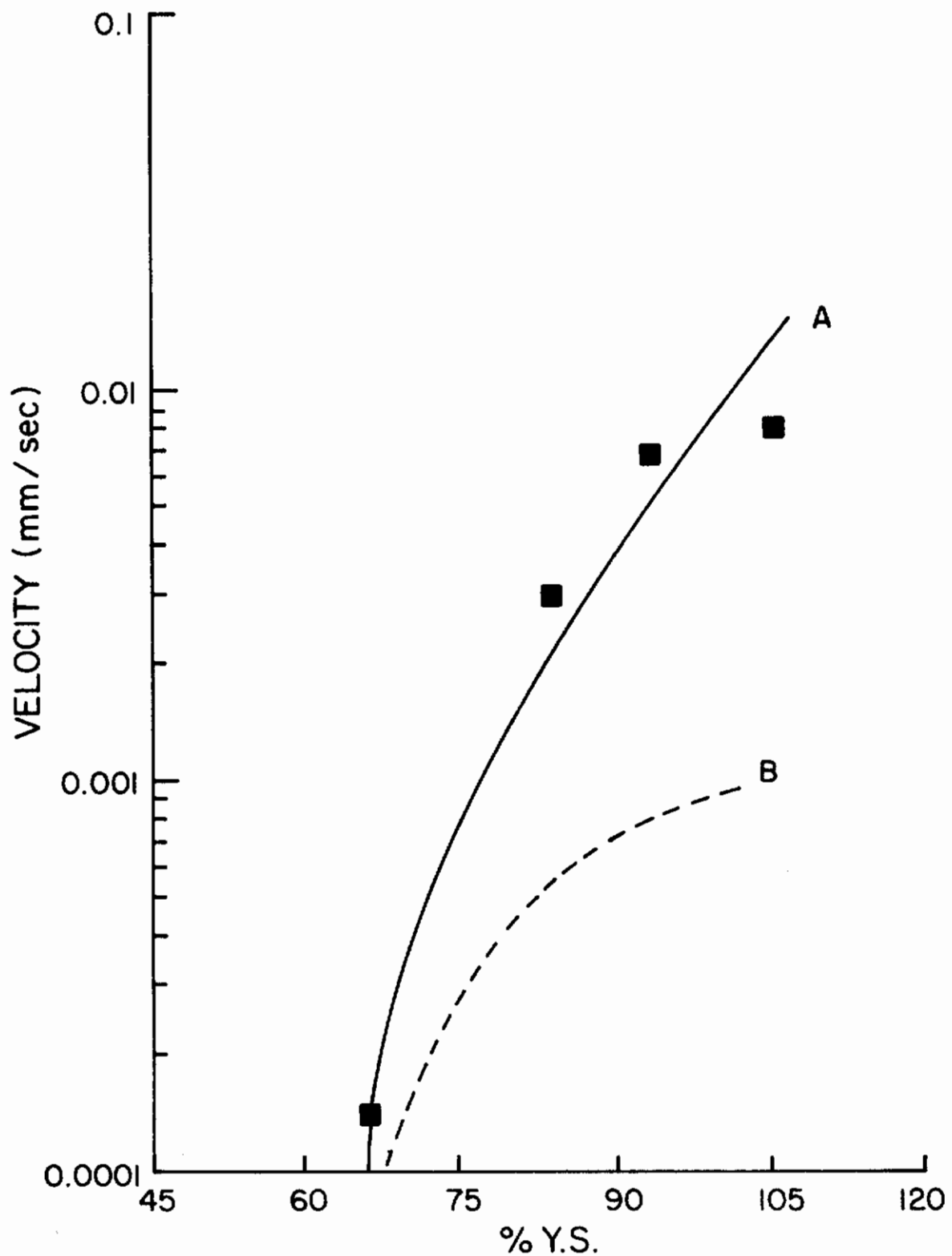


Fig. 5 - The Effect of Stress Level upon Crack Velocity. Specimen Polarized at 0 mV in Methanol-0.3% Water Saturated NaCl (A--measured on tension surface during test) (B--calculated from total failure time minus initiation time)

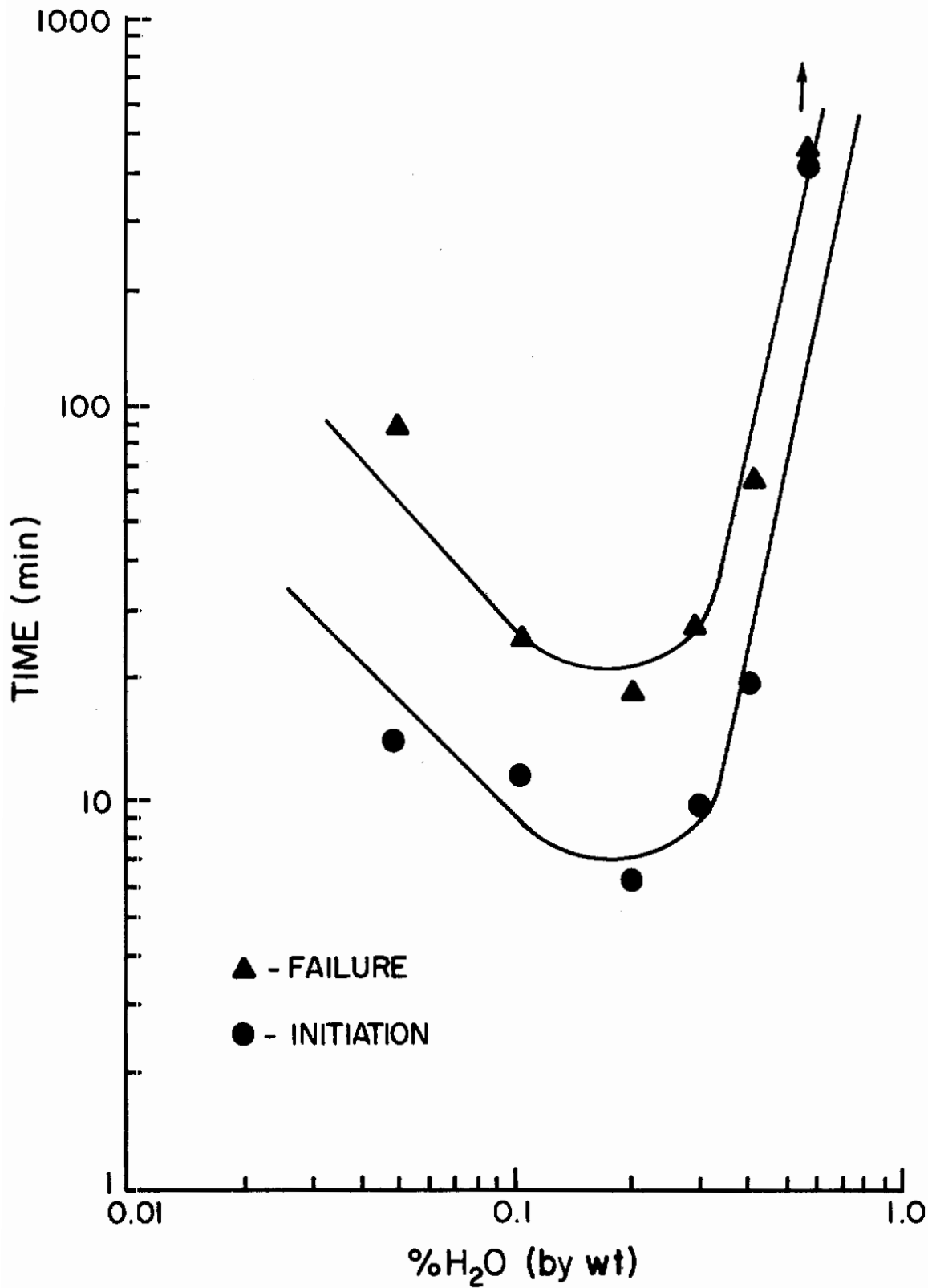


Fig. 6 - The Effect of Water Content upon Crack Initiation Time and Failure Time. Specimens Polarized at 0 mV and Stressed to 80% of the Yield Strength in Methanol-Saturated NaCl

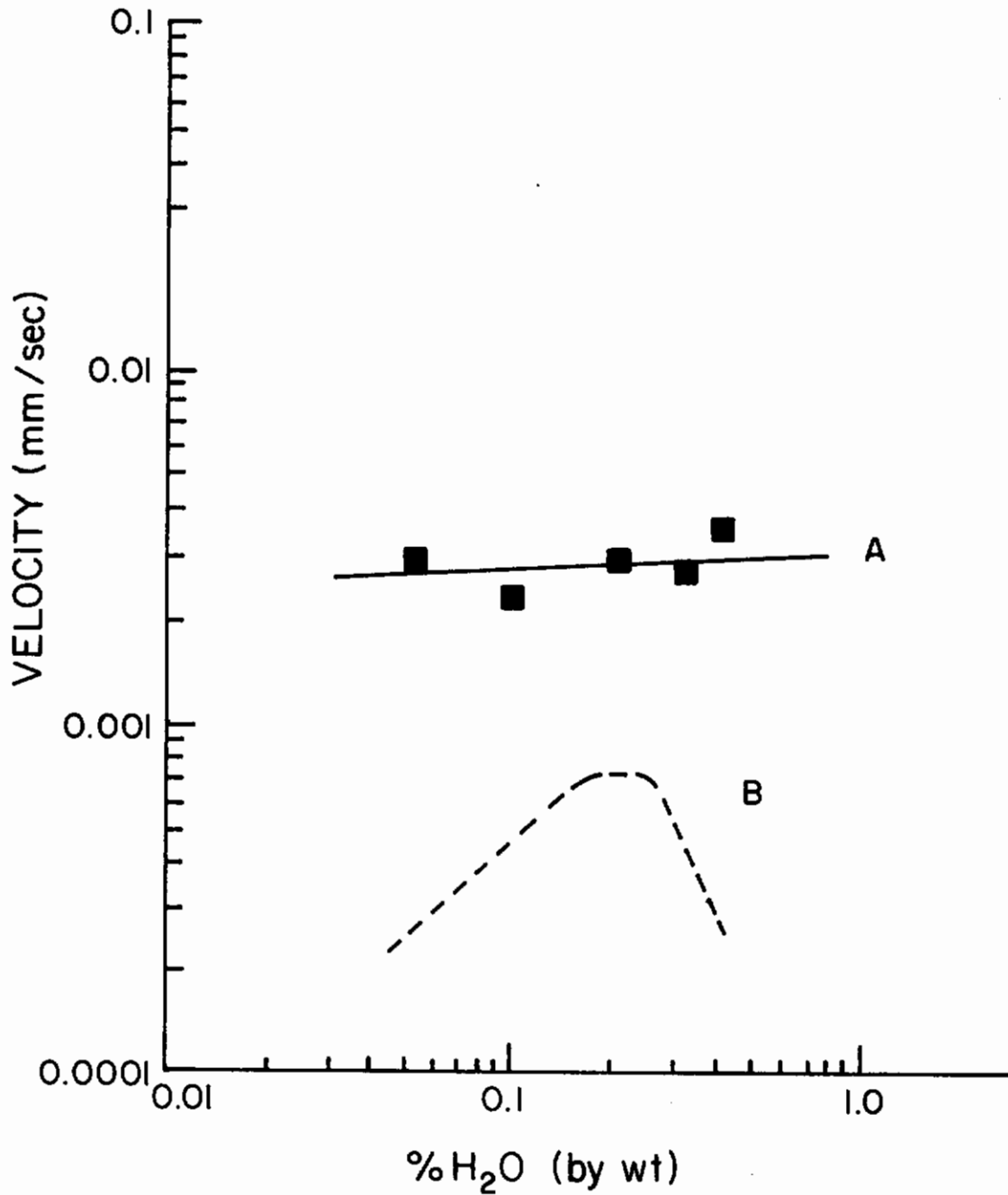


Fig. 7 - The Effect of Water Content upon Crack Velocity. Specimen Polarized at 0 mV and Stressed to 80% of the Yield Strength in Methanol-Saturated NaCl (A--measured on tension surface during test)(B--calculated from total failure time minus initiation time)

Figures 8 and 9 show that crack initiation time and failure time decrease with increasing sodium chloride concentration and that the minimum times occur in a saturated sodium chloride solution; i.e., at 0.195N NaCl. Only two points exist for the change in crack velocity with sodium chloride concentration; it appears that velocity was relatively independent of the chloride content (curve A) and increased slightly with NaCl concentration (curve B). The most aggressive environment for causing stress-corrosion cracking of Ti-6Al-4V alloy appears to be CH₃OH containing 0.2% water and saturated with NaCl.

d. Visual and Metallographic Results

Crack initiation and propagation were observed at 60X on smooth specimens of Ti-6Al-4V alloy in CH₃OH-H₂O-NaCl solutions. After the potential was applied, black spots (surface pits) began to appear on the surface. During the incubation time, these pits would grow in diameter and in depth until much black corrosion product was evident around the pits. Abruptly, cracks were seen propagating from the pits in a direction perpendicular to the applied tensile stress. The individual cracks would then proceed to grow until another crack from another pit was encountered. The total failure of the specimen resulted from cracks being formed at various pits on the surface and interconnecting with one another across the specimen width. At the cathodic potentials, little general surface dissolution occurred; however, as the potential was increased, the surface dissolution was increased until at approximately +500 mV the entire sample was covered with a black corrosion product and no pits were seen.

Photomicrographs of cracks that propagated from surface pits appear in Figs. 10 and 11 and emphasize how localized disintegration occurs around the pits. Figure 12 shows selective attack of the α - β interface and β particles during pit formation and disintegration. Stress-corrosion cracks in a failed specimen are shown in Fig. 13. Cracking is intergranular along α - β interfaces and transgranular through some α grains. Figures 14 and 15 are electron fractographs from failed specimens and show that failure was associated with intergranular fracture, cleavage fracture, and ductile fracture. Figure 15 also shows quasi-cleavage fracture.

4. Discussion

The results presented in Figs. 2 - 15 support the observations of Sedriks et al.¹ that the stress-corrosion cracking of smooth specimens of Ti-6Al-4V alloy in CH₃OH-H₂O-NaCl solutions can be separated into a crack initiation stage that is associated with anodic dissolution, and a crack growth stage that is associated with predominantly mechanical failure. During the crack initiation stage, preferential corrosion was observed at the α - β interfaces and intergranular β particles, and resulted in localized anodic disintegration and pit formation. The crack growth stage was associated with intergranular cracking and transgranular cleavage cracking. The crack velocity on the tension surface

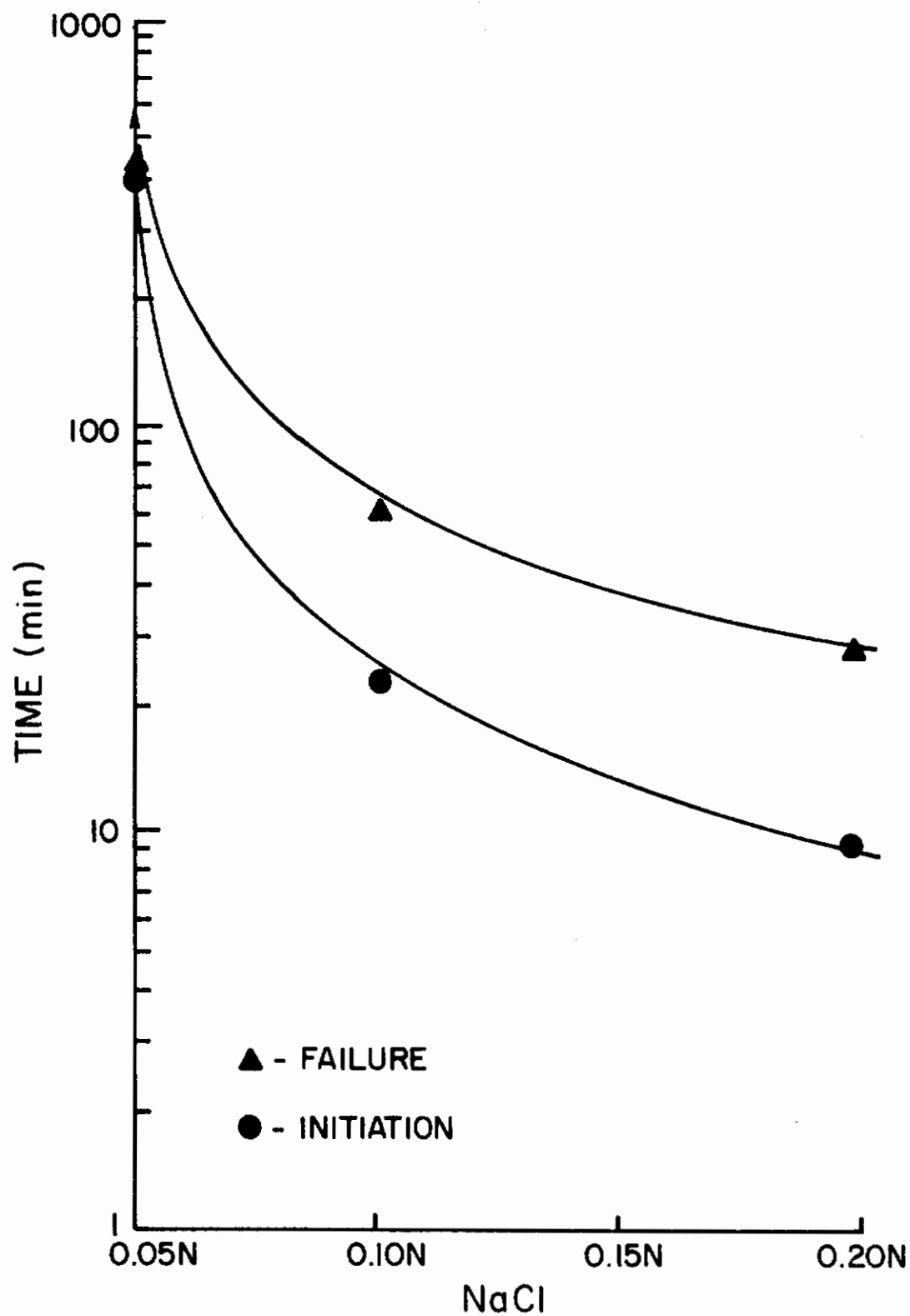


Fig. 8 - The Effect of NaCl Content upon Crack Initiation and Failure Times. Specimens Polarized at 0 mV and Stressed to 80% of the Yield Strength in Methanol-0.3% Water

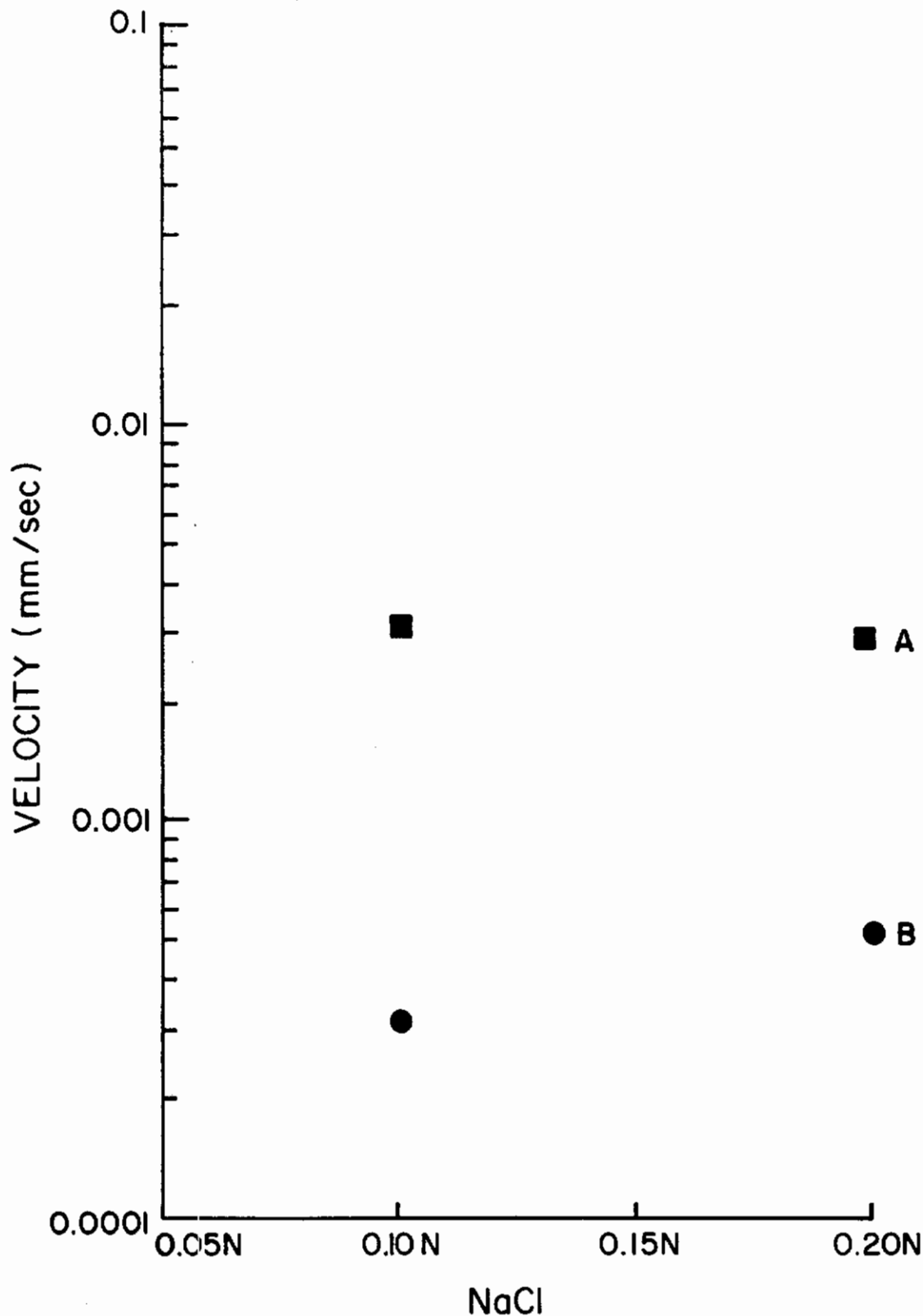


Fig. 9 - The Effect of NaCl Content upon Crack Velocity. Specimens Polarized at 0 mV and Stressed to 80% of the Yield Strength in Methanol-0.3% Water (A--measured on tension surface during test) (B--calculated from total failure time minus initiation time)



Fig. 10 - Crack Propagation from a Pit.
Magnification 250X. Unetched.

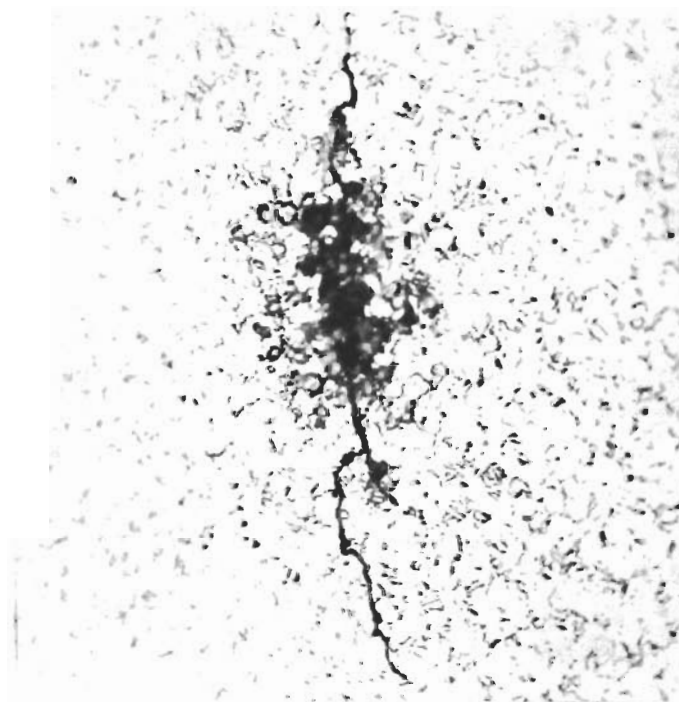


Fig. 11 - Crack Propagation from a Pit.
Kroll's Etch. Magnification 500X.

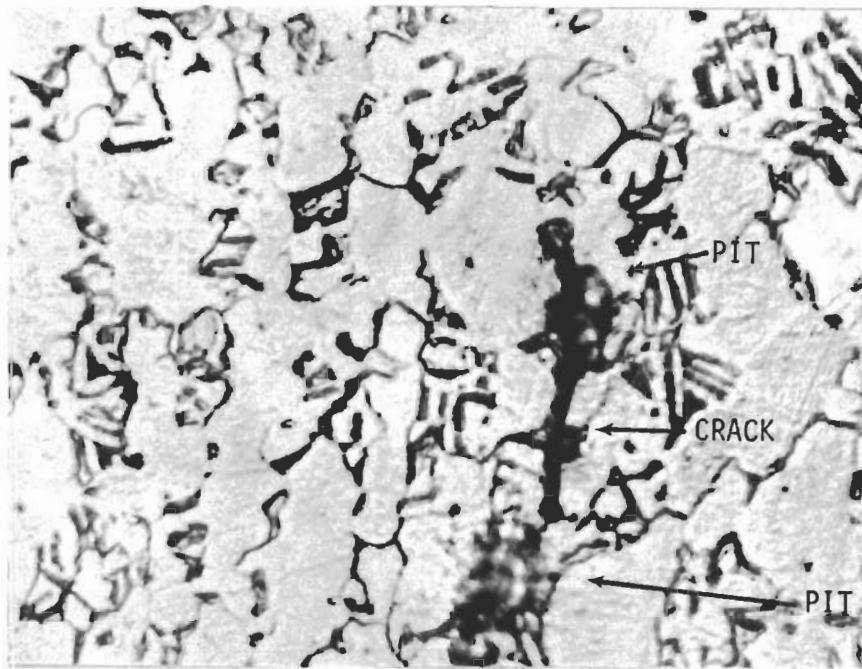


Fig. 12 - Preferential Corrosion at the α - β Interface and β Phase in Ti-6Al-4V. (Note: micro-crack between two small pits) Kroll's Etch. Magnification 2000X.

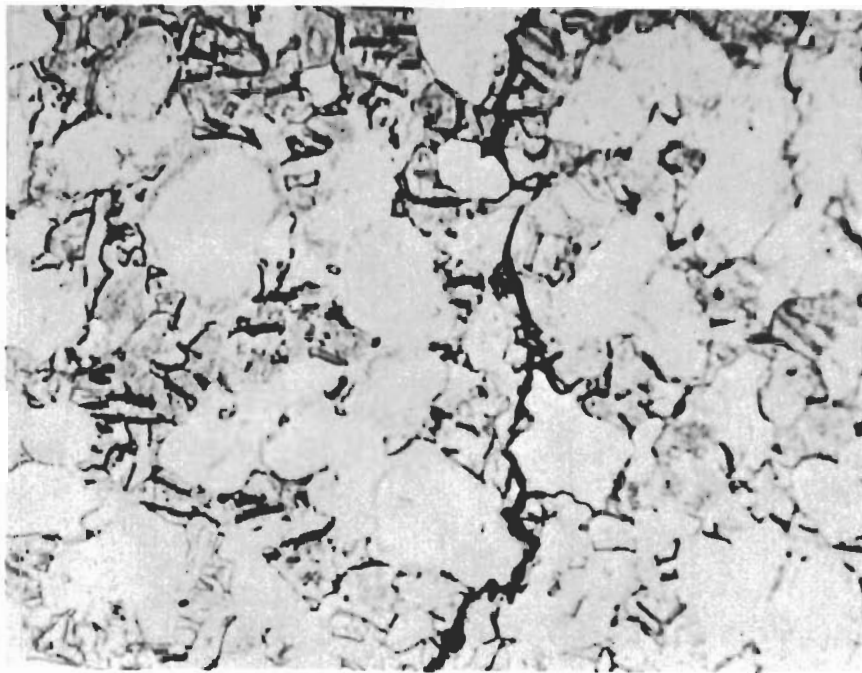


Fig. 13 - Cracks in a Failed Ti-6Al-4V Specimen. (Note: black areas associated with preferential α - β interface corrosion) Kroll's Etch. Magnification 2000X.



Fig. 14 - Electron Micrograph of Fracture Surface of Ti-6Al-4V Specimen. (Note: cleavage fracture) Magnification 7000X.

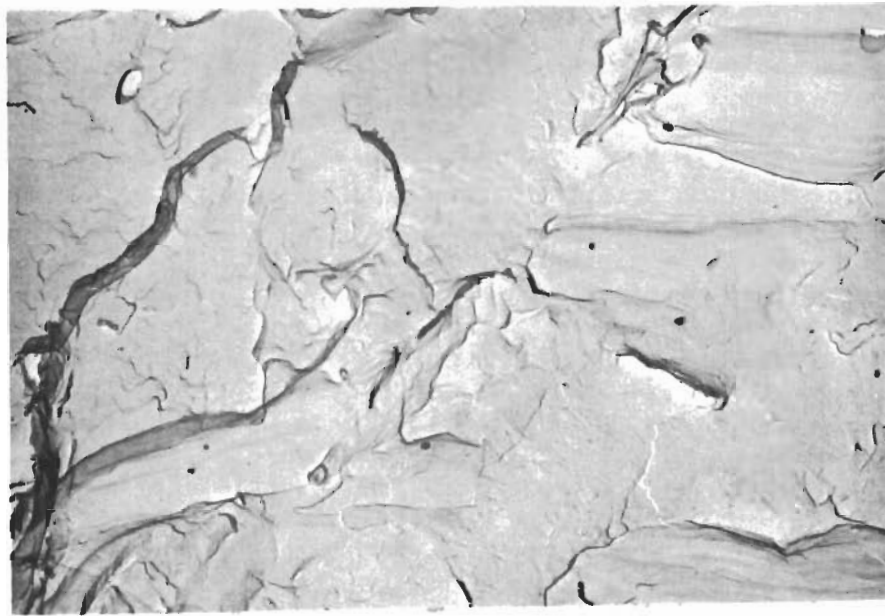


Fig. 15 - Electron Micrograph of Fracture Surface of Ti-6Al-4V Specimen. (Note: intergranular fracture and quasi-cleavage fracture) Magnification 7000X.

was found to be independent of applied potential but very dependent upon stress level.

Significantly, the crack initiation stage is shown in Figs. 2 and 3 to have the predominant influence upon the total time-to-failure of the specimens since crack velocity is essentially constant over the entire potential range. This result is in agreement with the work of Green and Myers⁶ who found that crack propagation in Type 302 stainless steel in boiling MgCl_2 did not appear to have an appreciable effect upon the total time-to-failure. The variation in failure times of the specimens is attributed to the variation in crack incubation time. Thus, if the crack initiation time is long, the total failure is long, and vice versa. Therefore, by controlling the crack initiation time, the total failure time of the specimen can be controlled.

Figure 2 shows the variation of crack initiation time with applied potential in CH_3OH -0.3% H_2O -saturated NaCl solution. From this, and from visual and metallographic results, it is apparent that the crack incubation stage of the stress-corrosion process in smooth specimens of Ti-6Al-4V alloy consists of localized anodic dissolution of the metal at α - β interfaces, β particles, and some grain boundaries. This produces disintegration and eventual pit formation at localized areas. Corrosion continues to occur at these sites until a pit of sufficient depth to cause crack growth is formed. The presence of a black corrosion product at the pits was identified by others.⁷

As the potential is increased in the anodic direction past the open-circuit corrosion potential of the specimens (-550 mV), significant localized anodic dissolution occurs on the surface and, in time, a few scattered pits form. A further increase in potential in the anodic direction (in the susceptible range) results in more pits being formed and in an increase in current density at these pits. Menzies and Averill⁷ observed that anodic disintegration of titanium in CH_3OH -HCl solutions began at localized areas and progressed over the entire surface as the current density was increased. This effect explains why the crack initiation time was decreased with increasing potential in this range.

In the susceptible potential range (i.e., up to approximately +150 mV) corrosion of the specimen is confined to pits and adjacent areas (Fig. 10 and 11). However, as the potential is increased past +150 mV, black corrosion product begins to appear over more and more of the surface until at a potential of +500 mV the entire surface is covered. Thus, the localized anodic disintegration and pitting in the susceptible range changed to general disintegration over the entire surface as the potential was increased above +150 mV. Although the corrosion rate was more rapid at the higher potentials, the anodic disintegration occurred uniformly over the surface so that no deep pits could form. This effect explains why the Ti-6Al-4V specimens appear to become more resistant to stress-corrosion cracking at the higher anodic potentials (< +150 mV). The high resistance of Ti-6Al-4V specimens to crack initiation at cathodic potentials (below -650 mV) is related to the lack of corrosion, i.e., black corrosion product.

Figure 4 shows that increasing the stress level brought about a decrease in the incubation time for cracking and is associated with exposing more of the alloy surface (active sites) to the solution. Thus, the pits could form at a faster rate at the higher stresses, and, in turn, could reduce the crack initiation time.

The effect of water concentration upon crack initiation time, failure time, and crack velocity, as illustrated in Figs. 6 and 7 concur with those of Haney et al.² and can be explained in a similar manner.

It is concluded that the minimum in the failure time versus water concentration curve occurred when the grain boundaries were barely passivated. As more water is added to the methanol solutions, at constant potential, the quality of passivity on the bulk grain surface improves and the current densities at the active α - β interfaces and the β particles increases so that less time is required for the pits to grow to the critical depth. The critical water content, 0.2% H_2O , is associated with the α - β interfaces and intergranular β particles being barely passivated. At water contents above 1 wt.%, the entire alloy surface is passivated and no corrosion occurs.

The effect of the sodium chloride concentration upon crack initiation time (Fig. 8) may be explained as follows: As the corrosion pits form on the surface of the Ti-6Al-4V alloy in $CH_3OH-H_2O-NaCl$ solution, chloride ions diffuse from other areas on the surface or from the solution to the pits in order to continue the anodic disintegration associated with the crack initiation stage. At low sodium chloride concentrations much migration of the chloride ions would have to occur to continue pitting attack; and, therefore, the time taken for this build-up of chloride ion concentration could account for the increased incubation period. This effect would be more pronounced the lower the sodium chloride concentration.

T. R. Beck⁸ has shown that in aqueous NaCl solutions the crack velocity in Ti-8Al-1Mo-1V increased with increasing chloride concentration and increasing anodic potential, and concluded that crack velocity was dependent upon electrochemistry. He qualified this conclusion by stating that it was applicable only to those titanium alloys without α_2 dispersion strengthening and, therefore, of low yield strength. However, for titanium alloys that have been heat treated to give a dispersion of α_2 (Ti Al) in the matrix, and to have a high yield strength, Beck concluded that the crack velocity was given by the expression:

$$v = v_o + v_m, \text{ where}$$

$$\begin{aligned} V &= \text{total crack velocity,} \\ V_o &= \text{electrochemical term, and} \\ V_m &= \text{mechanical term.} \end{aligned}$$

V_o increases with increasing sodium chloride concentration, applied potential, and increasing stress level, while V_m increases with increasing stress level.

Since the Ti-6Al-4V alloy in the present study was heat treated at a temperature to precipitate α_2 in the matrix and, thus, have a high yield stress, the equation for total crack velocity was valid in this work. From Figs. 3 and 5, V_o , the electrochemical velocity, was found to be negligible, and, therefore, the crack velocity in $\text{CH}_3\text{OH}-\text{H}_2\text{O}-\text{NaCl}$ solutions was associated primarily with V_m , the mechanical failure velocity.

Greene⁹ has observed a potential drop of approximately one volt down a stainless steel crevice specimen in aqueous sodium chloride solutions; recently, Chen¹⁰ has shown the same effect for a Ti-8Al-1Mo-1V alloy crevice specimen immersed in $\text{CH}_3\text{OH}-0.63\% \text{H}_2\text{O}-0.37\% \text{HCl}$ solution. A potential drop of approximately 150 mV was observed and increased with decreasing crevice width. Therefore, although the potential applied on the surface of a stress-corroding specimen may be anodic, the potential at some depth below the surface in a pit or a crack might be low enough to cause hydrogen evolution. Crack initiation time could be associated with the time needed for the pit to reach the critical depth where hydrogen evolution could occur, and either hydride or hydrogen embrittlement resulting from this crevice effect could account for the cleavage fracture observed in this system.

B. CREVICE EFFECT DURING POLARIZATION OF Ti-8Al-1Mo-1V ALLOY IN AQUEOUS AND METHANOL ENVIRONMENTS (C. M. Chen)

1. Introduction

If polarization is applied for either anodic^{11,12,13,14}, or cathodic¹⁵ protection, a crevice effect in some special cases will be important.⁹ The same effect should also occur at the apex of cracks or fissures in stress-corrosion specimens during polarization and it is clear that a large potential gradient could exist in the crevice. This gradient is caused by the high resistance of the narrow electrolyte path.^{9,16} Thus, although a crack exterior is polarized to a certain potential, the crack interior could remain at a different potential. The purpose of the present experiments is to determine the factors influencing this crevice effect at the crack apex when polarization is applied to a stress-corrosion specimen.

2. Experimental

Experiments were performed with the apparatus illustrated in Fig. 16. A sheet specimen of Ti-8Al-1Mo-1V alloy measuring 4.5" x 0.025" of the composition given in Table I was secured to one side of the specimen holder through the backup plate by screw, S_1 , and the crevice size was adjusted by screw, S_2 . After setting the crevice size the crevice assembly was tightly wrapped with Teflon tape up to the position indicated to prevent solution from entering the crevice from the edges. The entire assembly was then immersed into the test solution to the indicated

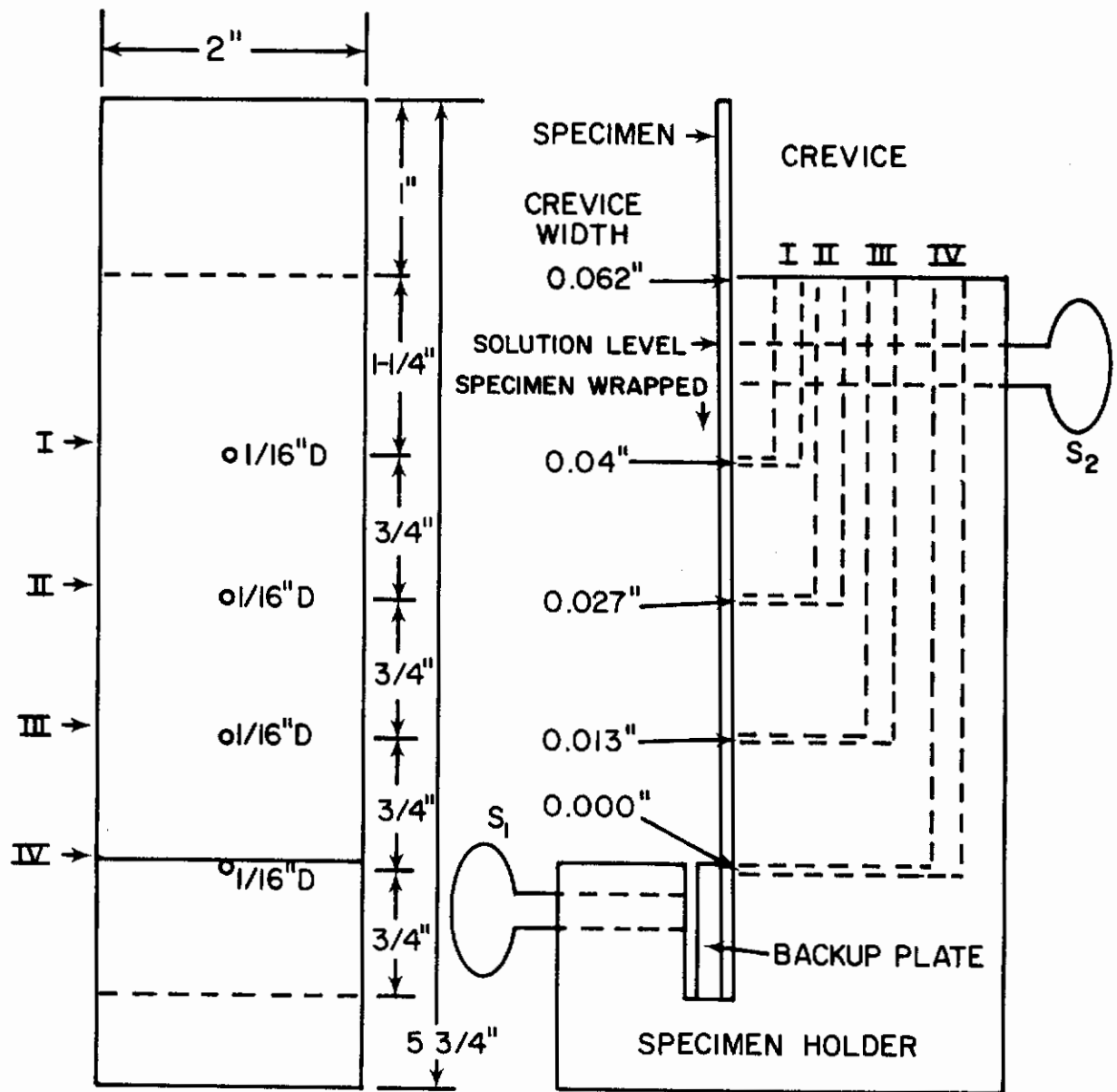


Fig. 16 - Cell for Crevice Effect on Ti-8Al-1Mo-1V Alloy (Specimen holder, backup plate and screws S₁ and S₂ are lucite)

level and the specimen was polarized using a platinum electrode and a Luggin probe located at the crevice exterior. Potentials in the crevice were measured by four Luggin probes inserted in the four probe openings (in the Lucite specimen holder) which were located at 3/4-inch intervals into the crevice. All potentials were measured against saturated calomel electrodes.

3. Results

a. Crevice Effect in Sulfuric Acid Solution

Polarization potential at the crevice interior is plotted as the ordinate and polarization potential at the crevice exterior is plotted as the abscissa in the following figures. When the experiment was carried in 1N H_2SO_4 solution, there was essentially no crevice effect as shown in Fig. 17. Upon increasing the acid in the solution to 10N H_2SO_4 , the critical current density for passivation was greatly increased and a crevice effect occurred as a result of the large anodic dissolution current in the active potential region as shown in Fig. 18. When the crevice exterior became passive, the crevice interior remained active until a certain higher polarization potential was attained. Finally, when the potential at the crevice exterior was high enough, say 1100 mV for crevice I (see Fig. 16), a potential of 1000 mV was observed for crevices II and III and 200 mV for crevice IV; in time, the respective crevice regions gradually became passive from exterior to interior and the crevice effect gradually disappeared.

b. Crevice Effect in KBr Solution

As shown in Fig. 19, the anodic current is very small at polarization potentials below that for halogen ion attack and there is no observed crevice effect. When the anodic polarization was increased to approximately 1100 mV, bromide ion attack occurred and a crevice effect appeared. The potential in the crevice remained constant with a further increase in anodic polarization.

c. Crevice Effect in KI Solution

No crevice effect appeared until the anodic reaction, $2I^- \rightarrow I_2 + 2e$ occurred at approximately 650 mV as shown in Fig. 20 and the potential in the crevice remained constant as the polarization potential was raised to about 2050 mV. When the polarization potential was further increased above 2050 mV, pitting due to halogen ion attack occurred and the current again increased. Although pitting occurred at the crevice exterior, it did not occur within the crevice and the potential within the crevice remained constant.

d. Crevice Effect in Methanol Solutions

When anodic polarization was applied to the titanium-methanol system in the absence of a passivator, anodic dissolution or

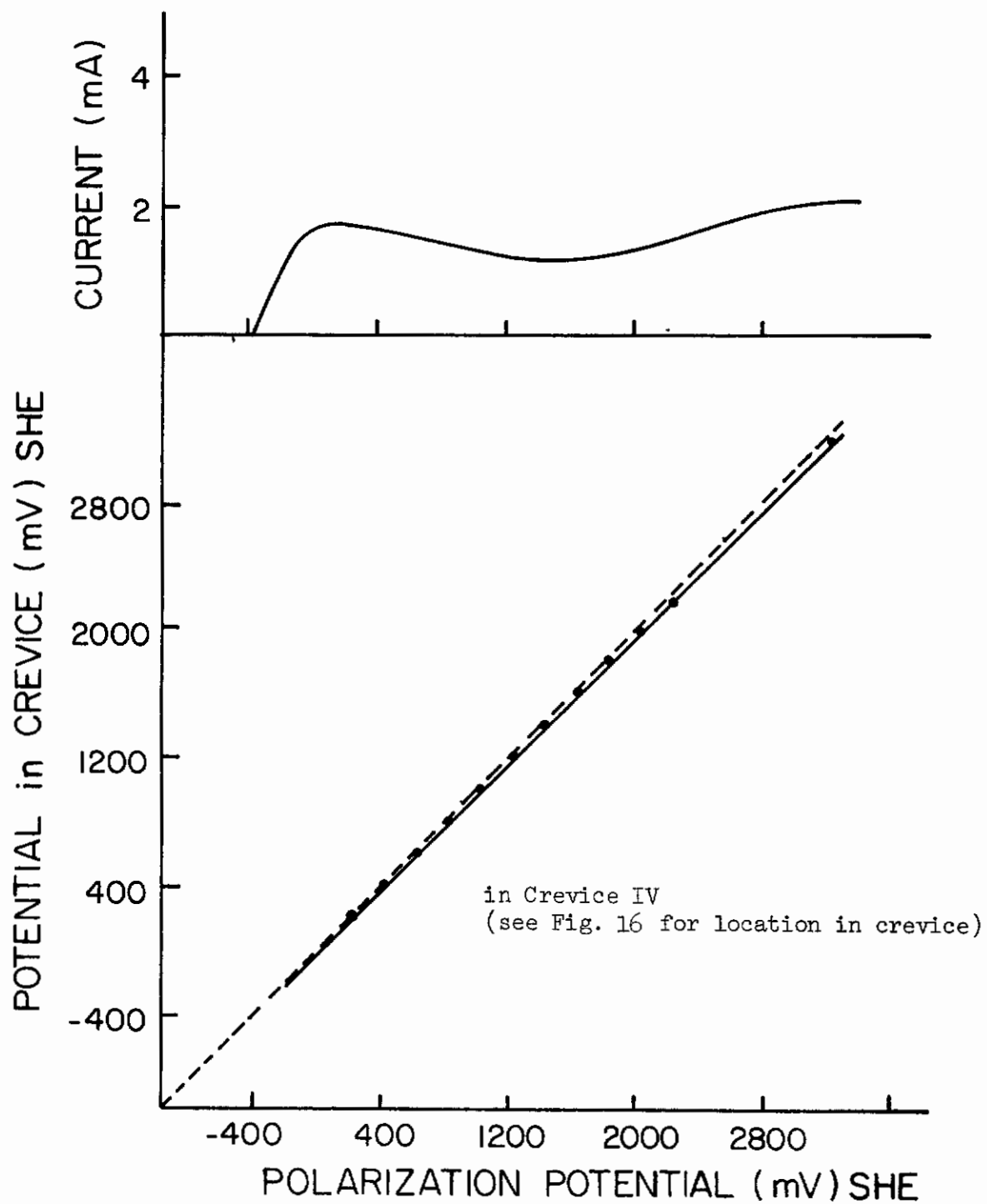


Fig. 17 - Polarization Potential at Crevice Exterior vs. Potential in Crevice (Ti-8Al-1Mo-1V in 1N H_2SO_4)

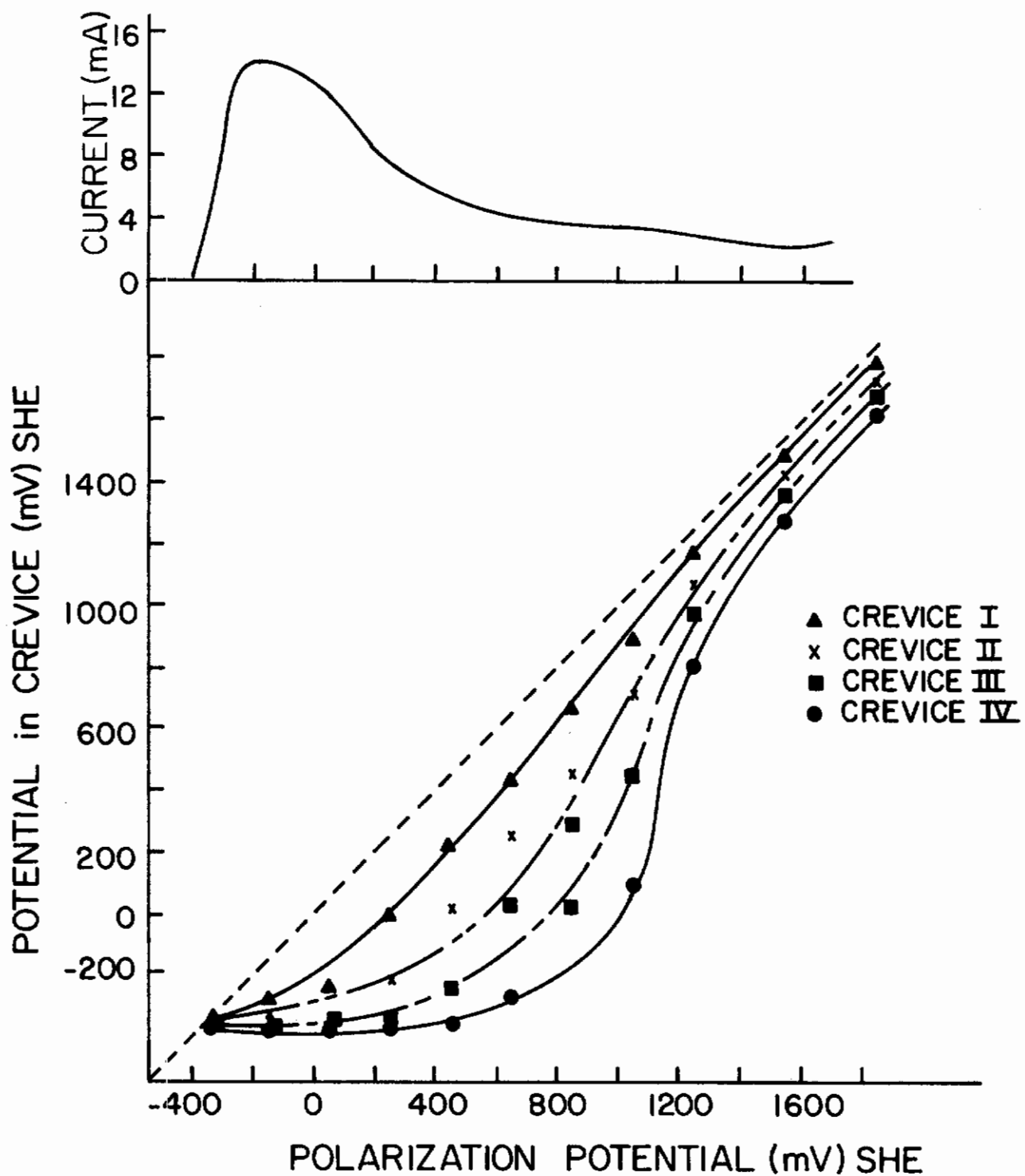


Fig. 18 - Polarization Potential at Crevice Exterior vs. Potential in Crevice (Ti-8Al-1Mo-1V in 10N H_2SO_4)

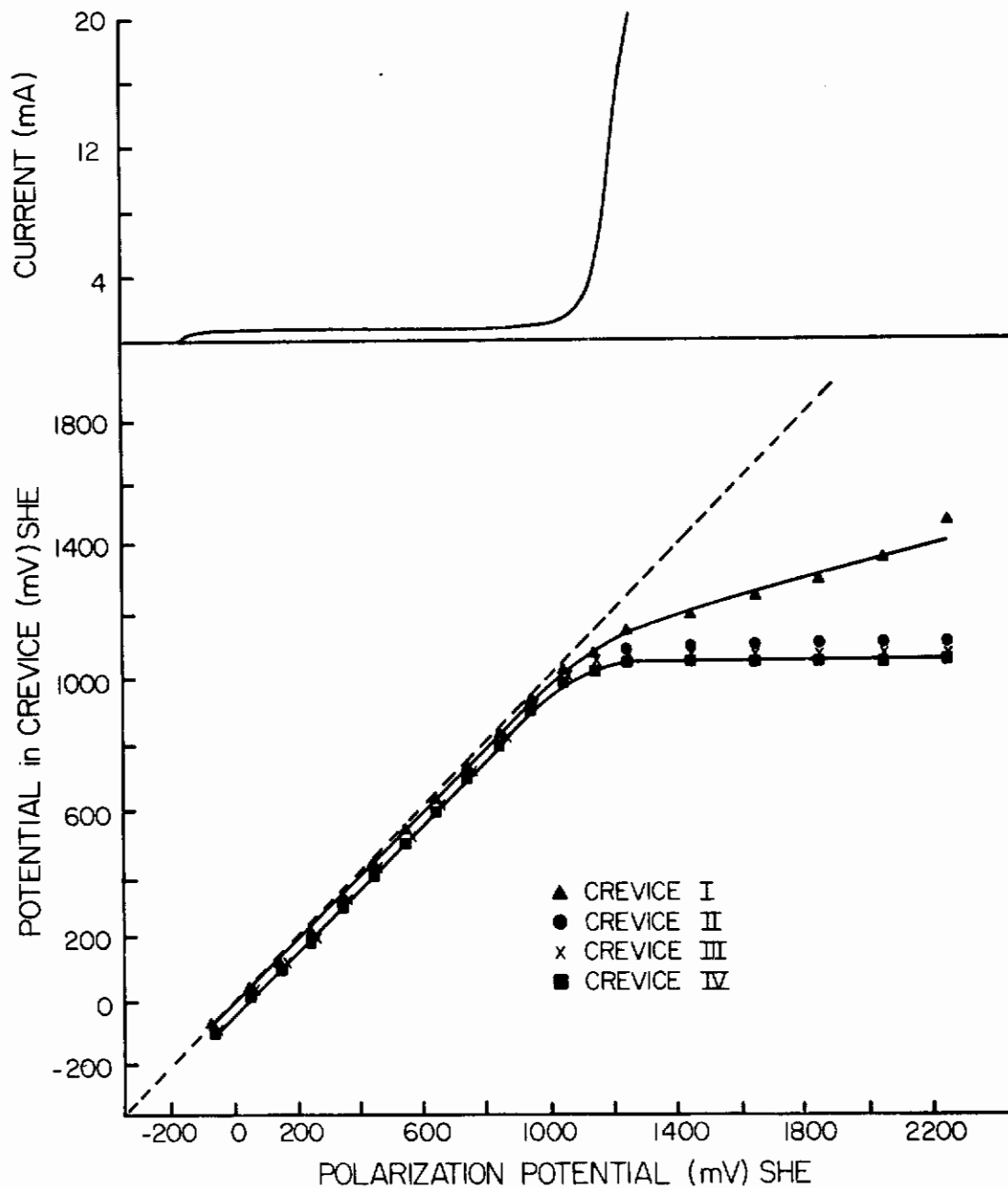


Fig. 19 - Polarization Potential at Crevice Exterior vs. Potential in Crevice (Ti-8Al-1Mo-1V in 0.6N KBr)

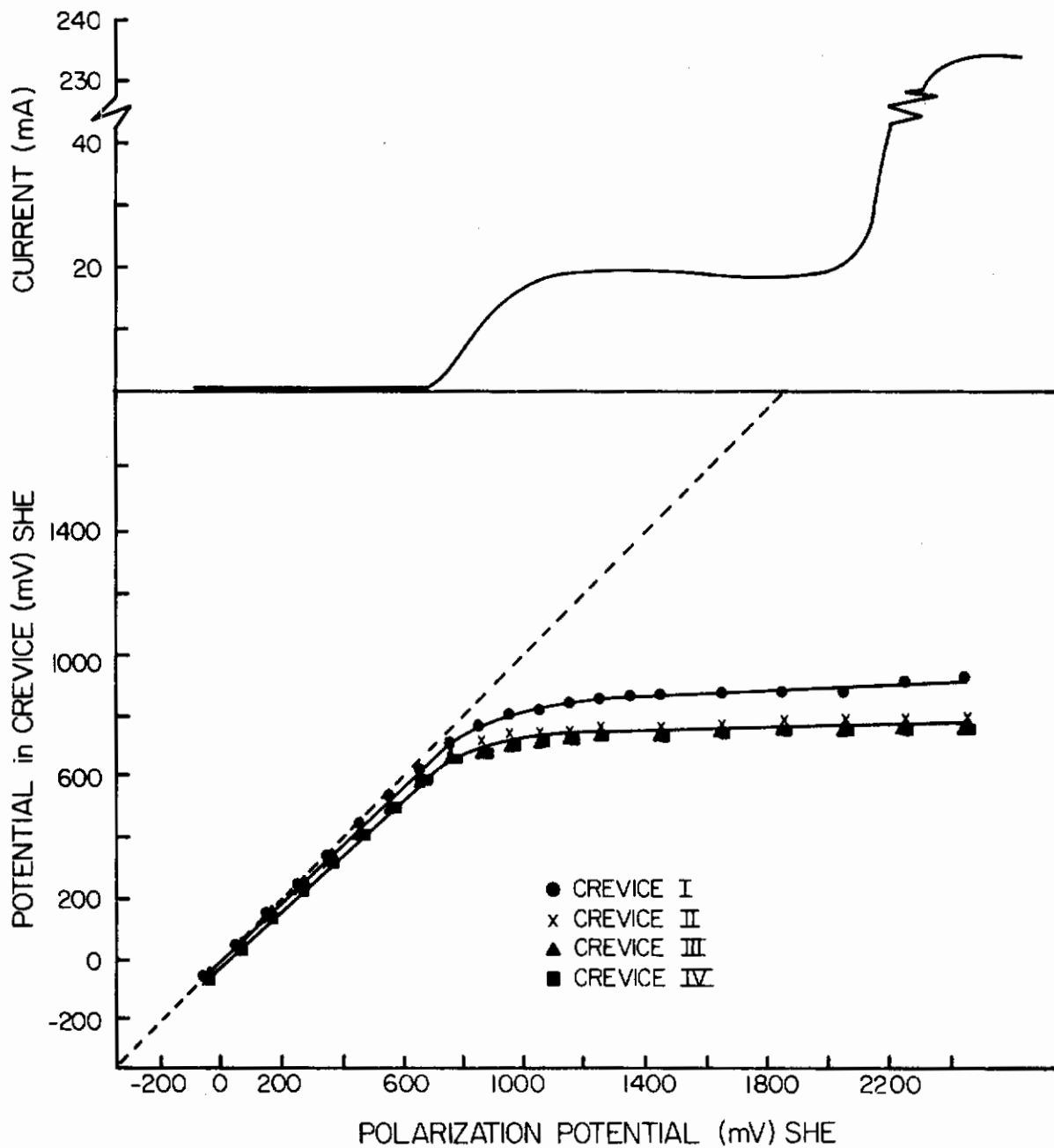


Fig. 20 - Polarization Potential at Crevice Exterior vs. Potential in Crevice (Ti-8Al-1Mo-1V in 0.6N KI)

halogen ion attack occurred and a crevice effect appeared. Figure 21 is for titanium in methanol + HCl solution and Fig. 22 is for titanium in $\text{CH}_3\text{OH} + \text{H}_2\text{SO}_4$ solution.

e. Crevice Effect during Cathodic Polarization

Figure 23 shows the crevice effect resulting from cathodic polarization of titanium in 0.6M KI solution. When hydrogen gas evolution occurred, the crevice effect appeared. The crevice effect in cathodic polarization results in the crevice potential deviating to the more anodic direction; whereas, in anodic polarization the potential shifts in the more cathodic direction.

4. Discussion

It has been shown^{17, 18} that the susceptibility of titanium and its alloys to stress-corrosion cracking is potential dependent. Further, it is demonstrated in the present paper that a crevice effect should exist in a crack, and that the polarization potential and the potential at the crack apex can be quite different. This crevice effect occurs from IR drops in the crevice. Therefore, when certain electrochemical reactions occur and, in so doing, cause the polarization current to increase, an IR drop becomes predominant and a crevice effect is observed. When the polarization curve shows an active-passive phenomenon, the critical current density for passivation is the prominent factor influencing the crevice effect. If the current is very large, the crevice exterior becomes passive while the crevice interior remains active; however, when the polarization potential is high enough, passivation occurs inside the crevice and, in time, the crevice effect disappears.

In neutral environments, such as aqueous NaCl and KBr solutions, the anodic current is small at applied potentials below that required for halogen ion attack and there is little or no crevice effect. When halogen ion attack occurs, the crevice effect appears simultaneously and thereafter the potential in the crevice interior remains constant. Here it should be noted that in spite of the crevice effect the crevice interior is also polarized to a potential high enough for halogen ion attack. However, in KI solution, the reaction $2\text{I}^- \rightarrow \text{I}_2 + 2\text{e}$ occurs prior to halogen ion attack and the crevice effect appears to be due to this reaction; therefore, the potential in the crevice remains constant. When the potential is further increased, halogen ion attack occurs at the crevice exterior and the current increases rapidly; however, the potential in the crevice interior remains unchanged and so halogen ion attack occurs.

In methanol solutions, in the absence of a passivator, anodic dissolution or halogen ion attack occurs in the very active potential region and the crevice effect appears simultaneously. In this case the potential in the crevice is high enough for the above reactions to occur.

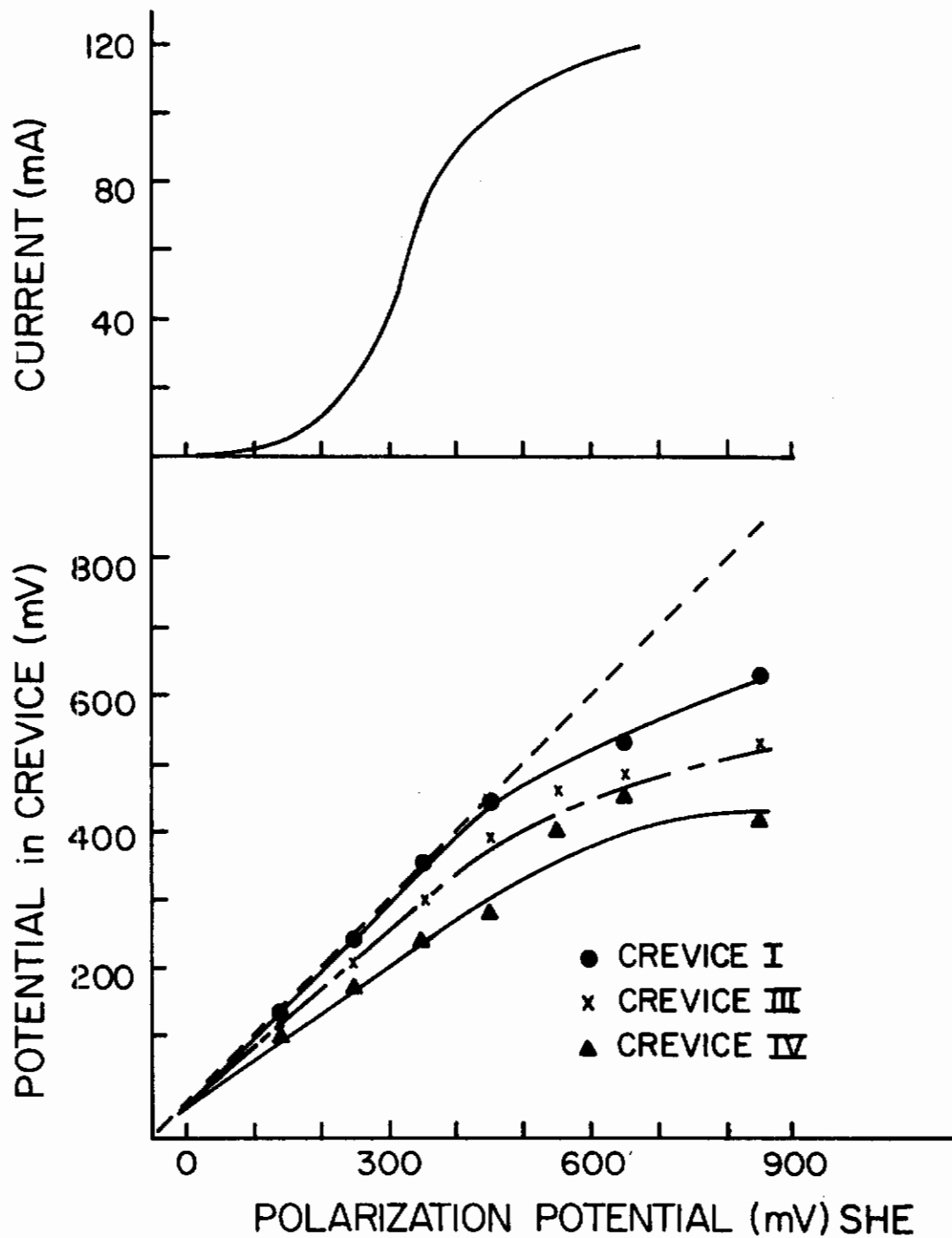


Fig. 21 - Polarization Potential at Crevice Exterior vs. Potential in Crevice (Ti-8Al-1Mo-1V in $\text{CH}_3\text{OH} + 0.37\% \text{HCl} + 0.63\% \text{H}_2\text{O}$)

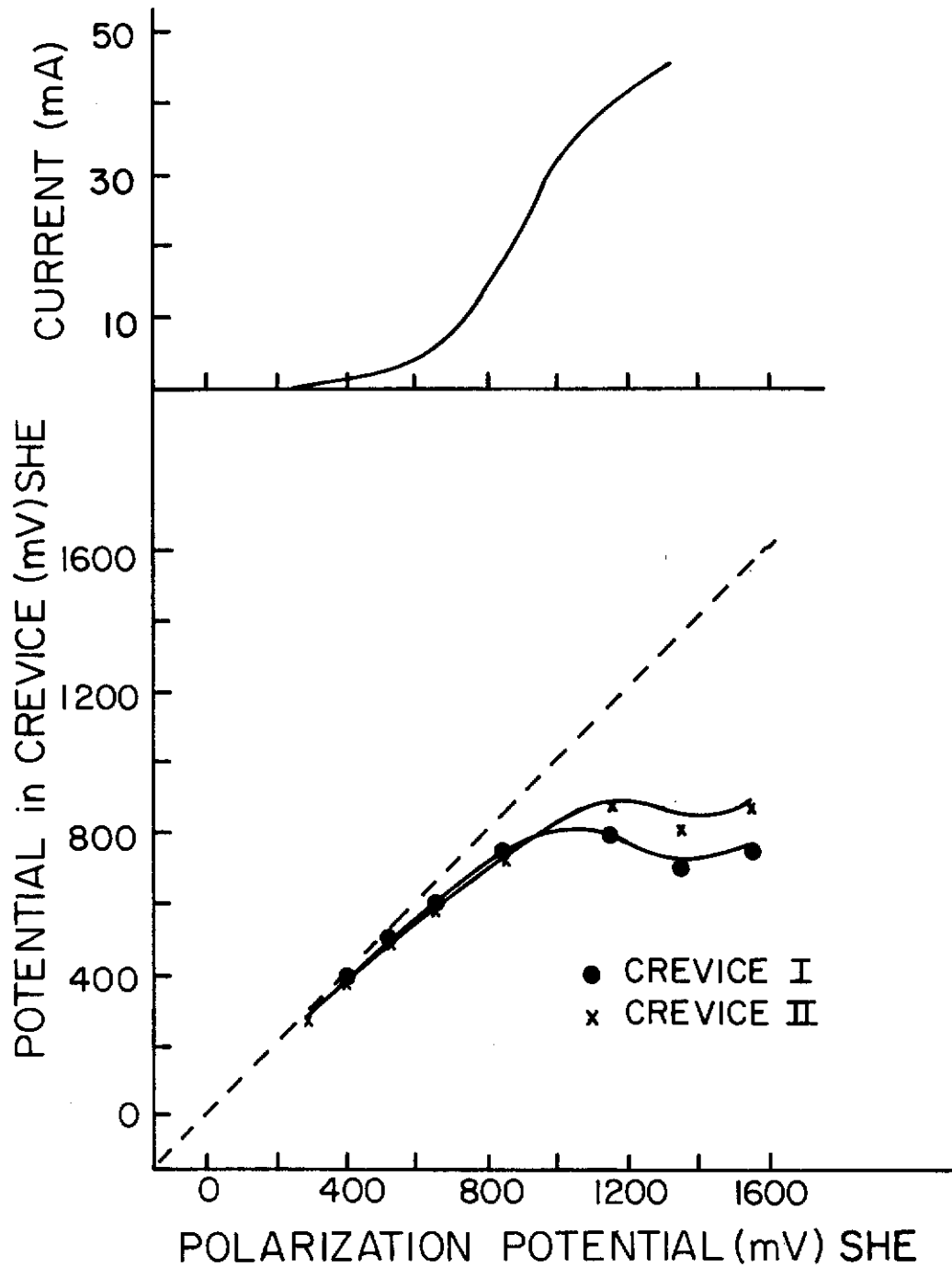


Fig. 22 - Polarization Potential at Crevice Exterior vs. Potential in Crevice (Ti-8Al-1Mo-1V in $\text{CH}_3\text{OH} + 2\% \text{H}_2\text{SO}_4$)

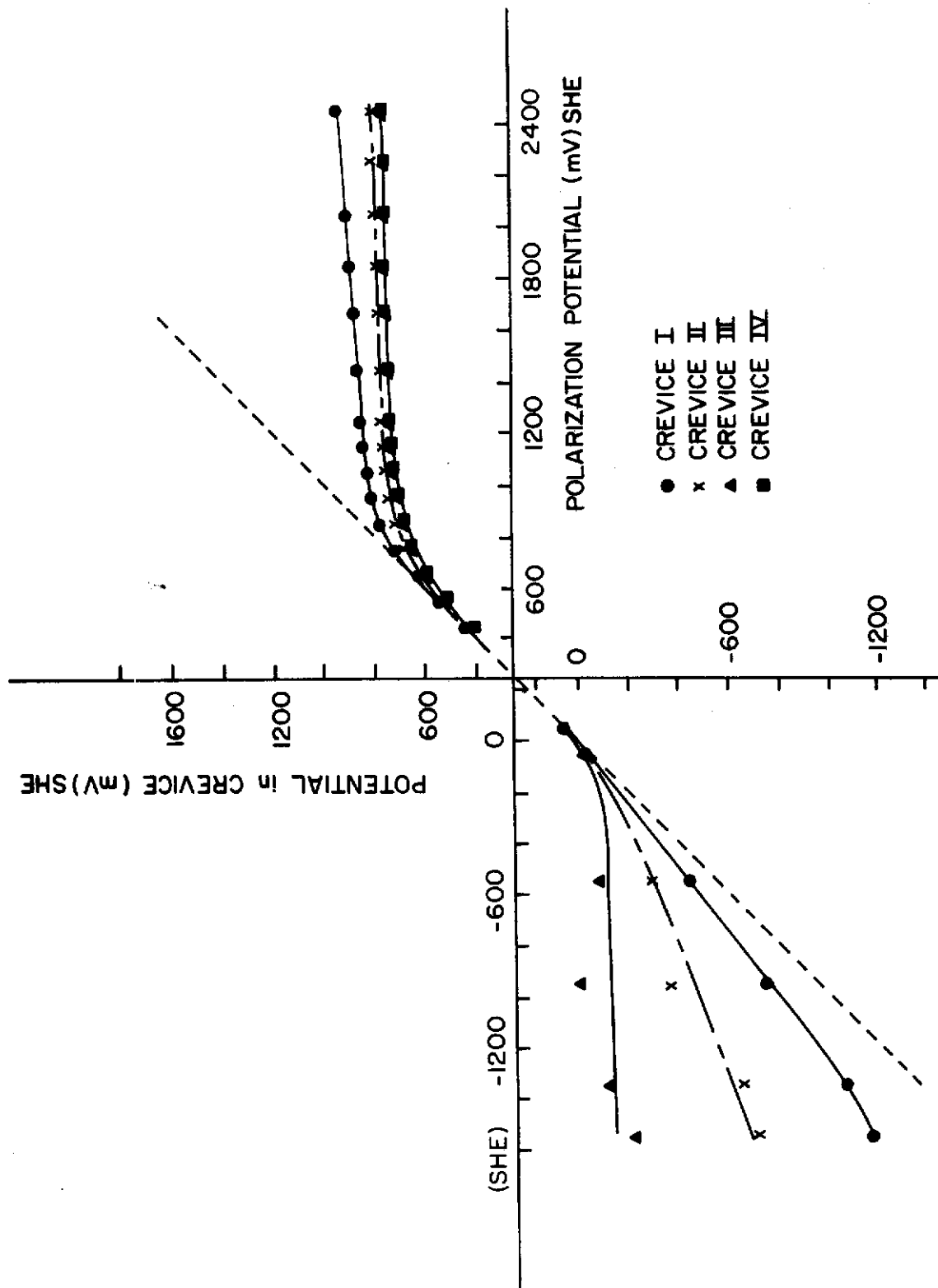


Fig. 23 - Crevice Effect by Anodic and Cathodic Polarization (Ti-8Al-1Mo-1V in 0.6M KI)

Although the artificial crevice used here is different from a real stress-corrosion crack or fissure, the crevice effect in an actual crack can be discussed in a similar manner. Stress-corrosion cracking susceptibility vs. potential data in NaCl and KBr solutions^{17,18} show cathodic and anodic protection zones and susceptible zones of which are near the corrosion potential and halogen ion attack regions. From the present results it is reasonable to assume that halogen ion attack occurs at the apex of the crack when the specimen is polarized in the susceptible zone of the halogen ion attack region where the crevice effect occurs. In KI solutions the tendency for susceptibility is different from NaCl and KBr solutions and there is no anodic protection zone as shown in Fig. 24. In this case halogen ion attack occurs at the crack exterior only, and it is not possible for halogen ion attack to occur at the apex because of the occurrence of the $2I^- \rightarrow I_2 + 2e$ reaction; these different tendencies for cracking in the KI and KBr solutions suggest different mechanisms. In methanol solutions it is reasonable to assume that anodic dissolution or halogen ion attack occurs at the crack apex; the susceptibility vs. potential data do not show an anodic protection zone for this environment.

Regardless of the electrochemical reaction in the crevice, whether it be anodic dissolution, halogen ion attack, hydrogen evolution, etc., the crevice effect appears at the crack apex and makes it difficult or impossible to increase polarization within the crack. For example, Fig. 25 shows failure time and propagation time vs. polarization potential in the halogen ion attack region in a 0.6M KBr solution. Figures 2 and 3 show failure time and crack initiation time vs. potential and crack propagation rate vs. potential, respectively, for Ti-6Al-4V in CH₃OH + saturated NaCl + 0.3% H₂O solution.¹⁹ Although failure time and crack initiation time are greatly affected by the polarization potential, the effect of polarization potential on the crack propagation time or propagation rate is small. This implies that once the electrochemical reaction causing stress corrosion cracking susceptibility occurs, it is difficult to increase polarization at the crack apex because of the crevice effect.

C. EFFECTS OF STRAIN RATE AND POLARIZATION POTENTIAL ON THE SUSCEPTIBILITY OF Ti-6Al-4V ALLOY TO STRESS-CORROSION CRACKING BY METHANOL-0.166% HYDROCHLORIC ACID-WATER SOLUTIONS (C. M. Chen)

(Dr. C. M. Chen moved to The Air Force Materials Laboratory on 3 April, 1969, pursuant to the coupling aspects of the research program. This part of the research (Section II-C) was done by Dr. Chen while at AFML. Future studies by Dr. Chen will include other alloys of titanium.)

1. Introduction

Report AFML-TR-69-16 summarized research on the stress-corrosion cracking of Ti-8Al-1V-1Mo alloy in aqueous and methanolic

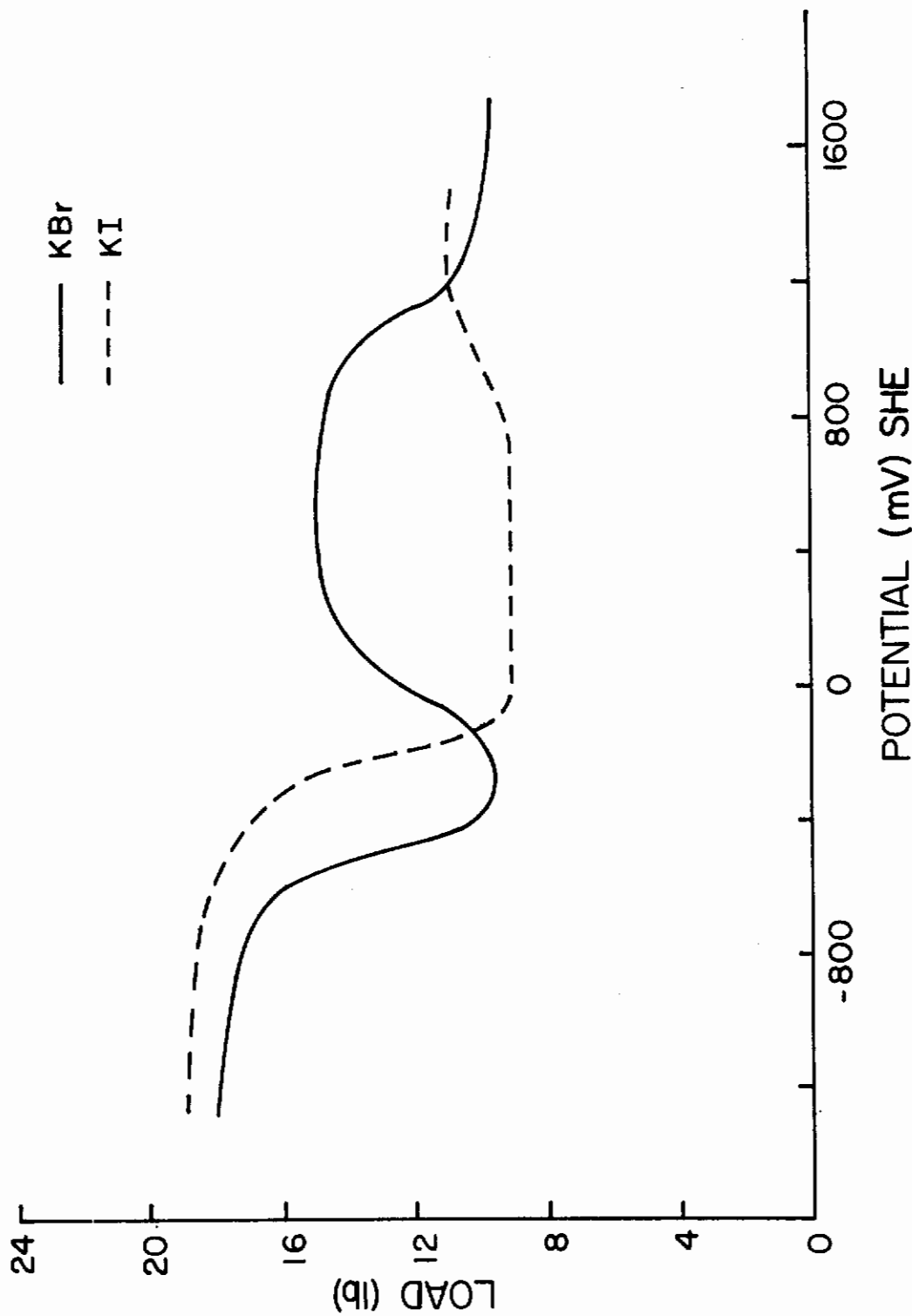


Fig. 24 - Fracture Load vs. Potential (Bend Specimens) (Ti-8Al-1Mo-1V in 0.6M KBr and 0.6M KI Solutions)

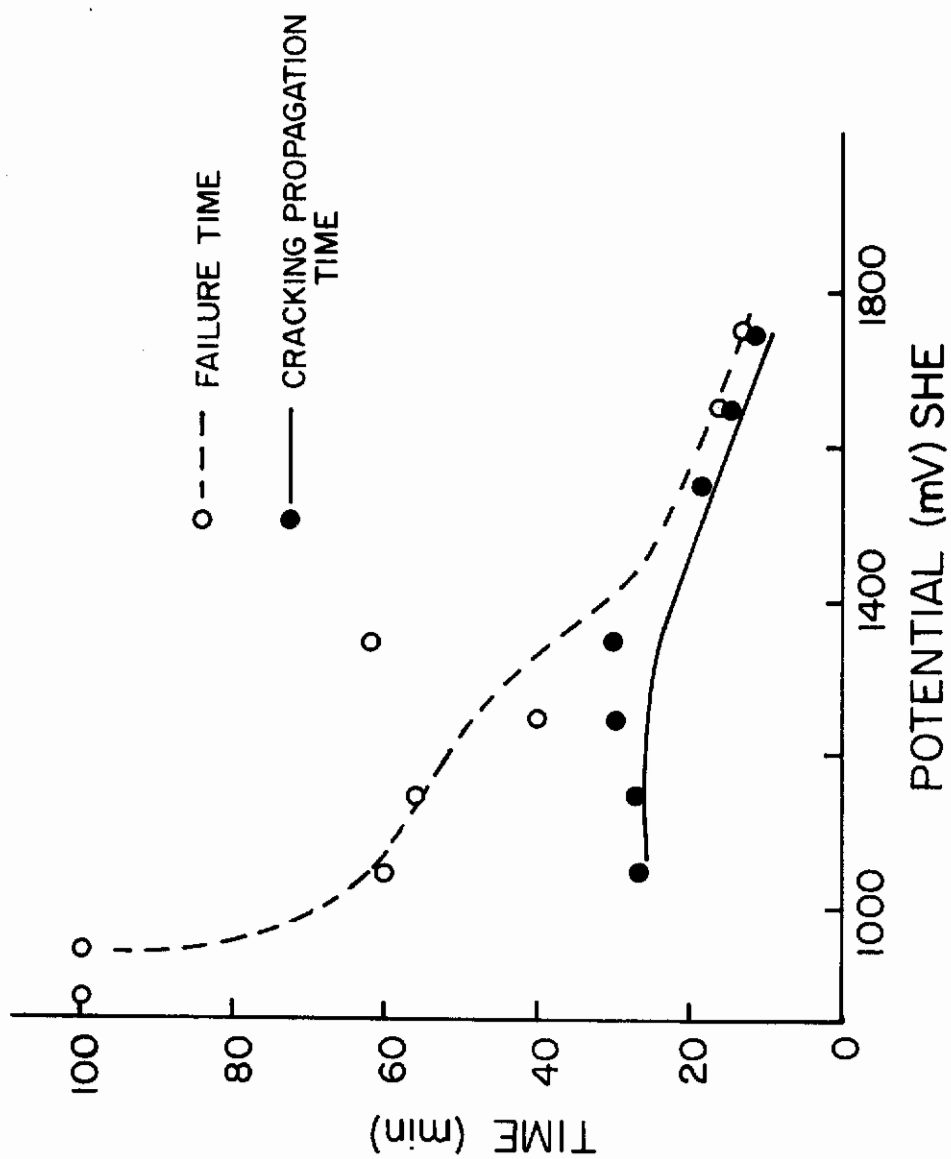


Fig. 25 - Failure Time and Cracking Propagation Time vs. Potential (Ti-8Al-1Mo-1V in 0.6M KBr) (Notched tensile specimens, Load = 80.5 lb, $K_I = 7.15/\text{in}$)

environments. It was emphasized that susceptibility was highly dependent on polarization potential. The research described in the present report includes similar studies on Ti-6Al-4V alloy in methanol + hydrochloric acid + water solutions. In addition, considerable data were obtained through the use of straining electrodes and the direct observation of crack initiation and propagation.

2. Experimental

Smooth tensile and bend specimens of the dimensions given in Fig. 26 were prepared from rolled Ti-6Al-4V sheet material of composition No. 2, Table I. Specimens were oriented with the long axis either parallel or perpendicular to the rolling direction. The material was used in the annealed condition. Tensile specimens were placed in the test cell illustrated in Fig. 27 and were strained during testing with an Instron machine at strain rates ranging from 0.005 to 0.5 cm/min. Bend specimens were restrained in short lengths of one-inch diameter glass tubing as shown in Fig. 28. Electrical contact to the tensile specimen was made through the specimen grip, while contact with the bend specimen was made by spot welding an insulated wire to one leg of the specimen. Cylindrical platinum counter electrodes surrounded the specimens and Luggin probes were placed in the cells as illustrated. A zooming stereo microscope was used in conjunction with a closed circuit TV camera to observe crack propagation on the bend specimen.

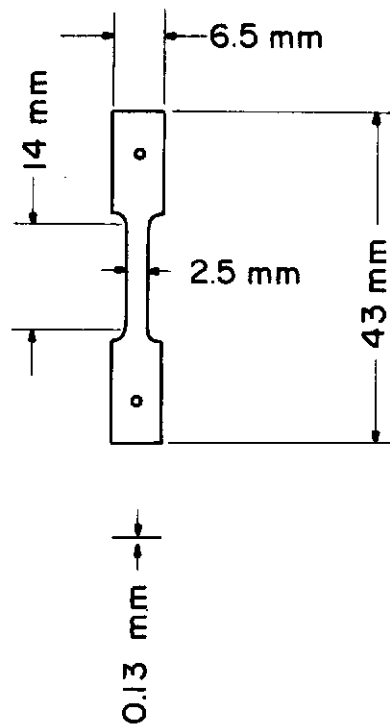
All specimens were polished through 600-grit emery, degreased in acetone, and rinsed in distilled water prior to being placed in the test solution (absolute methanol containing 0.166% hydrochloric acid and from 0.28 to 1.31% distilled water as desired). The external electrical connections were then made through a potentiostat and the test was started.

3. Results

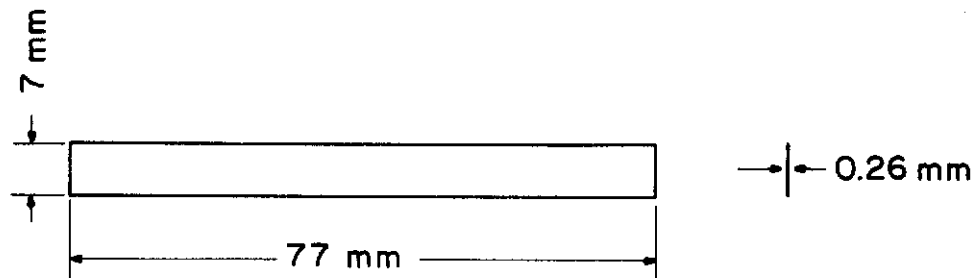
a. Effect of Water Content on Elongation of Specimens at Corrosion Potential (strain rate = 0.005 cm/min)

The effect of water concentration in CH_3OH -0.166HCl- H_2O solutions on the elongation of Ti-6Al-4V specimens in which the tensile axis is parallel and perpendicular to the rolling direction is shown in Figs. 29-a and b, respectively. In "pure" methanol solution the specimens with the rolling direction oriented parallel to the tensile axis have an elongation of about 6.4% compared to about 7% in air. This value is reduced to about 3.5 to 4.5% when the CH_3OH -HCl environment contains water in the range of about 0.2 to 0.7%. The elongation increases rapidly to more than 6% when the water is increased from 0.7 to 0.8% as shown in Fig. 29-a.

Specimens with the rolling direction oriented perpendicular to the tensile axis show the same tendency as for the parallel



(a)



(b)

Fig. 26 - Specimen Configuration:
(a) Tensile Specimen for Straining Electrode Tests
(b) Bend Specimen for Static Tests

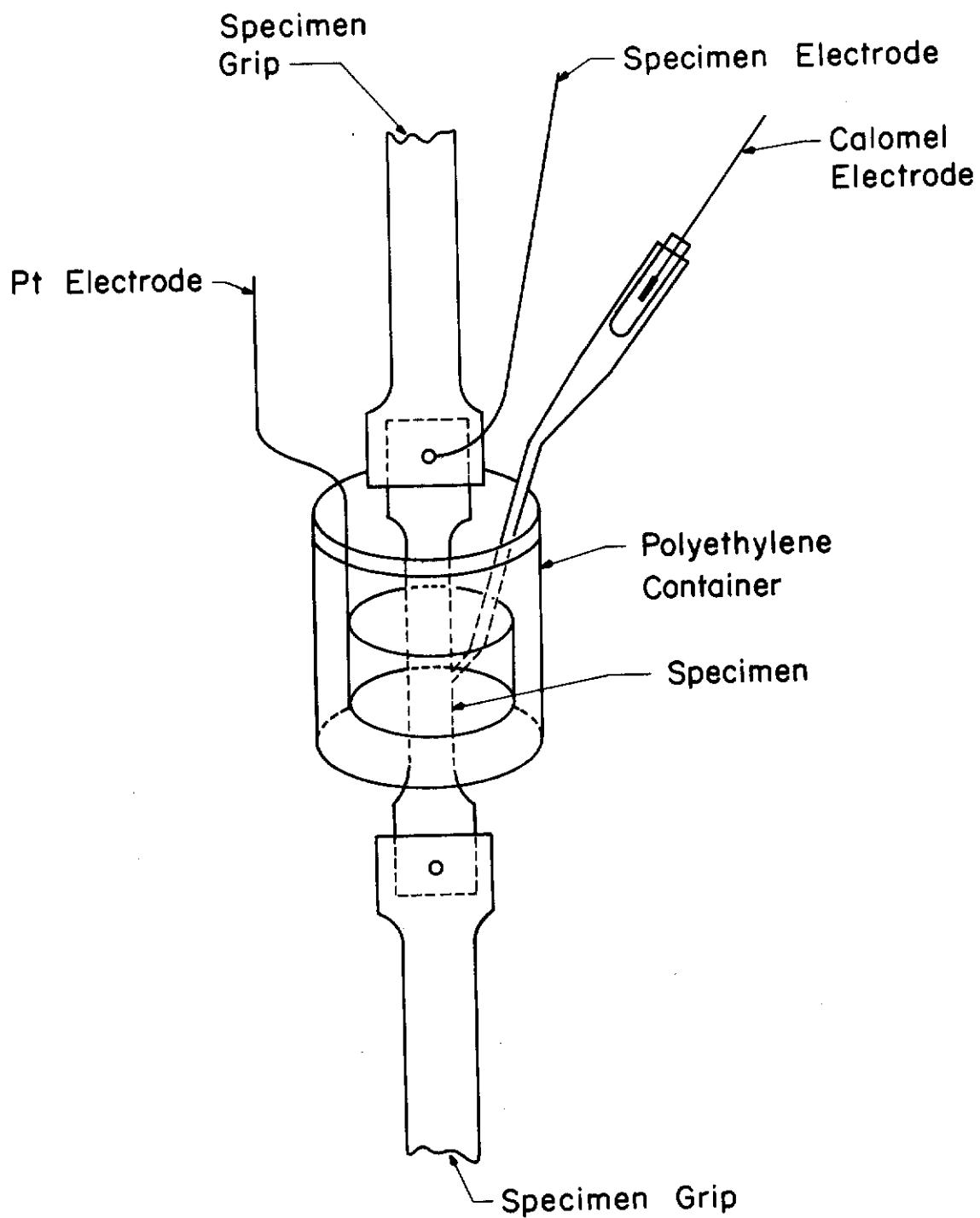


Fig. 27 - Cell for Straining Electrode Tests

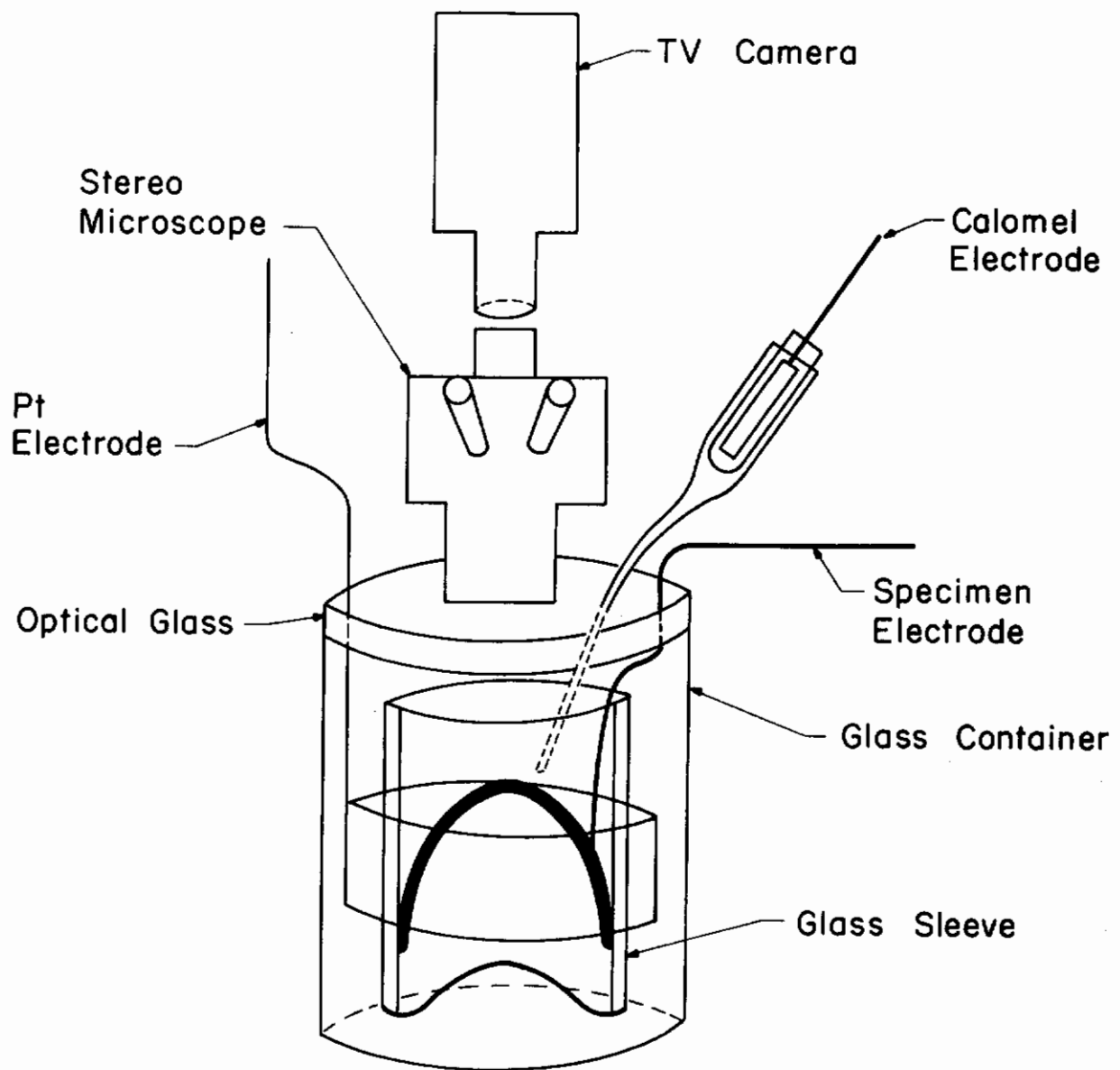


Fig. 28 - Cell for Stress Corrosion Bend Tests

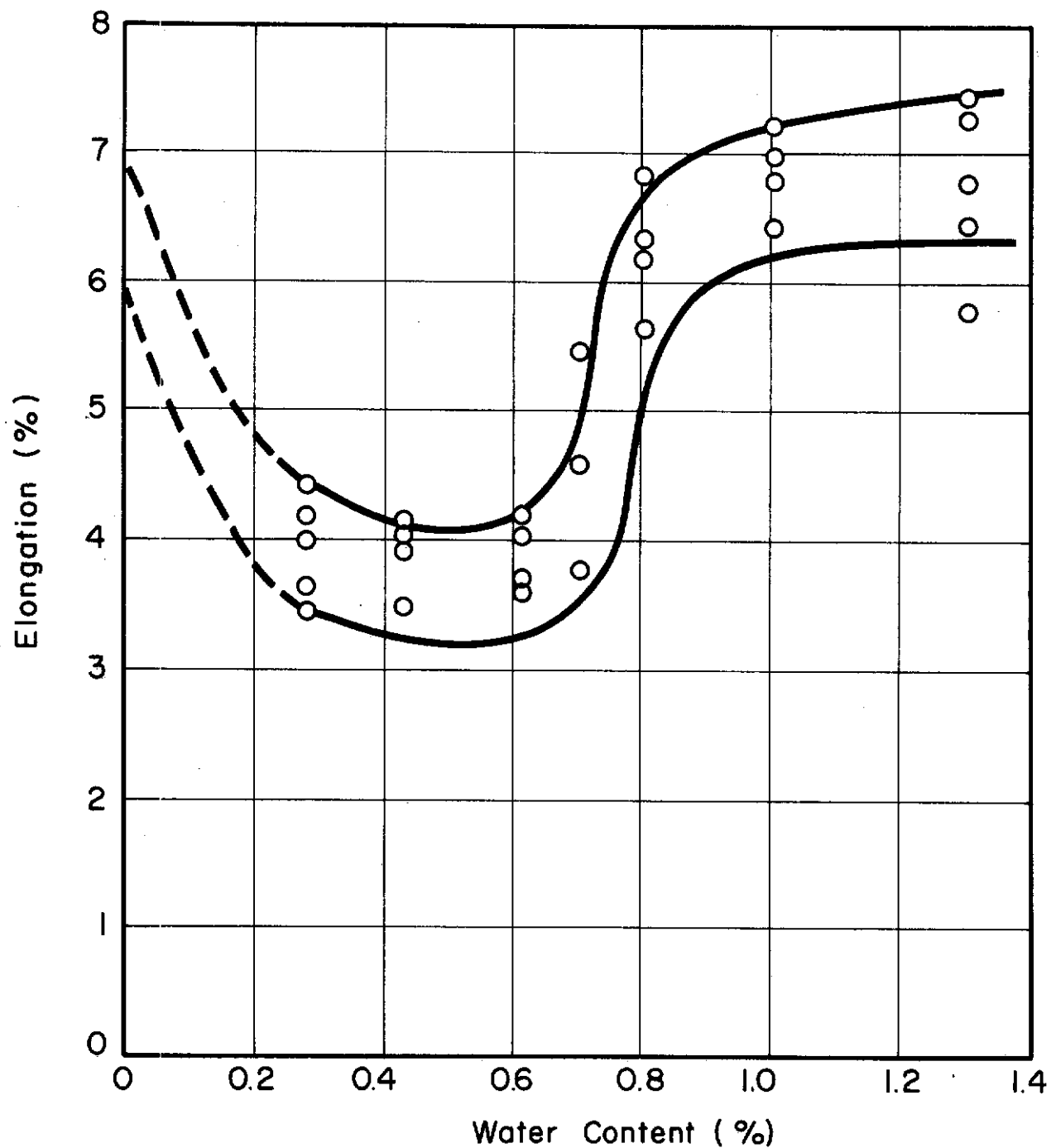


Fig. 29-a - Elongation vs. Water Content. $\text{CH}_3\text{OH} + 0.166\% \text{HCl} + \text{H}_2\text{O}$
 (a) Tensile direction parallel to rolling direction.
 Strain rate 0.005 cm/min)

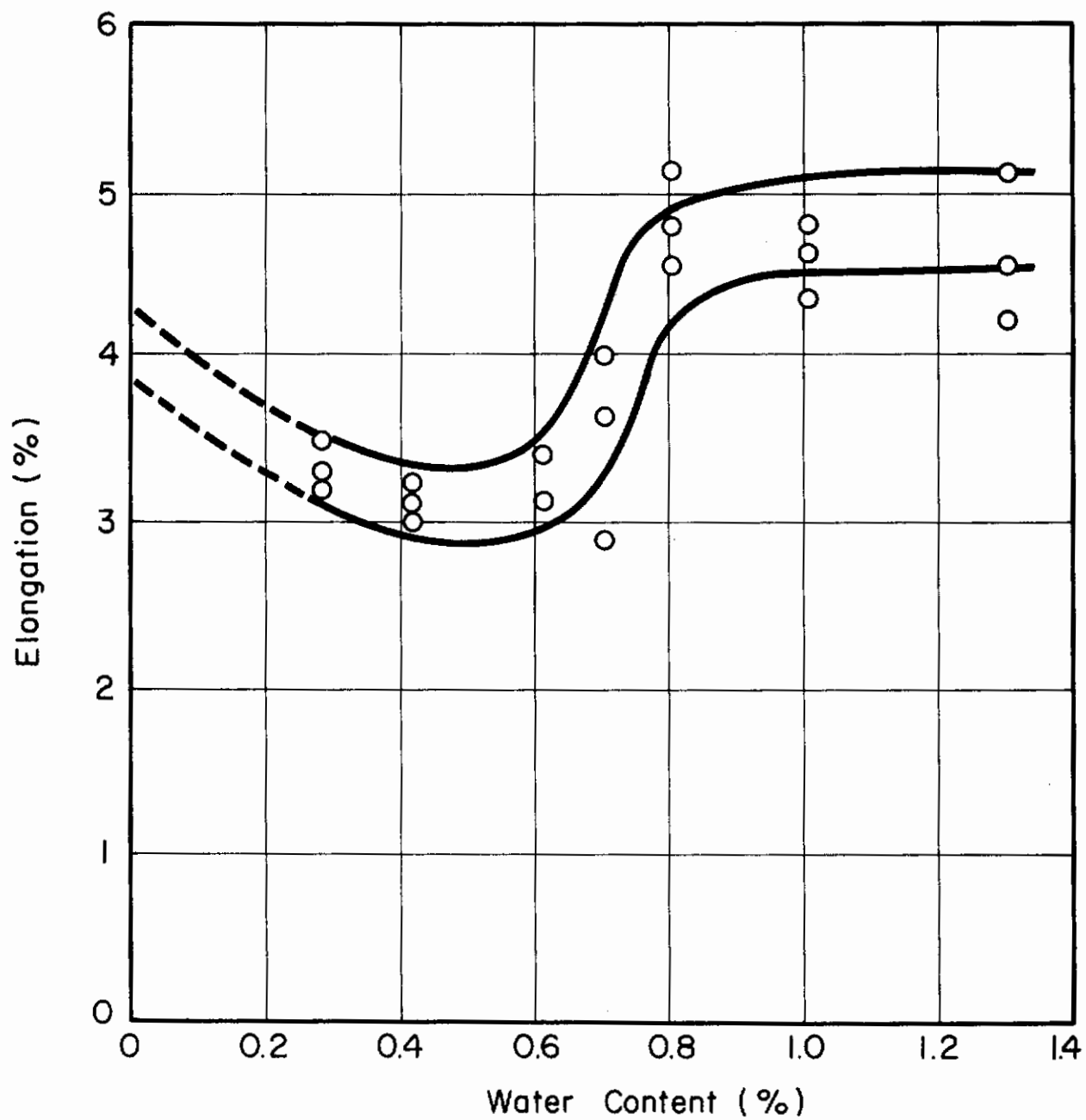


Fig. 29-b - Elongation vs. Water Content. $\text{CH}_3\text{OH} + 0.166\% \text{HCl} + \text{H}_2\text{O}$
 (Tensile direction perpendicular to rolling direction.
 Strain rate = 0.005 cm/min)

orientation described above. The curve for the perpendicular orientation is shifted to lower values; i.e., about 3.9% in "pure" methanol, 5% in air, less than 3% in the critical water range (0.2 to 0.7% water), and 4 to 5% at water concentrations of 0.8% and greater. All specimens were strained at a rate of 0.005 cm/min.

b. Effect of Water and Polarization
Potential on Elongation

Figure 30-a shows that when cathodic polarization is applied to specimens tested in $\text{CH}_3\text{OH-HCl}$ solutions containing 0.28 to 0.99% H_2O , the elongation is about 7%. Under anodic polarization, the elongation is reduced to about 3.5% when the solution contains 0.7% and less water. The transient potential at which the elongation changes from the higher to the lower value is a function of the water content, as illustrated in Fig. 30-b. In the low-water-content range (approx. 0.2-0.7%) the transient potentials are located in the corrosion potential range (shaded zone of Fig. 30-b). The transient potentials are more anodic than the corrosion potential for solutions containing water in excess of 0.7%.

The above data are for specimens having the tensile axis oriented parallel to the rolling direction and tested at a strain rate of 0.005 cm/min.

c. Effect of Water Content on Corrosion Potential
of Strained and Nonstrained Electrodes

The effect of water content on the corrosion potential in the absence of an applied strain is shown in Fig. 31-a (readings were taken after the specimens were exposed to the test solution for four minutes). The corrosion potential increases rapidly and linearly in the anodic direction with water content in the range of about 0.2-0.8%. At 0.8% water and above there is little effect of water on the corrosion potential.

When specimens are strained in solutions containing 0.8% water or less, the corrosion potential increases in the anodic direction when the specimen is going to fail as shown in Fig. 31-b. The corrosion potential then decreases rapidly in the cathodic direction. At water concentrations in excess of 0.8% the corrosion potential was observed to shift gradually in the cathodic direction when the strain was near the yield and finally a rapid cathodic shift was observed at failure. A strain rate of 0.005 cm/min was used.

d. Effect of Water Content on Polarization

Figure 32 shows that water content has little effect on cathodic polarization; however, water has a great effect on the potential at which a rapid anodic current increase is observed; that is, the

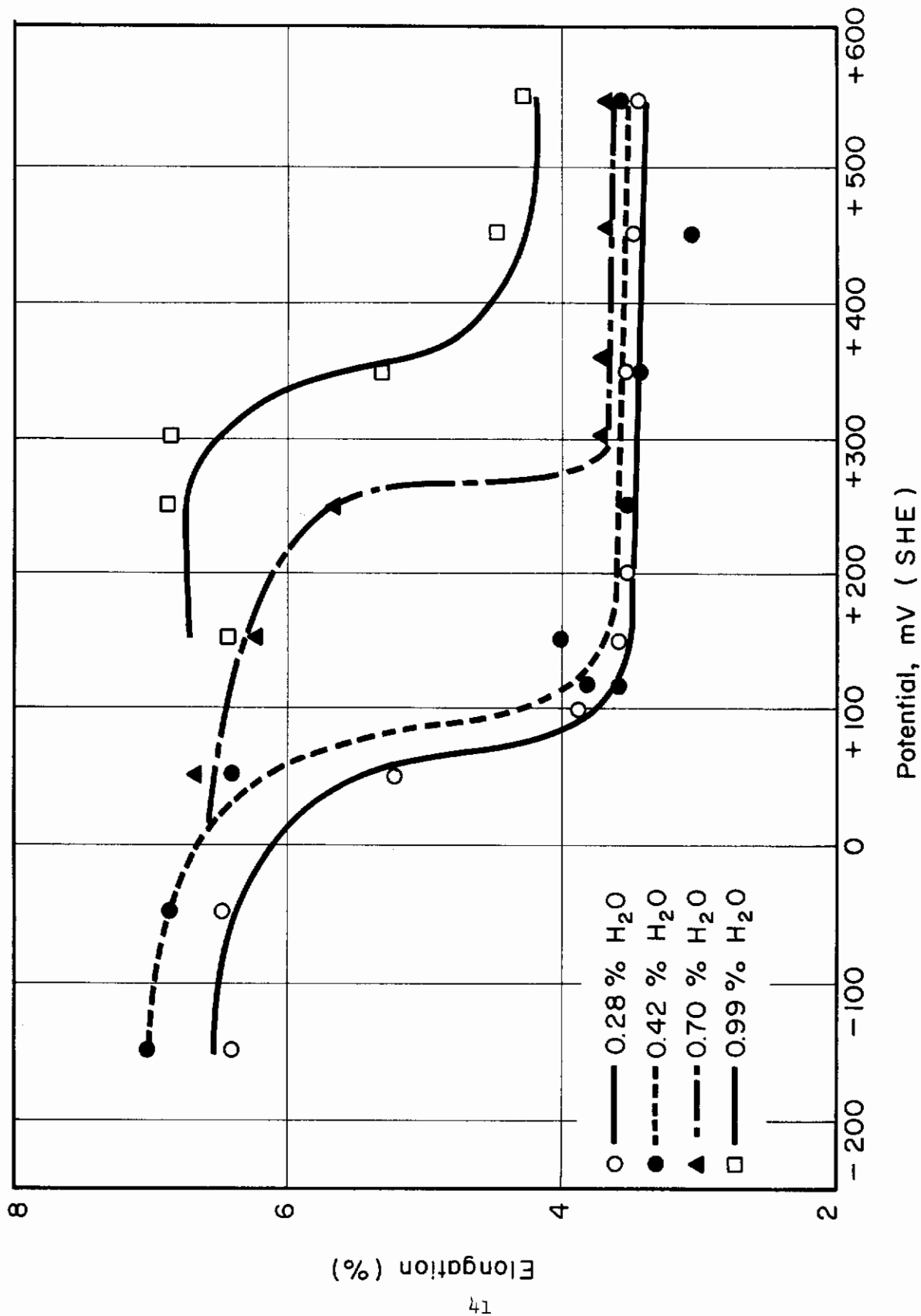


Fig. 30-a - Effect of Polarization Potential on Elongation (%)

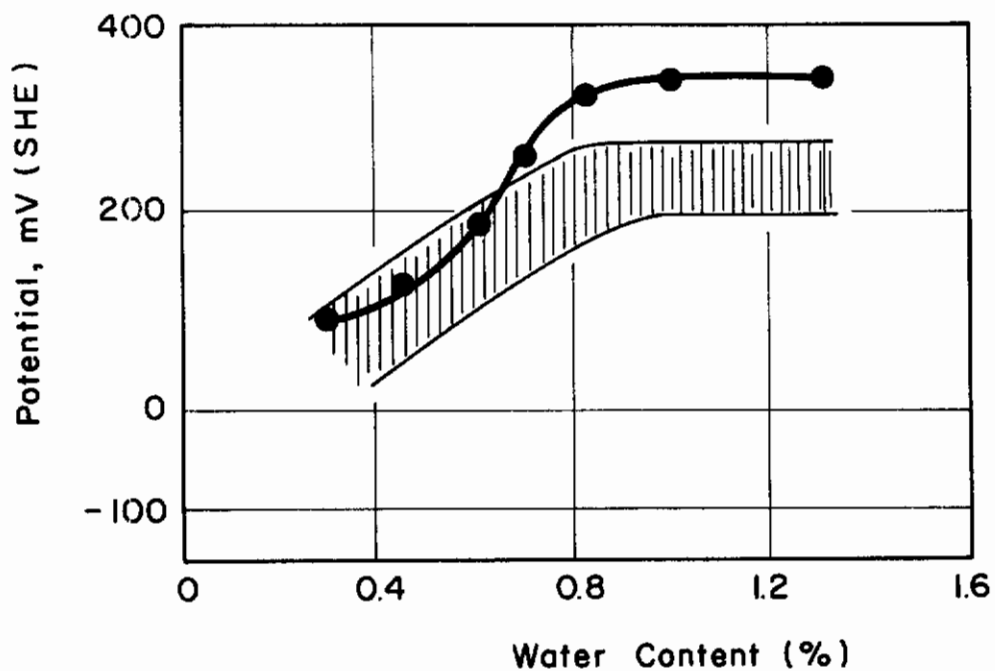


Fig. 30-b - Potential vs. Water Content (%)

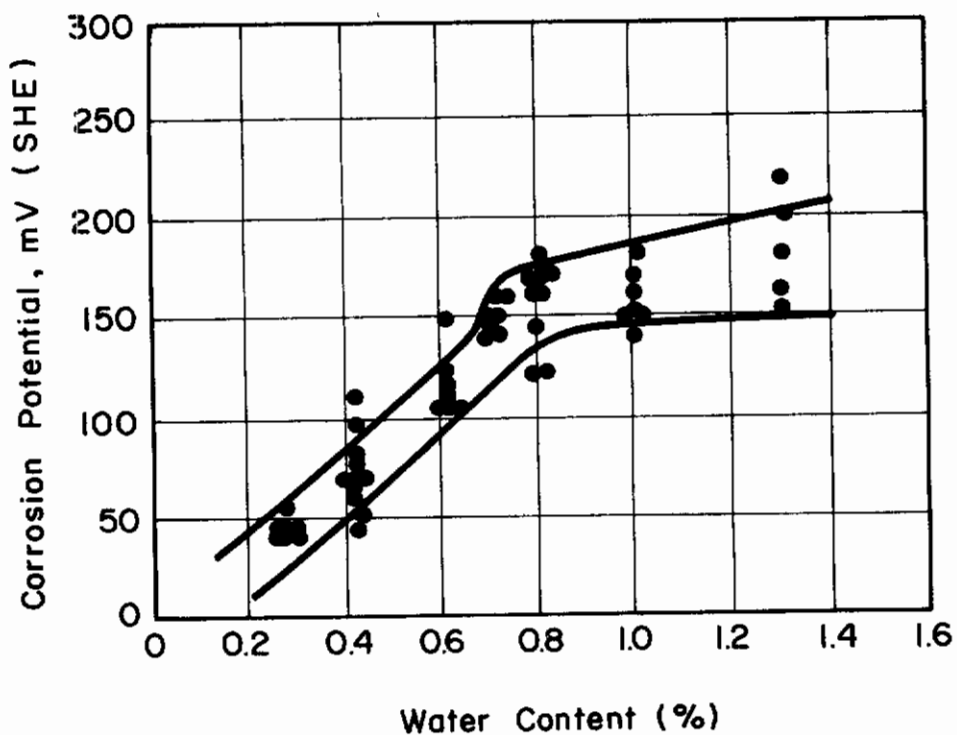


Fig. 31-a - Corrosion Potential vs. Water Content
 $\text{CH}_3\text{OH} + 0.166\% \text{HCl} + \text{H}_2\text{O}$ (no applied load)

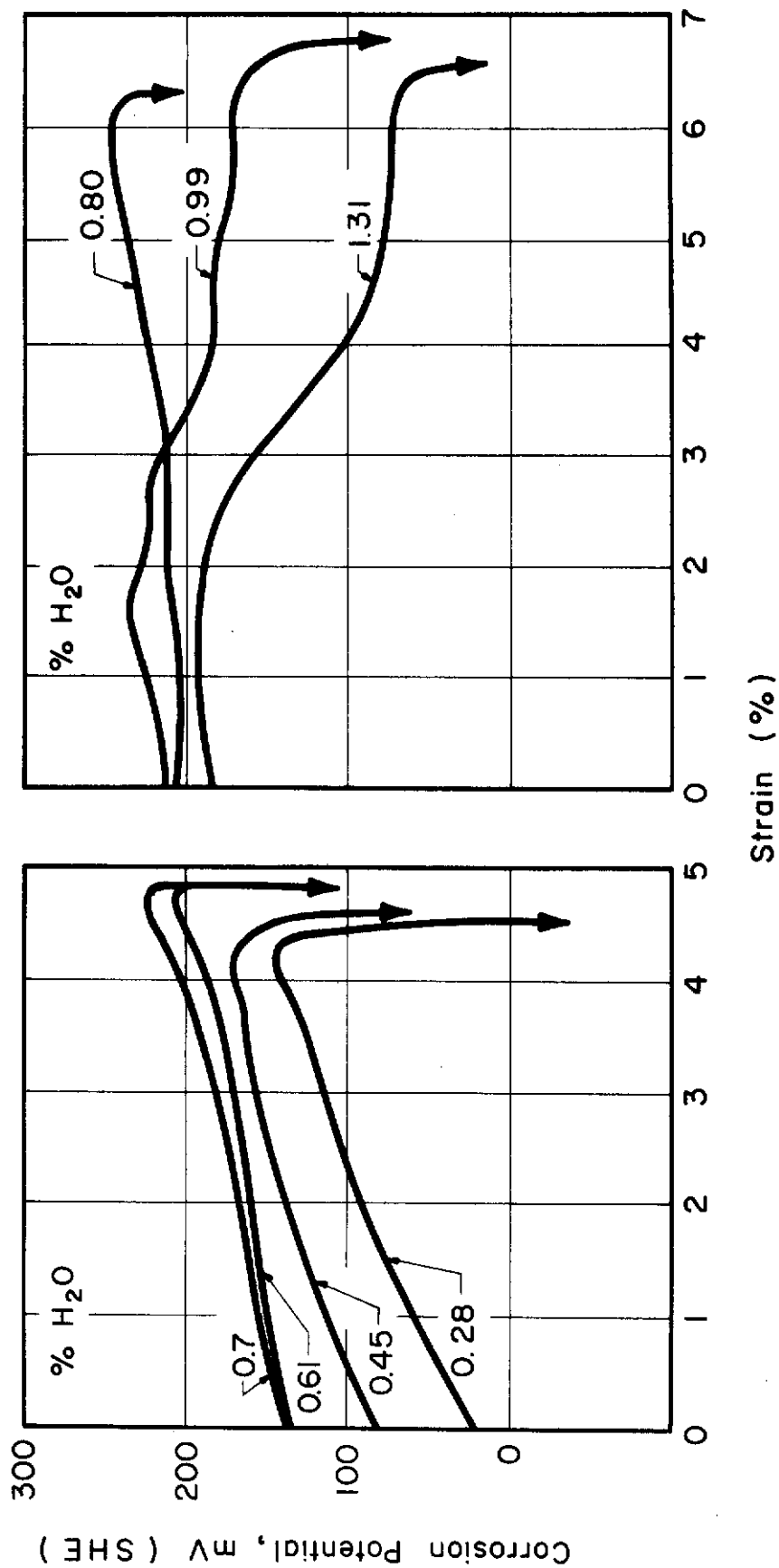


Fig. 31-b - Corrosion Potential vs. Elongation in CH₃OH + 0.166% HCl + H₂O

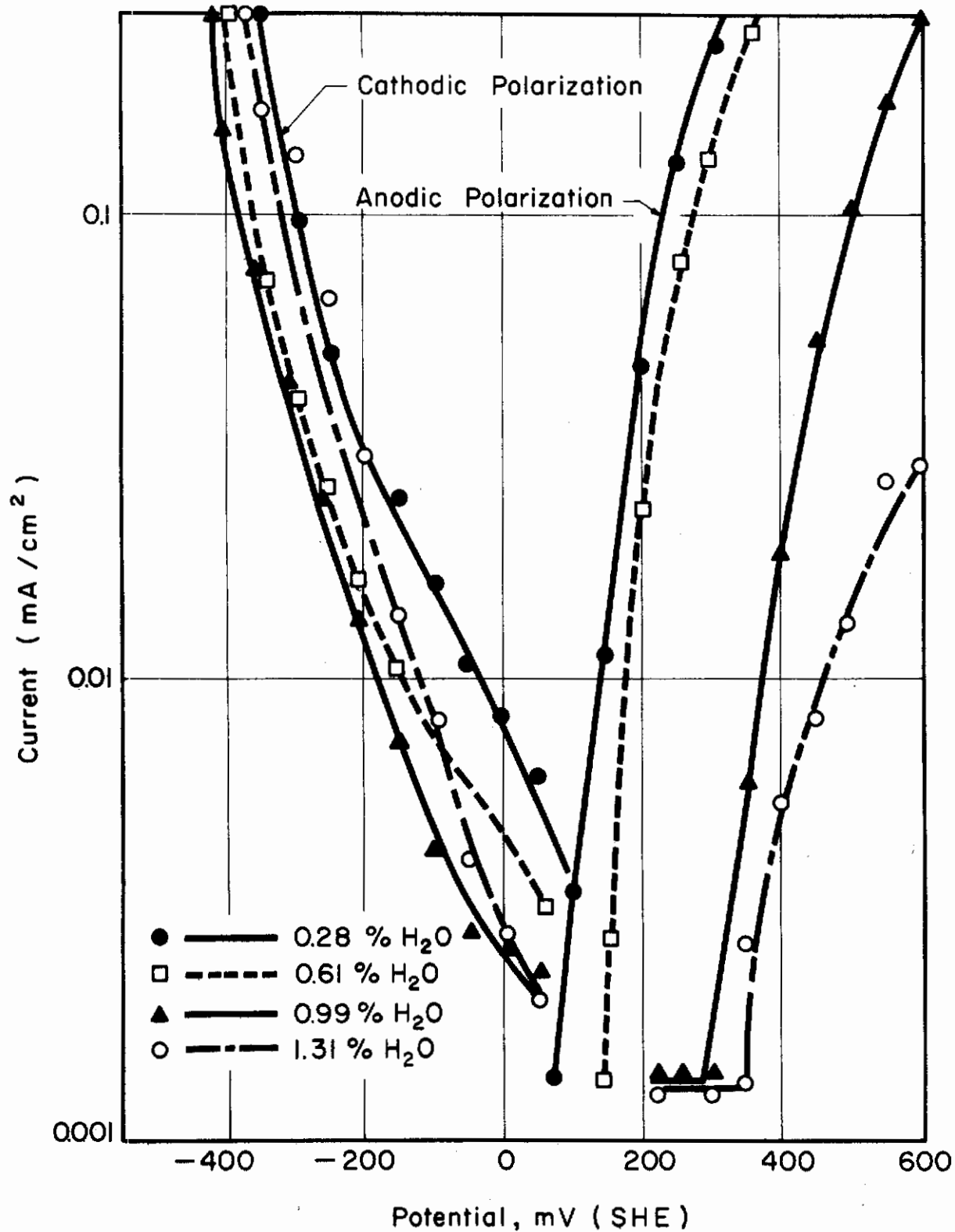


Fig. 32 - Effect of Water Content on the Polarization Curves in CH₃OH + 0.166% HCl + H₂O (scanning rate 25mV/min)

higher the water content, the more anodic the potential for chloride ion attack.

e. Effect of Strain Rate on Current and Elongation

Figure 33-a shows the effect of strain rate on current vs. time for Ti-6Al-4V tested in $\text{CH}_3\text{OH} + 0.166\% \text{HCl} + 0.42\% \text{H}_2\text{O}$ solution at the anodic potential of +350 mV. As the strain rate was increased from 0.005 to 0.5 cm/min, the current increased at a more rapid rate. However, when the current is plotted against strain for the different strain rates, it is observed that the higher rates cause a more gradual increase in current, as illustrated in Fig. 33-b. Figure 33-c, elongation vs. strain rate, shows an elongation of about 6% at high strain rates (greater than about 0.03 cm/min) and an elongation of about 3.7% at low strain rates (0.005 cm/min).

When the specimens are polarized in the anodic region near the corrosion potential (+200 mV) they show the same tendency as described above for the +350 mV tests. Current vs. strain and elongation vs. strain curves are plotted in Figs. 34-a and b, respectively.

When the specimens are polarized in the cathodic region (+50 mV) the behavior is different from the anodically polarized specimens. The higher the strain rate the more rapid the increase of current with time (Fig. 35-a), as was the situation for the anodically polarized specimens; however, the current vs. strain curves in Fig. 35-b show that the current remains almost constant and at a low value until a little more than 3% strain is introduced. Thereafter, the current increases and, the higher the strain rate the more rapidly the current increases with strain. Figure 35-c shows that elongation is constant at about 7% at all strain rates.

Results similar to the above were obtained when the water content of the test solution was increased from 0.42 to 0.8%. The effect of strain rate on current vs. strain is shown in Fig. 36-a, while Fig. 36-b is for elongation vs. strain rate. All specimens were polarized at + 550 mV.

f. Effect of Strain Rate on Corrosion Potential

Figures 37-a and b show the effect of strain rate on corrosion potential vs. strain in solutions containing less than 0.8% water. When the strain rate is slow, the corrosion potential increases in the anodic direction; however, at fast strain rates the corrosion potential decreases in the cathodic direction.

At water contents greater than 0.8% the corrosion potential decreases in the cathodic direction regardless of the strain rate as shown in Fig. 37-c. Strain rates in the range 0.005 to 0.5 cm/min were used in the above series of tests.

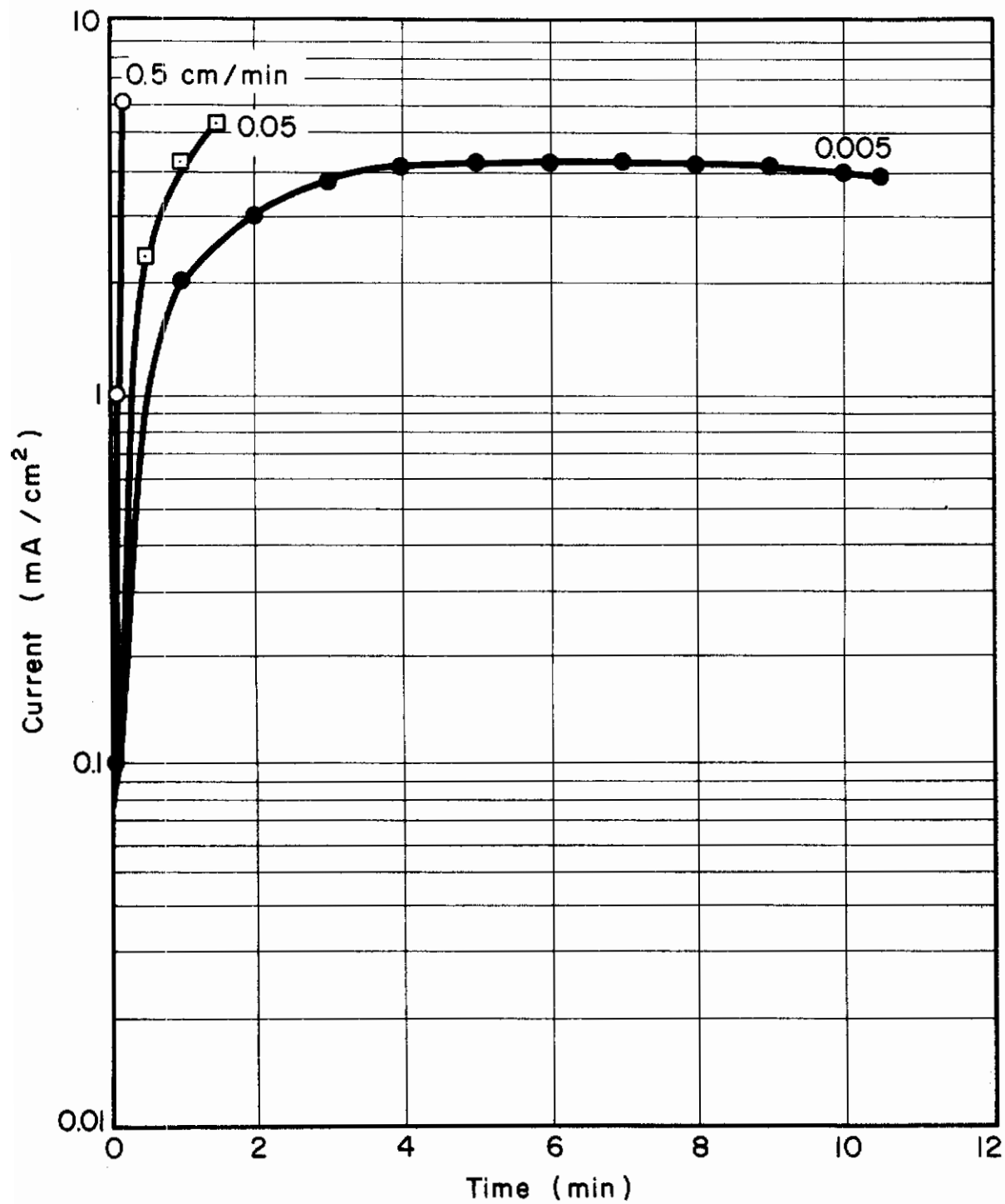


Fig. 33-a - Effect of Strain Rate on Current vs. Time in CH₃OH + 0.166% HCl + 0.42% H₂O at +350 mV (SHE)

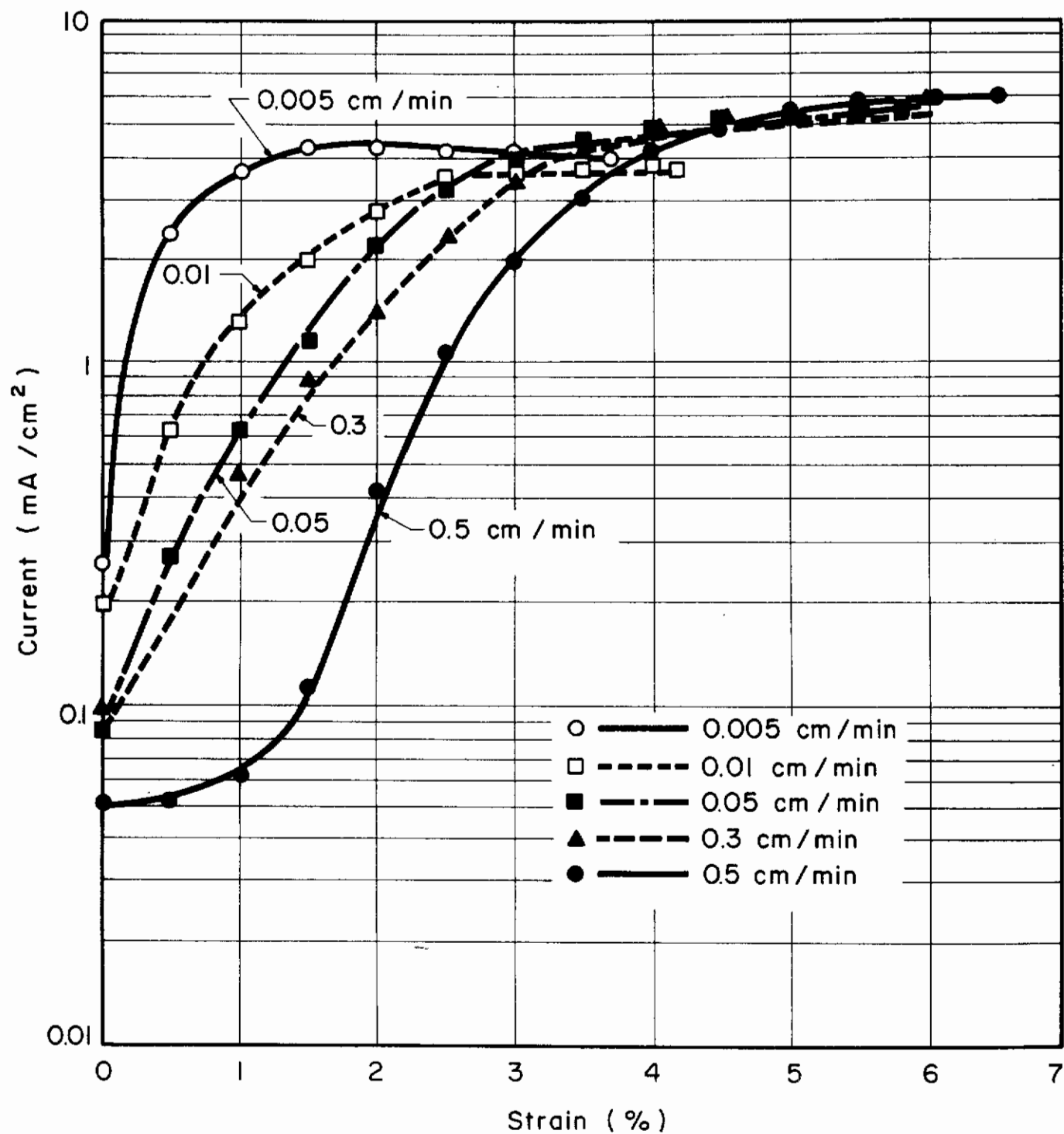


Fig. 33-b - Effect of Strain Rate on Current vs. Strain at +350 mV(SHE) in CH₃OH + 0.166% HCl + 0.42% H₂O

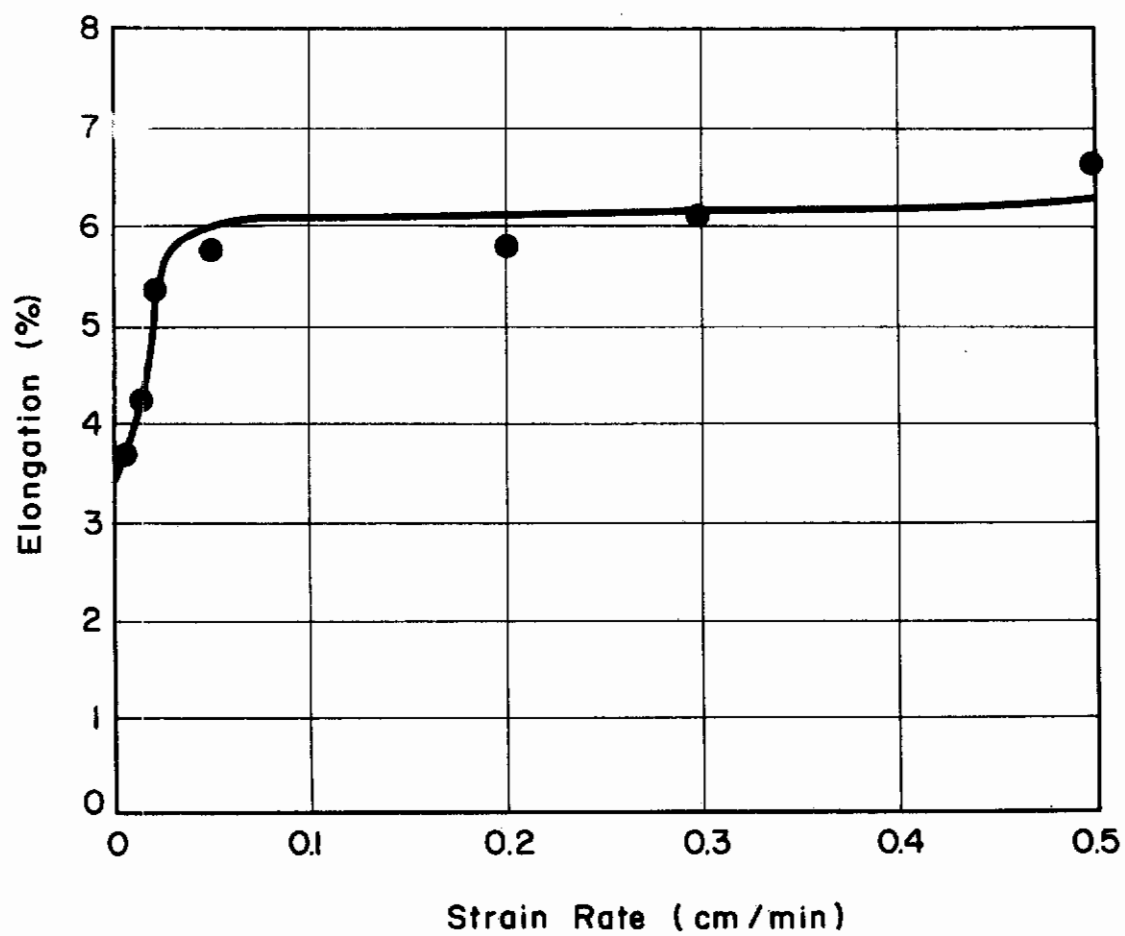


Fig. 33-c - Effect of Strain Rate on Specimen Elongation at +350 mV (SHE)

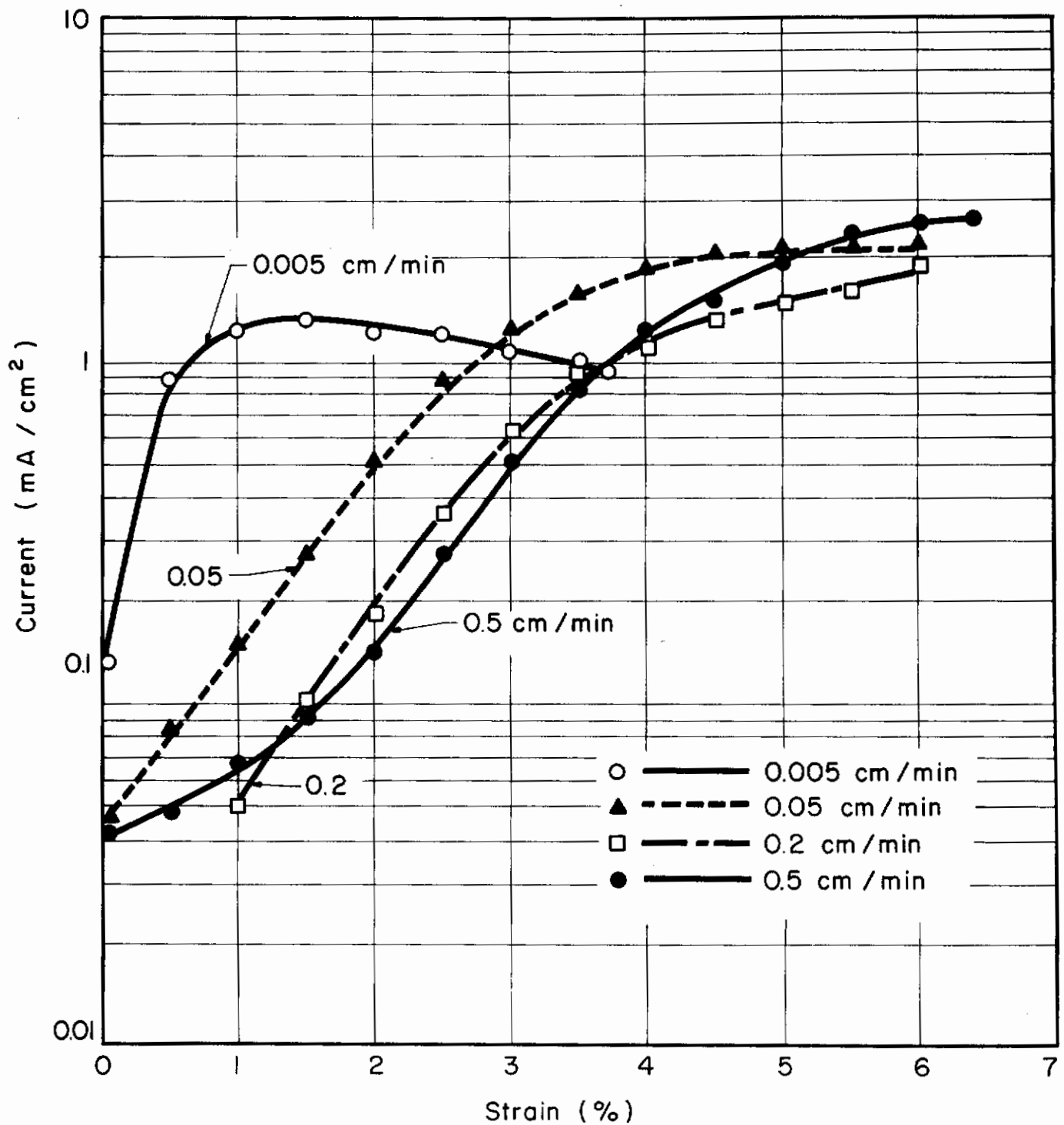


Fig. 34-a - Effect of Strain Rate on Current vs. Strain at +200 mV(SHE) in CH₃OH + 0.166% HCl + 0.42% H₂O

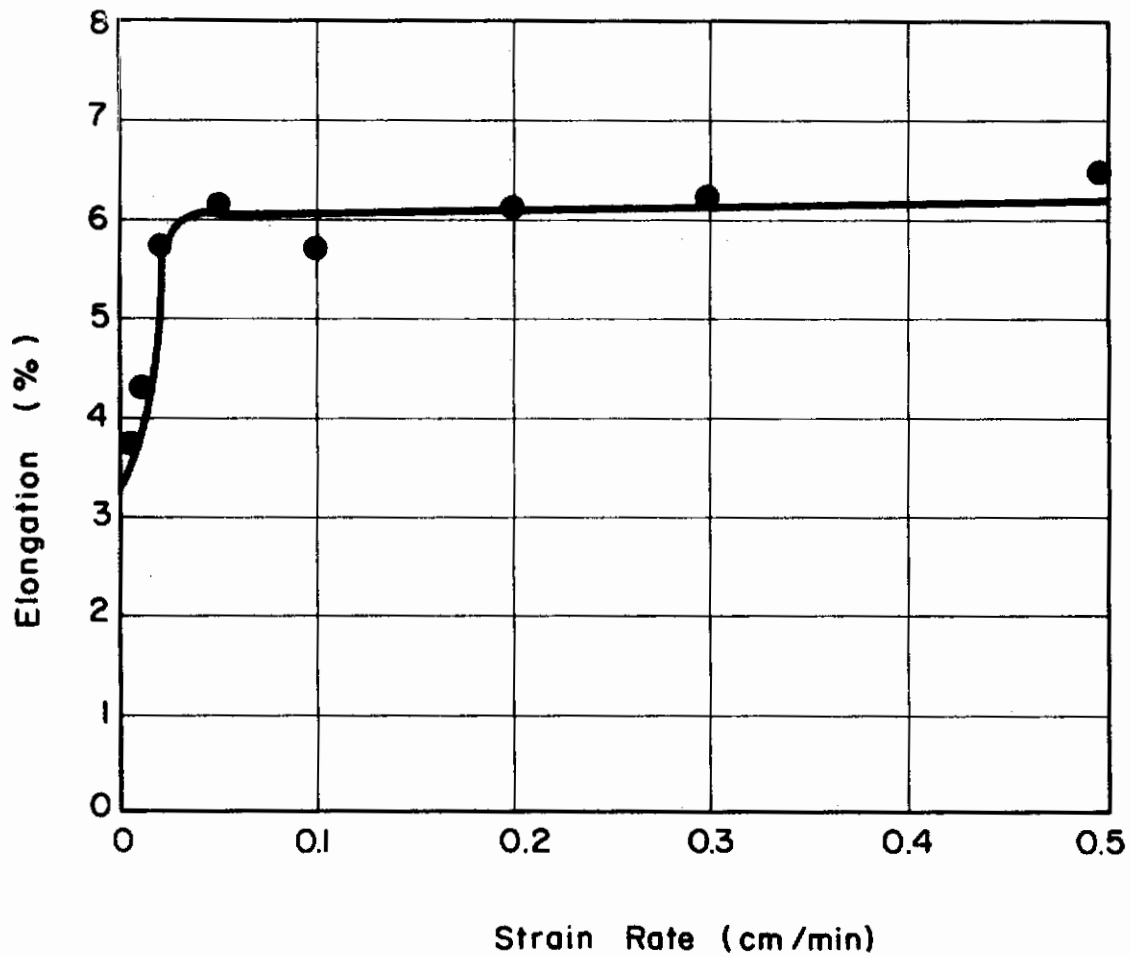


Fig. 34-b - Effect of Strain Rate on Specimen Elongation at +200 mV(SHE)
(same environment as 34-a)

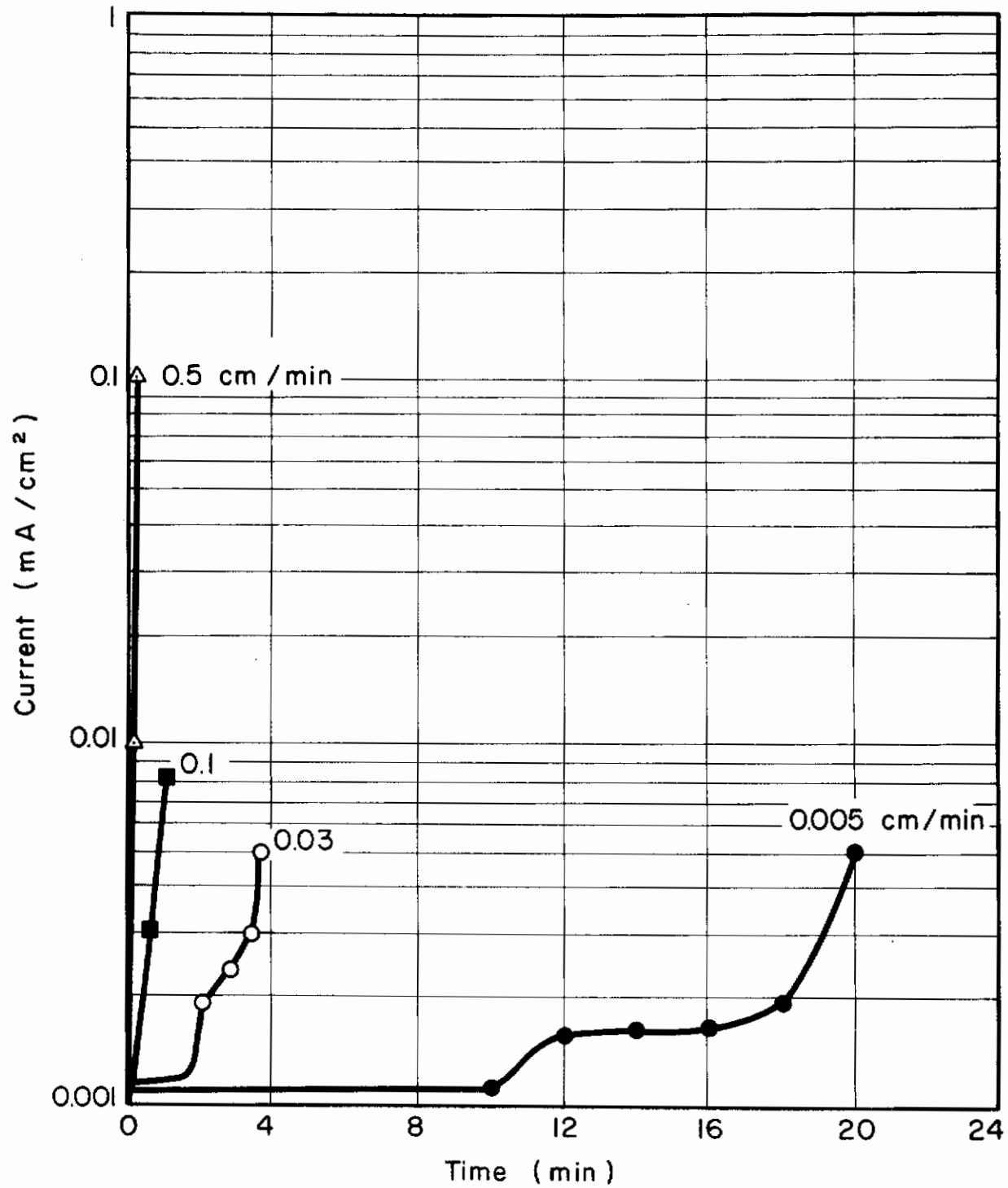


Fig. 35-a - Effect of Strain Rate on Current vs. Time in $\text{CH}_3\text{OH} + 0.166\% \text{HCl} + 0.42\% \text{H}_2\text{O}$ at +50 mV (SHE)

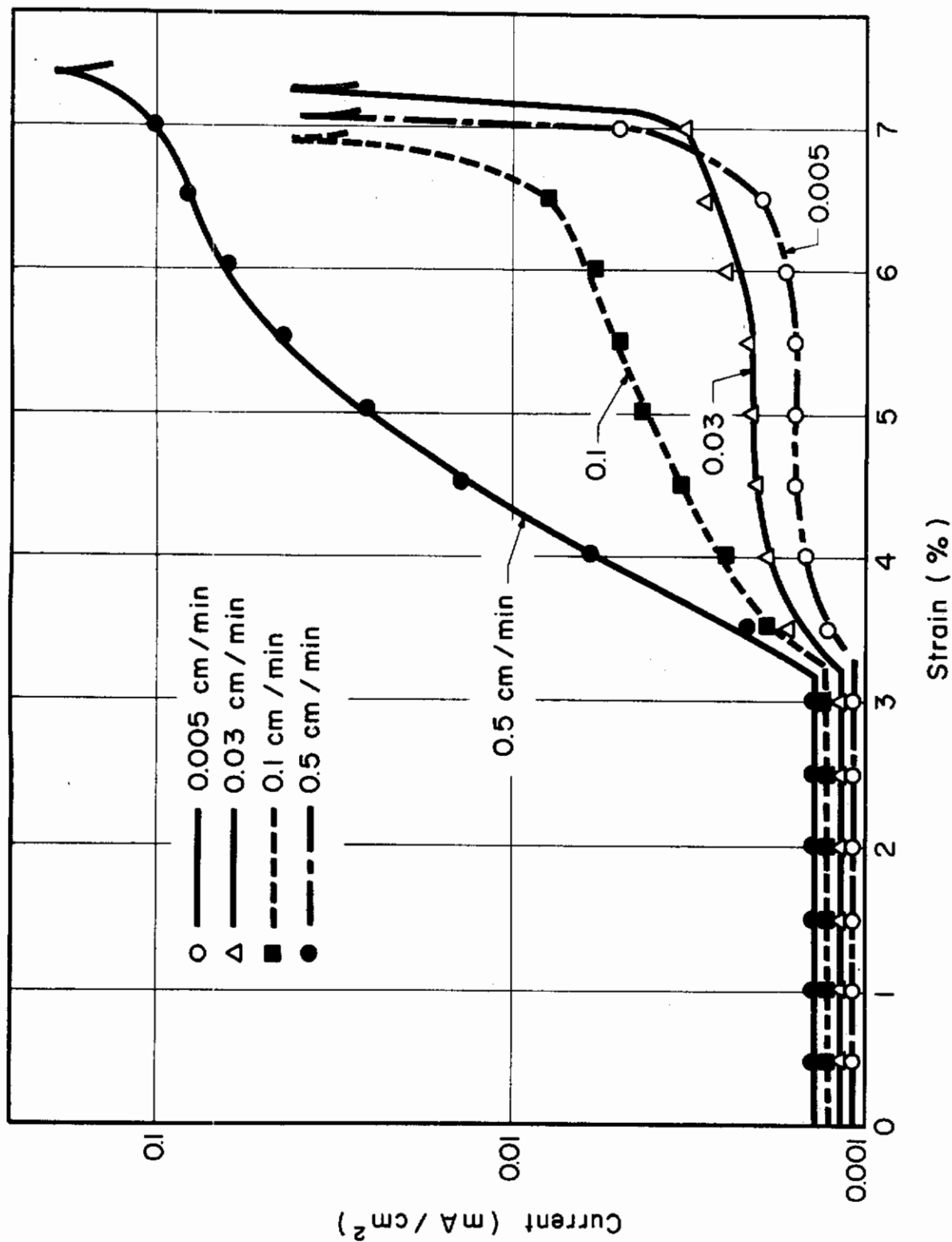


Fig. 35-b - Effect of Strain Rate on Current vs. Strain at +50 mV(SHE) in $\text{CH}_3\text{OH} + 0.166\% \text{HCl} + 0.42 \text{H}_2\text{O}$

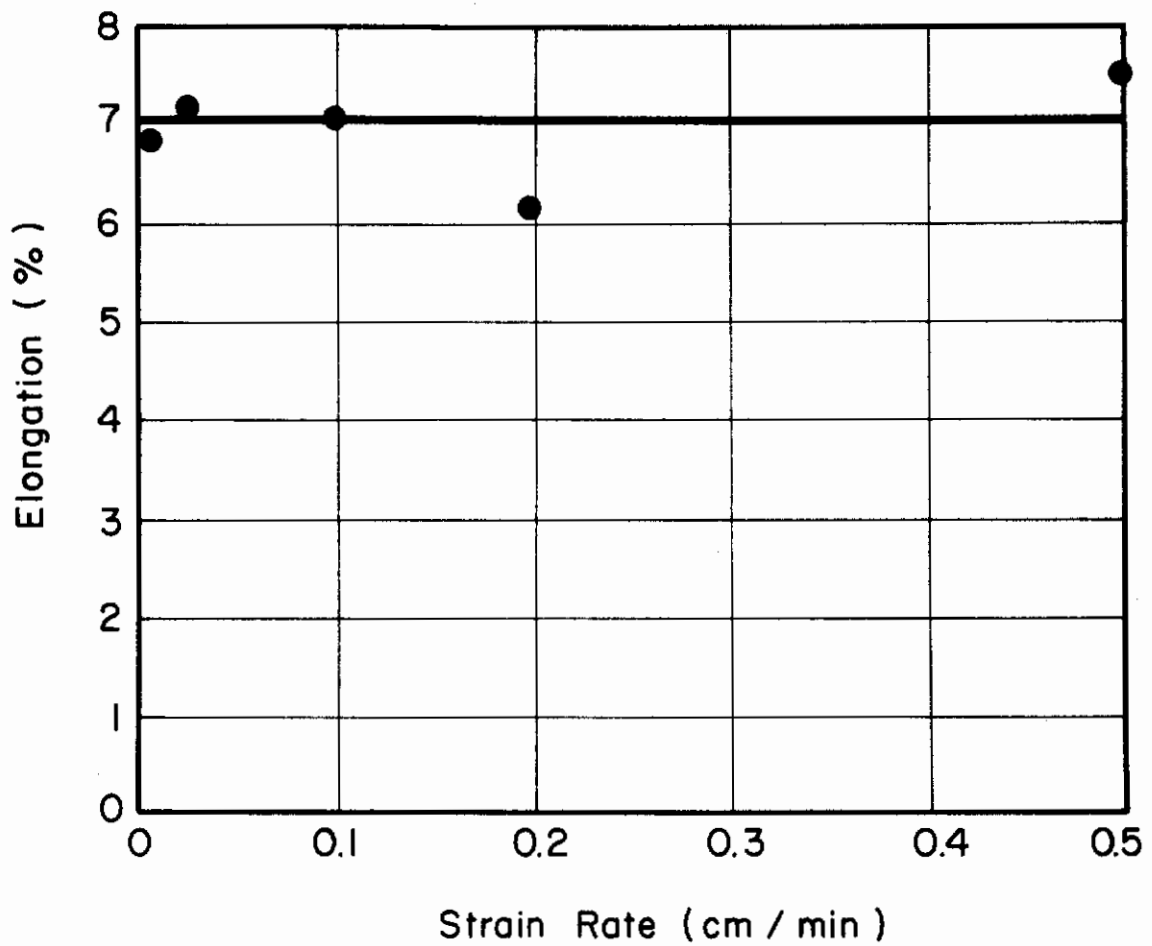


Fig. 35-c - Effect of Strain Rate on Specimen Elongation at +50 mV(SHE)
(same environment as Fig. 35-a and -b)

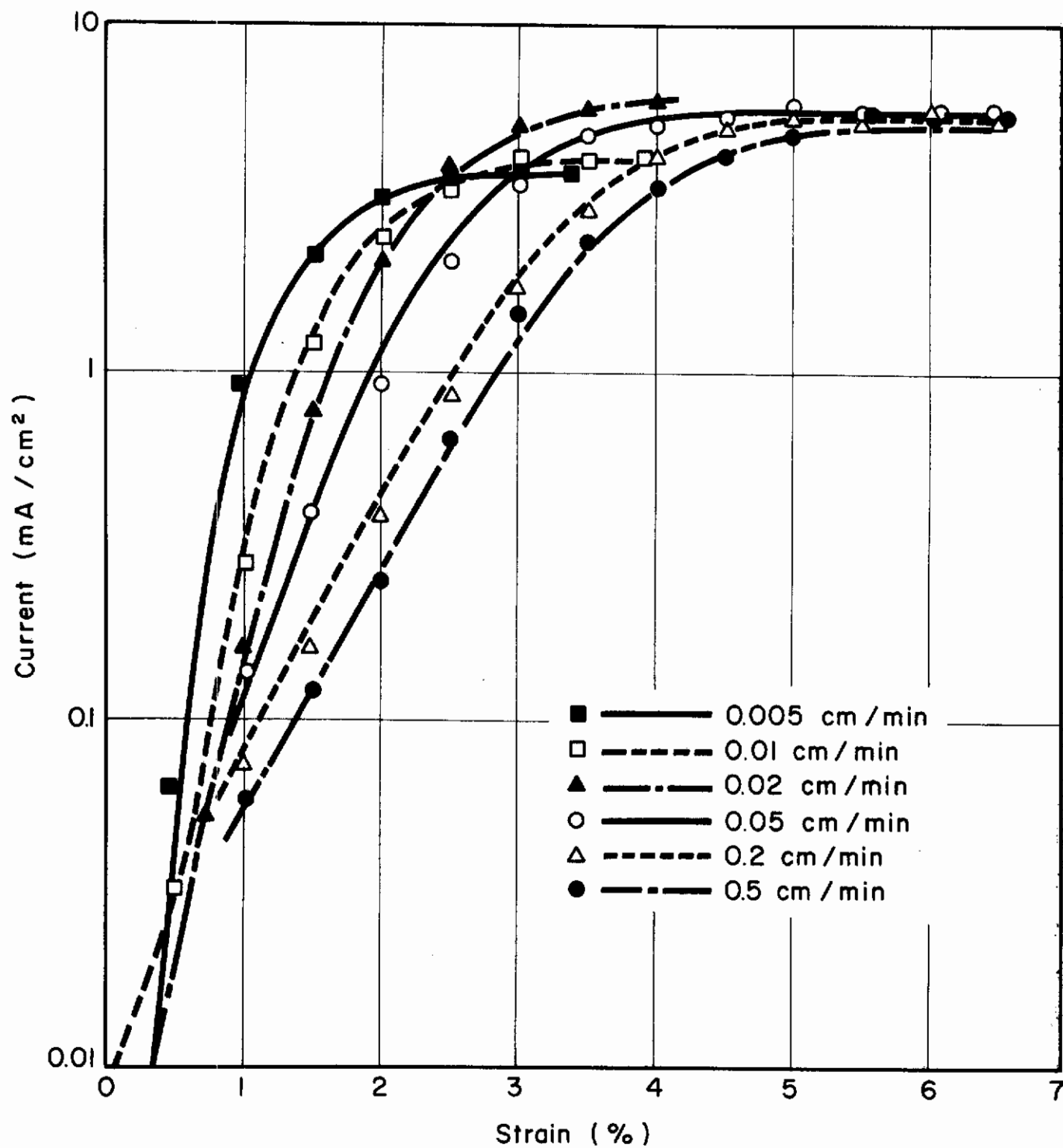


Fig. 36-a - Effect of Strain Rate on Current vs. Strain at +550 mV (SHE) in CH₃OH + 0.166% HCl + 0.80% H₂O

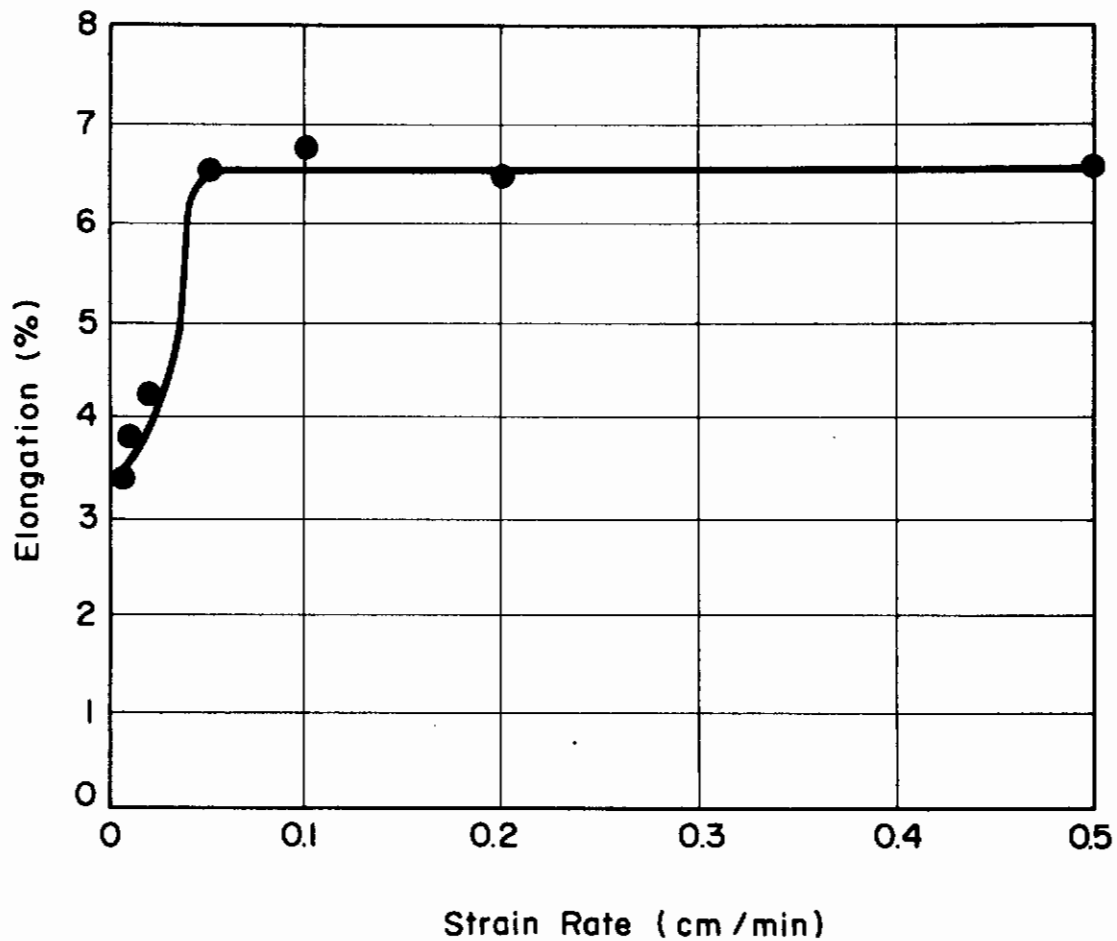


Fig. 36-b - Effect of Strain Rate on Specimen Elongation at +550 mV(SHE)
(same environment as Fig. 36-a)

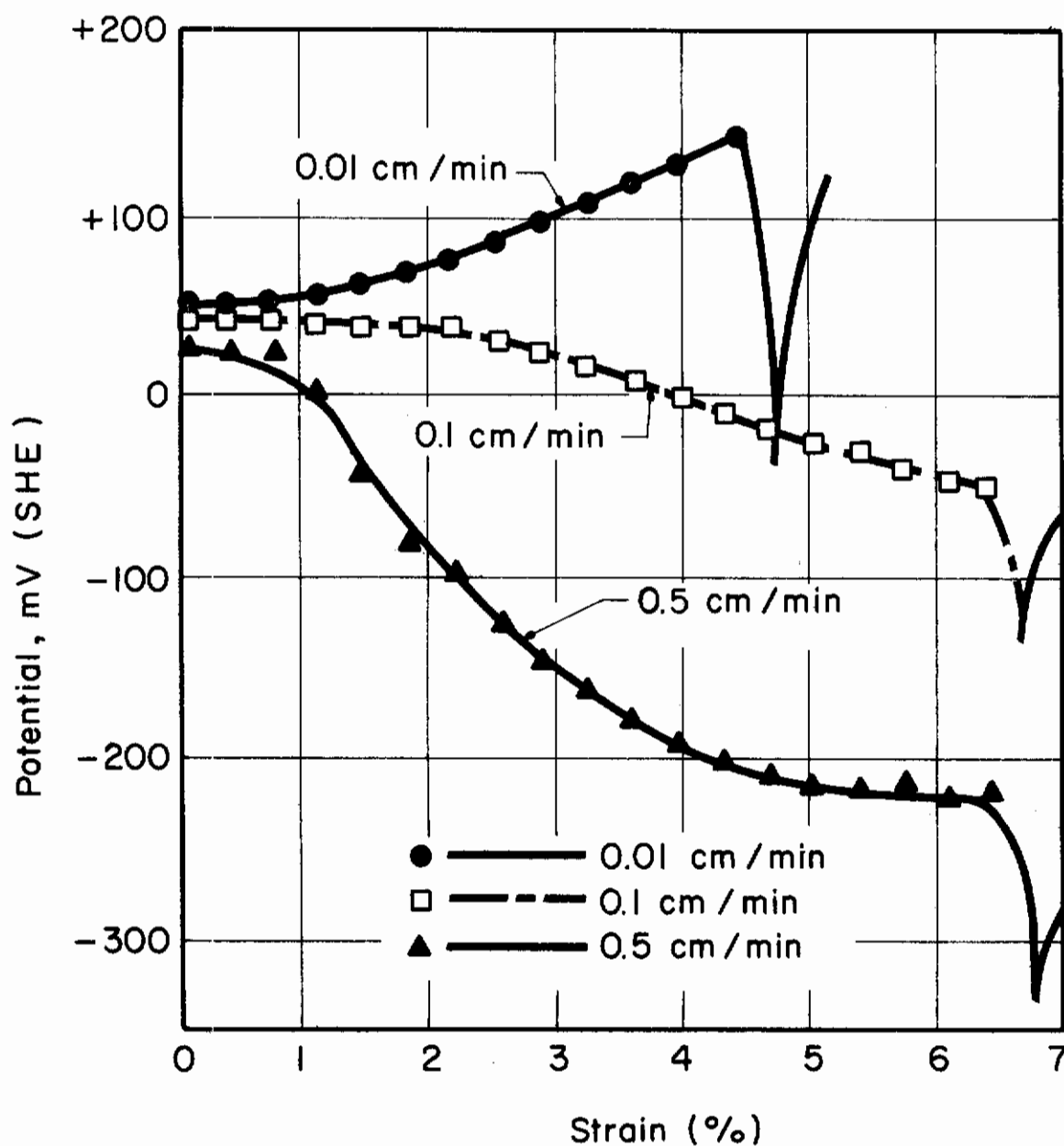


Fig. 37-a - Effect of Strain Rate on Corrosion Potential vs. Strain in $\text{CH}_3\text{OH} + 0.166\% \text{HCl} + 0.28\% \text{H}_2\text{O}$

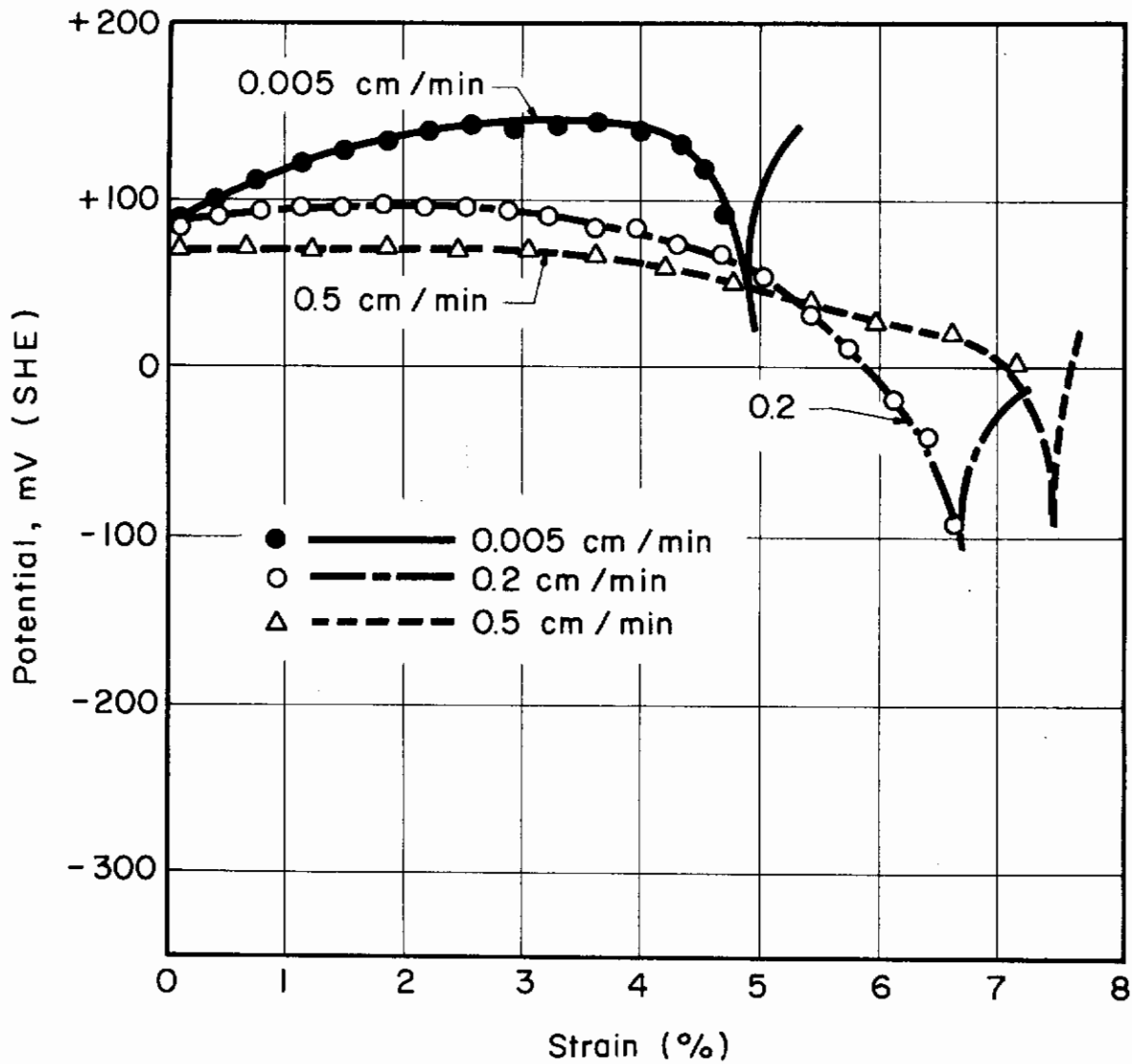


Fig. 37-b - Effect of Strain Rate on Corrosion Potential vs. Strain in $\text{CH}_3\text{OH} + 0.166\% \text{HCl} + 0.42\% \text{H}_2\text{O}$

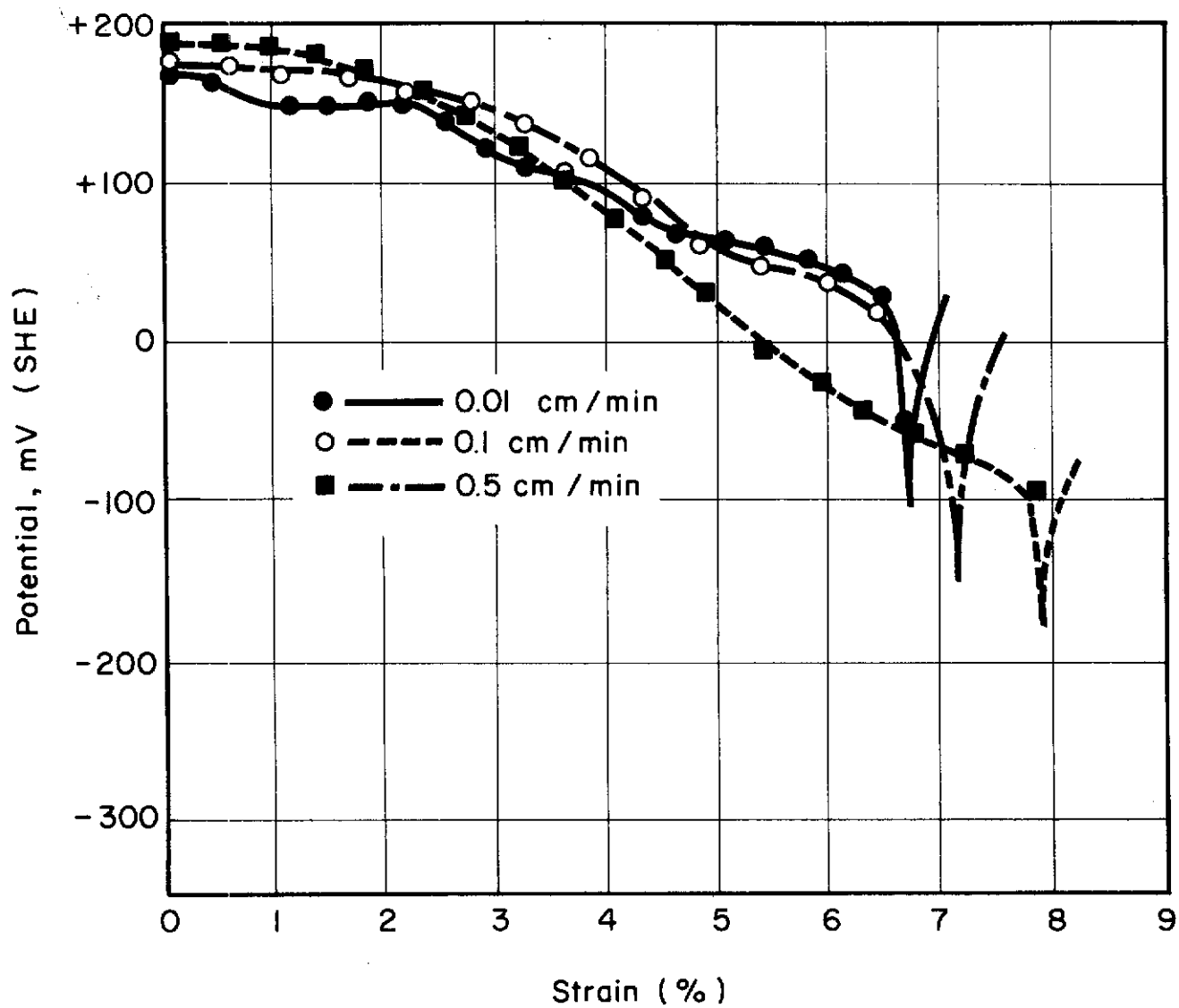


Fig. 37-c - Effect of Strain Rate on Corrosion Potential vs. Strain in $\text{CH}_3\text{OH} + 0.166\% \text{ HCl} + 0.99\% \text{ H}_2\text{O}$

g. Effect of Water Content on Failure Time of Bend Specimens at Corrosion Potential

Eight specimens were exposed to pure methanol for a period of 200 hours; no failures occurred in this period. In $\text{CH}_3\text{OH} + 0.166\% \text{HCl} + \text{H}_2\text{O}$ solutions the cracking time varies with water content, as illustrated in Fig. 38. Failure times are very short in the range of approximately 0.2 to 0.8% water.

h. Effect of Polarization Potential on Failure Time of Bend Specimens

The effect of failure time was determined as a function of polarization potential in $\text{CH}_3\text{OH} + 0.166\% \text{HCl} + 0.99\% \text{H}_2\text{O}$. Results of these experiments are plotted in Fig. 39 which shows short failure times (about 15 minutes) in the anodic range of +250 to 800 mV. Specimens cathodically polarized in the approximate range of -500 to +250 mV did not crack during the 12-hour test periods used. At high cathodic potentials (more cathodic than about -500 mV) cracking occurred within a few hours.

4. Discussion

From the results of both dynamic and static tests presented above, it is clear that about 0.8% water in $\text{CH}_3\text{OH} + 0.166\% \text{HCl} + \text{H}_2\text{O}$ solutions is a critical concentration. Electrochemical behavior and cracking susceptibility vary greatly depending on whether the water content is greater or less than this critical concentration. It would appear that the water, when present in concentrations of 0.8% and greater, is sufficient to repair defects which might exist in air-formed oxide films or which are introduced into films during straining. However, less than 0.8% water is insufficient to repair an oxide film. On this basis the following interpretation is made.

When titanium specimens are placed in the methanolic solutions, the portions of the specimen containing the defects described above act as anode areas while the remaining oxide covered surface behaves as a cathode. The anodes will become passivated (oxide film repair) by the presence of water. The number of defects, therefore, decreases with increasing water content and the corrosion potential will shift in the anodic direction, as illustrated in Fig. 31-a. When the water content is high enough (0.8%) all defects will be repaired and the system will approach a steady-state condition.

If a specimen is strained (especially beyond the yield) ruptures will occur in the oxide film causing an increase in active sites, and chloride ion attack will take place in these sites when the solution contains insufficient water for film repair. Under these conditions the corrosion potential will move in the anodic direction. However, when the water content is high enough to repair the film the corrosion potential



Fig. 38 - Failure Time vs. Water Content at Corrosion Potential

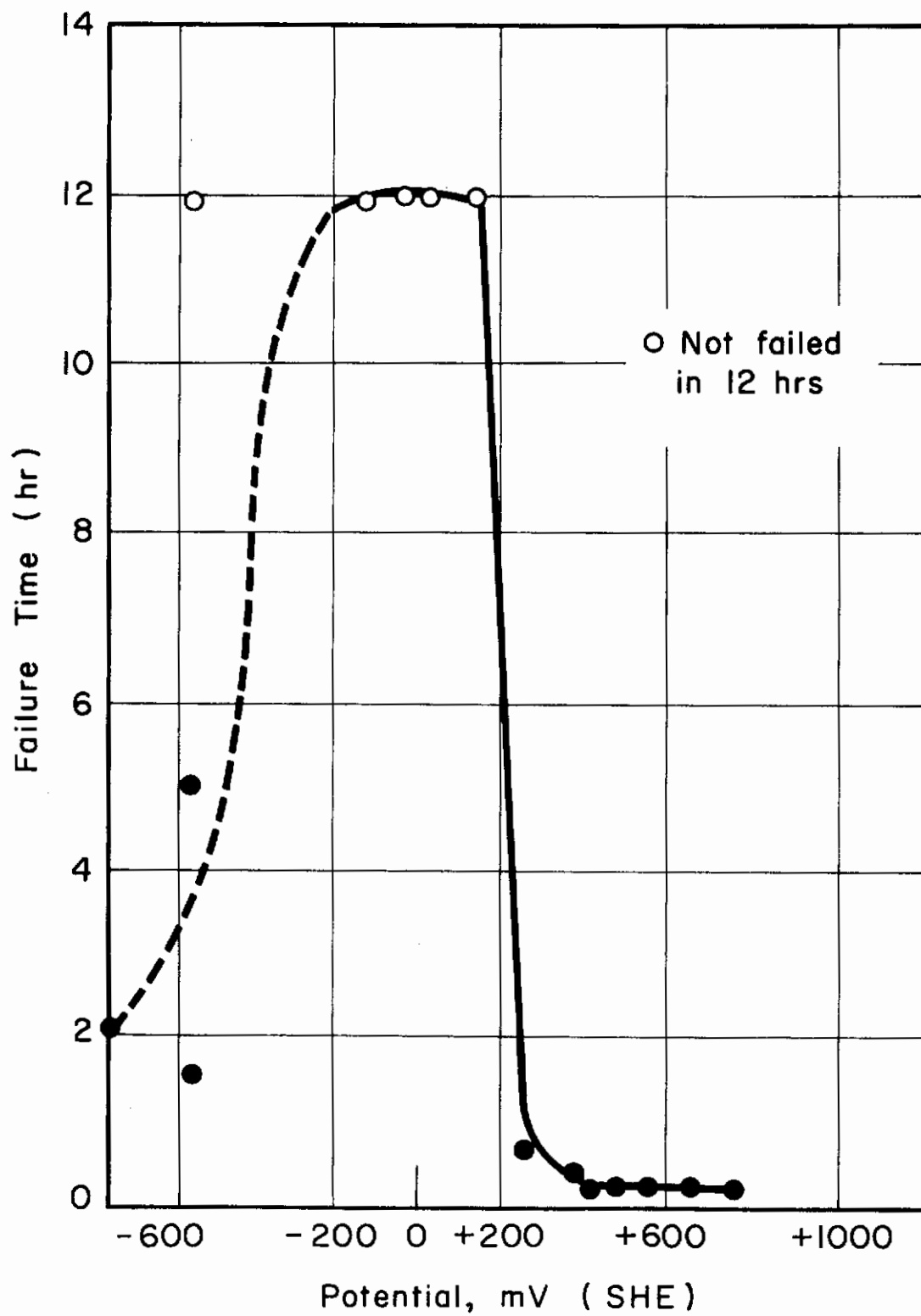


Fig. 39 - Failure Time vs. Polarization Potential in
 $\text{CH}_3\text{OH} + 0.166\% \text{HCl} + 0.99\% \text{H}_2\text{O}$

will move in the cathodic direction, as illustrated in Fig. 31-b, since strain continues to provide new active regions.

Figures 37-a and b show that the corrosion potential becomes more anodic at low strain rates when the environment contains less than the critical amount of water for passivation. This is the result of chloride ion attack. At high strain rates new active regions are provided rapidly enough to prevent chloride ion attack in the newly formed active regions and the increased anodic region causes the potential to move in the cathodic direction. However, when the water content is greater than the critical concentration chloride ion attack does not occur regardless of the strain rate and the corrosion potential will move in the cathodic direction, as illustrated in Fig. 37-c.

When a specimen is strained while at the corrosion potential in a solution containing less than the critical amount of water, the resulting chloride ion attack will cause a substantial decrease in elongation. The application of cathodic polarization or the addition of water to a concentration greater than the critical value prevents chloride ion attack and under either of these conditions no loss in elongation is observed (Figs. 29 and 30). However, if the specimen in the inert environment (critical amount of water added) is polarized in the anodic direction to induce chloride ion attack, the elongation will again be reduced to the low value as in the active environment at the corrosion potential.

The increased current observed during straining under anodic polarization is controlled by the diffusion of chloride ions to the active sites. This current effect is greatest at the low strain rates under conditions promoting the low elongation values described in Figs. 33, 34, and 36. During cathodic polarization the current increase appears to result from anodic dissolution and oxide film formation, and, therefore, the higher the strain rate the more rapid the increase in current with strain. When the strain rate is low some of the newly formed defects will be repaired (oxide film formation) and the increase in current with strain will be more gradual, as shown in Fig. 35.

Failure time of bend specimens was greatly reduced for those stress-corrosion specimens tested in solutions containing less than the critical amount of water. It is suggested that under these conditions, when the water content is insufficient to repair defective regions in the film, some of the active sites will support chloride ion attack. This chloride attack then leads to stress-corrosion failure. When the water content is greater than the critical concentration, longer times will be required for failure to occur (Fig. 38). However, the application of anodic polarization will induce chloride ion attack and cause failure within a short time. In this same environment a low cathodic polarization potential will prevent chloride ion attack and greatly increase failure time. Highly cathodic polarization potentials, however, will reduce failure time. This latter effect probably involves hydrogen embrittlement and, therefore, is different from the mechanism causing

failure of specimens polarized in the anodic potential region.

D. AN ELECTROCHEMICAL INVESTIGATION OF THE FACTORS
AFFECTING THE STRESS CORROSION CRACKING BEHAVIOR
OF TITANIUM-BASE ALLOYS IN METHANOL ENVIRONMENTS
(J. F. Gloz)

It has been known for some time that titanium and titanium alloys undergo stress-corrosion cracking in aqueous halide environments. One explanation of this susceptibility to cracking in a normally passive material is attributed to breakdown of the passive film by the action of aggressive halide ions, particularly chloride. The electrochemical nature of the process is demonstrated by the variation of susceptibility with potential; that is, in certain potential regions cracking can be inhibited.

Recently, however, titanium and titanium-base alloys have been shown to be susceptible to cracking in other environments including methanol, ethanol, ethylene glycol, and other organics nominally halide free. Considering this observation in light of the known aggressiveness of halide environments, two conclusions are possible.

- (1) A very small concentration of halide ions, sufficient to cause halide ion attack, is present in the titanium-methanol system.
- (2) Some mechanism other than halide ion attack is responsible for the susceptibility of these materials in methanol and other organic environments.

The possibility of traces of halide ions cannot be dismissed even though extensive precautions are taken to avoid contamination. For example, a small but finite amount of chloride, usually less than 50 ppm, is found in commercial titanium. Although Haney et al.²⁰ indicate that halide ions must be in the methanol to produce susceptibility, the occurrence of halide ions in the regions of attack (because of local dissolution of halide-containing base metal) has not been definitely determined. To investigate the effect of residual chloride on stress-corrosion behavior, a series of tests will be carried out in pure anhydrous methanol on titanium specimens of known but varied chloride concentrations.

Hydrogen-containing complexes are also of interest since there is a growing amount of evidence to suggest that hydrogen plays a key role in the stress-corrosion cracking of titanium. Attention will, therefore, be given to the chemistry of the methanol. Hydrogen complexes may react with bare titanium metal at an emergent slip-step to inhibit repassivation or form methoxide ions.²¹ To evaluate such possibilities special attention will be given to reactions in this environment.

The observation of in situ initiation and propagation of a stress corrosion crack by x-ray microscopy will be attempted. This investigation should provide a more complete understanding of the factors involved in the stress-corrosion cracking of titanium by methanol and, in particular, the role of the electrochemical factors.

E. EFFECTS OF TEXTURE AND GRAIN SIZE ON STRESS CORROSION CRACKING OF TITANIUM-BASE ALLOYS (I. J. Loomba)

Previous experiments on titanium demonstrated that stress-corrosion cracks in titanium alloys exposed to methanol-hydrochloric acid-water solutions originate from pits which, in turn, are associated with β phase and α - β interfaces. Also, a strong tendency exists for the pits to be elongated in the rolling direction and for stress-corrosion cracks to propagate parallel to the rolling direction.

Crack initiation and propagation studies are being continued on Ti-6Al-4V alloy in the above environment. Large-grained specimens, prepared by strain annealing, are being used in this work. It is hoped that strain annealing will provide large enough grains to permit studies of selected crystals of known crystallographic orientation. Although the specimens prepared thus far show substantial grain growth, none contains crystals large enough for individual studies. The large-grained specimens are being used for crack initiation studies under potentiostatically controlled conditions in an apparatus similar to that described in Fig. 1.

F. EFFECT OF STATE OF STRESS ON THE SUSCEPTIBILITY OF TITANIUM-BASE ALLOYS TO STRESS CORROSION CRACKING (S. Mahmoud)

Two complementary avenues of approach are being used to investigate the phenomenon of stress-corrosion cracking in two titanium-base alloys. In the first, or micro-mechanical method, the effects of various factors such as heat treatment, texture, and grain size are being studied. In the second, or phenomenological method, the general macroscopic laws for fracture are being studied. Eventually, the two investigations will be correlated to provide a single self-consistent approach to stress-corrosion cracking problems.

The state of stress in a homogeneous isotropic metal is completely defined by the three principal stresses. Therefore, the stress state at fracture can be represented by a stress in three-dimensional Cartesian coordinate stress space. The specific influence of the state of stress on susceptibility to stress-corrosion cracking has not been studied in detail nor well defined.

Laboratory work is being undertaken to study chemical cracking as a function of state of stress. It is planned to survey the first two stress quadrants which contain tensile stress

$$(1) \sigma_x = +, \sigma_z = +; \quad (2) \sigma_x = -, \sigma_z = +.$$

It is hoped that the initiation and the propagation stages can be defined by monitoring the pitting stage by electrochemical techniques and establishing a suitable criterion for the onset of the propagation stage.

1. Material and Experimental Analysis

Ti-6Al-4V and Ti-8Al-1Mo-1V sheets, 0.025-inch and 0.050-inch thick, are being used for the bending and tensile studies. The same alloys, in the form of a 0.25-inch diameter rod, are being used for the torsion-bending testing. The heat treatments of the two alloys are as follows:

(a) Ti-6Al-4V

- (1) Annealed for one-half hour at 1700/1725°F in an argon atmosphere followed by a water quench.
- (2) Aged for four hours at 1250°F followed by an air quench.

(b) Ti-8Al-1Mo-1V

Reheated mill-annealed material at 1450°F for 15 minutes in an argon atmosphere followed by an air quench.

In this research various states of stress are being used. The following is a brief summary of each method:

Uniaxial tension: Un-notched specimens.

Biaxial tension: Bending of flat specimens having various ratios of width-to-thickness, w/t , will provide two states of stress. Narrow specimens (small ratio of w/t) provide a state of plane stress; wide specimens (large ratio of w/t) provide a state of plane strain.

Combined bending-torsion: Figure 40 illustrates the apparatus to obtain various ratios of maximum normal stress to maximum shear stress. Load ($P/2$) is put on the specimen (1) lying on the supports (2) through the arms (3). The specimen undergoes torsion and bending. Here the relationship of maximum normal stress to the maximum shear stress remains constant during testing. The relationship is

$$\frac{\sigma_{\max}}{\tau_{\max}} = 1 + \frac{1}{\sqrt{1 + (a/k)^2}} \quad (2)$$

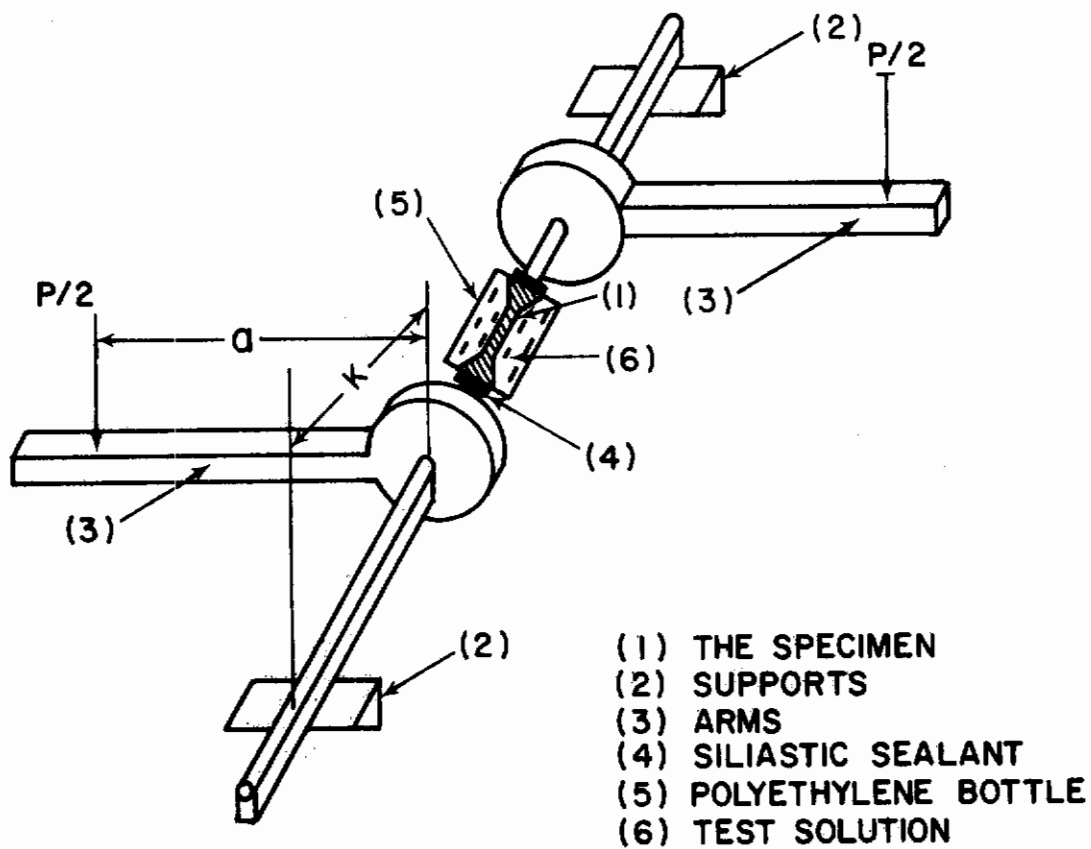


Fig. 40 - Schematic Diagram of Combined Bending-Torsion Apparatus
 (1) specimen (2) supports (3) arms (4) siliastic sealant
 (5) polyethylene bottle (6) test solution

Parameters a and k are defined in the figure.

The apparatus is designed to provide stress conditions over a range of $1 \leq (\sigma/\tau) \leq 2$. Furthermore, the angle between the maximum normal stress plane and the plane perpendicular to the specimen axis is given by

$$\sin 2\phi = \frac{1}{\sqrt{1 + (k/a)^2}} \quad (3)$$

From Eq. (2) it is evident, that while modifying the ratio a/k , one is able to change the state of stress from simple bending to torsion.

Notched bend specimens: Experiments to define the state of stress in the vicinity of a notch are in progress. Twenty specimens of the design illustrated in Fig. 41 were prepared from Ti-6Al-4V alloy in the duplex-annealed condition. These specimens will be used to investigate the role of notch plasticity on crack initiation and propagation in various environments, including $\text{CH}_3\text{OH-HCl}$ -water solutions.

Using a scaled up Bakelite model and with the assistance of Dr. L. J. Segerlind (Department of Engineering Mechanics, OSU) the stress analysis for the above geometry was determined. Experimental data and the stress distribution agreed very closely with the theoretical treatment. (A completely elastic solution to this problem was obtained by G. A. Griffis²² and J. W. Spretnak using the finite differences method). The theoretically and experimentally obtained values of the elastic stress concentration factor for the specimen considered are 2.06 and 2.10, respectively. The proposed boundary conditions in the theoretical analysis were verified experimentally and it was found that (1) a parabolic shear stress distribution, (2) a linear bending stress distribution, and (3) no shift in the neutral axis exist for measurements made 10 mm to the right and left of the centerline of the specimen.

Experiments are in progress to (1) relate the bend angle and plastic zone size with the applied bending moment, (2) observe crack initiation at mid-section of the notch and along its sides, (3) determine effect of chemical environments on the plastic action at the notch tip, and (4) determine notch ductility, instability, initiation, and propagation energy.

2. Future Work

(a) Loading under certain state of stress and recording the changes in current vs. time.

(b) Mapping out susceptibility regions; i.e., potential vs. stress level.

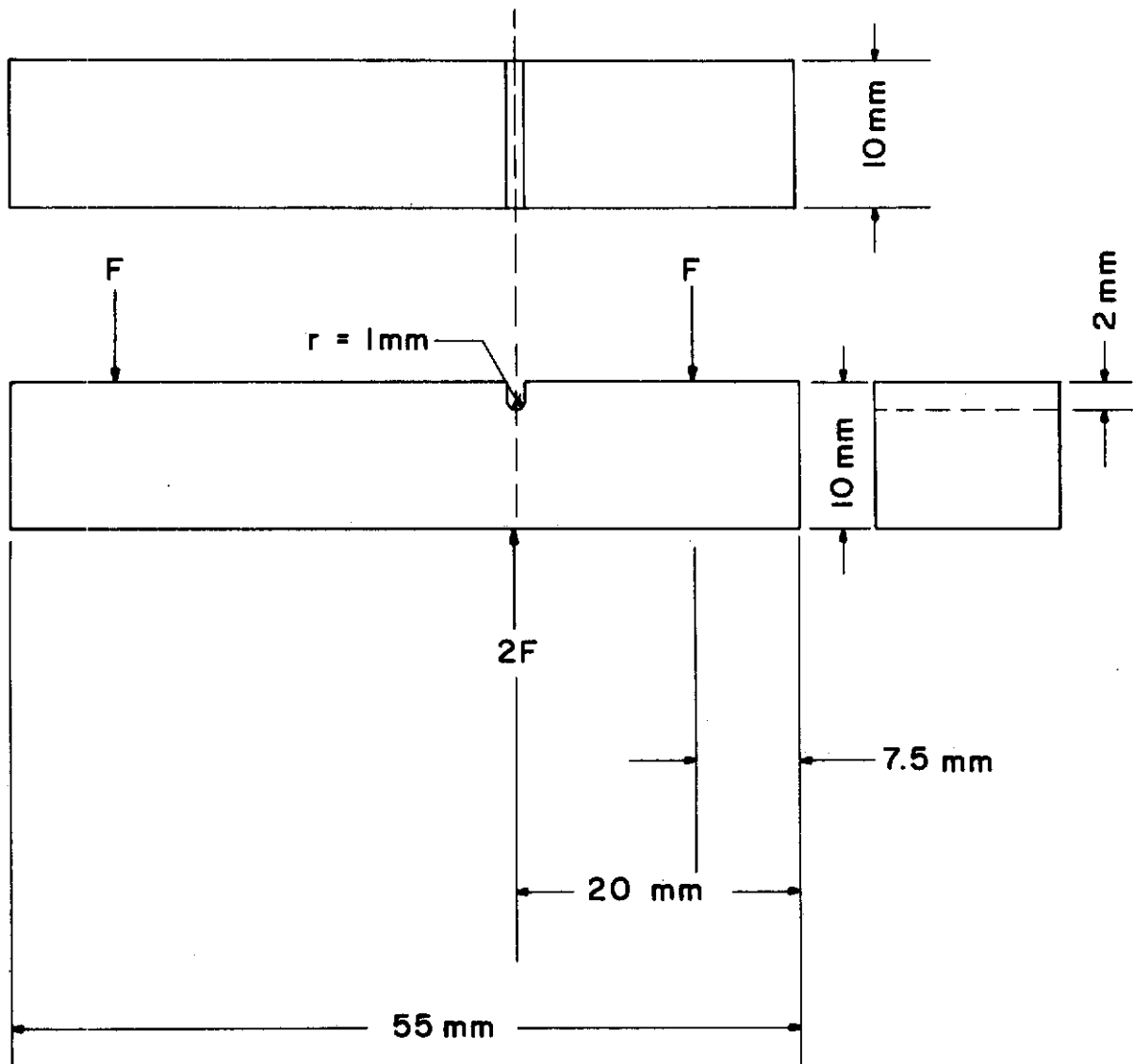


Fig. 41 - Notched Bend Specimen

(c) Initiation studies will be continued using the dry stripped plastic replica method. This method is rapid, reproducible, and does not require destruction of the sample. If several replicas are made during testing, one can trace back in time the initiation and propagation of cracks in any given area.

(d) An attempt will be made to determine the specific influence of the macroscopic state of stress on the shape of the failure envelopes²³ (Tresca and Von Mises criteria) in the $\text{CH}_3\text{OH-HCl-H}_2\text{O}$ environment.

SECTION III

STRESS CORROSION CRACKING OF STEELS (R. W. Staehle)

A. OBJECTIVES AND SCOPE

The aim of this program is to identify and quantify the processes which are fundamental to the initiation and propagation of stress corrosion cracks. The individual efforts described herein are considered to be key factors from which an effective quantitative basis for stress corrosion cracking can be developed.

The ultimate aim of the work is to provide a quantitative basis for designing high strength alloys and heat treatments which are resistant to catastrophic stress corrosion cracking.

B. CONTROLLED PHENOMENOLOGICAL STUDY OF CRACK PROPAGATION (G. E. Kerns and J. S. Sneary)

1. Objectives and Background

The objective of this investigation is to obtain a set of reliable phenomenological information on the propagation of stress corrosion cracks in several high strength steels exposed to well controlled gaseous and aqueous environments. The specific quantities being measured are: Crack velocity as a function of stress intensity, fractographic features, and sonic emission rate. Important features of the environments being controlled are: Partial pressure of gas, concentration of impurities added to gas, buffered pH of solutions, electrochemical potential.

2. Experimental Procedure for Crack Length Determination

All specimens tested were AISI 4335 steel, heat treated as follows: 1150°F for one hour, oil quench, and a temper of 400°F for one

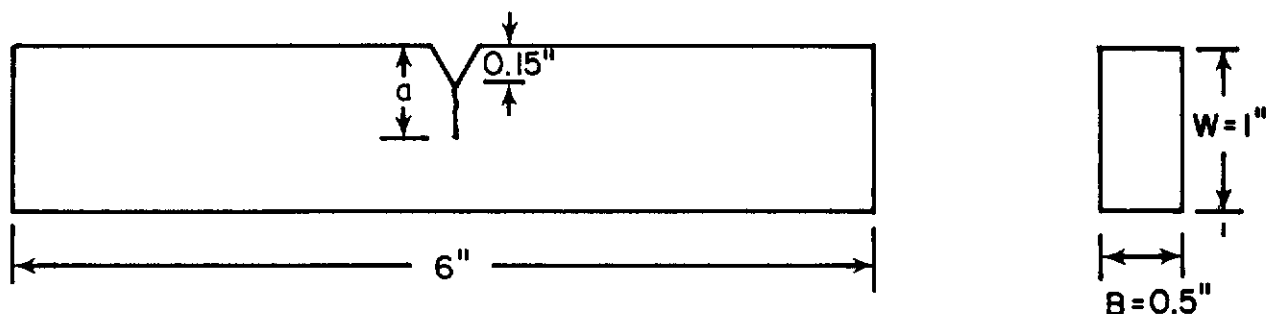
hour, air cool. Specimen dimensions, as well as the relationship for stress intensity factor, are given in Fig. 42. All specimens were tested under plane strain conditions, using cantilever beam type loading. The data reported herein was obtained using gaseous H_2/Ar mixtures. The impurity levels of the as-received gases were below 100 ppm. Figure 43 shows the purifying apparatus for the gaseous mixtures.

The electronic system for the detection of acoustic emissions is shown in Fig. 44. A description of the system will be presented later. Figure 45 shows the actual loading apparatus for the cantilever beam specimens. A Daytronic Model DS1000 transducer, mounted normal to the beam was used in series with a Daytronic Model 201B transducer exciter-demodulator to measure beam deflection. This reading, in millivolts, was reduced on an Esterline Angus strip chart recorder.

Preliminary testing was conducted to determine the relationship between crack length and deflection under constant load. Cantilever beam specimens were fatigue cracked to various depths. A cracked specimen would be loaded in 12-pound increments, allowed to equilibrate, and the beam deflection was then measured. The resultant data, shown in Fig. 46, were then used to predict crack length as a function of load and deflection. It was noted that crack growth in hydrogen gas gives a microscopically dark fracture surface, while catastrophic failure or propagation in air leaves a bright surface. Therefore, the end of the hydrogen-induced growth zone could be discerned from the color transition on the fracture surface. The curves described above were used to predict the crack length at which a specimen underwent catastrophic failure at constant load. This fracture stage is characterized by an extremely rapid change in crack growth and acoustic emission rates. The observed crack length at the end of the hydrogen propagation zone was compared to that predicted by the calibration curves, since the deflection and load at the onset of catastrophic failure were known. Errors, often times ranging to 20%, were observed.

In order to obtain a compliance curve which accounted for the crack front geometry, 14 specimens were fatigue-cracked giving initial crack lengths of approximately 0.350 inch. The specimens were then loaded to a starting K_I value of 35-40 ksi-inch^{1/2}. After equilibration in an argon atmosphere, hydrogen gas was introduced, giving rise to slow crack growth. Oxygen gas was then introduced to halt crack growth at a desired value of deflection. While in an oxygen environment, the specimen was rapidly loaded to failure. As shown in Brown and Srawley's text²⁴ on plane strain fracture toughness testing, the parameters $E \sqrt{B/P}$ and a/W are the significant variables for a calibration curve of this type, where

E = Young's modulus (psi)
 ν = compliance change (in.)
 B = specimen thickness (in.)
 P = load (lb)
 a = crack length (in.)
 W = specimen width (in.)



$$K_I \text{ (plane strain conditions)}$$

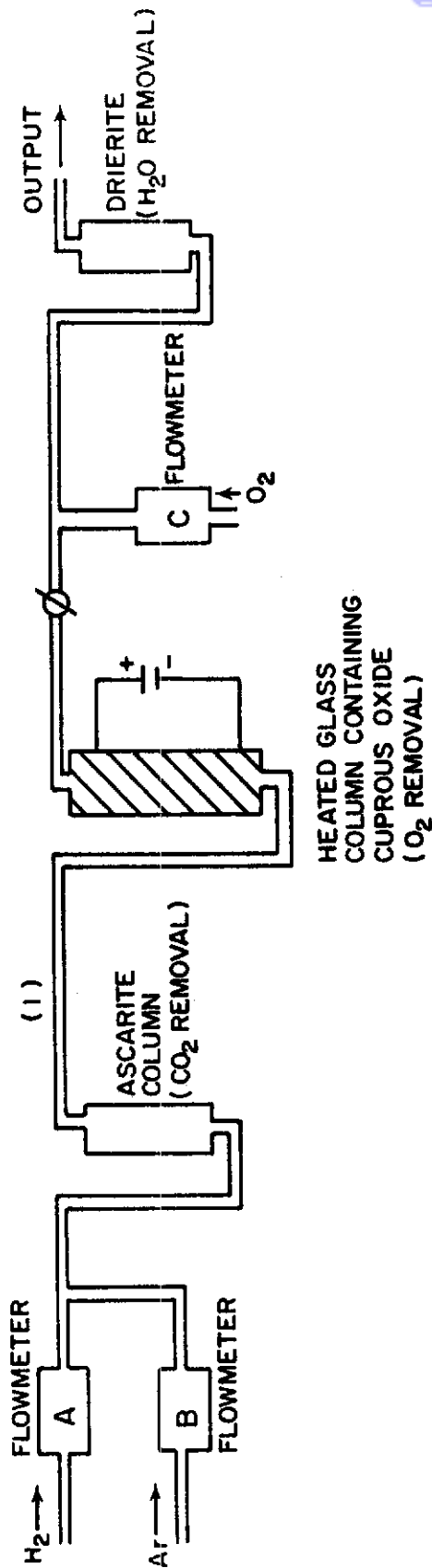
$$K_I = \frac{4.12(\Sigma M)\sqrt{1/\alpha^3 - \alpha^3}}{BW^{3/2}}$$

(psi-in.^{1/2})

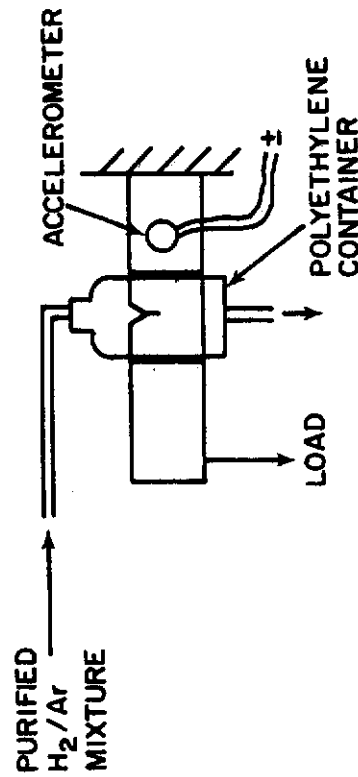
$$\alpha = 1 - a/W$$

ΣM = sum of moments (in.-lbs.)
about the fixed end of the
specimen

Fig. 42 - Specimen Size and Relationship Governing Stress Intensity Factor



Flowmeters A and C are of the multi-range monometer type, while meter B is a single range monometer.



(1) Copper and glass tubing was used throughout the system to avoid oxygen pickup

Fig. 43 - Gas Purification System Being Used for Crack Propagation Studies

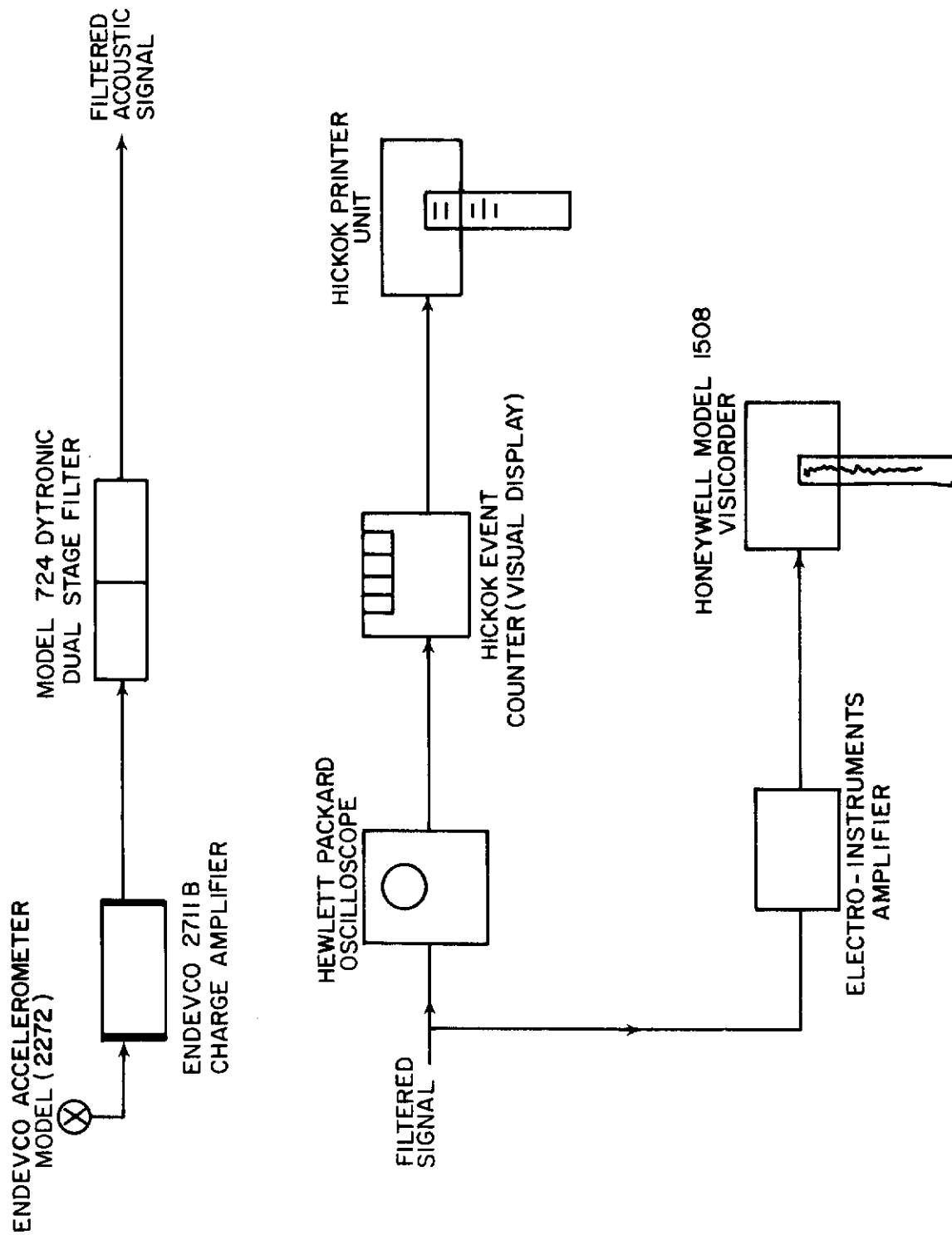


Fig. 44 - Electronic System for Detection of Acoustic Emissions

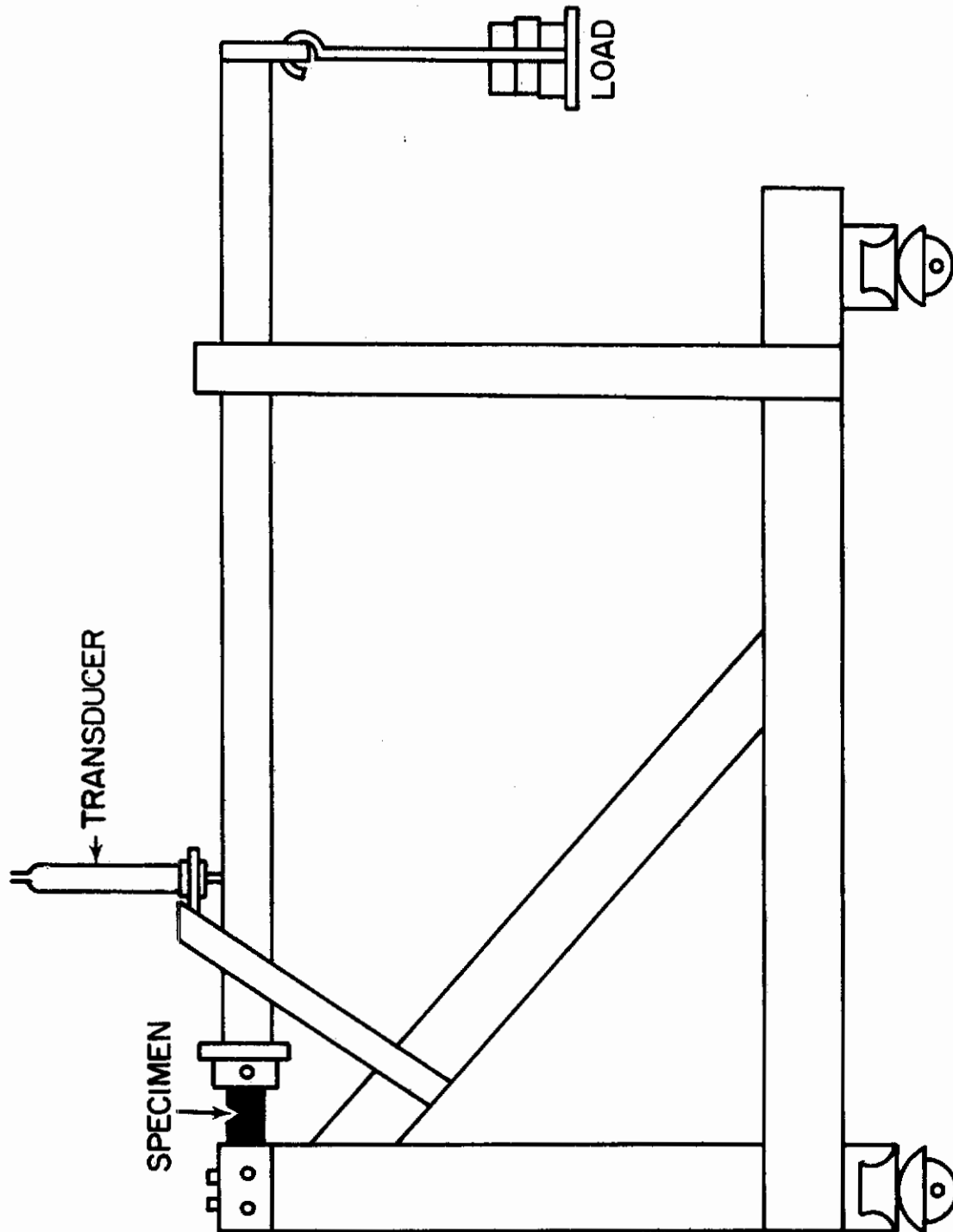


Fig. 45 - Cantilever Beam Apparatus

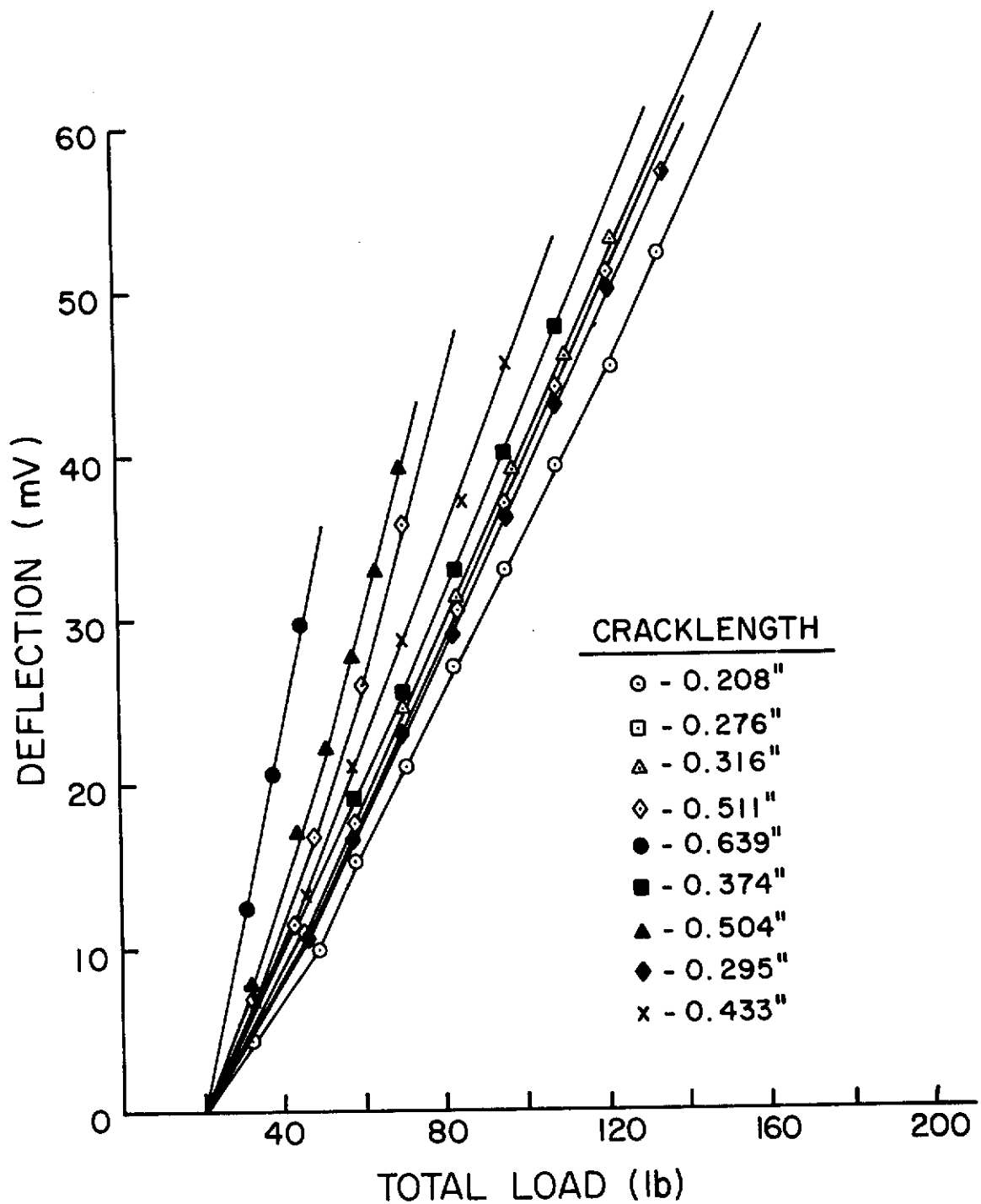


Fig. 46 - Relationship between Crack Length, Load, and Deflection as Determined in Argon Atmosphere for 4335 Steel

Such a calibration curve is independent of stress intensity factor and is based on the assumption of no plastic deformation.²⁵

For the purpose of this investigation, the elastic compliance, U , is determined by the conversion of the beam deflection (mV) and the transducer calibration curve in Fig. 47; i.e., 0.005 inch/mV. Since the deflection is due to a change in crack length, the crack length, a , is replaced by $(a_f - a_c)$, where

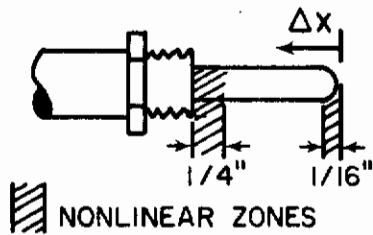
a_f = crack length at end of hydrogen
propagation, and
 a_c = initial center crack length.

Because of the fact that E and P (static load) are constant, as well as U being a linear function of deflection (δ) in millivolts, the data are plotted in Fig. 48 as δB (millivolt-inches) vs. $a_f - a_c/W$ (unitless). The 95% confidence limits on the least squares plot in Fig. 48 are also shown.

3. General Description of Acoustic Technique

As the crack propagates, a fraction of the stored elastic energy at the crack tip is released with each increment of crack growth. This energy translated through the lattice as stress waves may be detected by a piezoelectric crystal fastened to the surface of the specimen. As the accelerometer is accelerated by the stress wave, crystal resonance and a sinusoidal charge difference across the crystal are produced. Treating the accelerometer as a single-degree-of-freedom spring mass system results in various solutions for the displacement of the crystal with respect to time as different forcing functions are used. If the crystal is subjected to a spike pulse (large force for a very short time), mathematical solutions such as those found in Kinsler and Frey²⁶ show that the displacement, acceleration, and charge differential of a piezoelectric crystal are of a damped sinusoidal form. Therefore, when a stress wave is emitted from a growing crack and strikes the accelerometer, the output voltage of the accelerometer is of a sine wave nature, but decaying with time. The response of the accelerometer is maximum at its natural resonance frequency. By filtering the various frequencies emitted by the crystal using a pass band filter, the resonance frequency component for each emission can be examined. The size and number of resonance peaks associated with each output of the crystal can be taken as a relative measure of the size of the initial phonon or energy release from the crack tip. The advantages of an accelerometer are that the resonance frequency is quite independent of mounting techniques and the voltage across the accelerometer can be converted into an absolute acceleration or force. It must be noted here that the output of the crystal is a strong function of frequency above $1/5$ of the natural resonance frequency, so that the use of an accelerometer at its natural resonance frequency allows it to be used as a comparative tool only. The acceleration values obtained at this frequency will always be higher than the true values. However, the increased response of the crystal in this frequency range enables it to be a more sensitive tool.

DISPLACEMENT MEASURED
FROM FULL OPEN POSITION



LINEAR PORTION
1-3/16" FULL SPAN

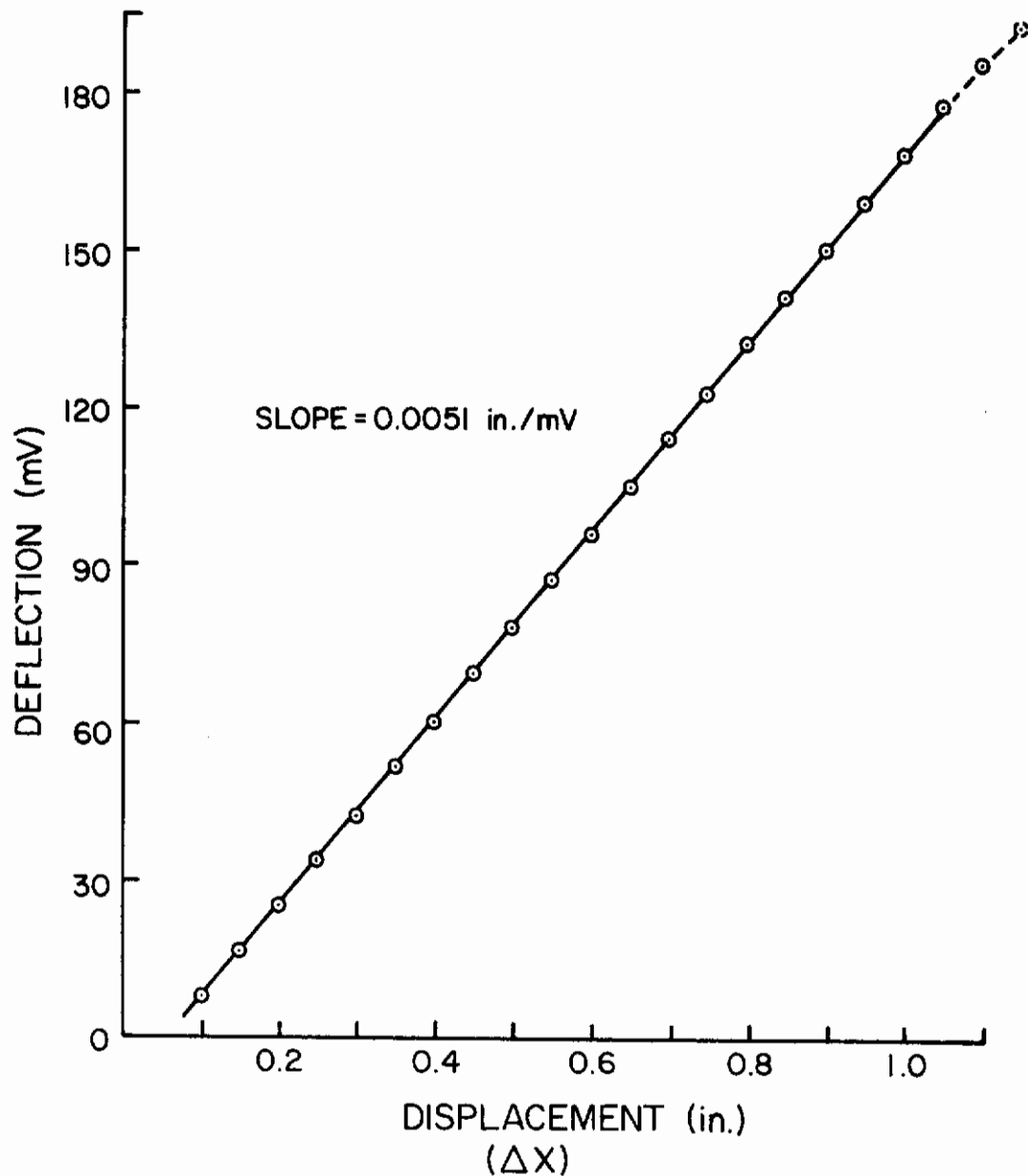


Fig. 47 - Deflection of Beam vs. Displacement for Cantilever
Beam Specimen

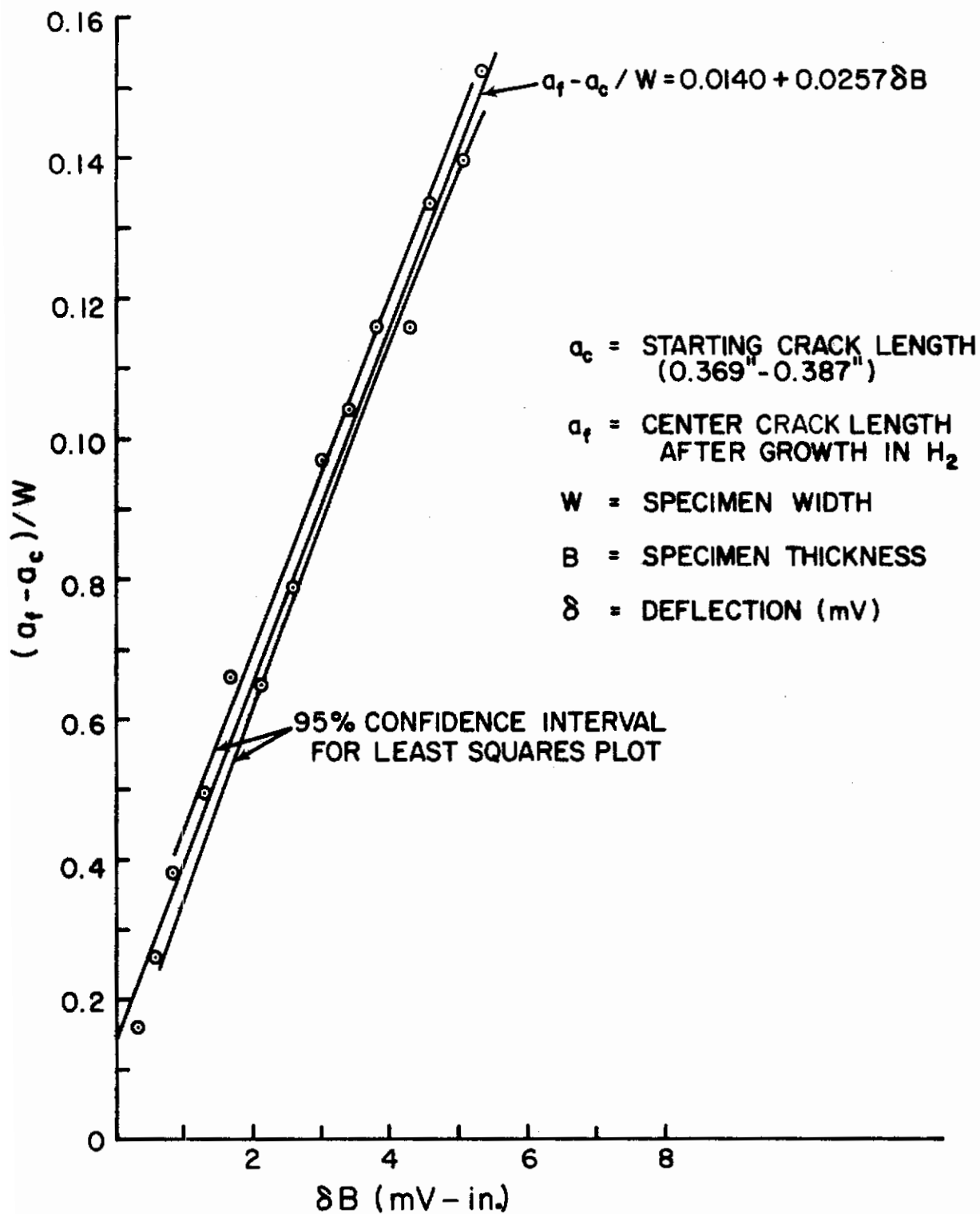


Fig. 48 - Calibration Curve for Pre-Cracked 4335 Cantilever Beam Specimens

In this investigation the number of resonance peaks above a certain voltage value will be used as a relative measure of the size of the emission. A larger energy release from the crack tip will resonate the crystal with a larger amplitude or for a longer time, or both. The number of resonance peaks associated with the emission above a certain voltage level will be larger.

4. Description of Acoustic Detection System

The acoustic emission is detected by an Endevco Model 2272 accelerometer (natural resonance frequency of 37 kHz), and amplified, using an Endevco Model 2711B charge amplifier. The output of the amplifier is 5V/g. The amplifier output is sent into a Daytronic Model 724 filter, operating in a 15 kHz double-high pass mode. The gain of the filter for a 33.3 kHz signal is 0.204. For viewing purposes the output of the filter is fed into a Hewlett-Packard Model 132A dual beam oscilloscope. The output of the oscilloscope was fed into a Hickok Model DMS 3200P mainframe, containing a DP-150 1 MC counter plug-in unit. The events counted by the plug-in unit were recorded, using a four-digit Hickok PR 4900 printer. This system was used in conjunction with an Electro Instruments Model A20B-34 amplifier in series with a Honeywell Model 1508 visicorder. The two electronic systems allow three measurements to be made as shown below.

- a. The Hickok event counter permits the counting of the number of resonance peaks associated with each acoustic emission. The output is the number of resonance peaks recorded during the print cycle. This parameter is used as a relative measure of the energy release from the crack tip, and therefore, the amount of crack growth.
- b. A Hewlett-Packard Model 197A oscilloscope camera is used with the oscilloscope. The oscilloscope is triggered by the slope of any incoming signal, thereby allowing the emissions to be successfully photographed without over-exposure due to the intensity of the base line on the oscilloscope over a long period of time. In this manner the amplitude and period of the signals can be recorded.
- c. The Honeywell visicorder, with a frequency response of only 13 kHz, allows individual emissions to be recorded without resolving the number of resonance peaks contained in a given emission.

This instrumentation allows the use of acoustic emission detection as a quantitative technique in the monitoring of hydrogen-induced slow crack growth.

5. Experimental Procedure for Detection of Acoustic Signals

The trigger level for the Hickok event counter was adjusted to record all resonance peaks above 0.01 g (as determined by the voltage-acceleration constant for the accelerometer). Because of the resonance of the crystal, the real acceleration value required for triggering the counter is much less than 0.01 g. However, the correction factor is constant and can be neglected, but only in a comparative study. The effects of stress intensity factor on crack growth rate and emission rate are given for four specimens of AISI 4335 steel at low hydrogen partial pressures in Tables II-V. Photographs of acoustic emission signals obtained from specimens during crack growth are shown in Fig. 49.

Table II - Stress Intensity Factors, Crack Growth Rates, and Emission Rates for a Hydrogen Level of 3.3%

Stress Intensity Factor** (ksi-in. ^{1/2})	Crack Growth Rate (in./min)	Resonance Peaks Counted* per Minute
55.1	.0009	10.5
56.1	.0009	23.0
57.2	.0010	10.0
58.4	.0008	38.0
59.3	.0010	9.0
61.3	.0011	23.0
62.8	.0013	26.0
64.8	.0010	50.5
66.9	.0013	36.0
69.2	.0017	52.5
72.4	.0020	120.0
77.2	.0035	401.0

Initial stress intensity - 51.5 ksi-in.^{1/2}

* Trigger level set at 0.0085 g using square wave generator

** K_I values based on maximum cracked length for parabolic crack front

Table III - Stress Intensity Factors, Crack Growth Rates,
and Emission Rates for a Hydrogen Level of 6.9%

Stress Intensity Factor** (ksi-in. ^{1/2})	Crack Growth Rate (in./min)	Resonance Peaks Counted* per Minute
55.2	.0014	5.0
56.1	.0014	22.0
57.1	.0018	83.0
58.2	.0018	16.0
59.2	.0018	16.0
60.5	.0020	56.0
62.0	.0023	116.0
63.7	.0024	24.0
65.6	.0027	32.0
67.8	.0027	18.0
70.3	.0031	61.0
73.2	.0038	128.0
77.4	.0051	249.0

Initial stress intensity - 50.4 ksi-in.^{1/2}

* Trigger level set at 0.01 g using a square wave generator

** K₁ values based on maximum crack length for parabolic
crack front

Contrails

Table IV - Stress Intensity Factors, Crack Growth Rates,
and Emission Rates for a Hydrogen Level of 7.1%

Stress Intensity Factor** (ksi-in. ^{1/2})	Crack Growth Rate (in./min)	Resonance Peaks Counted* per Minute
51.8	.0019	30.0
52.5	.0024	10.0
53.1	.0024	32.0
54.0	.0027	23.0
54.8	.0034	132.0
56.0	.0037	140.0
57.2	.0047	144.0
58.6	.0044	219.0
60.2	.0056	307.0

Initial stress intensity - 48.0 ksi-in.^{1/2}

* Trigger level set at 0.01 g using a square wave generator

** K₁ values based on maximum crack length for parabolic
crack front

Table V - Stress Intensity Factors, Crack Growth Rates,
and Emission Rates for a Hydrogen Level of 7.7%

Stress Intensity Factor** (ksi-in. ^{1/2})	Crack Growth Rate (in./min)	Resonance Peaks Counted* per Minute
53.8	.0027	38.0
55.1	.0027	29.0
56.5	.0034	257.0
58.1	.0034	43.0
59.9	.0034	67.0
62.0	.0045	56.0
64.5	.0047	114.0
69.1	.0075	365.0

Initial stress intensity - 48.6 ksi-in.^{1/2}

* Trigger level set at 0.01 g using a square wave generator

** K₁ values based on maximum crack length for parabolic
crack front

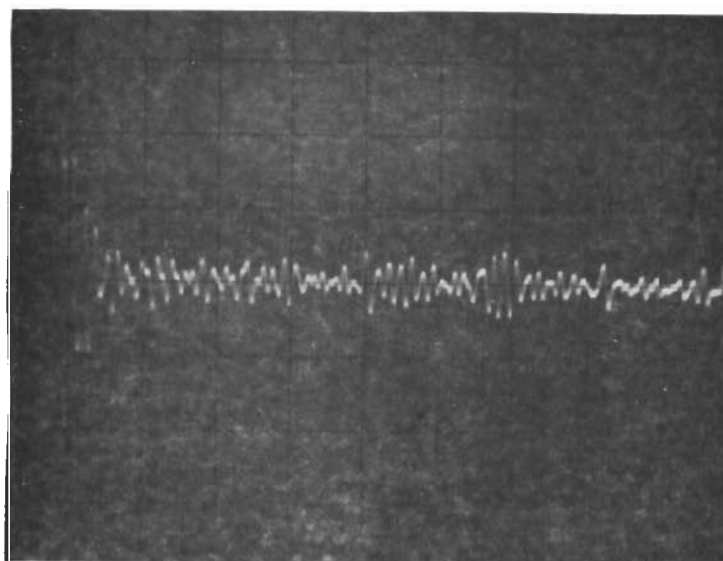
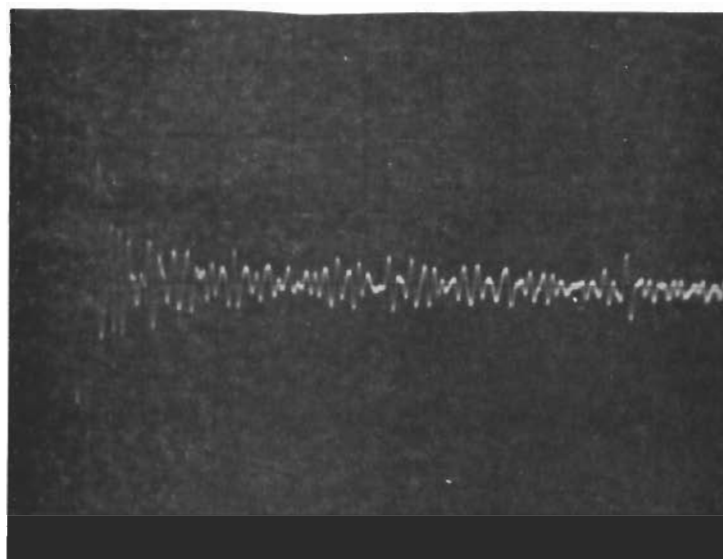


Fig. 49 - Photographs of Oscillographic Trace Produced by Acoustic Emission During Crack Propagation in 4335 Steel.
Vertical Scale - 0.02 g/cm; Horizontal Scale - 0.2 msec/cm

6. Discussion

Examination of the emission data showed a sporadic pattern while the crack growth rate showed a relatively steady increase with increasing stress intensity factor. During the testing of the specimens, it was noticed that ultra-high frequency interference was present which occurred in bursts. After consultation with the manufacturer of the Model 724 filter, it was learned that operation of the filter in a band-pass (30 to 40 kHz) mode eliminated the interference. This interference may explain, in part, the sporadic emission data. Investigation of the trigger level adjustment for the Hickok counter showed conclusively that the trigger level must be set using a sinusoidal wave form of the same frequency as that for accelerometer resonance. Square-wave generators and low-frequency sine wave generators were found to be unsatisfactory. In order to determine the optimum trigger level for detecting the maximum number of emissions, while eliminating extraneous background noise, a third investigation was conducted. The accelerometer was mounted on a loaded 4335 steel specimen exposed to air. The trigger level of the counting system was lowered until background noise was detected. The results of this test are shown in Fig. 50. A trigger level of at least 0.013 g was required to avoid extraneous background noise.

7. Conclusions

- a. Hydrogen-induced slow crack growth does occur in AISI 4335 steel at hydrogen partial pressures of less than 0.01 atm.
- b. Oxygen gas, as shown in Ref. 27 by Johnson and Hancock, when introduced into a hydrogen-argon environment, halts slow crack growth in its early stages.
- c. Acoustic emissions may be detected during slow crack growth in the presence of hydrogen gas.
- d. Crack growth rate increases with the stress intensity factor when 4335 steel undergoes hydrogen--induced crack growth.

C. EFFECT OF ENVIRONMENTAL ADDITIVES--HYDRAZINE (R. D. McCright, P. L. Carter, and J. S. Snerry)

1. Objectives and Background

The objective of this work is to assess the behavior of certain environmental species known to interact with surface processes. By using various additives, in environments in which cracks are propagating it should be possible to obtain additional information on

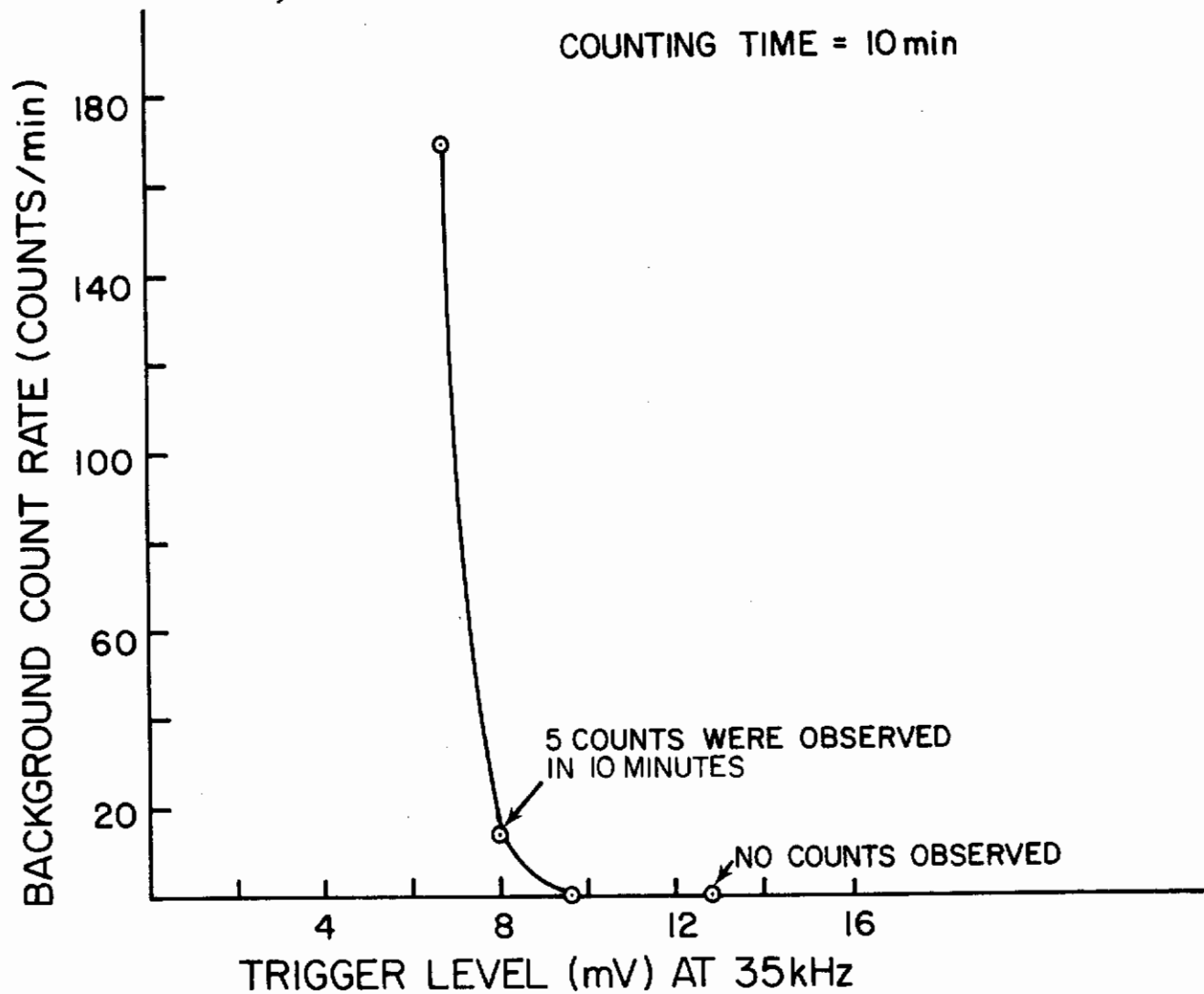


Fig. 50 - Background Count Rate vs. Trigger Level Setting (mV) of Peak Counter for a Specimen of 4335 Steel Loaded but Undergoing no Crack Growth

critical processes occurring at the crack tip. The work described herein was performed using hydrazine additives to aqueous solutions. In order to obtain an understanding of the cracking behavior, polarization and hydrogen permeation experiments were conducted.

2. Experimental

a. SCC Experiments

The cantilever beam experiment as shown in Fig. 45 was used for studying crack propagation. The base solution was 3.5% NaCl; hydrazine was added in the range 0 to 2.0%. The crack propagation data are summarized in Fig. 51. Additives of hydrazine are shown clearly to exert a slowing effect on crack propagation. The total time-to-cracking is increased by a factor of about 10 and the crack propagation rate in the early stages is substantially slowed. All specimens were heat treated as described in Section III-B-2.

b. Polarization Experiments

Potentiokinetic polarization curves were run on AISI 1010 steel. A small specimen (area = 0.504 cm^2) was cut from a coupon and ground with 600 grit paper. The specimen was polarized in 3.5% NaCl solution, with and without hydrazine (NH_2NH_2) additions. Solutions were deaerated for at least two hours before the test and during the test by bubbling high-purity tank nitrogen through the system. In the tests in which hydrazine was used, this compound was added shortly before the test was started because of its volatility. The bubbling nitrogen thoroughly mixed the liquid hydrazine with the salt solution. The potential was scanned at 5000 mV/hr beginning at -1600 mV(SCE) which is on the cathodic side of the rest potential. The potential was scanned in the noble direction passing through the rest potential, and the scan was continued into the region of intense anodic dissolution. In no case was there anodic passivation. The scan was reversed at the point of intense anodic dissolution, and the potential was scanned in the active direction, through the rest potential and to the starting potential [-1600 mV(SCE)].

The active-to-noble and noble-to-active scans are shown in Figs. 52, 53, and 54, with the first corresponding to neutral w/o hydrazine, the second to the chloride + 0.02 w/o hydrazine, and the third to 0.2 w/o hydrazine. Figure 55 shows only anodic scans comparing effects of hydrazine but at a lower scan rate.

The rest potential of the active-noble scans varied with the composition, ranging from -875 mV(SCE) [-1105 mV(SHE)] with no hydrazine, to -975 mV(SCE) [-1205 mV(SHE)] at 0.02 w/o NH_2NH_2 , to -1025 mV(SCE) [-1265 mV(SHE)] at 0.2 w/o NH_2NH_2 (see Fig. 55). This is in accord with the "scavenger" behavior of the hydrazine. The chief cathodic reaction in a neutral pH solution such as this is oxygen

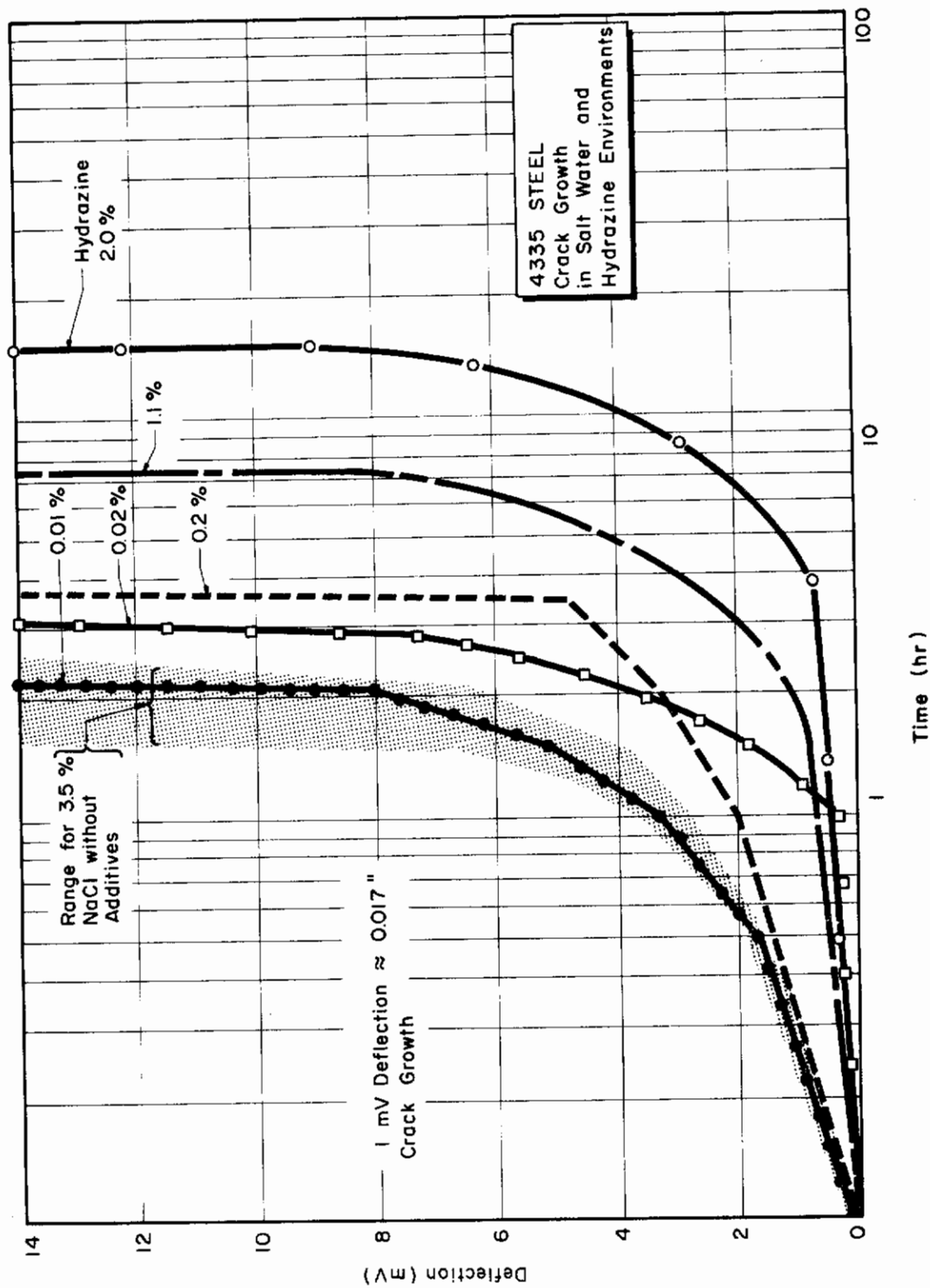


Fig. 51 - 4335 Steel Crack Growth in Salt Water and Hydrazine Environments

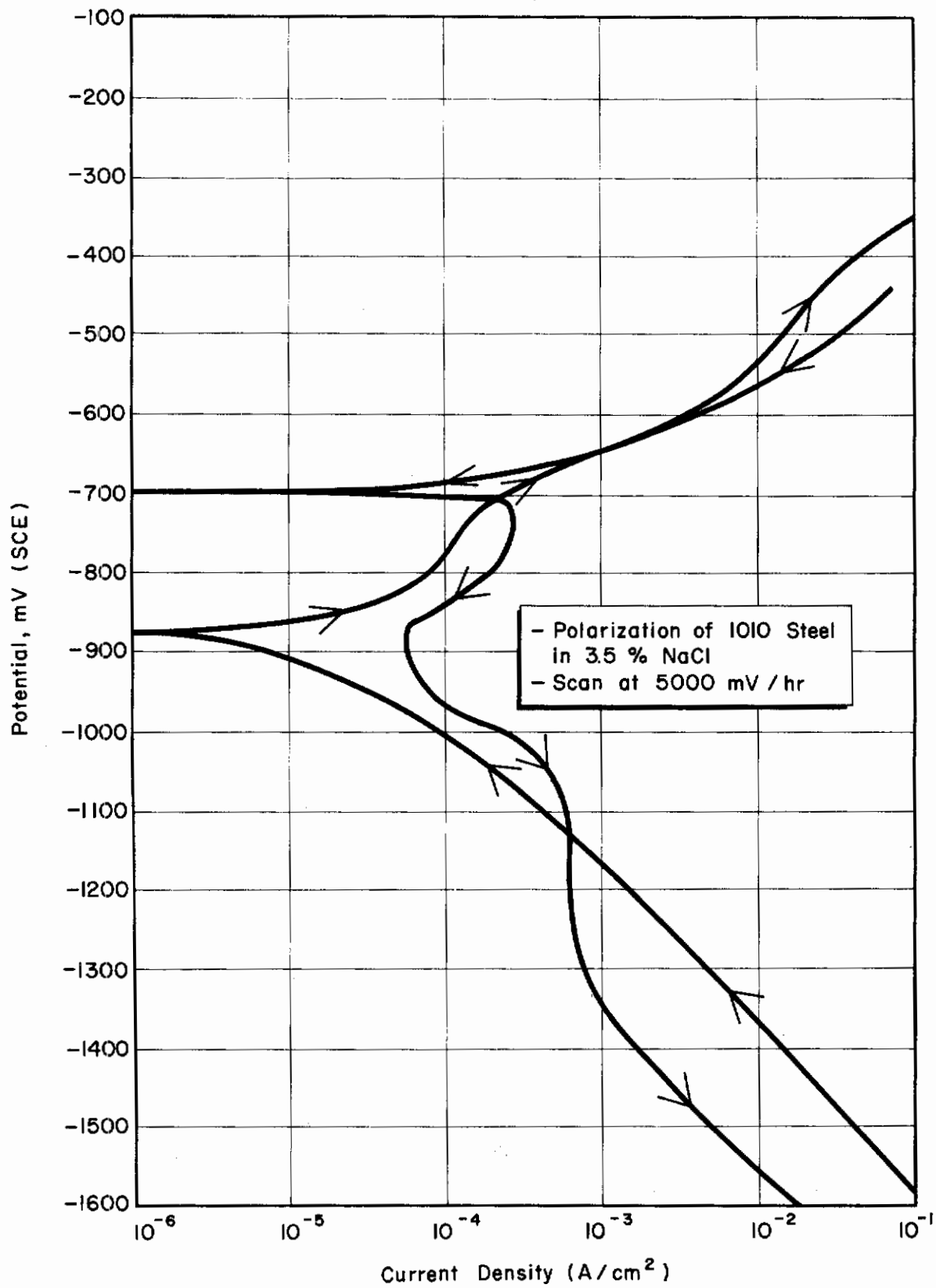


Fig. 52 - Polarization of 1010 Steel in 3.5% NaCl. Scan at 5000 mV/Hr

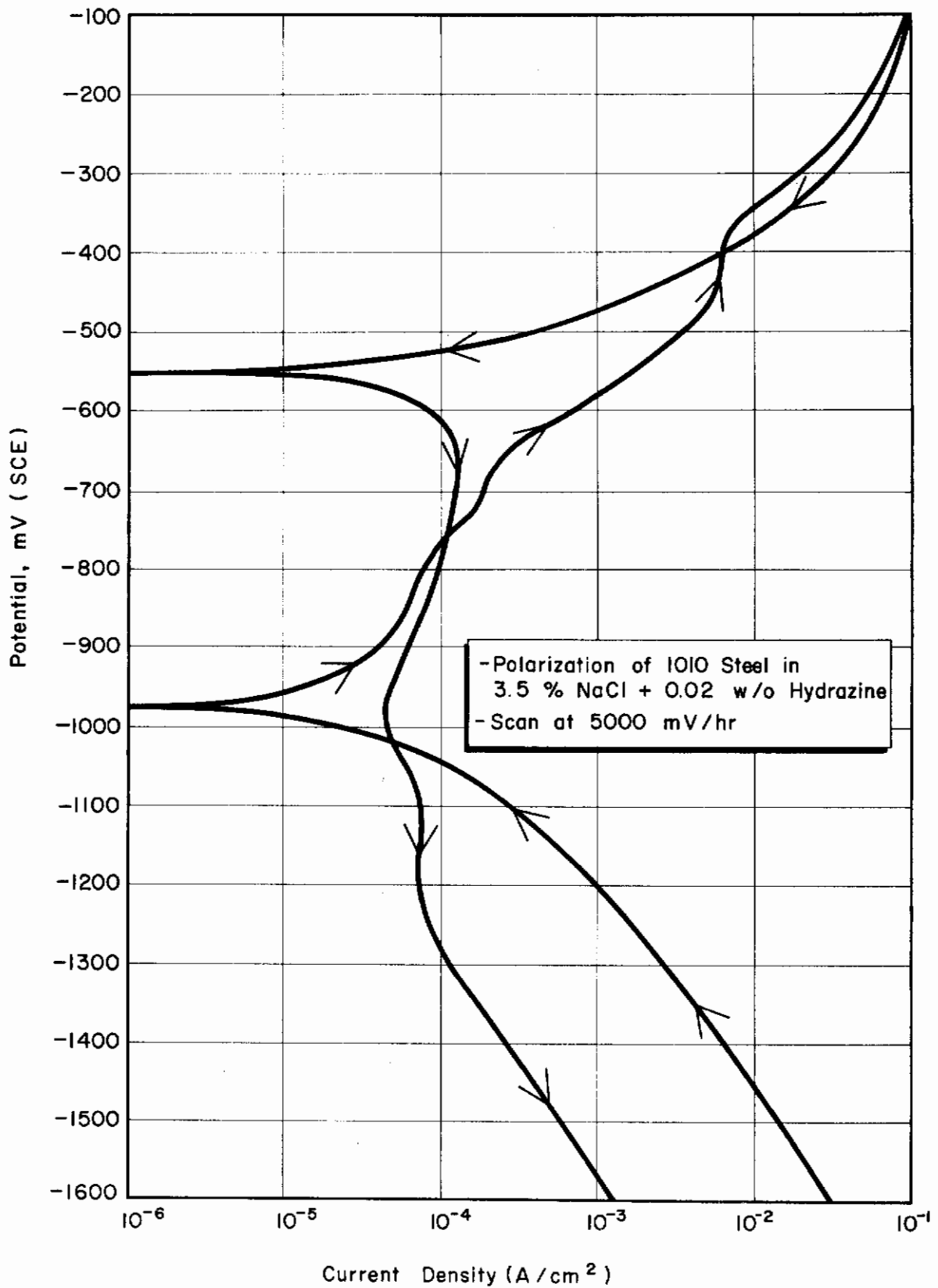


Fig. 53 - Polarization of 1010 Steel in 3.5% NaCl + 0.02 w/o Hydrazine. Scan at 5000 mV/Hr

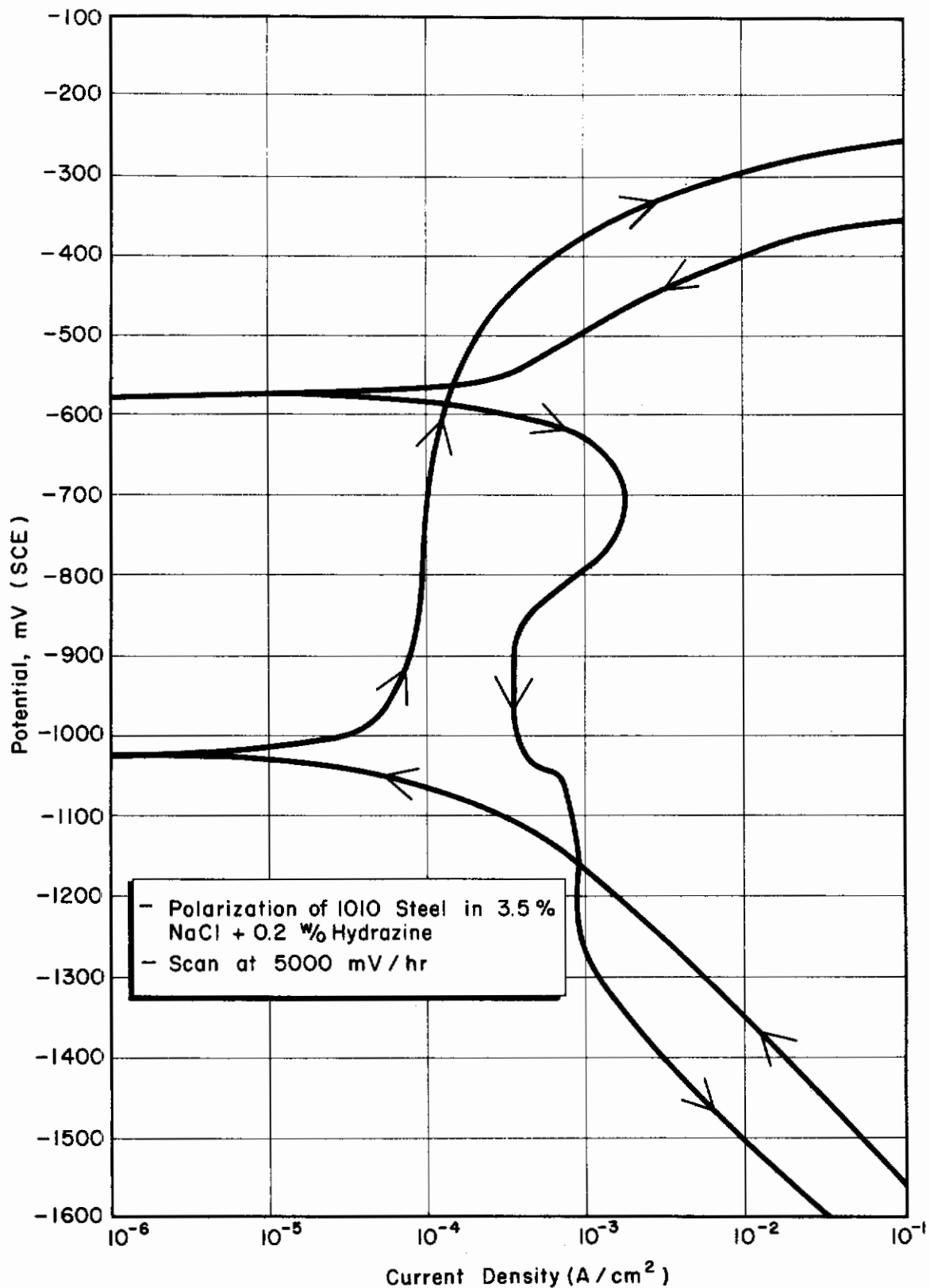


Fig. 54 - Polarization of 1010 Steel in 3.5% NaCl + 0.2 w/o Hydrazine. Scan at 5000 mV/Hr

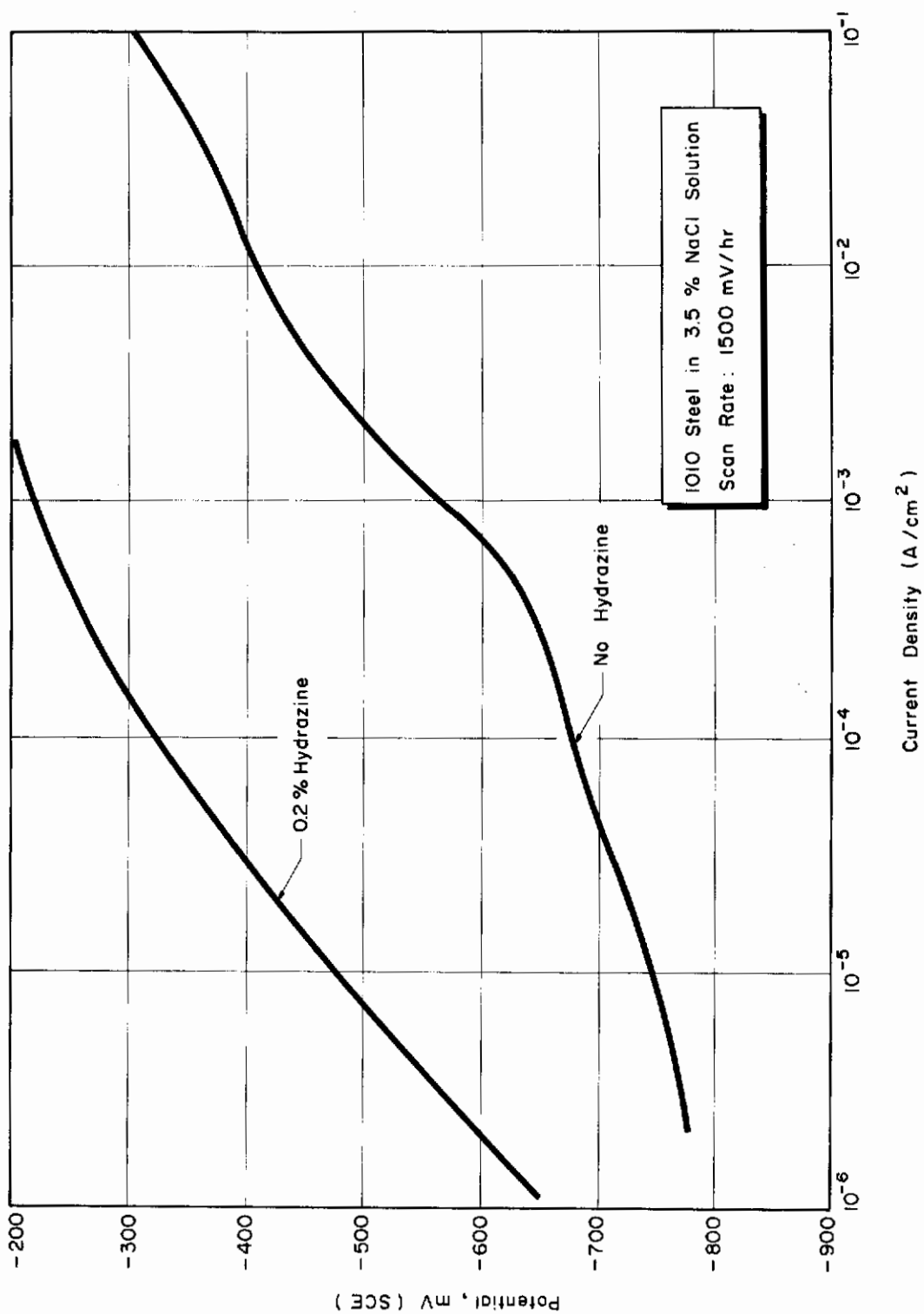


Fig. 55 - Anodic Scans Comparing Effects with and without Hydrazine for 1010 Steel

reduction. By chemically removing residual oxygen, the half-cell potential of the oxygen electrode is shifted to more active values. The pH of these solutions was 6.9. There was considerable hysteresis on the back scan (noble-to-active) and the rest potentials of these were much more noble than those of the active-to-noble scans. This was probably a result of the oxidation of iron to ferrous ions and ferrous ions to ferric ions at the high anodic potentials and the subsequent influence of the ferrous/ferric redox potential on the rest potential. At these high potentials, the corrosion of the sample was rapid and the solution became dark green colored and finally rusty colored as the oxidation continued.

c. Hydrogen Permeation Experiments

Hydrogen permeation experiments were conducted on AISI-1010 steel 0.2 mil thick. The specimens had been vacuum annealed at 650°C for two hours and polished with 600 grit paper. Solutions were 3.5 w/w NaCl at pH 6.9 without and with hydrazine addition at 0.2 and 0.02 w/o.

The apparatus used was the standard electrochemical technique shown in Fig. 56. Hydrogen ions are reduced and hydrogen is charged at negative potentials on the left side of the membrane, and on the right side hydrogen is oxidized ($H \rightarrow H^+$) in a 0.1N NaOH (pH 12.8) solution. This oxidation current is then the permeation current.

The anodically polarized side is maintained at +300 mV (SCE). With no hydrogen charging from the other side, the current on the anodic side decayed until a steady state value was achieved. This is called the residual current. We assume that the current corresponding to oxidation of the hydrogen at this surface is in addition to the residual current. The difference between the total anodic current when hydrogen is charged through the system and the residual current is the permeation current as shown in Fig. 57. Once a steady-state residual current obtains, the charging current was switched on. The hydrogen production on the cathodically polarized side was controlled amperostatically at 14 mA (specimen area = 2 cm² so $i_c = 7$ mA/cm²). The potential during charging on this side was in the region -1450 to 1500 mV(SCE). Then, while hydrogen charging, the anodic current increased. These transients are shown in Fig. 57. In the larger amounts (0.2 w/o) of hydrazine, the hydrogen permeability is increased. In the lower amounts (0.02 w/o) the hydrogen permeation kinetics are decreased.

3. Discussion

The key observations here are

- (a) the crack velocity is slowed by hydrazine additions,
- (b) the anodic kinetics are slowed by hydrazine, and
- (c) the permeation kinetics are accelerated.

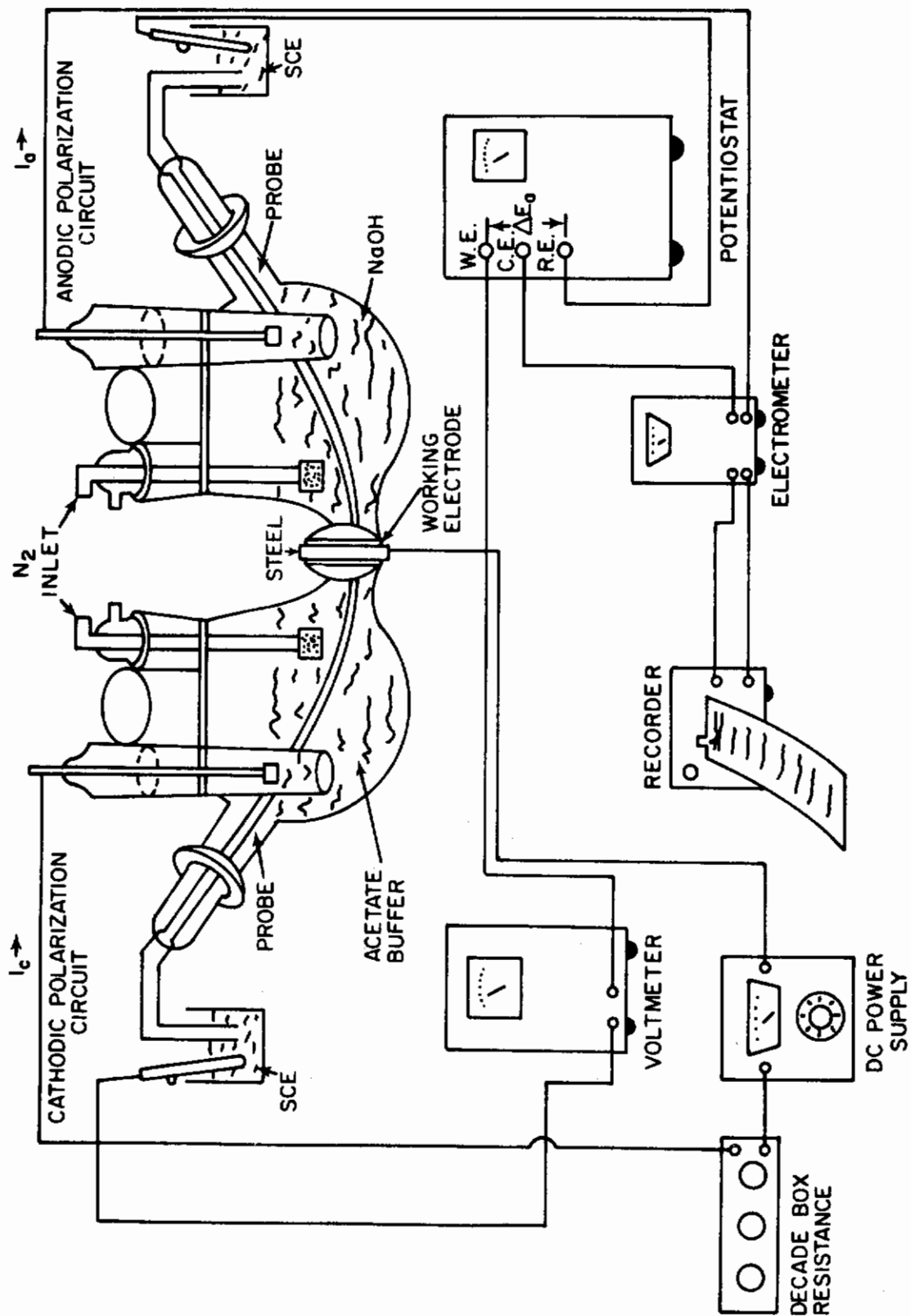


Fig. 56 - Schematic Arrangement of Apparatus Used for Measuring Hydrogen Permeation

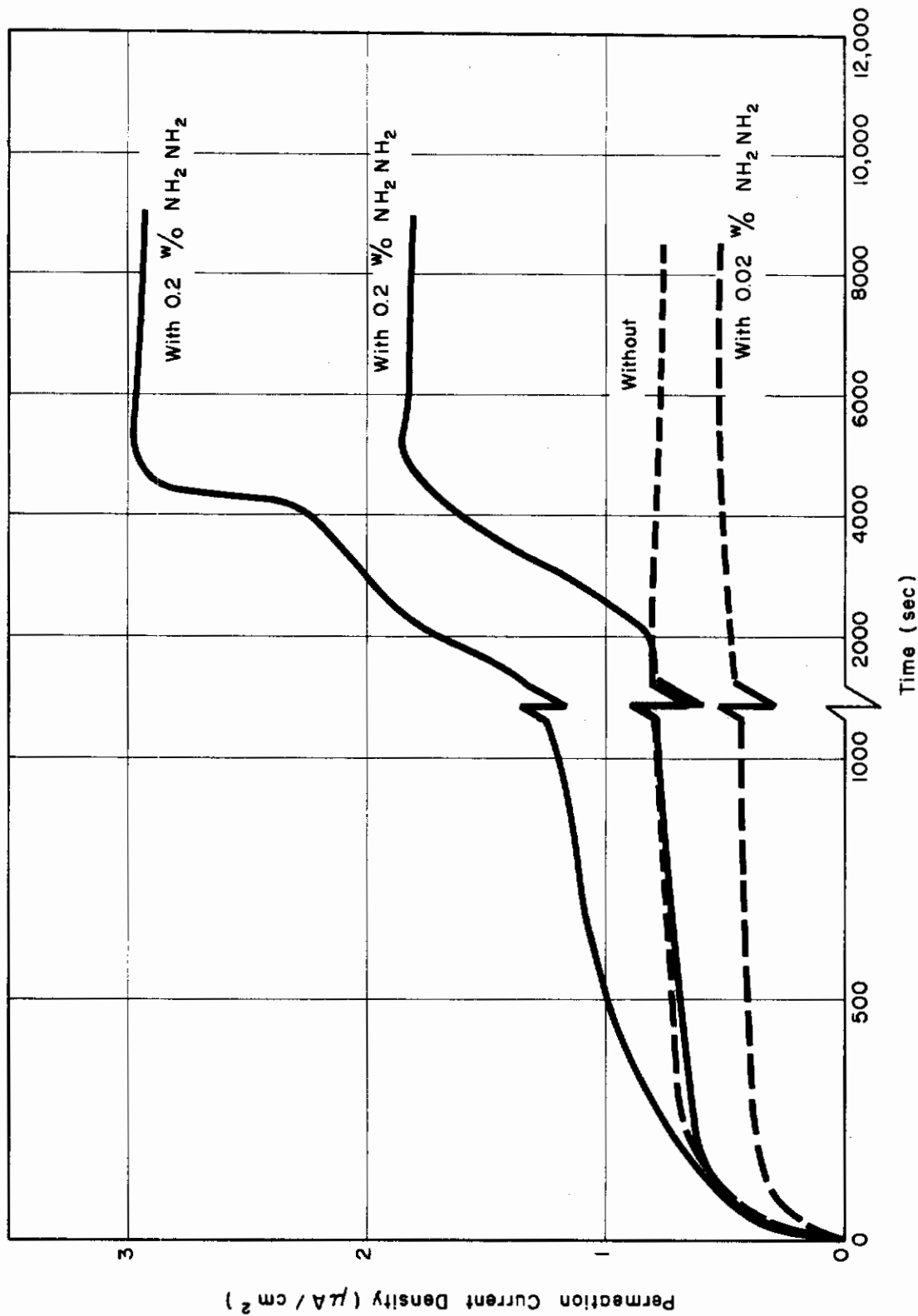


Fig. 57 - Permeation of Hydrogen through a 1010 Steel Membrane as Affected by the Presence of Hydrazine in a 3.5% NaCl Solution.

These facts suggest that the hydrazine must be affecting some aspect of the anodic kinetics at the crack tip. A fairly reasonable interpretation of the data may be that the availability of hydrogen at the crack tip is controlled by the anodic reaction. Although the permeation is increased by a factor of about three, the anodic kinetics are reduced by a factor of 10-100. Therefore, cracking should be slowed.

D. INTERACTION OF HYDROGEN WITH STEEL (R. D. McCright and P. L. Carter)

1. Objectives and Background

The purpose of this work is to determine how hydrogen interacts with metal structure. To accomplish this an experimental apparatus has been set up to monitor hydrogen permeation. Initial work has considered the permeation of hydrogen into carbon steel and the factors affecting its entry.

2. Experimental

Experiments are being conducted on charging steel specimens (AISI-1010) with hydrogen from acetate buffer solutions. The quantitative aspects of the effect of sodium arsenite additions to the acetate on the hydrogen permeation through the steel are being determined.

In the experimental arrangement of Fig. 56, the cathodically polarized side of the specimen is amperostatically controlled. The polarization of the anodic side (hydrogen exit side) is potentiostatically controlled.

a. Alternate Charging and Discharging

A test was run on an AISI 1010 steel sample in which the cathodic charging current at the entry side (see Fig. 58) was alternately turned on and off, during which time an oxidation potential was kept continuously on the hydrogen exit side. Thus, permeation current rise and decay transients were recorded. The diffusivity can be calculated from these transients, as explained in the previous report,²⁸ by approximating suitable equations to the transient. These² are, for the rise transient,

$$i_p - i_{p_\infty} = 2 i_{p_\infty} \exp\left[-\frac{D\pi^2}{L^2} t\right]$$

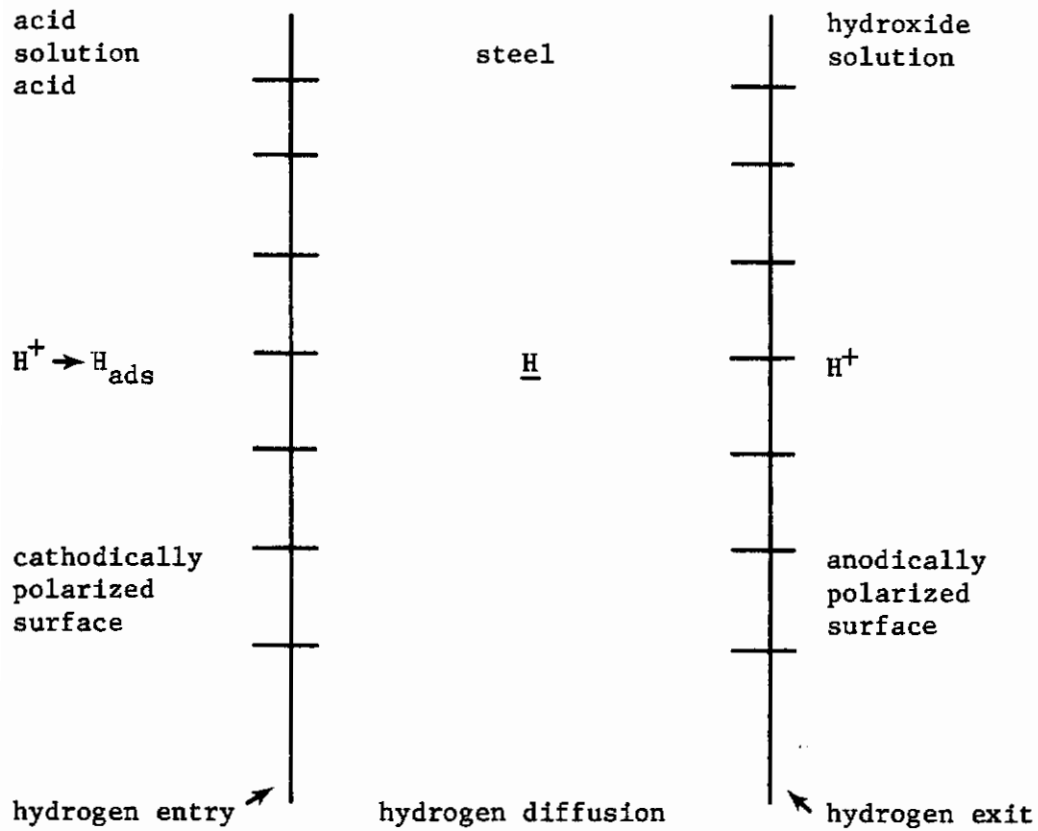


Fig. 58 - Schematic Model for Permeation of Hydrogen through a Membrane

where

i_p = value of the permeation current at time, t ,
 $i_{p_{\infty}}$ = steady state value of permeation current,
 \bar{D} = hydrogen diffusivity,
 L = sample thickness, and
 t = time from when cathodic current turned on (rise) and or off (decay);

and, for the decay transient,

$$i_p = i_{p_{\infty}} \exp\left[-\frac{D\pi^2}{L^2} t\right],$$

Therefore, D can be found from the slopes of the respective plots,

$$\log\left(\frac{i_p - i_{p_{\infty}}}{i_{p_{\infty}}}\right) \text{ vs } t \text{ and } \log\left(\frac{i_p}{i_{p_{\infty}}}\right) \text{ vs } t.$$

The specimen was 10 mils thick and was vacuum annealed at 650°C for an hour. The surface was ground lightly with emery paper and cleaned with acetone. The charging solution was acetate buffer (pH 4.3) with an addition of 1 g/l of thiourea. The solution on the anodically polarized side was 0.1N NaOH (pH 12.8). The test temperature was 24°C. A galvanostatic system was set up for this test since it was felt that, because of the long time between hydrogen entry and exit, a potentiostatic charge-system would not allow the exit condition to reflect the conditions at the entering surface because of the change of the cathodic current with time.

The charging current density was 45 mA/cm²; the potential at the exit side was kept at +100 mV(SEC). The results of this test are shown below.

Transient Type	Diffusivity (cm ² /sec)
First rise	7.9 x 10 ⁻⁸
First decay	8.2 x 10 ⁻⁸
Second rise	7.0 x 10 ⁻⁷
Second decay	1.7 x 10 ⁻⁷
Subsequent rises and decays	10 ⁻⁷

The steady-state permeation current for the first rise was 7.1 μA/cm²; that for the second and third rises was 2.8 μA/cm².

The increase of diffusivity upon continued charging seems to substantiate the theory³⁰ that the mobile hydrogen atoms inside the metal first seek to lodge at or near structural defects. Since the mean time of stay for an atom in these sites is greater than in an interstitial lattice site, the apparent diffusivity is low (all of these experimentally determined diffusivities are apparent). This network of "rifts" is unconnected³¹ and this should slow diffusion.

After these sites are filled, diffusion should be slower, and additional hydrogen atoms can locate only on interstitial lattice sites where their mean time of stay is shorter. Hence, the diffusivity increases. These tests were run with the rise transients being spaced about $3/4$ to 2 hours apart (longer at the beginning since it took longer to come to steady state). When a decay transient is run for a longer time, as in some of the other experiments, (overnight or longer) the behavior of the subsequent rise transient is usually the same as the initial rise transient (no hydrogen in the steel). This would indicate that the first hydrogen discharged from the steel is the interstitial lattice hydrogen and after prolonged hydrogen discharge of the steel the hydrogen associated with structural defects diffuses out.

For shorter time intervals between rise transients, the value of the permeation current decreases from run to run, as it did in this experiment. When the sample is allowed to discharge overnight, the permeability is restored to its initial value and often exceeds it (see next section). Again, this is consistent with the supposition that the permeation should be highest when there is the largest number of accommodating sites (interstitials and rifts vs. interstitials alone).

b. Effect of Oxidizing Potential at the Exit Side

A significant amount of hydrogen discharged from the steel at the anodically polarized side undergoes the recombination reaction to form molecular hydrogen instead of the oxidation reaction of atomic hydrogen to hydrogen ion. Since the former reaction does not contribute to the current, the true permeability is higher than the apparent one. The higher (more noble) the potential at this surface, the less thermodynamic tendency for the recombination reaction. At all the potentials considered molecular hydrogen is unstable, but its presence apparently results from the high bond energy in molecular hydrogen. Since this loss of hydrogen flux cannot be measured by permeation current, many investigators plate palladium on this side of the specimen.

The initial rise transients for 2-mil-thick, AISI 1010 steel samples held at different anodic potentials on the exit side exposed to 0.1N NaOH are shown in Fig. 59. The conditions at the cathodically polarized side were the same in all cases; i.e., acetate buffer (pH 4.3) plus $5 \times 10^{-4}M$ NaAsO₂ (375 μg As/ml), cathodic current density of 10 mA/cm² galvanostatically controlled, specimen surface lightly ground. The steady-state permeation current (plateau of transient) increases as the potential increases in the noble direction.

Shown in Fig. 60 are permeation transients for the same specimens and conditions but after the charged specimen was allowed to expel hydrogen overnight. In all but one case the next-day transients were higher than the initial ones. In some cases these next-day transients show an anomalous permeation maximum and decrease of permeability with time.

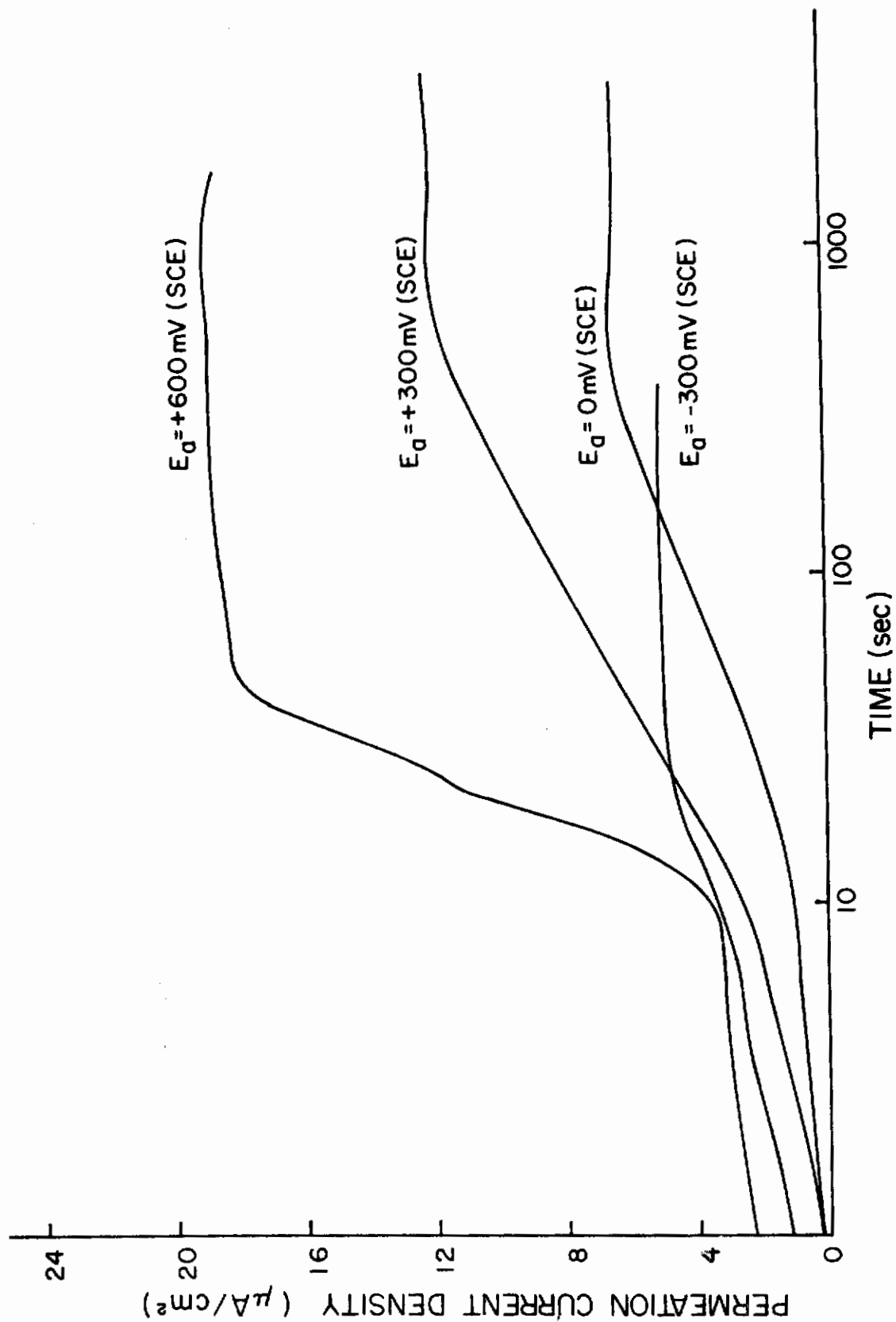


Fig. 59 - Initial Transients for Hydrogen Permeation

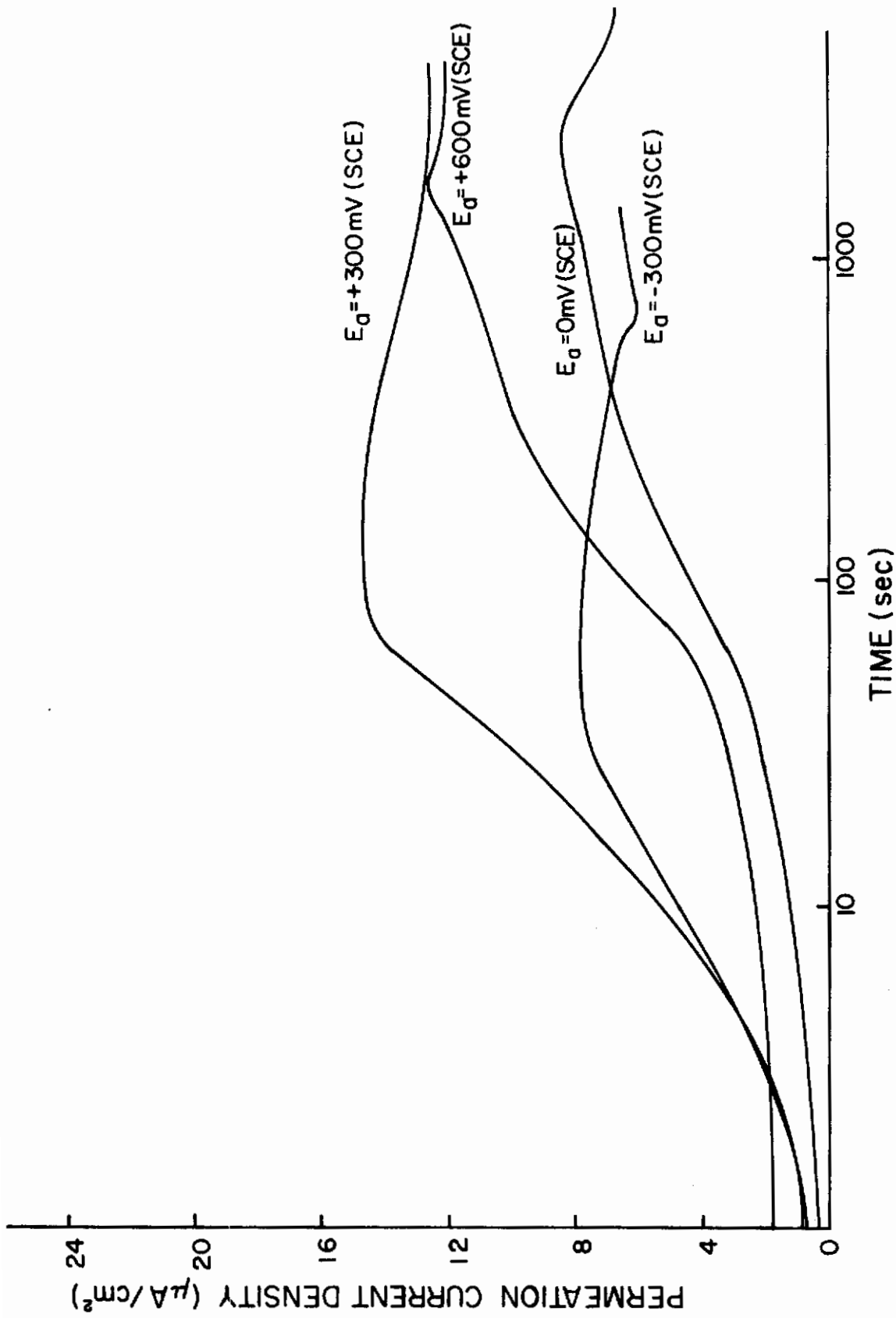


Fig. 60 - Rise Transients for Experiment Conducted on Subsequent Day

c. Effect of Palladium Plating

A thin coating of palladium was electrolytically plated on the hydrogen exit side. This is the surface which is exposed to NaOH solution as shown in Fig. 58. The effect of the palladium was to show a large increase in the hydrogen permeation for a given set of boundary conditions (charging and discharging parameters). Figure 61 illustrates the enormous increase in the permeation current when the exit surface is palladized. It is believed that the emerging hydrogen atom is more rapidly oxidized to hydrogen ion or water on the palladium surface because of the high exchange current (10^{-3} A/cm² for hydrogen on palladium compared to 10^{-7} A/cm² on iron). As a result, the permeation current through a palladized sample is a measure of the true permeability of hydrogen. The diffusivity² of hydrogen in palladium is $\sim 10^{-7}$ cm²/sec, comparable to that of the steel; and the palladium plate is much thinner than the thinnest steel specimen used (Pd plate about 6×10^{-6} cm thick and the thinnest steel specimen, 5×10^{-3} cm thick). Thus, the hydrogen diffusion through the steel is the slowest reaction in the permeation series and the time lag to reach steady state in the permeation current transient is inversely proportional to the hydrogen diffusivity in the steel. Permeation is the overall process of reducing the hydrogen ion at the cathodically polarized surface, transporting the hydrogen across the metallic phases, and oxidizing it at the anodically polarized surface. Diffusion, then, is associated only with the transport through the metallic phases (steel, and palladium in some cases).

Unless otherwise stated, the specimens used in the tests reported in this text were 2 mils thick (5×10^{-3} cm).

d. Effect of Arsenite Additions to the Charging Solution

The presence of species like sodium arsenite (hydrolyzed to arsenious acid) generally increases the hydrogen entry rate into the steel. The data in Table VI show this effect. The charging solution was acetate buffer, pH 4.5.

Table VI - Effect of Arsenite Additions on the Hydrogen Permeability of Unpalladized AISI-1010 Steel at Room Temperature

Concentration, expressed as μ g Elemental As per ml solution	Charging Current Density (mA/cm ²)	Potential at Exit Surface (mV _H)	Permeation Current Density (μ A/cm ²)
0	20	+540	0.75
3.9	20	+540	19.3
77.0	20	+540	20.8
394.0	20	+540	19.0
768.0	20	+540	16.3

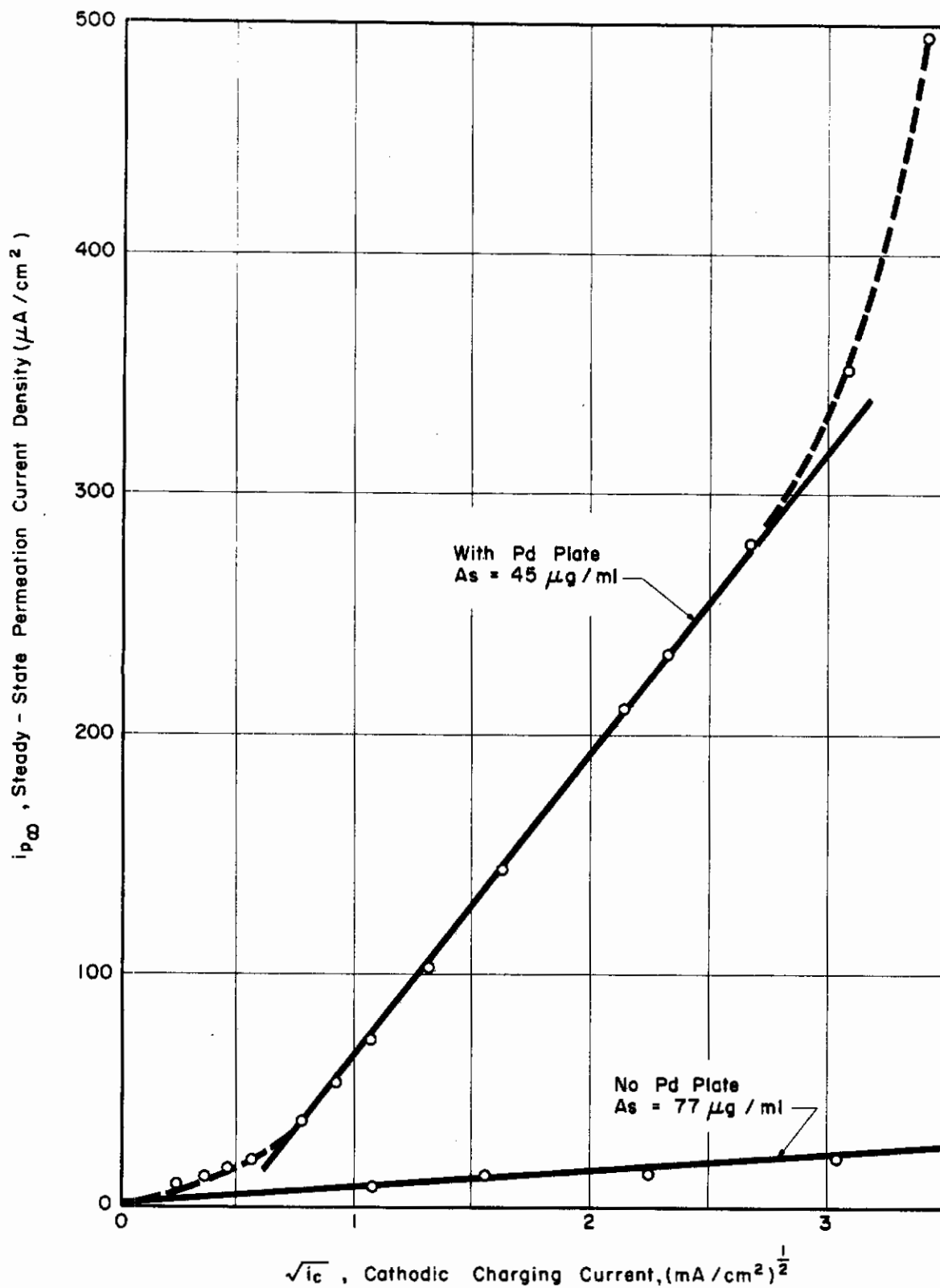


Fig. 61 - Effect of Palladium Plating of the Exit Surface on the Hydrogen Permeability in AISI-1010 Steel

When sodium arsenite is added to the acetate buffer, the rest potential of the steel electrode moves in the noble direction, as shown in Fig. 62. The arsenite/arsenic couple is more noble than the hydrogen ion/hydrogen gas couple. The pH of the solution is unchanged until large amounts of the arsenite (a weak base) are added. This is also shown in Fig. 62.

The cathodic polarization behavior of the acetate and acetate-arsenite solutions is shown in Fig. 63 for a wide range of arsenite concentrations, expressed in terms of elemental arsenic. At small arsenic concentrations (up to about 6 $\mu\text{g/ml}$ typified by the curve for 4.1 $\mu\text{g/ml}$) the arsenic increases the cathodic kinetics. Thus arsenic deposition occurs simultaneously with hydrogen deposition. As the potential becomes more active, the ratio of the partial currents for arsenic deposition to hydrogen deposition becomes smaller as the polarization curve for the dilute arsenite-acetate solution approaches that of the solution without arsenite. At higher concentrations of arsenic, the curves show a "two hump" behavior. The first corresponds to As deposition and the second, at more active potentials, to H^+ reduction. The depression of the hydrogen evolution region may be caused by changes in the local pH brought on by a very high arsenite concentration. The apparent limiting current obtained in the arsenic reduction region does not correspond to the bulk solution. Thus, if the reduction rate of arsenite were controlled by mass transfer from the solution, the limiting currents would be directly proportional to the concentration of arsenite in solution. This is not the case and it must be concluded that the critical step is some sort of surface diffusion.

Hydrogen permeation experiments were conducted by charging from arsenite-containing solutions into AISI-1010 steel palladized at the exit surface. This method gave high permeabilities, even at low charging current densities. In Fig. 64, the permeation rise transients are shown for hydrogen charging from acetate alone, and acetate plus small and large additions of arsenite. The boundary conditions were a charging current of 125 $\mu\text{A/cm}^2$ and a potential at the exit side of 0 mV(SCE) [240 mV_H]. The highest permeability was from the solution with the small As concentration. These data are tabulated in Table VII.

Table VII - Effect of Arsenite Additions on the Hydrogen Permeability of Palladized AISI-1010 Steel at Room Temperature

Concentration, Expressed as μg Elemental As per ml Solution	Charging Current Density (mA/cm^2)	Potential at Exit Surface (mV _H)	Permeation Current Density ($\mu\text{A/cm}^2$)
0	0.125	+540	42
3.9	0.125	+240	61.5
7.8	0.125	+240	48.0
19.7	0.125	+240	39.5
39.4	0.125	+240	44.0

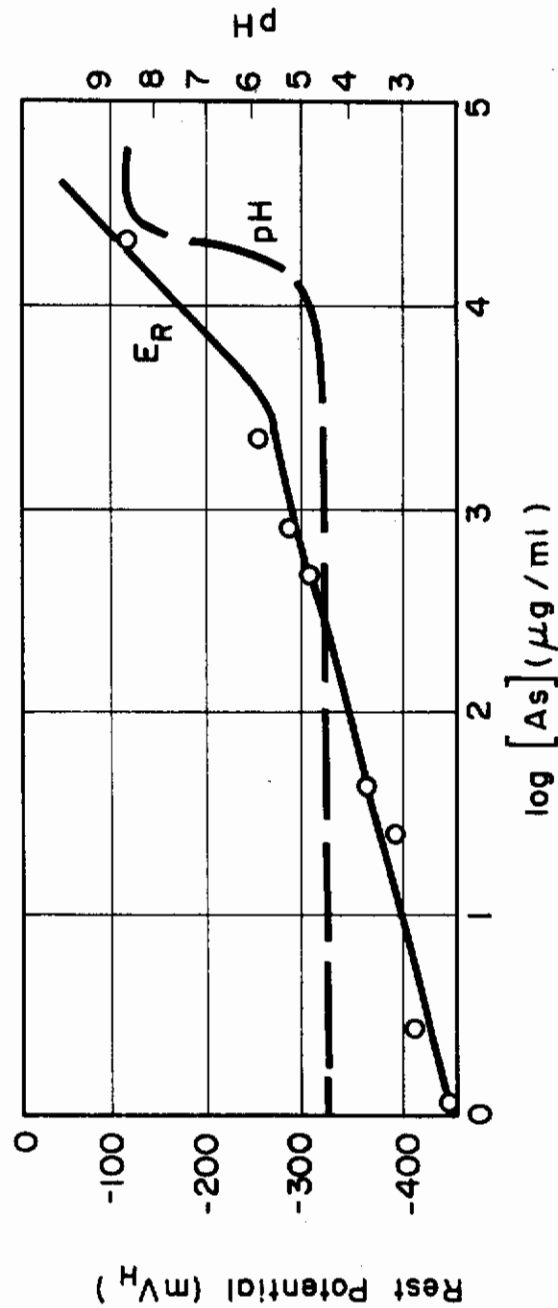


Fig. 62 - Effect of Arsenite Additions to Acetate on Solution pH and Rest Potential of 1010 Steel.

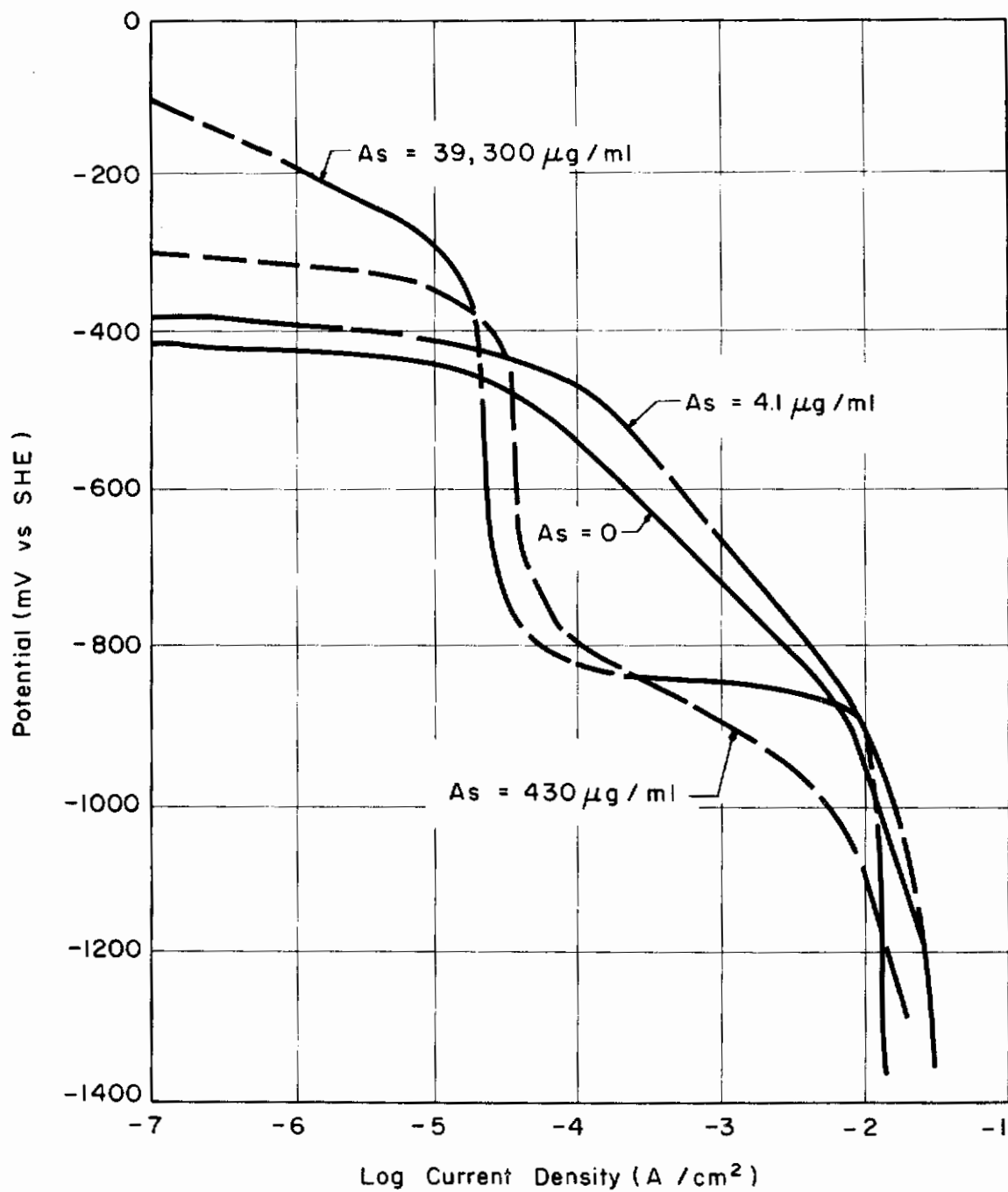


Fig. 63 - Cathodic Polarization of 1010 Steel in Acetate Buffer with Arsenite Additions

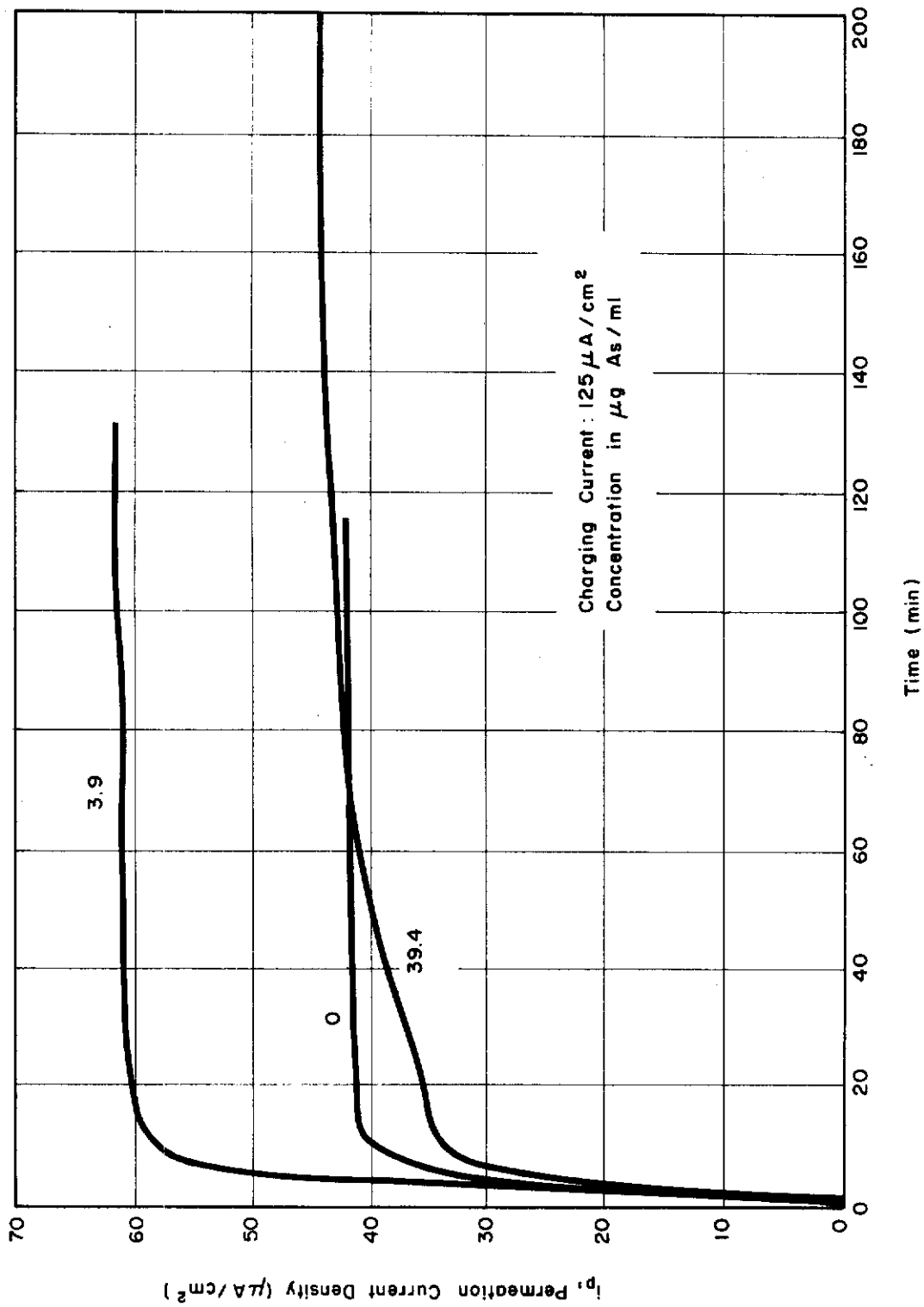


Fig. 64 - Rise Transients for Hydrogen Permeation in Palladized AISI 1000 Steel

The highest permeation occurred when there was simultaneous deposition of the arsenic and the hydrogen ($3.9 \mu\text{g As/ml}$). Chronopotentiometric measurements during the charging showed that the potential decreased from an initial value of -450 mV(SHE) to -620 mV at 180 seconds (onset of steady-state diffusion). At the higher arsenite concentrations there was an initial deposition of arsenic followed by co-deposition of arsenic and hydrogen, with hydrogen predominating as illustrated in the polarization diagram, Fig. 63. In these cases the potential at steady state hydrogen diffusion was -700 mV and lower. These latter solutions had permeation behavior characteristic of the pure acetate as tabulated in Table VII.

However, as the charging current was increased the permeation current increased. At high charging currents, the permeation current for all As-containing solutions greatly exceeded that of the acetate-only solution.

In Fig. 65, the permeation current at steady state (the plateau current in Fig. 64) is plotted against the square root of the charging current. This relationship has been developed in the literature³³ and applies when recombination of the freshly deposited nascent hydrogen atoms on the metal surface is the rate-controlling step in the cathodic reduction process. The constant of proportionality involves the diffusivity of hydrogen, the thickness of the specimen, and the specific rate constants for the recombination and absorption reactions. When recombination is hindered, the competitive absorption reaction, $\text{H (absorbed, surface)} \rightarrow \text{H (absorbed, lattice)}$, is promoted. The deposited arsenic can hinder recombination in a purely geometric way or by a chemical coordination with the hydrogen. Presumably the chemical compound can break down and release hydrogen to the steel. Qualitative tests for compound AsH_3 in the charging solution showed none present.

Figure 66 shows an anomalous effect. At low charging currents a higher permeability obtains from the solution containing no arsenic. Up to a charging current of 0.31 mA/cm^2 , the transients show the "plateau behavior" for this solution. Above this charging current value, steady state does not occur and the permeation falls off with time. Since the permeability is proportional to the product of the diffusivity and the solubility, either or both of these must decrease. When the same experiment was run, charging from an arsenited solution, the series of plateaus for charging current increases was observed up to 20 mA/cm^2 . Beyond this value, the "saw-tooth" shape response was noted. Thus the presence of arsenite in the solution would not affect the hydrogen diffusivity, but the arsenic deposits on the surface have a great influence on the fugacity of the adsorbed hydrogen and, therefore, on the hydrogen solubility just inside the steel. Therefore, the appearance of this "saw-tooth" behavior is not a criterion for detecting hydrogen trapping (decreased diffusivity due to preferential hydrogen migration to structural defects where the mean time of stay is longer and the migration away is a slow process).

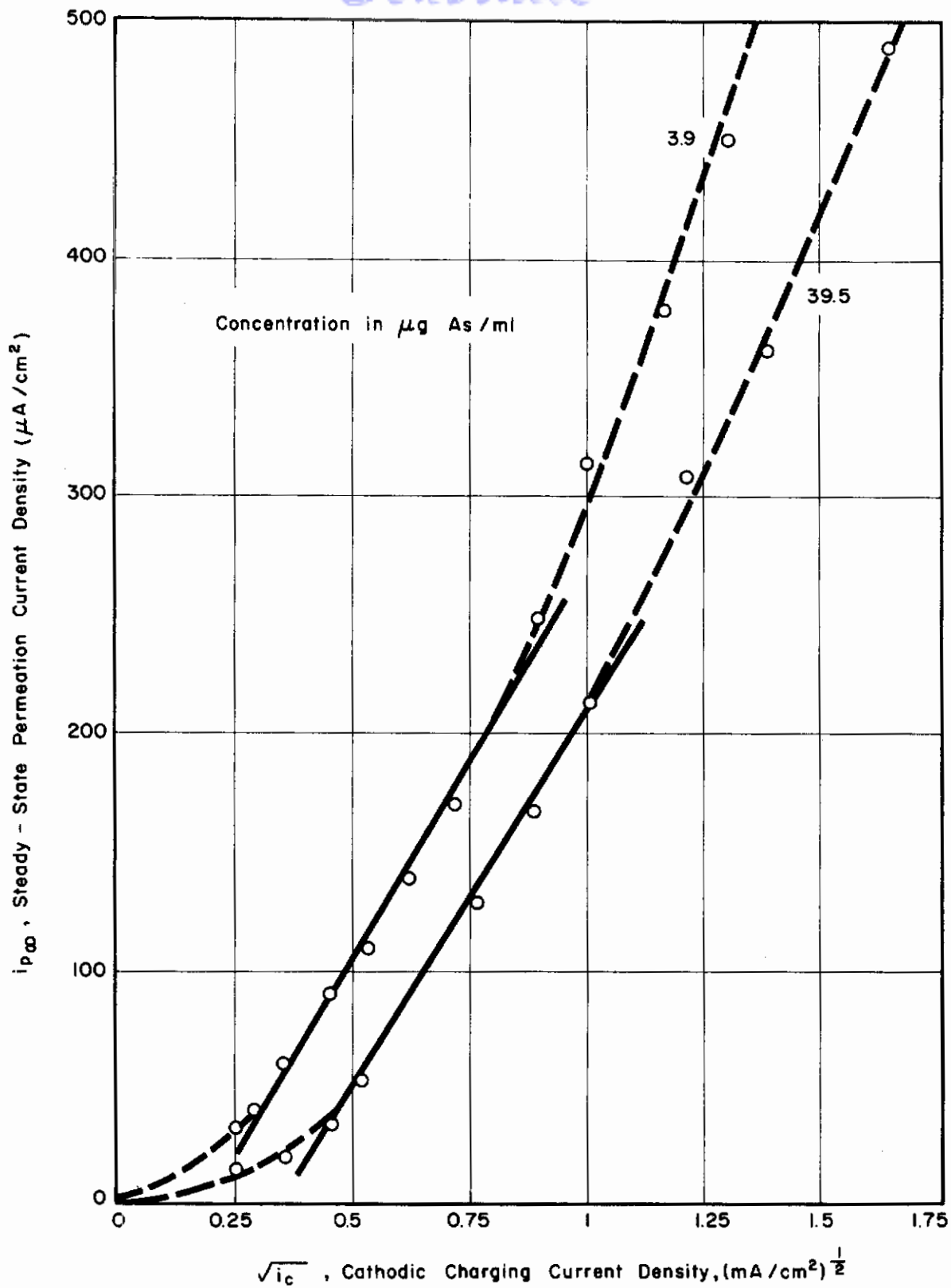


Fig. 65 - Relationship of Permeation Current to Charging Current

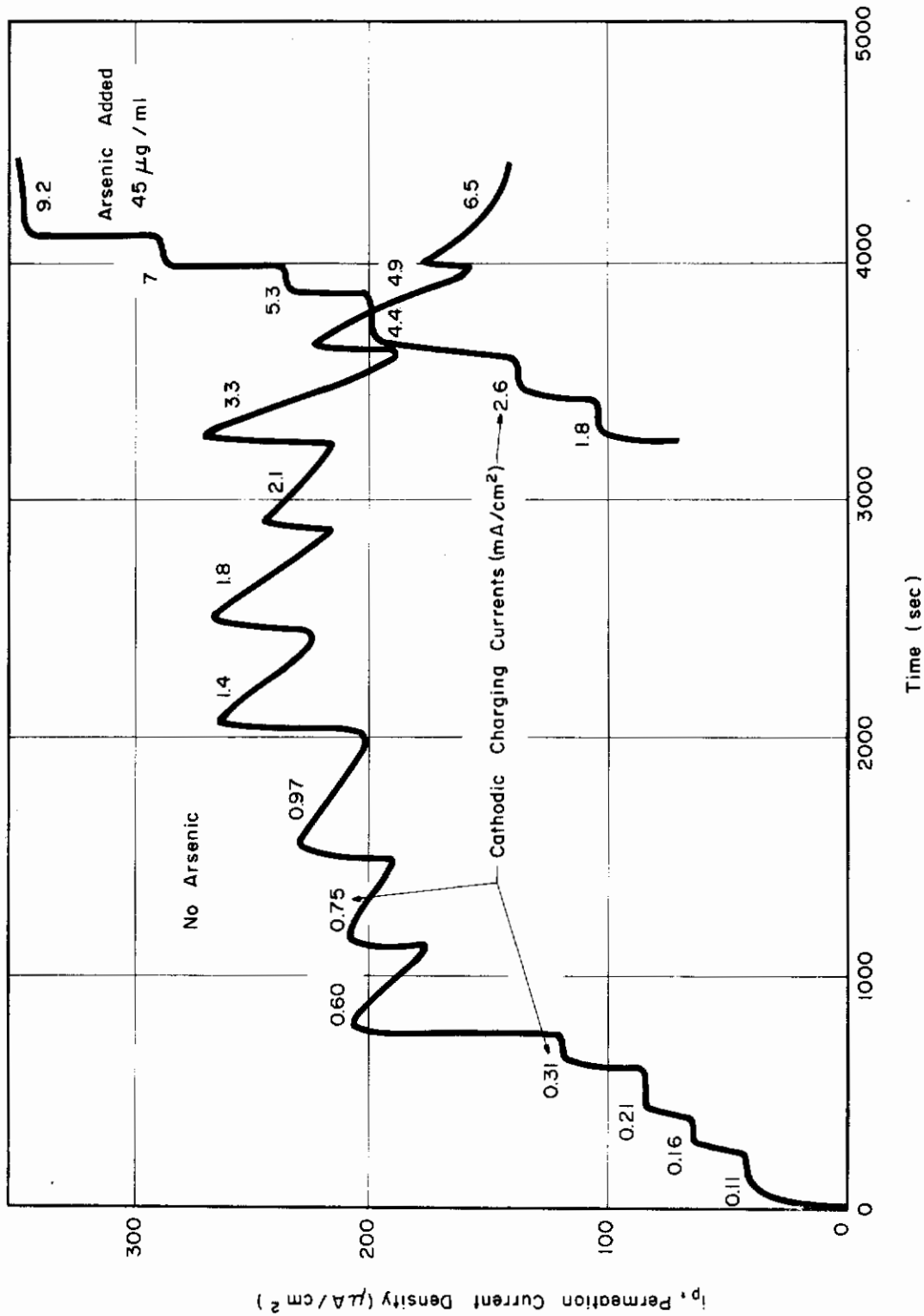


Fig. 66 - Nonsteady-State Behavior Permeation Transients

e. Effect of Co-deposition

In order to show that arsenic and hydrogen co-deposition (i.e., as opposed to As on the surface) was a necessary condition for enhanced permeation rates, a steel sample was deliberately plated with 50 millicoulombs of arsenic which was an amount of arsenic estimated to be deposited during a hydrogen permeation test for the conditions corresponding to the maximum permeation rate in Fig. 67. This sample was then placed in an acetate solution with no arsenite present, and a hydrogen permeation transient was obtained. This permeation behavior of this arsenic-plated specimen is compared to that of a sample charged from a solution containing no arsenite and the one containing arsenite. Figure 67 shows the highest permeation for the case of simultaneous arsenic and hydrogen deposition and about the same rates for (arsenic plated specimen) hydrogen deposition only. The thickness of these specimens was 3 mils.

f. Calculation of Diffusivity

The analytical bases for diffusivity calculations is described in Section D-2-a

The results of experiments on hydrogen diffusivity are tabulated below.

Table VIII - Diffusivity of Hydrogen in Palladized AISI-1010 Steel.
Hydrogen Charged from Arsenite-Acetate Solutions. Units:
 $\text{cm}^2/\text{sec.}$

Method of Calculation	Arsenic Concentrations ($\mu\text{g}/\text{ml}$)			
	3.9	7.8	19.7	39.4
Lag Time	4.98×10^{-8}	0.378×10^{-8}	2.73×10^{-8}	2.32×10^{-8}
Time Rise Constant	12.5×10^{-8}	0.426×10^{-8}	4.73×10^{-8}	1.76×10^{-8}
Decay Transient	4.65×10^{-8}	2.39×10^{-8}	1.63×10^{-8}	2.17×10^{-8}

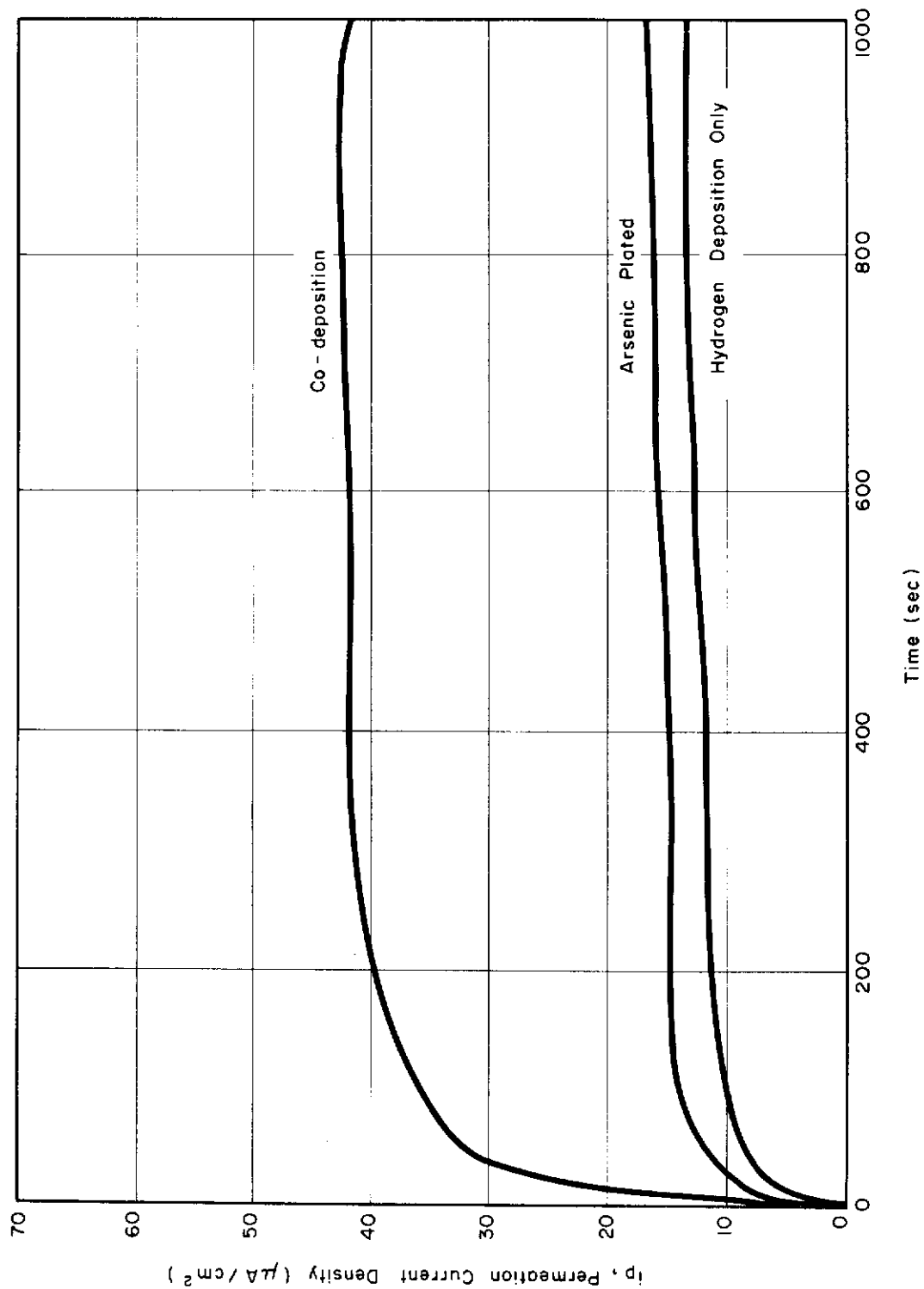


Fig. 67 - Effect of Deposition Processes on Hydrogen Permeation

Table IX - Diffusivity of Hydrogen in Palladized
AISI-1010 Steel for Various Thicknesses

Method of Calculation	Sample Thickness (mils x 10 ⁻³)			
	2	3	5	10
Time Lag	0.378	1.57	3.02	2.32
Time Rise Constant	0.426	3.35	1.67	7.36
Decay Transient	2.39	1.20	1.92	2.87

The decay transients give the most consistent values since neither the thickness nor the charging solution should affect the diffusivity. The diffusivity can therefore be taken as approximately 2×10^{-8} cm²/sec.

g. Morphology of the Arsenic Deposits

It was established that elemental arsenic was deposited on the charging surface during permeation tests by electron diffraction of this surface. In addition, there was agreement of gravimetric and coulometric determinations of the amount of arsenic deposited at constant potential [-1000 mV(SHE)] and from a high concentration of arsenite in acetate solution. Scanning electron photomicrographs were taken of the arsenic-deposited surface, as shown in Figs. 68 and 69. In Fig. 68, the steel substrate can be seen since the preparation scratches are visible. The arsenic plate is not uniform. In Fig. 69, the cracks show the plate is brittle, and the arsenic appears to adhere poorly to the substrate. It appears that an initial thick plate is formed on top of this. The plate thickness was estimated to be 8000Å.

3. Discussion

Most of the above work is aimed at establishing parameters for subsequent experiments. The work on arsenic co-deposition sheds new light on the mechanism for the absorption of hydrogen. It would appear that the absorption is influenced by the ionic form of arsenic rather than noncharged arsenic.

The diffusivities observed are in general accord with those in the literature. The equipment and techniques appear to be reproducible and in good working order. The next efforts will be directed toward studying the interaction between hydrogen and interfacial

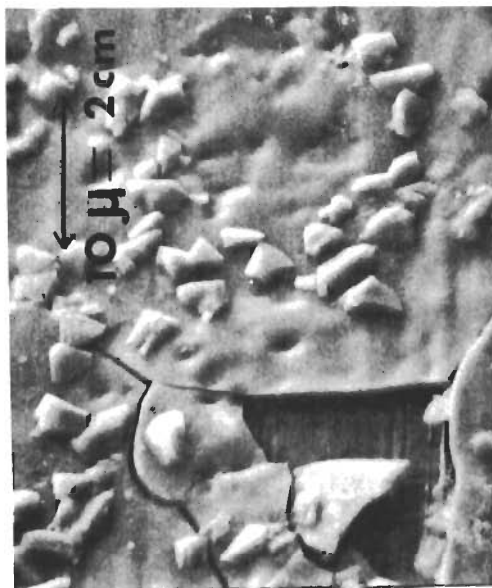


Fig. 69 - Arsenic Deposits on Steel
Substrate 2000X



Fig. 68 - Arsenic Deposits on Steel
Substrate 500X

boundaries in an Fe-Cu alloy where matrix-precipitate coherency can be varied by heat treatment. These foils, appropriately hydrogenated, will be deformed and subsequently examined by TEM to assess the interaction among hydrogen, interfacial coherency, and strain-induced dislocation activity.

E. DISSOLUTION OF FERRITE-CARBIDE HETEROGENEOUS STRUCTURE (C. Cron and J. Payer)

1. Objectives

High-strength steels are complex materials containing a number of chemically and structurally different phases. This work is aimed at elucidating the detailed nature of the local dissolution processes in these materials. The work reported in the first description of local dissolution in Progress Report AFML TR-67-240 showed clearly that there was a great difference in the relative reactivity of the iron matrix and the complex carbide of quenched and tempered 4340 steel. In order to obtain a less ambiguous understanding, a pure Fe-C (1045 nominal) alloy is being used where there is less uncertainty about the Fe_3C and ferrite compositions and structures.*

2. Experimental

Specimens are prepared by first thinning to the thickness required for transmission electron microscopy. The specimens are then mounted in an electrochemical cell with the salt bridge probe adjacent at various values of pH (0, 4, 10, 14). Figure 70 shows these potentials and pH's relative to schematic figures of the potential-pH diagrams for iron- H_2O and carbon- H_2O . In addition, the effect of various anions was examined at pH 4 and pH 14. All experiments are performed at 25°C. All potentials are reported on the standard hydrogen scale.

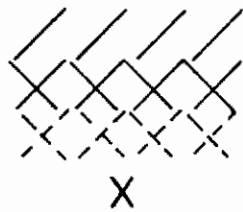
After exposing the specimens at specified potentials and pH's, they are examined in the transmission electron microscope. Figure 71 shows the specimens prior to exposure at constant potential to the environments. Examples of the various types of attack observed are shown in Fig. 72.

3. Results

a. pH 0

Electron micrographs of specimens exposed to a pH 0 KCl-HCl buffer solution are shown in Fig. 73. After one hour at -1000 mV,

*This material was furnished through the generosity of Dr. B. F. Brown of the Naval Research Laboratory.



REGION OF PASSIVATION
 REGION OF STABILITY FOR Fe
 REGION OF STABILITY FOR C
 TEST CONDITIONS FOR VARIOUS SPECIMENS

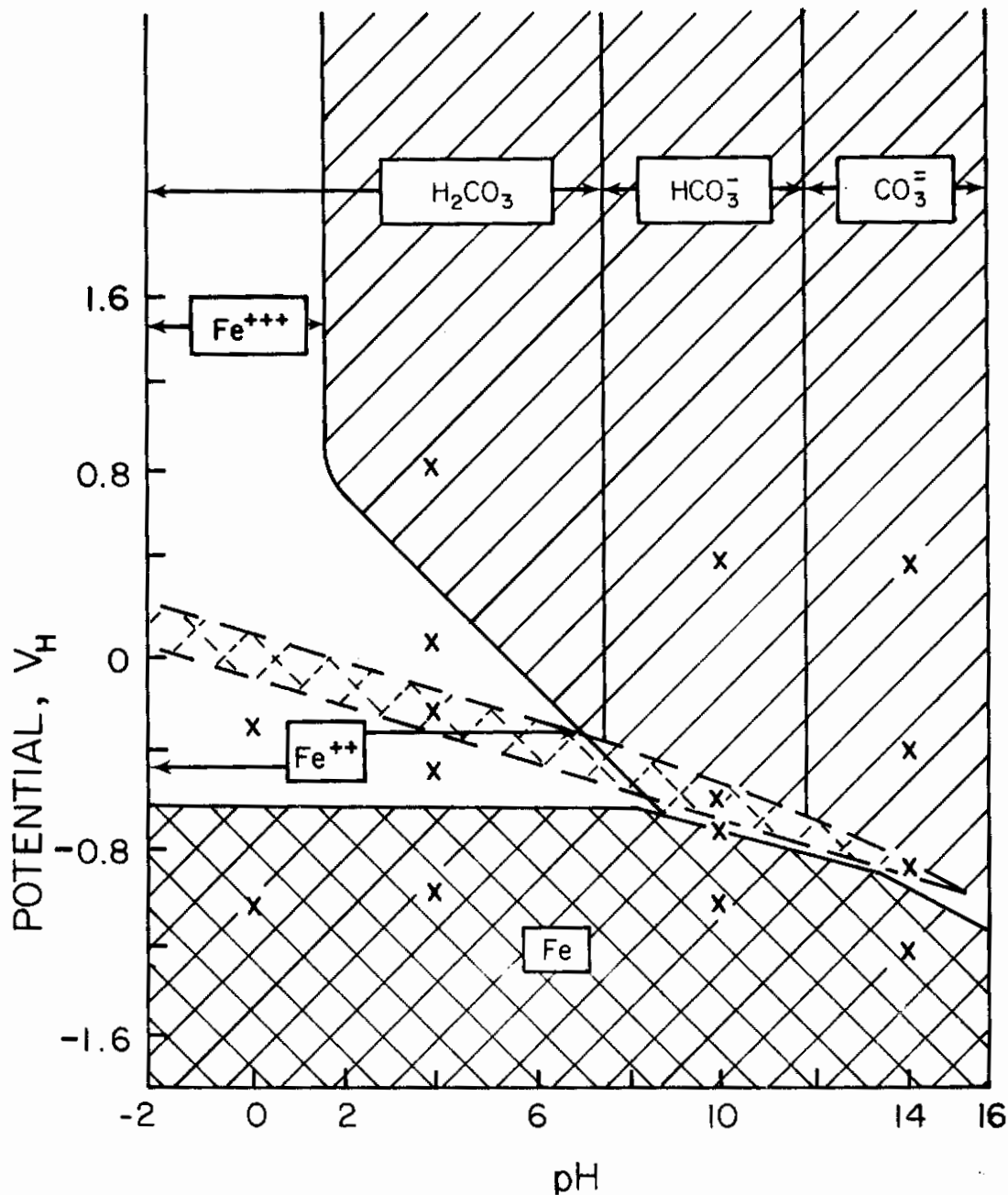
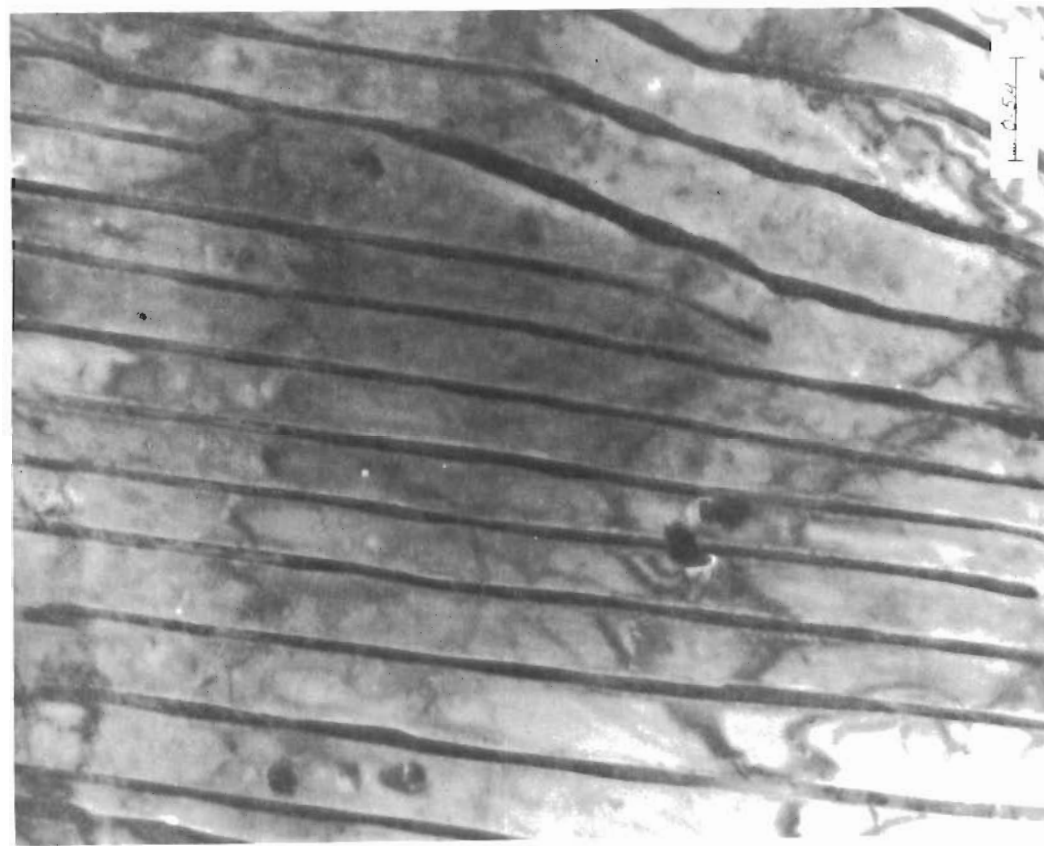
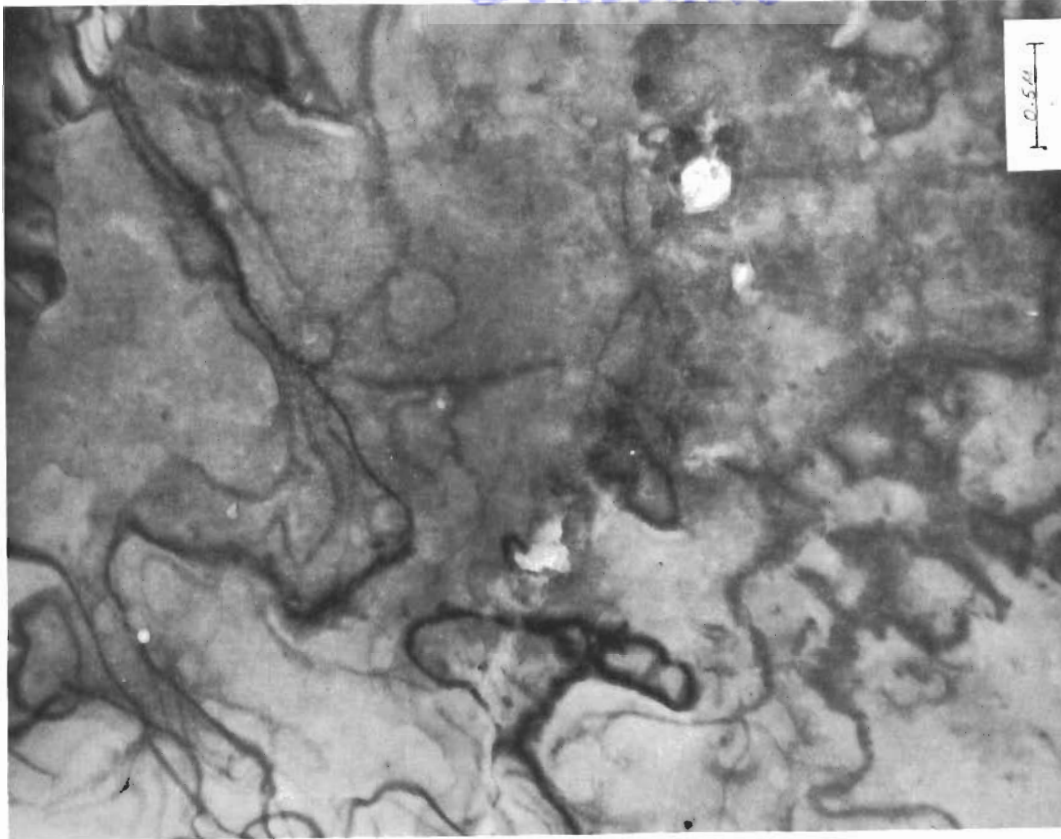


Fig. 70 - Schematic Potential-pH Diagram for Fe-H₂O at 25°C Showing the Potentials at which Specimens Were Examined in the Electron Microscope



(a)



(b)

Fig. 71 - Electron Micrographs of the 1045 Carbon Steel Used in
These Investigations (as received)

MODES OF ATTACK

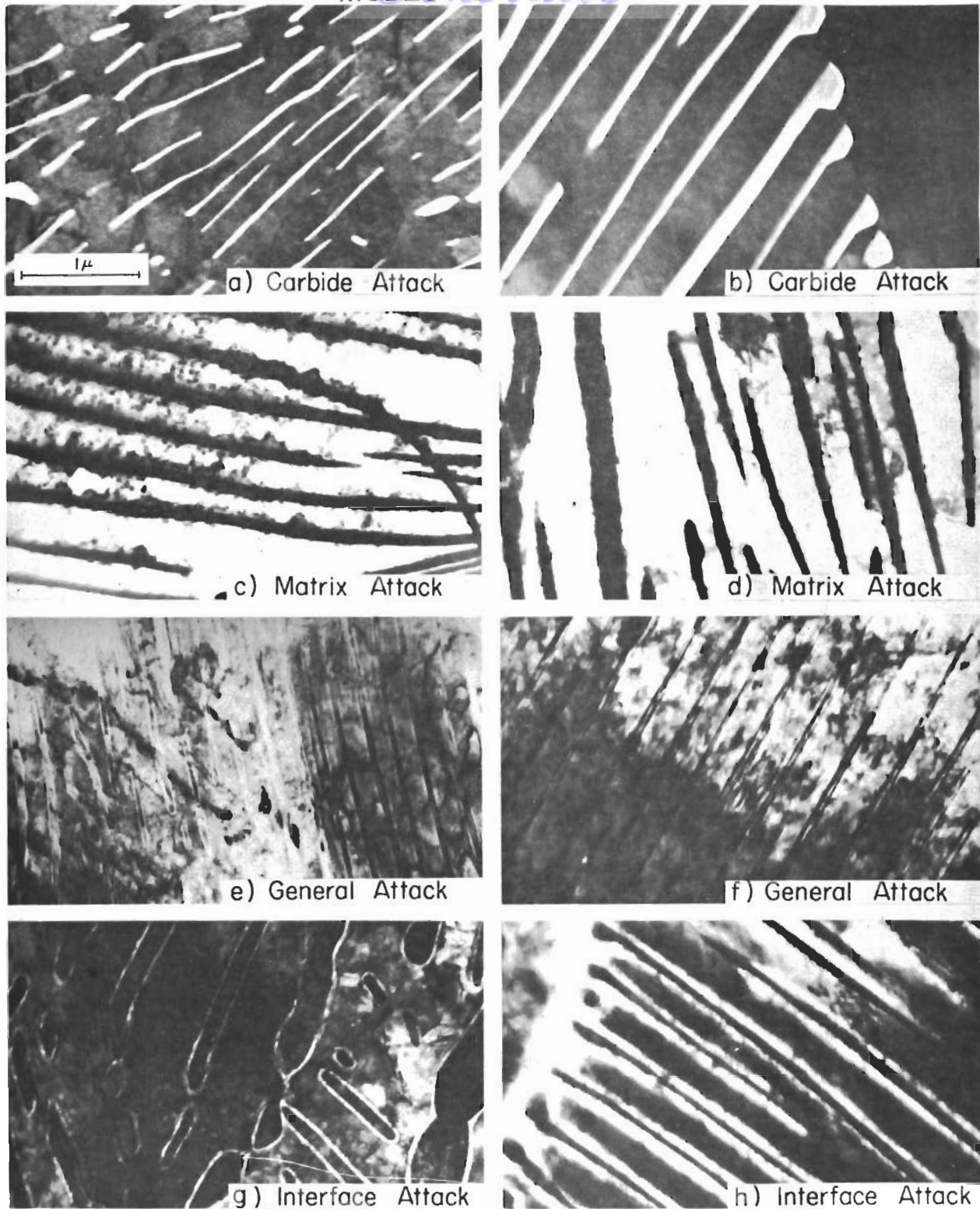


Fig. 72 - Electron Micrographs Showing Various Modes of Attack

Contrails
pH 0 KCl-HCl BUFFER

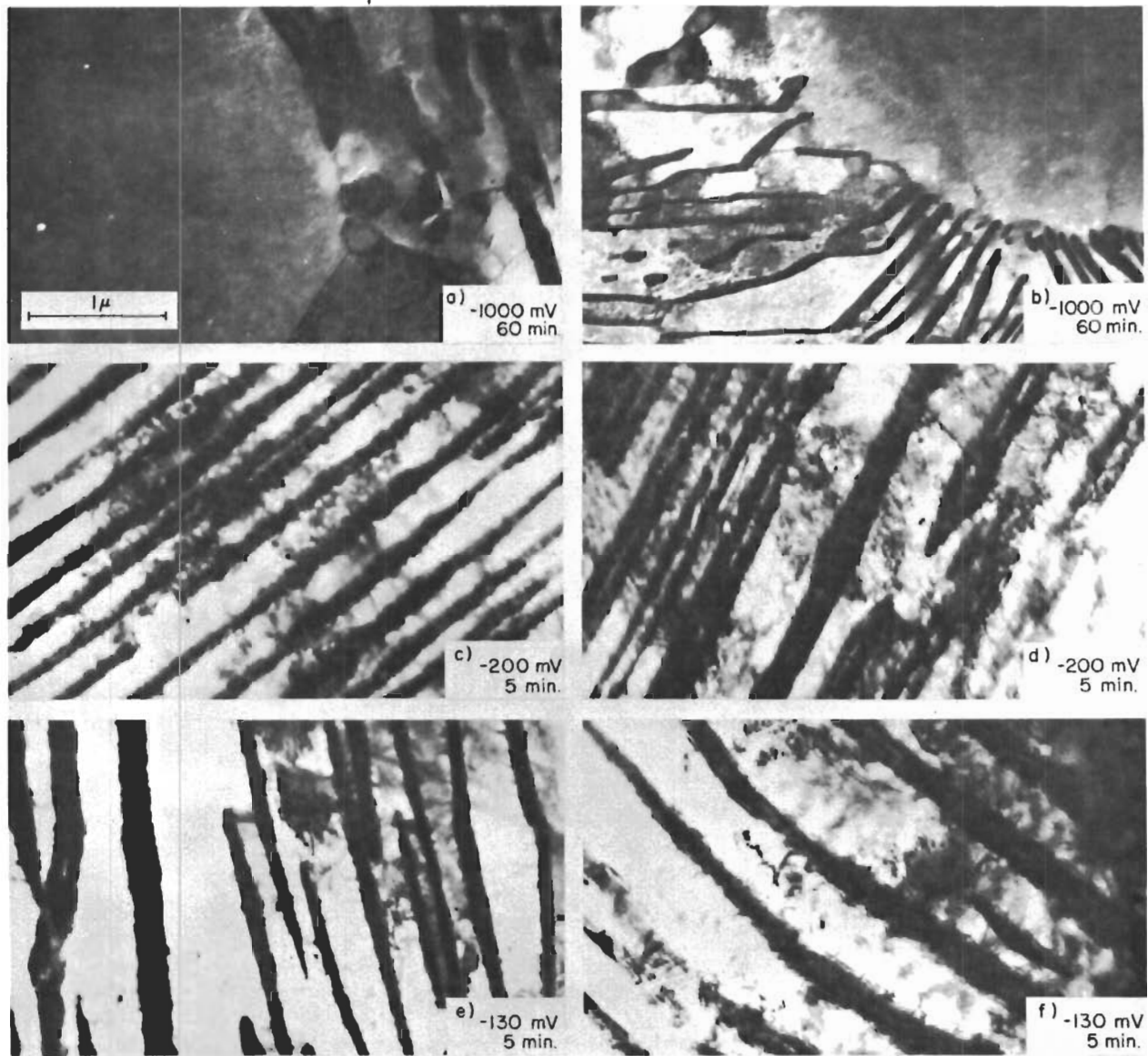


Fig. 73 - Electron Micrographs of Specimens Exposed at pH 0 in KCl-HCl Buffer

no reaction was observed (note the carbides appear black in the electron micrographs).

At -200 mV the specimen was exposed for 5 minutes. The overall attack occurred quite rapidly with the matrix being attacked more vigorously than the carbide; the same was true at -130 mV.

At more noble potentials the attack was too aggressive and foils were destroyed after very short exposure times.

b. pH 4

Specimens were exposed to environments containing various anions (i.e., SO_4^{2-} , Cl^- , NO_3^- , PO_4^{3-} , Ac^-) as well as a buffer solution. The attack varied with the anion present.

(1) H_2SO_4

Figure 74 shows electron micrographs of specimens exposed to a pH 4 H_2SO_4 solution. At -1000 mV, no attack was observed after 60 minutes exposure.

At -500 mV, after 60 minutes the matrix was attacked but the carbides are not attacked. Dissolution is most vigorous at the interface between the ferrite matrix and the iron carbide.

At -215 mV, the attack is more vigorous than at -500 mV. After 10 minutes exposure the matrix has been substantially attacked. More rapid attack of the interface is not observed. The carbides are attacked to a small degree.

At +100 mV, dissolution occurs too rapidly and specimens are destroyed after short times. At +800 mV, after 25 minutes, the specimen has undergone substantial general attack.

(2) HCl Solution

At -1000 mV, after 60 minutes exposure the carbides have been dissolved, whereas the matrix has undergone only slight dissolution (see Fig. 75). This is the only environment in which attack was observed at this potential.

At -500 mV, after 60 minutes, the carbides are again attacked although not as severely. The matrix attack is still slight. At -125 mV, the entire specimen is substantially attacked.

Contrails
pH 4 H₂SO₄

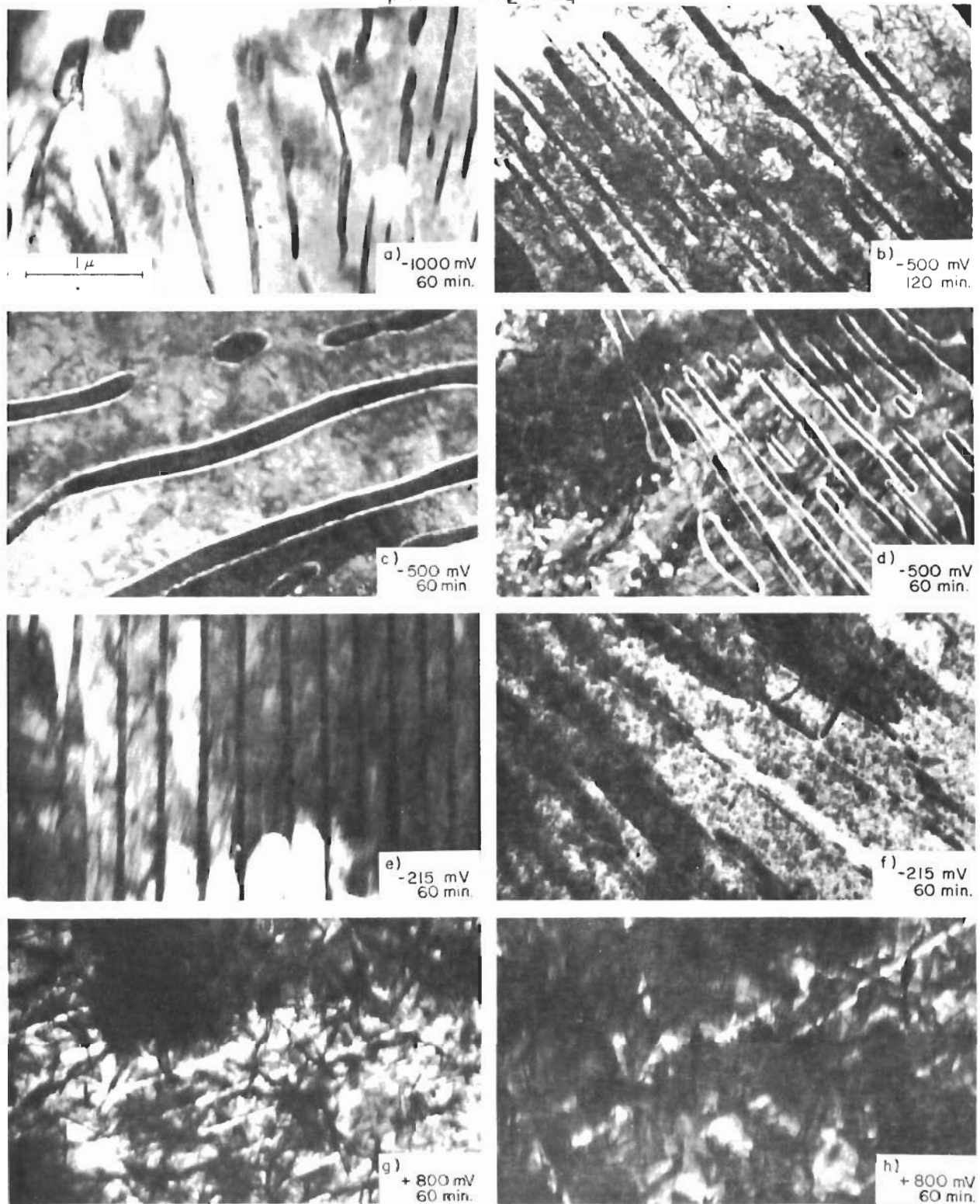


Fig. 74 - Electron Micrographs of Specimens Exposed at pH 4 in H₂SO₄

Contrails
pH 4 HCl

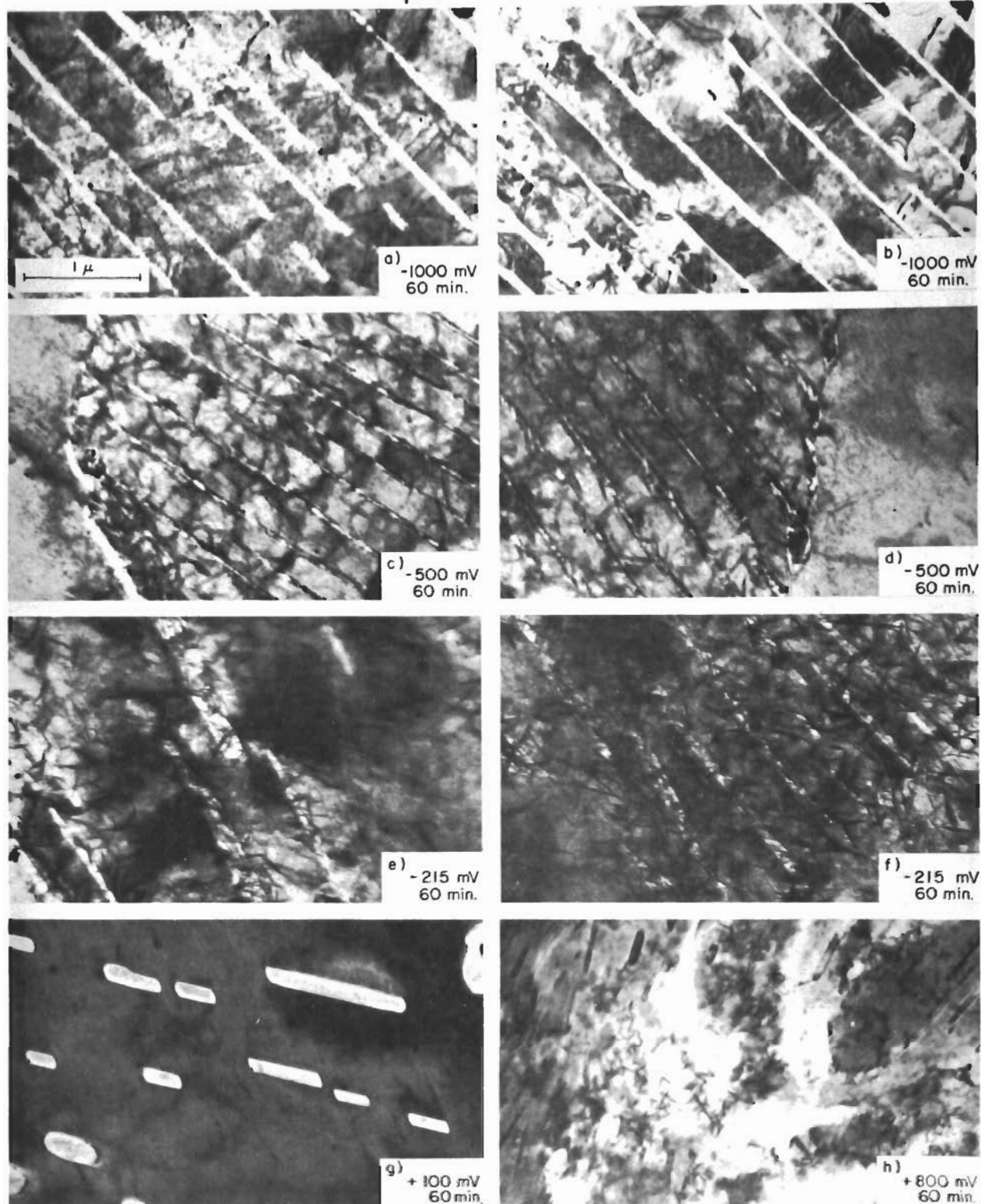


Fig. 75 - Electron Micrographs of Specimens Exposed at pH 4 in HCl

At +100 mV, the carbides are severely attacked while the matrix is untouched. Note the smooth cavities that remain where carbide has been. At +800 mV, the attack is again general and substantial.

The behavior of the specimens at all potentials except +800 mV is quite different in the HCl and the H₂SO₄ environments. In the former at -500 mV the carbides are attacked and the matrix is stable, whereas in the latter opposite behavior is observed.

(3) HNO₃ Solution

Electron micrographs of specimens exposed to pH 4 HNO₃ are shown in Fig. 76. At -500 mV, after 30 minutes exposure both matrix and carbide are attacked. The interfacial region is attacked most rapidly.

At +100 mV, two opposite types of behavior are observed on the same specimen. In one area the matrix is severely attacked and the carbides are stable while in another area the carbides dissolve and the matrix is stable. This is the only case found of this type. In all other tests behavior was consistent and reproducible.

At +800 mV, after 40 minutes exposure the matrix is unattacked while some carbide dissolution has occurred. This is in contrast to the behavior in HCl and H₂SO₄ where general attack was observed. This is a result of the passivating or inhibiting trend of the nitrate ion on the corrosion of iron.

(4) H₃PO₄ Solution (see Fig. 77)

At -1000 mV, no attack was observed. Substantial general attack was observed at both -500 mV and -215 mV, the attack being more vigorous at the nobler potential. At +100 mV attack was too vigorous and specimens were destroyed in a few seconds.

At +800 mV, after 60 minutes exposure only a slight amount of matrix dissolution has occurred. This points out the effect of the anion present. At +800 mV in HCl and H₂SO₄ substantial general attack is observed, whereas in HNO₃ and H₃PO₄ little or no attack occurs.

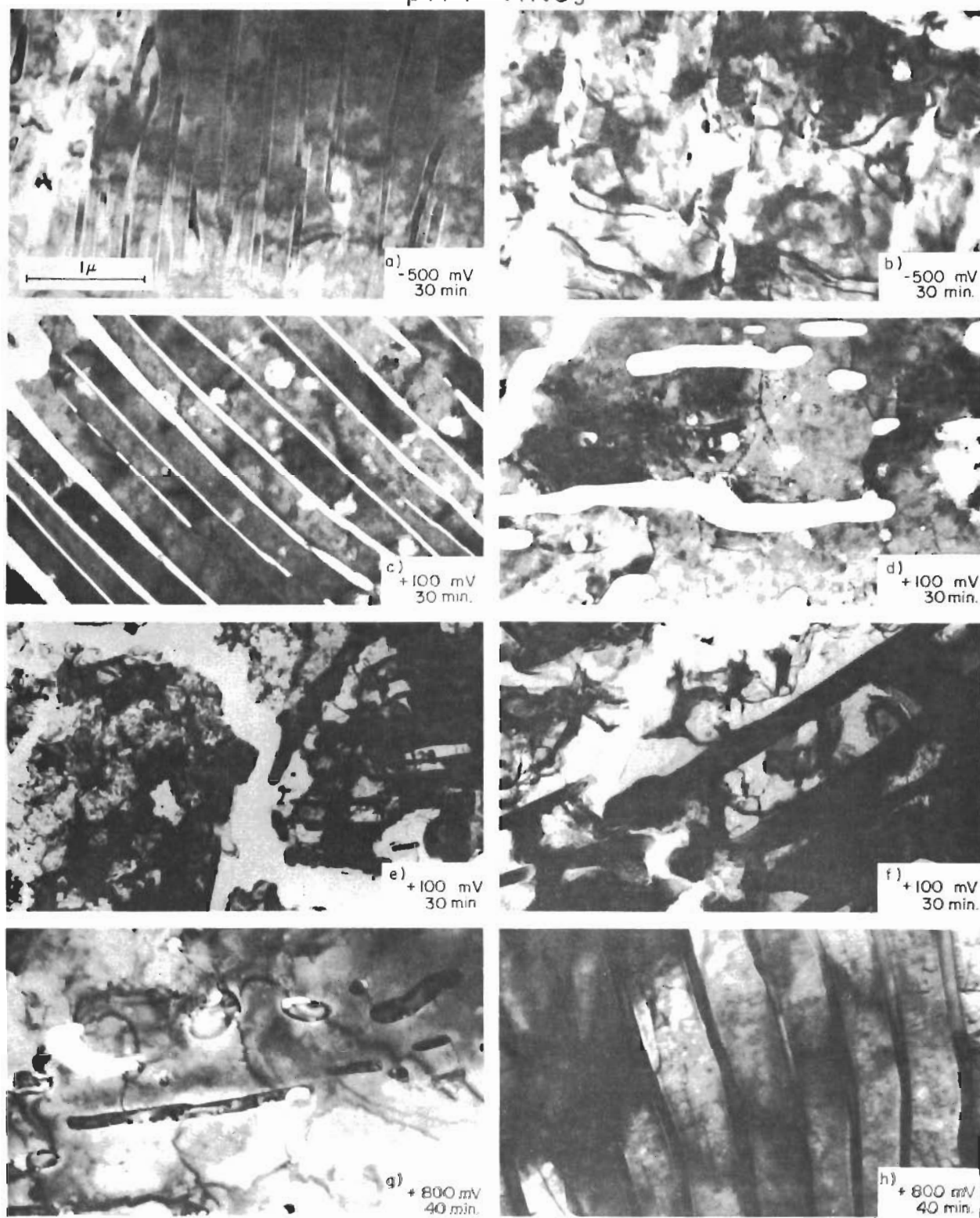
pH 4 HNO_3 

Fig. 76 - Electron Micrographs of Specimens Exposed at pH 4 in HNO_3

Contrails

pH 4 H_3PO_4

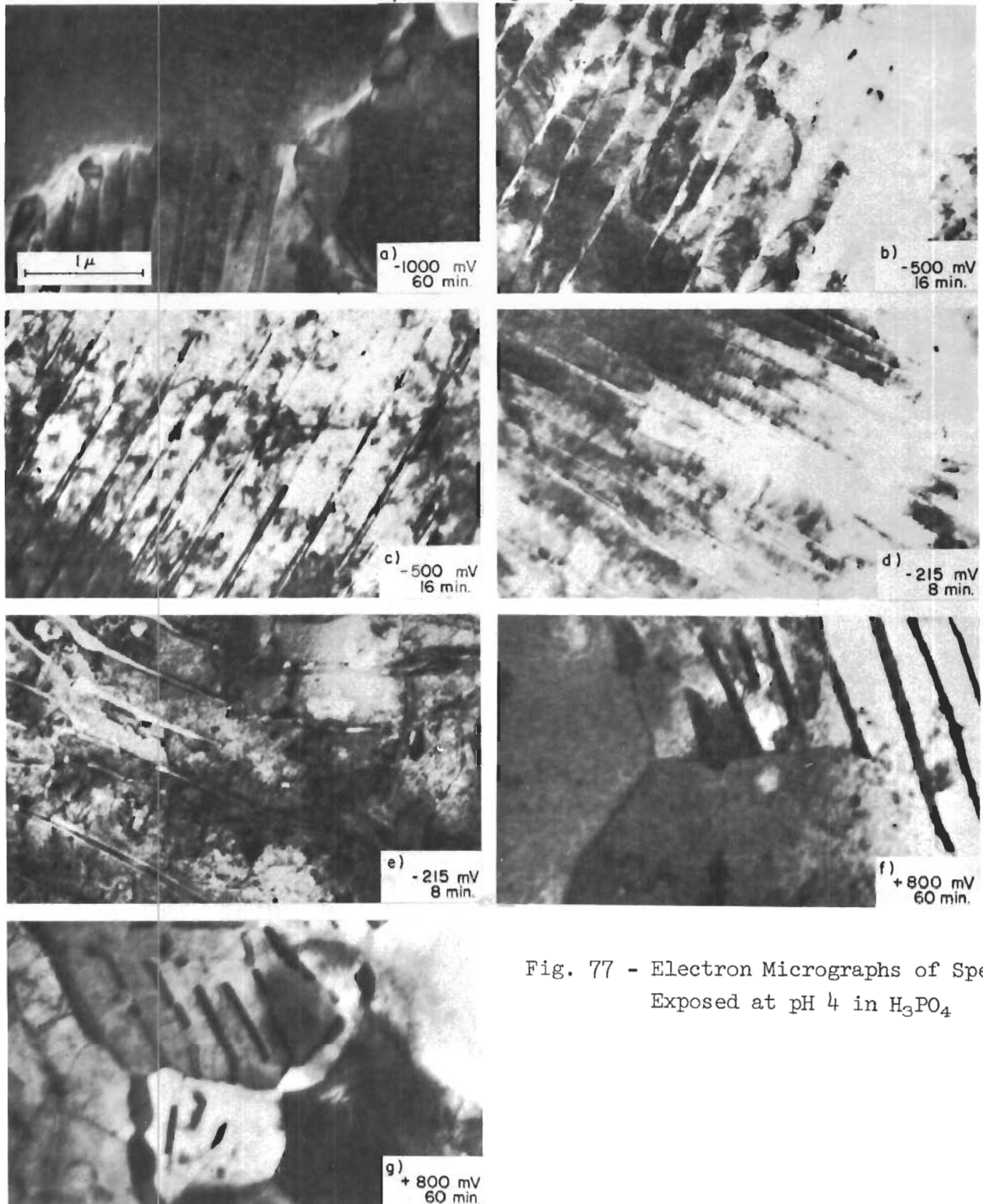


Fig. 77 - Electron Micrographs of Specimens
Exposed at pH 4 in H_3PO_4

(5) Acetic Acid Solution (Fig. 78)

At -1000 mV, no attack occurs. At -500 mV the matrix is attacked and the carbides are stable. At -215 mV, matrix attack is more vigorous than at -500 mV and the interface is the most severely attacked region.

At +100 mV, a reversal of behavior is observed in that the carbides are severely attacked while the matrix is unattacked. At +800 mV, attack is general with the interface again being attacked most vigorously.

(6) 0.1N NaOH-0.1M $\text{KHC}_8\text{H}_4\text{O}_4$ Buffer Solution (Fig. 79)

At -1250 mV, after 120 minutes exposure no attack was observed. At -290 mV, after 10 minutes exposure the matrix has been severely attacked while carbides remain unaffected. At -200 mV similar behavior was observed, with the matrix attack being more rapid. Large black areas are thought to be agglomerated iron carbide resulting from removal of nearly all of the supporting matrix material. At +800 mV, the matrix is again severely attacked and the carbides are not attacked.

In summary, at pH 4 the behavior is found to vary considerably depending upon the anion present. The HCl environment was unique in that it is the only environment in which attack was observed at -1000 mV. In general, severity of attack appears to pass through a maximum in going from -1000 mV to +800. This is consistent with the greater tendency of iron to passivate at the higher potentials.

c. pH 10

Electron micrographs of specimens exposed to a pH 10 0.1N NaOH-0.1M H_3BO_3 buffer solution are shown in Fig. 80. At -1200 mV, after 60 minutes exposure no attack was observed. At -680 mV, -580 mV, and +400 mV the matrix was vigorously attacked while the carbides were unaffected.

d. pH 14

Three environments were used to investigate the effect of the anion present on dissolution behavior.

Contrails
pH4 ACETIC ACID

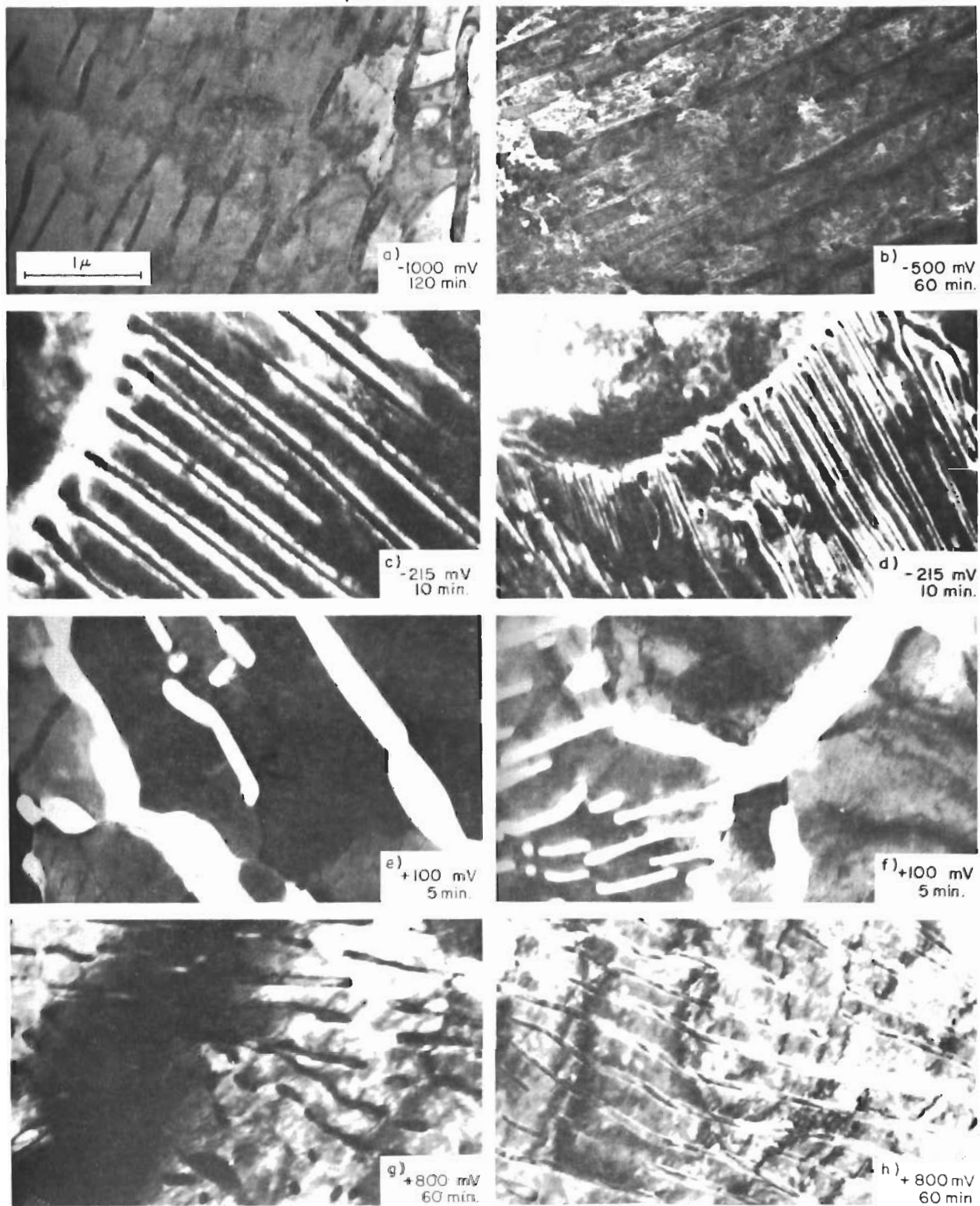


Fig. 78 - Electron Micrographs of Specimens Exposed at pH 4 in Acetic Acid

Contrails

pH4 0.1N NaOH - 0.1M $\text{KHC}_8\text{H}_4\text{O}_4$ BUFFER

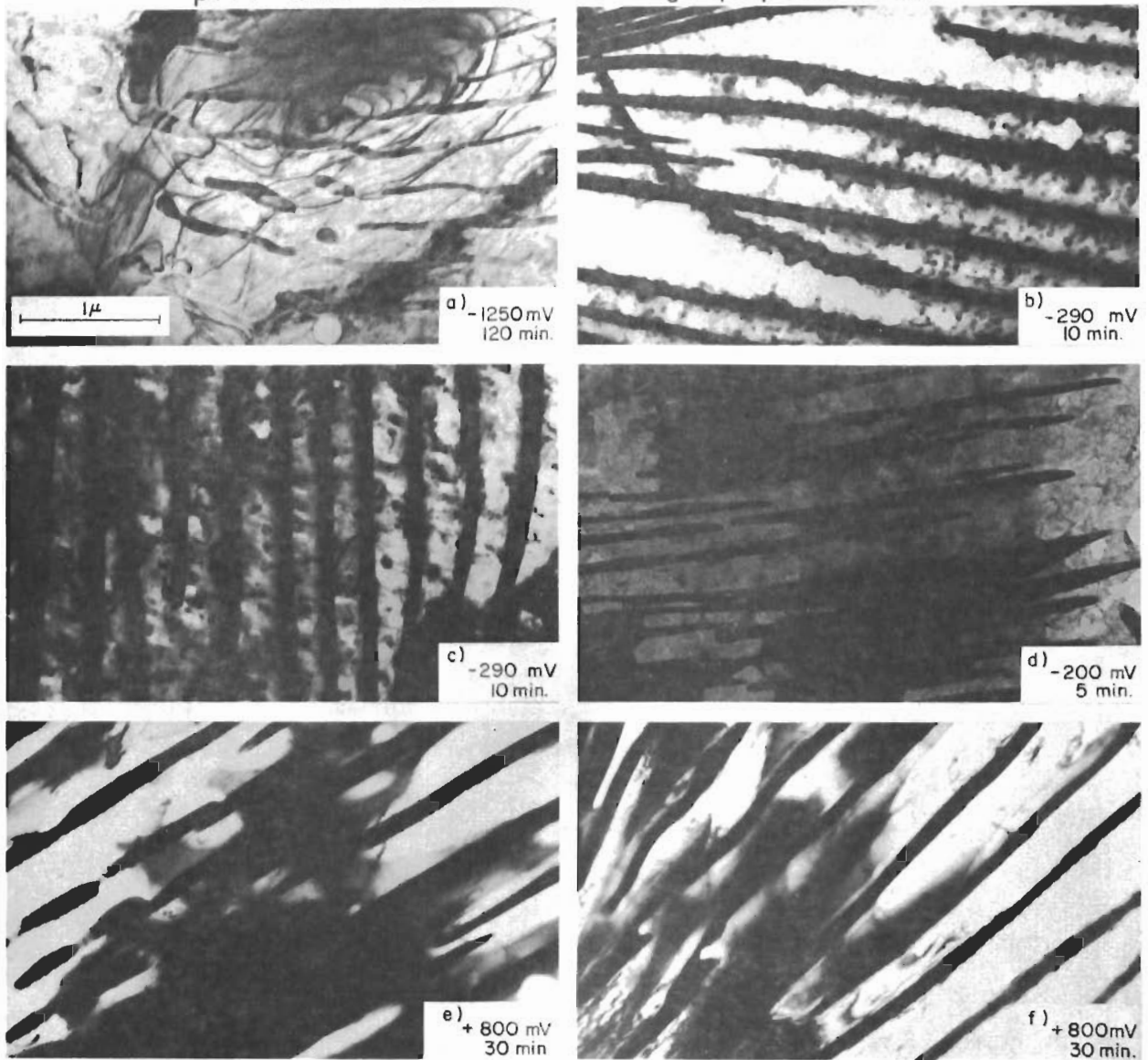


Fig. 79 - Electron Micrographs of Specimens Exposed at pH 4 in 0.1N NaOH - 0.1M $\text{KHC}_8\text{H}_4\text{O}_4$ Buffer

pH 10 0.1N NaOH - 0.1M H_3BO_3 BUFFER

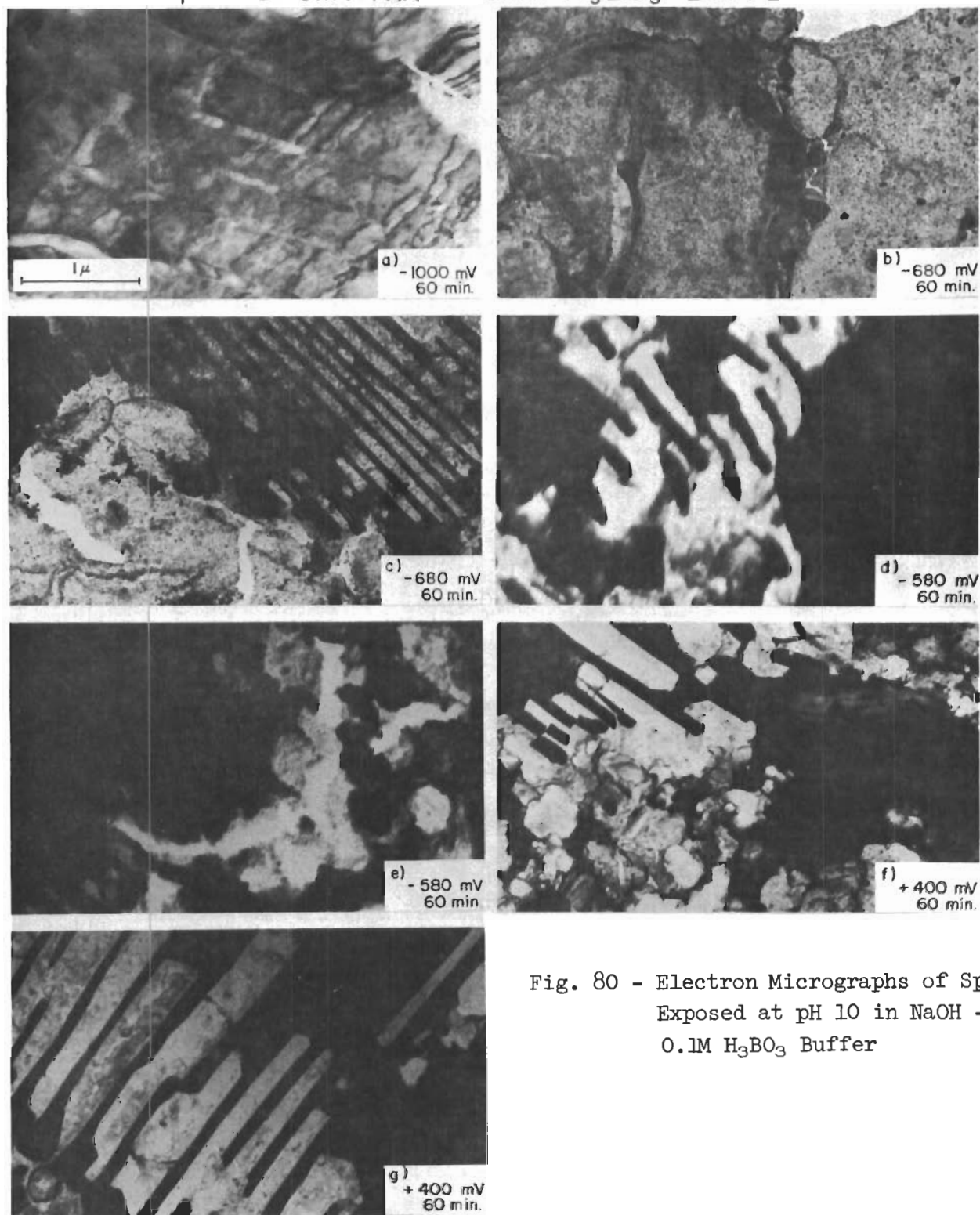


Fig. 80 - Electron Micrographs of Specimens
Exposed at pH 10 in NaOH -
0.1M H_3BO_3 Buffer

(1) 1N NaOH (Fig. 81)

At -1200 mV no attack was observed. At -860 mV substantial matrix attack occurred while the carbides were stable. At -400 mV substantial dissolution of both matrix and carbide have occurred, with the interface being attacked most vigorously. At +400 mV the carbides are severely attacked while the matrix was only slightly attacked.

(2) 1N NaOH+1M Na₂SO₄ (Fig. 82)

No attack occurred at -1200 mV. At -860 mV the matrix was not affected, while the carbides were severely attacked. At -400 the behavior was the same, with the carbide attack being less vigorous. At +400 mV the carbides are again severely attacked and the matrix unaffected.

(3) 1N NaOH+1M NaCl (Fig. 83)

The behavior is the same as in the 1N NaOH+1M Na₂SO₄. The only differences being that the matrix is slightly attacked at -400 mV and -860 mV, and that the carbide attack is not as vigorous at +400 mV.

e. The dissolution behavior in all the environments is summarized graphically in Fig. 84 which shows together the relative dissolution behavior of the matrix, interface, and carbide. Here are clearly four discrete dissolution modes; i.e., overall dissolution, preferential ferrite dissolution, preferential carbide dissolutions, and preferential interface dissolution.

f. Current Densities

The current densities measured during exposure of the foils are given in Table X.

g. Thermodynamic Calculations

Thermodynamic data have been used to predict the range of stability of the various species that may be formed during the dissolution of the carbide. The stabilities are determined as a function of potential and pH.

The results of these calculations are presented here in five sections: (1) iron stability (2) carbon stability (3) iron carbide (Fe₃C) stability (4) chromium carbide, (C₇C₃), stability (5) complex species stability. Table XI is a compilation of the free energy

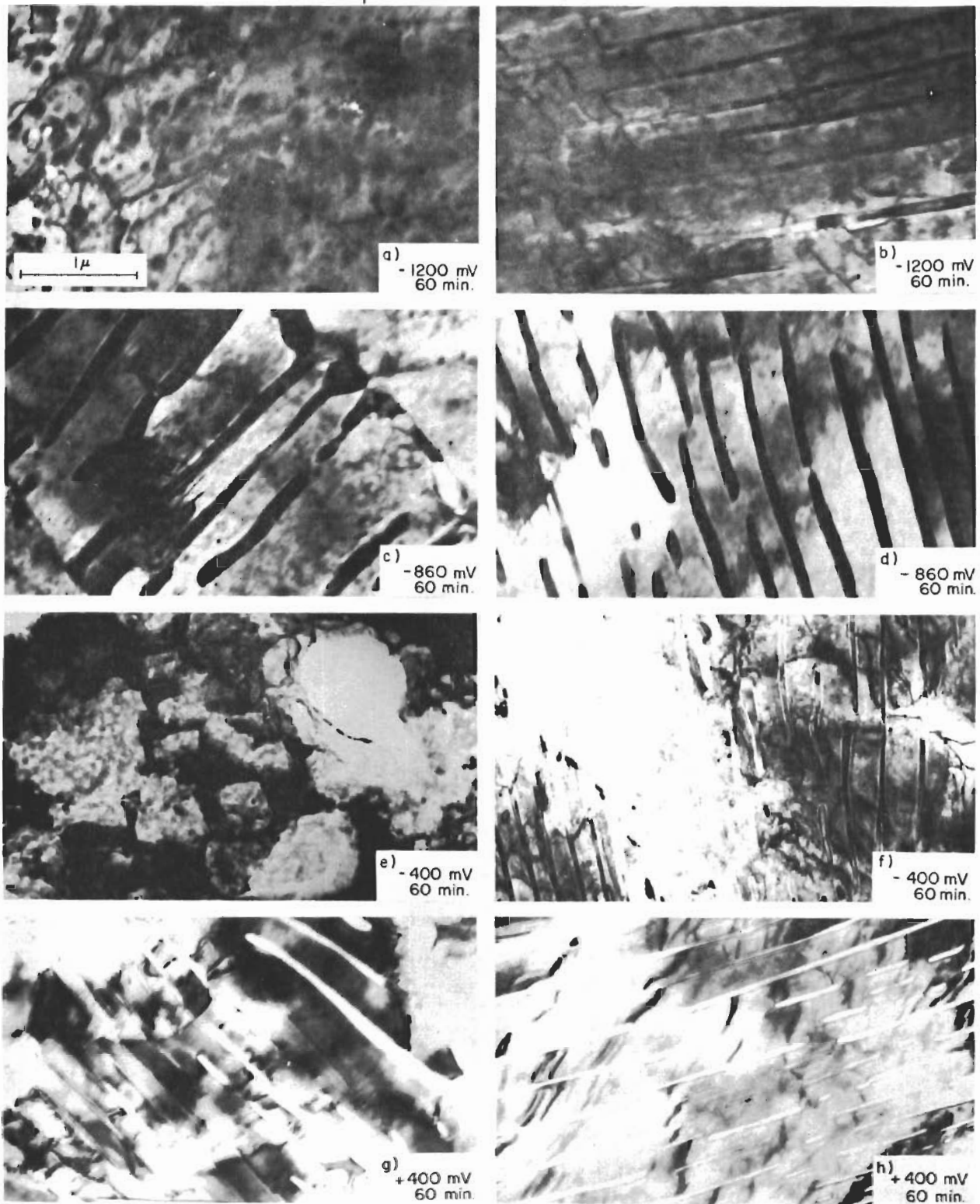


Fig. 81 - Electron Micrographs of Specimens Exposed at pH 14 in NaOH

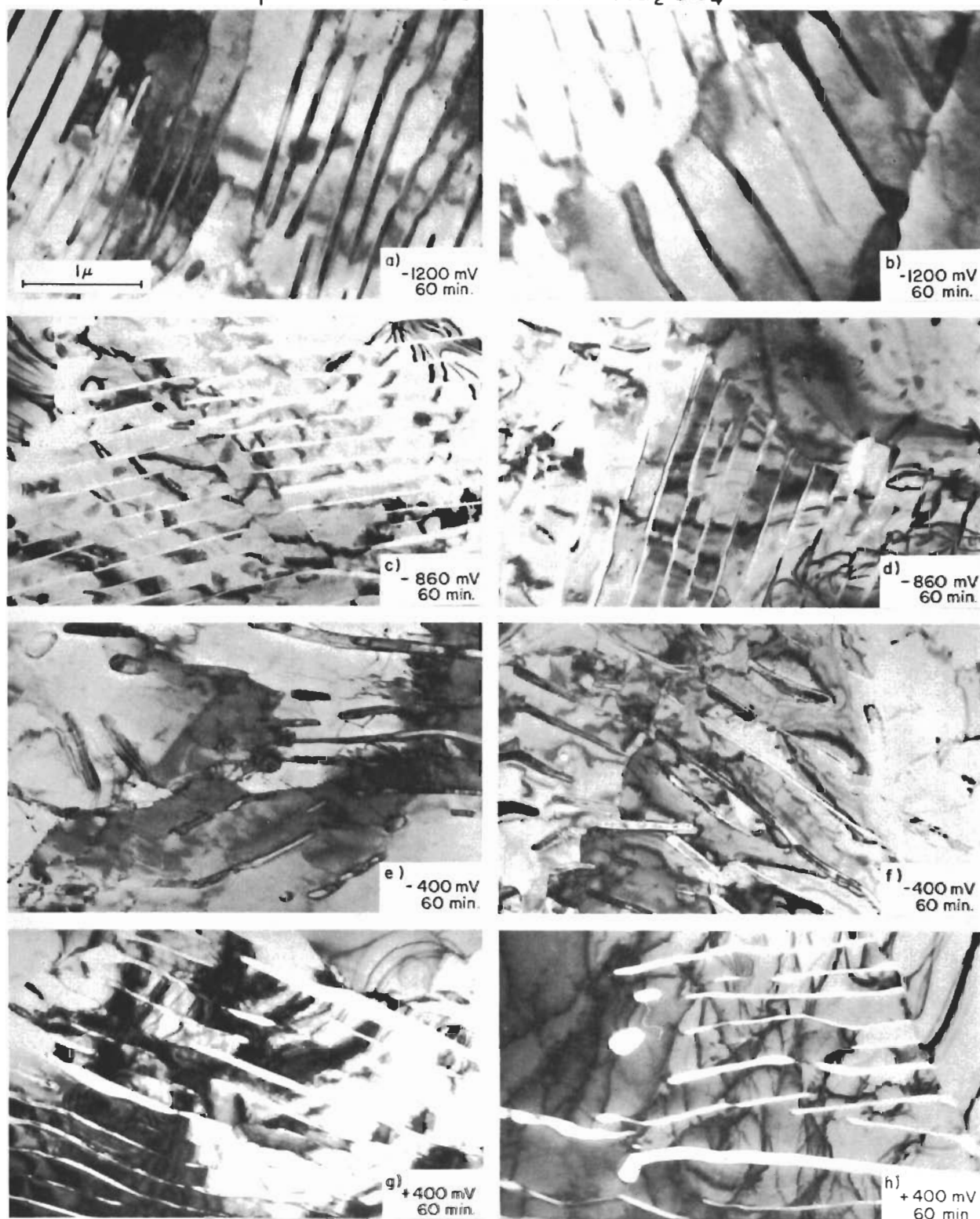
pH 14 1N NaOH + 1M Na₂SO₄

Fig. 82 - Electron Micrographs of Specimens Exposed at pH 14 in
1N NaOH + 1M Na₂SO₄

Controls
pH 14 IN NaOH + 1M NaCl

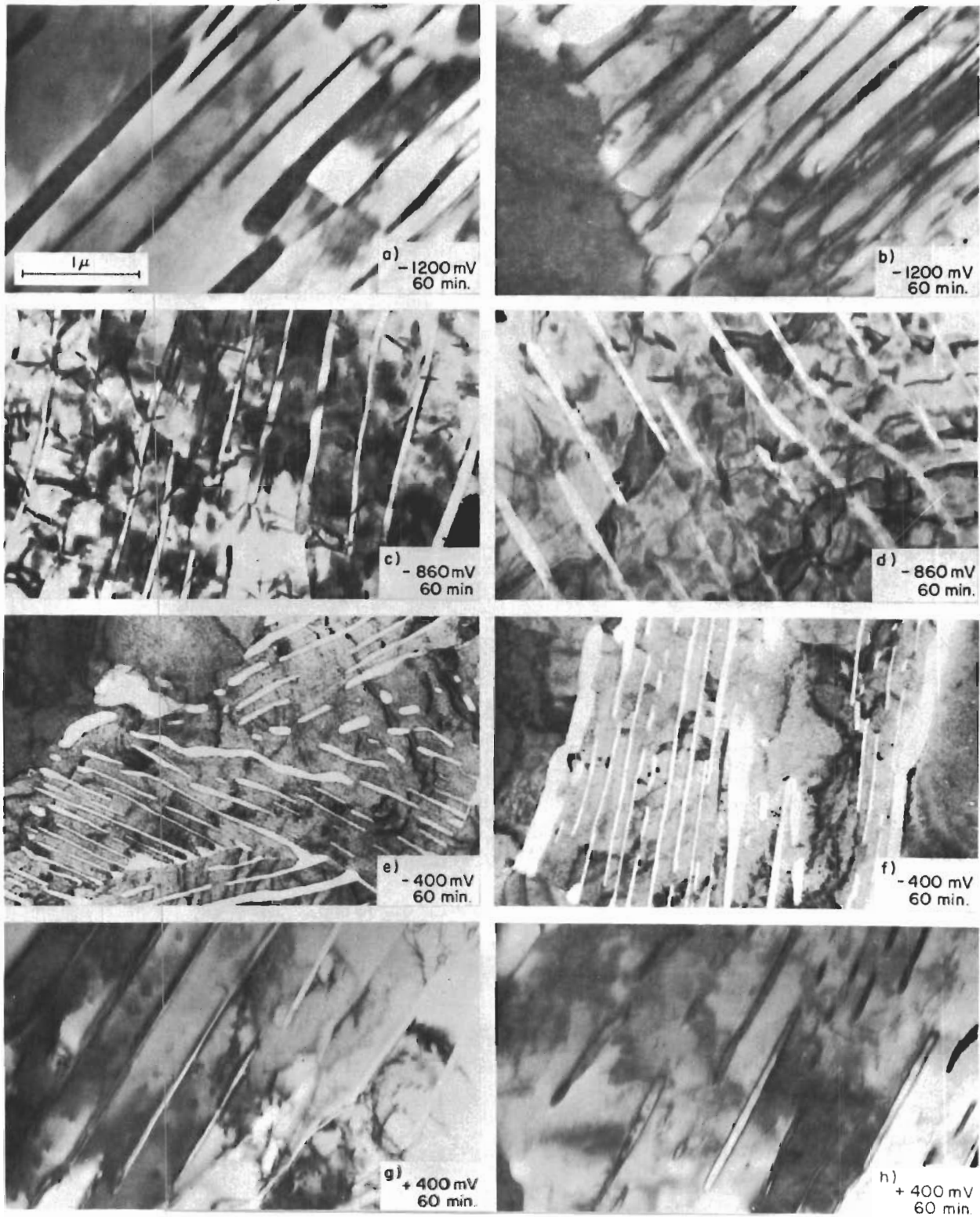


Fig. 83 - Electron Micrographs of Specimens Exposed at pH 14 in NaOH + 1N NaCl

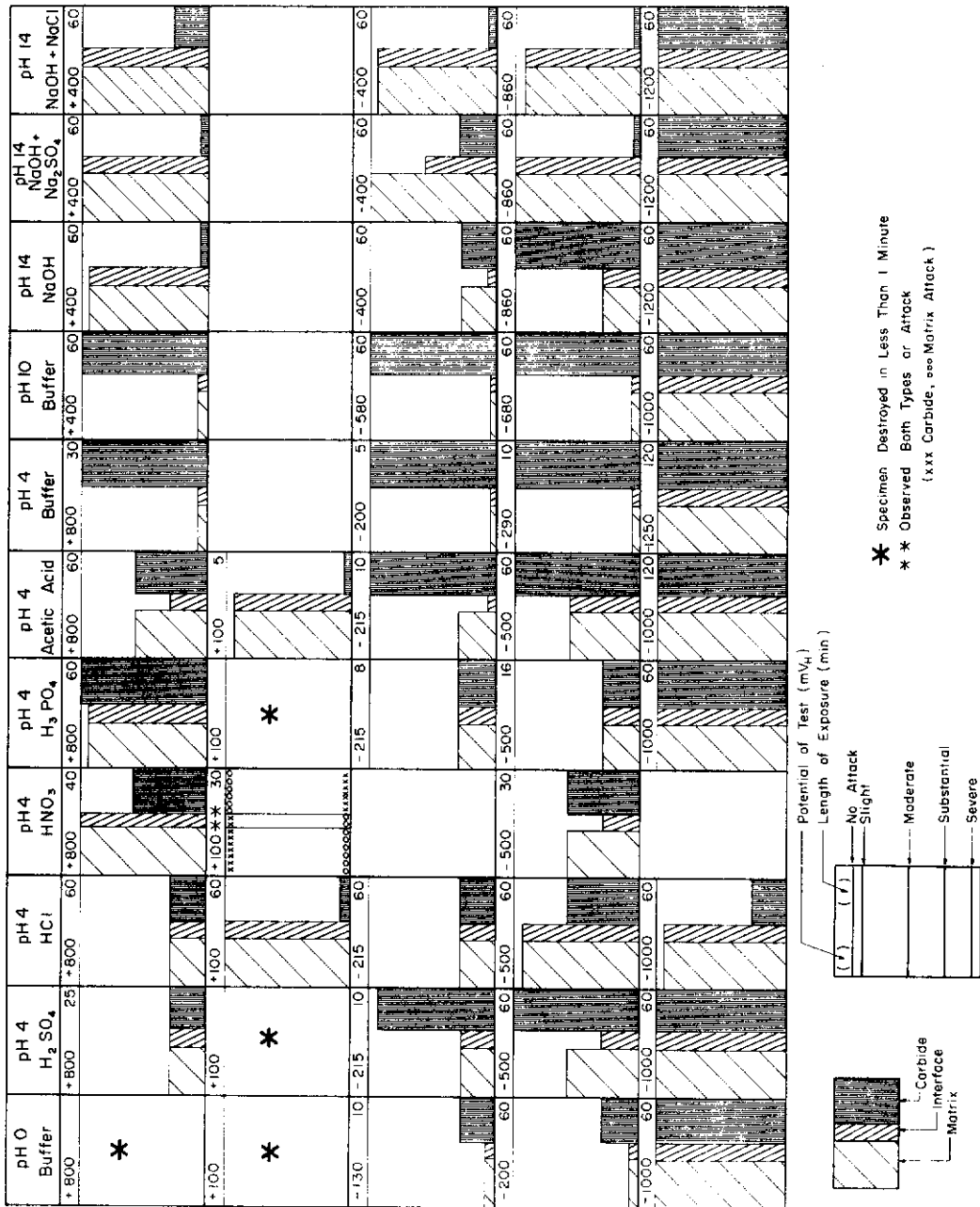


Fig. 84 - Degree of Attack as a Function of Potential and Environment

Table X - Current Readings during Tests

Environment	pH	Potential	Current (A/cm ²)
Buffer Solution (HCl-KCl)	0	+ 130	
	0	- 200	
	0	-1000	$2.2 \times 10^3(c) \rightarrow 3.7 \times 10^2$ after 60 min
H ₂ SO ₄	4	+ 800	0.7(a) \rightarrow 1.1 after 25 min
	4	+ 100	0.15(a) \rightarrow 0.37(a) after 4 min
	4	- 215	0.04(c) \rightarrow 0.04(a) after 10 min
	4	- 500	0.12(c)
	4	-1000	0.29(c)
HCl	4	+ 800	Varying 0.6(a) \leftrightarrow 0.17
	4	+ 100	0.097(a) \rightarrow 0.073(a)
	4	- 215	Varying 0.024 \leftrightarrow 0.12(c)
	4	- 500	0.97(c)
	4	-1000	Varying 0.24(c) \leftrightarrow 0.49(c)
HNO ₃	4	+ 800	0.096(a) \rightarrow 0.072(a)
	4	+ 100	0.024(a)
	4	- 500	0.12(c)
	4	-1000	
H ₃ PO ₄	4	+ 800	0.60(a) \rightarrow 1.2(a)
	4	- 215	0.012(a) \rightarrow nil after 8 min
	4	- 500	0.11(c) \rightarrow 0.096(c) after 16 min
	4	-1000	0.366(c)
Acetic Acid	4	+ 800	0.06(a) \rightarrow 0.096(a) after 60 min
	4	+ 100	0.36(a)
	4	- 215	0.12(a) \rightarrow 0.36(a) after 10 min
	4	- 500	0.12(c) \rightarrow 0.096(c) after 60 min
	4	-1000	0.48(c) \rightarrow 0.29(v) after 120 min

Table X - (Continued)

Environment	pH	Potential	Current (A/cm ²)
Buffer Solution			
0.1N NaOH + 0.1M KHC ₈ H ₄ O ₄	4	+ 800	Nil
	4	- 200	1.08(a) → 3.24(a) after 7 min
	4	- 290	1.08(a) → 1.08(a) after 10 min
	4	-1250	30(a) → 18(a) after 90 min
Buffer Solution			
0.1N NaOH + 0.1M H ₃ BO ₃	10	+ 400	Nil
	10	- 580	0.096(c)
	10	- 680	0.36(c) → -0.24(c) after 60 min
	10	-1000	1.08(c) → 2.4(c) after 60 min
1N NaOH			
	14	+ 400	0.024(a) → 0.048(a) after 60 min
	14	- 400	0.024(c) → 0.072(c) after 60 min
	14	- 860	0.24(c) → 0.60(c) after 60 min
	14	-1200	10.2(c) → 18(c) after 60 min
1N NaOH + 1M Na ₂ SO ₄			
	14	+ 400	0.012(a)
	14	- 400	Nil
	14	- 860	0.12(c) → 0.024(c) after 1 min
	14	-1200	7.2(c) → 8.4(c) after 60 min
1N NaOH + 1M NaCl			
	14	+ 400	6(a) → 21(a) after 2 min → 2.4 after 60 min
	14	- 400	Nil
	14	- 860	0.12(c)
	14	-1200	6(c) → 11(c) after 60 min

Area = 8.2×10^{-5} cm²
(c) = cathodic current
(a) = anodic current

Table XI - Free Energy of Formation
of Species Considered

Species	ΔG° (cal/mol)
H ₂ O	
Fe ⁺⁺	- 20,300
Fe ⁺⁺⁺	- 2,530
FeO (hydro)	- 58,880
Fe ₃ C	+ 4,760
CH ₃ OH	- 41,700
CH ₄	- 12,140
H ₂ CO ₃	-149,000
HCO ₃ ⁻	-140,310
CO ₃ ⁼	-126,220
CO ₂	- 94,260
Cr ₇ C ₃	- 43,840
Cr ⁺⁺	- 42,100
Cr ₂ O ₃ (hydro)	-250,200
CrO ₂ ⁻	-128,090
CrO ₃ ⁻³	-144,220
CrO (hydro)	- 83,810

of formation data used in the calculations.* Free energies of reaction were calculated for the reduction reaction in all cases regardless of the direction in which the reaction was written. Subsequently the Nernst equation, $G = nFE$, was applied to each reaction.

(1) Iron Stability

The equilibrium diagram for Fe-H₂O is shown in Fig. 85. The diagram has been taken from Pourbaix. The species considered for the diagram are Fe, Fe⁺⁺, Fe⁺⁺⁺, Fe(OH)₂, Fe(OH)₃, and HFeO₂⁻. The equilibrium formulae are given in Table XII. The region below lines 1, 2, and 3 is the region in which iron is thermodynamically stable in water at 25°C. Iron is unstable and will corrode in regions where the product of oxidation is soluble; i.e., in regions of Fe⁺⁺ and HFeO₂⁻. In regions where the corrosion product is a solid, iron can passivate; i.e., regions of Fe(OH)₂ and Fe(OH)₃. Lines a and b define the region of stability of water with respect to hydrogen gas and oxygen gas, respectively.

(2) Carbon Stability

The equilibrium diagram for C-H₂O is shown in Fig. 86. The species considered are C, CH₃, OH, CH₄, H₂CO₃, HCO₃⁻, CO₃⁼, and CO₂. Above lines 3, 4, and 5 carbon can be oxidized to H₂CO₃, HCO₃⁻, and CO₃⁼, respectively. Lines 7 and 8 define the regions of predominance of H₂CO₃, HCO₃⁻, and CO₃⁼. Below lines 2 and 4 carbon can be reduced to CH₄ and CH₃OH, respectively. It is of interest to note that carbon has no region of thermodynamic stability in aqueous solution. However, the strength of the carbon-carbon bond makes the system react irreversibly, thus graphite finds use as anodes in cathodic protection. The equilibria involved are listed in Table XII.

(3) Iron Carbide Stability

The species considered are Fe, C, Fe₃C, Fe⁺⁺, Fe(OH)₂, CH₃OH, CH₄, H₂CO₃, HCO₃⁻, CO₃⁼, and CO₂. The equilibria involved are listed in Table XII. Figure 87 (a-d) shows the potential-pH plots of the equilibria. Figure 87b lines 2 and 4 show

*Data from (1) Atlas of Electrochemical Equilibria in Aqueous Solutions, Marcel Pourbaix, and (2) Oxidation Potentials, Wendell M. Latimer.

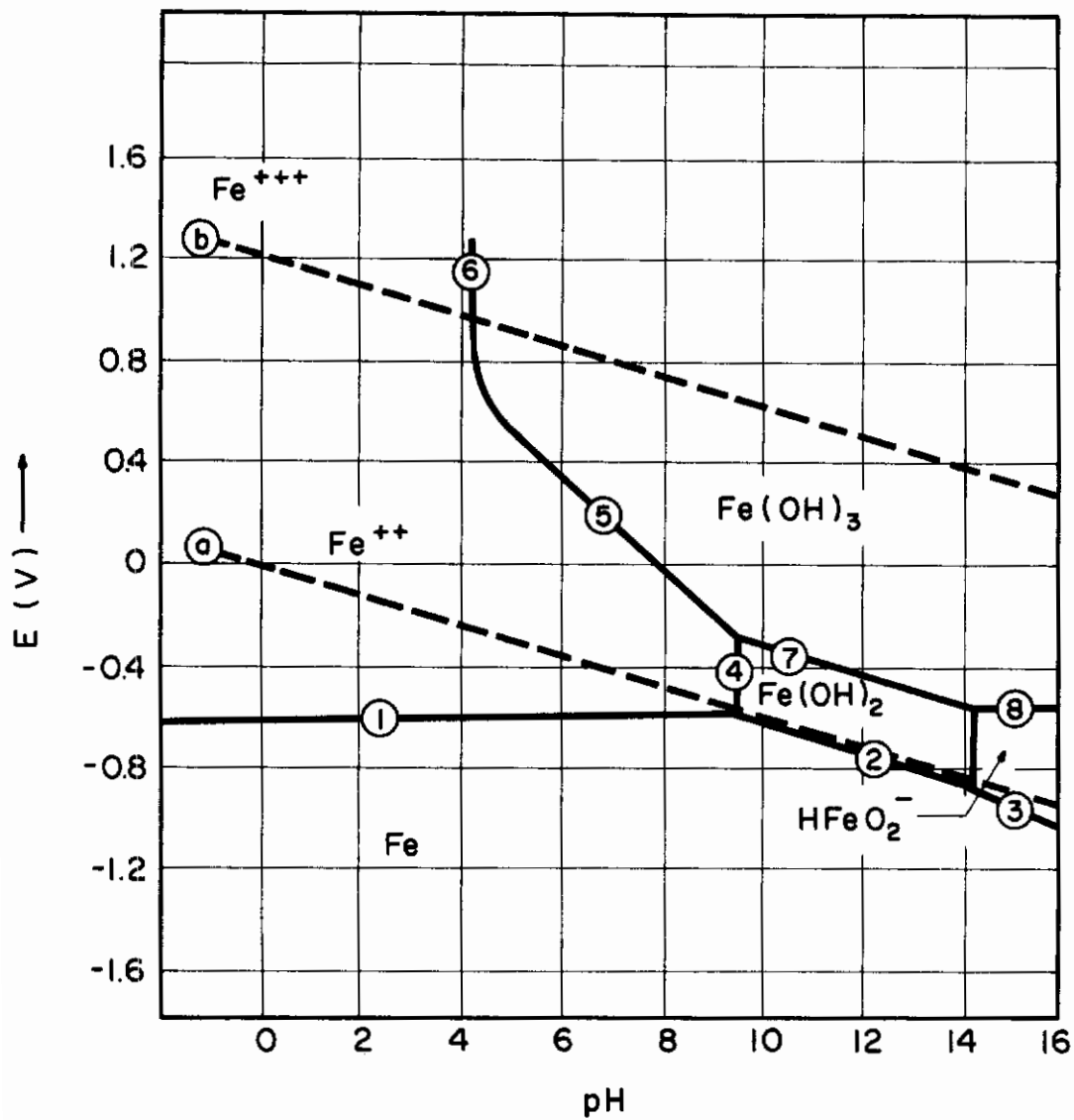


Fig. 85 - Potential-pH Diagram for the Iron-Water System at 25°C

Table XII - Reactions and Equilibrium Formulae

Iron-Water System

1. $\text{Fe} \rightarrow \text{Fe}^{++} + 2\text{e}^-$
 $E = -0.440 + 0.0295 \log [\text{Fe}^{++}]$
2. $\text{Fe} + \text{H}_2\text{O} \rightarrow \text{FeO} + 2\text{H}^+ + 2\text{e}^-$
 $E = -0.047 - 0.059 \text{ pH}$
3. $\text{Fe} + 2\text{H}_2\text{O} \rightarrow \text{HFeO}_2^- + 3\text{H}^+ + 2\text{e}^-$
 $E = -0.493 - 0.087 \text{ pH} + 0.0295 \log [\text{HFeO}_2^-]$
4. $\text{Fe}^{++} + \text{H}_2\text{O} \rightarrow \text{FeO} + 2\text{H}^+$
 $\log [\text{Fe}^{++}] = 13.29 - 2 \text{ pH}$
5. $2\text{Fe}^{++} + 3\text{H}_2\text{O} \rightarrow \text{Fe}_2\text{O}_3 + 6\text{H}^+ + 2\text{e}^-$
 $E = 1.057 - 0.177 \text{ pH} - 0.0591 \log [\text{Fe}^{++}]$
6. $2\text{Fe}^{+++} + 3\text{H}_2\text{O} \rightarrow \text{Fe}_2\text{O}_3 + 6\text{H}^+$
 $\log [\text{Fe}^{+++}] = 4.84 - 3 \text{ pH}$
7. $2\text{FeO} + \text{H}_2\text{O} \rightarrow \text{Fe}_2\text{O}_3 + 2\text{H}^+ + 2\text{e}^-$
 $E = 0.271 - 0.059 \text{ pH}$
8. $2\text{HFeO}_2^- \rightarrow \text{Fe}_2\text{O}_3 + \text{H}_2\text{O} + 2\text{e}^-$
 $E = -0.810 - 0.059 \log [\text{HFeO}_2^-]$

Carbon-Water System

1. $\text{CH}_3\text{OH} \rightleftharpoons \text{C} + \text{H}_2\text{O} + 2\text{H}^+ + 2\text{e}^-$
 $E = -0.325 - 0.0591 \text{ pH} - 0.0295 \log [\text{CH}_3\text{OH}]$
2. $\text{CH}_4 \rightarrow \text{C(s)} + 4\text{H}^+ + 4\text{e}^-$
 $E = 0.132 - 0.0591 \text{ pH} - 0.0148 \log [\text{PCH}_4]$

Table XII - (Continued)

3. $C + 3H_2O \rightarrow H_2CO_3 + 4H^+ + 4e^-$
 $E = 0.228 - 0.0591 \text{ pH} + 0.0148 \log [H_2CO_3]$
4. $C + 3H_2O \rightarrow HCO_3^- + 5H^+ + 4e^-$
 $E = 0.323 - 0.0739 \text{ pH} + 0.0148 \log [HCO_3^-]$
5. $C + 3H_2O \rightarrow CO_3^{=} + 6H^+ + 4e^-$
 $E = 0.475 - 0.0887 \text{ pH} + 0.0148 \log [CO_3^{=}]$
6. $CO_2 + 4H^+ + 4e^- \rightarrow C + 2H_2O$
 $E = 0.207 - 0.0591 \text{ pH} + 0.0148 \log [PCO_2]$
7. $H_2CO_3 \rightarrow HCO_3^- + H^+$
 $[H_2CO_3] = [HCO_3^-] \text{ @ pH } 6.38$
8. $HCO_3^- \rightarrow CO_3^{=} + H^+$
 $[HCO_3^-] = [CO_3^{=}] \text{ @ pH } 10.34$

Iron Carbide-Water System

1. $Fe_3C \rightarrow 3Fe^{++} + C(s) + 6e^-$
 $E = -0.475 + 0.0295 \log [Fe^{++}]$
2. $Fe_3C + H_2O + 2H^+ + 2e^- \rightarrow 3Fe(s) + CH_3OH$
 $E = 0.222 - 0.0591 \text{ pH} - 0.0295 \log [CH_3OH]$
3. $Fe_3C + H_2O + 2H^+ \rightarrow 3Fe^{++} + CH_3OH + 4e^-$
 $E = -0.549 + 0.0295 \text{ pH} + 0.0148 \log [Fe^{++}]^3 [CH_3OH]$
4. $Fe_3C + 4H^+ + 4e^- \rightarrow 3Fe(s) + CH_4(g)$
 $E = 0.183 - 0.0591 \text{ pH} - 0.0148 \log [PCH_4]$
5. $Fe_3C + 4H^+ \rightarrow 3Fe^{++} + CH_4 + 2e^-$
 $E = -1.687 + 0.1182 \text{ pH} + 0.0886 \log [Fe^{++}] + 0.0295 \log [PCH_4]$

Table XII - (Continued)

6. $\text{Fe}_3\text{C} + 3\text{H}_2\text{O} \rightarrow 3\text{Fe(s)} + \text{HCO}_3^- + 4\text{H}^+ + 4\text{e}^-$
 $E = 0.177 - 0.0591 \text{ pH} + 0.0148 \log [\text{H}_2\text{CO}_3]$
7. $\text{Fe}_3\text{C} + 3\text{H}_2\text{O} \rightarrow 3\text{Fe}^{++} + \text{H}_2\text{CO}_3 + 4\text{H}^+ + 10\text{e}^-$
 $E = -0.194 - 0.0236 \text{ pH} - 0.0059 \log [\text{H}_2\text{CO}_3] + 0.0177 \log [\text{Fe}^{++}]$
8. $\text{Fe}_3\text{C} + 3\text{H}_2\text{O} \rightarrow 3\text{Fe(s)} + \text{HCO}_3^- + 5\text{H}^+ + 4\text{e}^-$
 $E = 0.271 - 0.0739 \text{ pH} + 0.0148 \log [\text{HCO}_2^-]$
9. $\text{Fe}_3\text{C} + 3\text{H}_2\text{O} \rightarrow 3\text{Fe}^{++} + \text{HCO}_3^- + 5\text{H}^+ + 10\text{e}^-$
 $E = -0.156 - 0.0295 \text{ pH} + 0.0177 \log [\text{Fe}^{++}] + 0.0059 \log [\text{HCO}_3^-]$
10. $\text{Fe}_3\text{C} + 3\text{H}_2\text{O} \rightarrow 3\text{Fe(s)} + \text{CO}_3^{=} + 6\text{H}^+ + 4\text{e}^-$
 $E = 0.424 - 0.0886 \text{ pH} + 0.0148 \log [\text{CO}_3^{=}]$
11. $\text{Fe}_3\text{C} + 3\text{H}_2\text{O} \rightarrow 3\text{Fe}^{++} + \text{CO}_3^{=} + 6\text{H}^+ + 10\text{e}^-$
 $E = -0.095 - 0.0354 \text{ pH} + 0.0177 \log [\text{Fe}^{++}] + 0.0059 \log [\text{CO}_2^{=}]$
12. $\text{Fe}_3\text{C} + 2\text{H}_2\text{O} \rightarrow 3\text{Fe(s)} + \text{CO}_2 + 4\text{H}^+ + 4\text{e}^-$
 $E = 0.156 - 0.059 \text{ pH} + 0.0148 \log [\text{PCO}_2]$
13. $\text{Fe}_3\text{C} + 2\text{H}_2\text{O} \rightarrow 3\text{Fe}^{++} + \text{CO}_2 + 4\text{H}^+ + 10\text{e}^-$
 $E = 0.202 - 0.024 \text{ pH} + 0.018 \log [\text{Fe}^{++}] + 0.006 \log [\text{PCO}_2]$
14. $\text{Fe}_3\text{C} + 3\text{H}_2\text{O} \rightarrow 3\text{FeO(s)} + \text{C(s)} + 6\text{H}^+ + 6\text{e}^-$
 $E = -0.082 - 0.059 \text{ pH}$
15. $\text{Fe}_3\text{C} + 4\text{H}_2\text{O} \rightarrow 3\text{FeO} + \text{CH}_3\text{OH} + 4\text{H}^+ + 4\text{e}^-$
 $E = -0.040 - 0.059 \text{ pH} + 0.0148 \log [\text{CH}_3\text{OH}]$
16. $\text{Fe}_3\text{C} + 3\text{H}_2\text{O} \rightarrow 3\text{FeO} + \text{CH}_4 + 2\text{H}^+ + 2\text{e}^-$
 $E = -0.509 - 0.059 \text{ pH} + 0.0296 \log [\text{PCH}_4]$
17. $\text{Fe}_3\text{C} + 6\text{H}_2\text{O} \rightarrow 3\text{FeO} + \text{H}_2\text{CO}_3 + 10\text{H}^+ + 10\text{e}^-$
 $E = -0.042 - 0.059 \text{ pH} + 0.006 \log [\text{H}_2\text{CO}_3]$

Table XII - (Continued)

18. $\text{Fe}_3\text{C} + 6\text{H}_2\text{O} \rightarrow 3\text{FeO} + \text{HCO}_3^- + 11\text{H}^+ + 10\text{e}^-$
 $E = + 0.080 - 0.065 \text{ pH} + 0.006 \log [\text{HCO}_3^-]$
19. $\text{Fe}_3\text{C} + 6\text{H}_2\text{O} \rightarrow 3\text{FeO} + \text{CO}_3^{=2-} + 12\text{H}^+ + 10\text{e}^-$
 $E = + 0.141 - 0.071 \text{ pH} + 0.006 \log [\text{CO}_3^{=2-}]$
20. $\text{Fe}_3\text{C} + 5\text{H}_2\text{O} \rightarrow 3\text{FeO} + \text{CO}_2 + 10\text{H}^+ + 10\text{e}^-$
 $E = + 0.034 - 0.059 \text{ pH} + 0.006 \log [\text{P}_{\text{CO}_2}]$

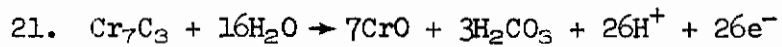
Chromium Carbide-Water System

1. $\text{Cr}_7\text{C}_3 \rightarrow 7\text{Cr}^{++} + 3\text{C}(\text{s}) + 14\text{e}^-$
 $E = - 0.775 + 0.0295 \log [\text{Cr}^{++}]$
2. $\text{Cr}_7\text{C}_3 + 3\text{H}_2\text{O} + 6\text{H}^+ + 6\text{e}^- \rightarrow 7\text{Cr}(\text{s}) + 3\text{CH}_3\text{OH}$
 $E = - 0.641 - 0.0591 \text{ pH} - 0.0295 \log [\text{CH}_3\text{OH}]$
3. $\text{Cr}_7\text{C}_3 + 3\text{H}_2\text{O} + 6\text{H}^+ \rightarrow 7\text{Cr}^{++} + 3\text{CH}_3\text{OH} + 8\text{e}^-$
 $E = - 1.09 + 0.044 \text{ pH} + 0.049 \log [\text{Cr}^{++}] + 0.021 \log [\text{CH}_3\text{OH}]$
4. $\text{Cr}_7\text{C}_3 + 12\text{H}^+ + 12\text{e}^- \rightarrow 7\text{Cr}(\text{s}) + 3\text{CH}_4$
 $E = 0.025 - 0.0591 \text{ pH} - 0.0148 \log [\text{P}_{\text{CH}_4}]$
5. $\text{Cr}_7\text{C}_3 + 12\text{H}^+ \rightarrow 7\text{Cr}^{++} + 3\text{CH}_4 + 2\text{e}^-$
 $E = - 6.23 + 0.354 \text{ pH} + 0.203 \log [\text{Cr}^{++}] + 0.089 \log [\text{P}_{\text{CH}_4}]$
6. $\text{Cr}_7\text{C}_3 + 9\text{H}_2\text{O} \rightarrow 7\text{Cr}(\text{s}) + 3\text{H}_2\text{CO}_3 + 12\text{H}^+ + 12\text{e}^-$
 $E = 0.387 - 0.0591 \text{ pH} + 0.0148 \log [\text{H}_2\text{CO}_3]$
7. $\text{Cr}_7\text{C}_3 + 9\text{H}_2\text{O} \rightarrow 7\text{Cr}^{++} + 3\text{H}_2\text{CO}_3 + 12\text{H}^+ + 26\text{e}^-$
 $E = - 0.313 - 0.027 \text{ pH} + 0.016 \log [\text{Cr}^{++}] + 0.007 \log [\text{H}_2\text{CO}_3]$
8. $\text{Cr}_7\text{C}_3 + 9\text{H}_2\text{O} \rightarrow 7\text{Cr}(\text{s}) + 3\text{HCO}_3^- + 15\text{H}^+ + 12\text{e}^-$
 $E = 0.481 - 0.074 \text{ pH} + 0.0148 \log [\text{HCO}_3^-]$

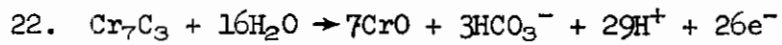
Table XII - (Continued)

9. $\text{Cr}_7\text{C}_3 + 9\text{H}_2\text{O} \rightarrow 7\text{Cr}^{++} + 3\text{HCO}_3^- + 15\text{H}^+ + 26\text{e}^-$
 $E = -0.269 - 0.0341 \text{ pH} + 0.0159 \log [\text{Cr}^{++}] + 0.0068 \log [\text{HCO}_3^-]$
10. $\text{Cr}_7\text{C}_3 + 9\text{H}_2\text{O} \rightarrow 7\text{Cr(s)} + 3\text{CO}_3^{=} + 18\text{H}^+ + 12\text{e}^-$
 $E = 0.634 - 0.0887 \text{ pH} + 0.0148 \log [\text{CO}_2^{=}]$
11. $\text{Cr C}_3 + 9\text{H}_2\text{O} \rightarrow 7\text{Cr}^{++} + 3\text{CO}_3^{=} + 18\text{H}^+ + 26\text{e}^-$
 $E = -0.199 - 0.0409 \text{ pH} + 0.0159 \log [\text{Cr}^{++}] + 0.0068 \log [\text{CO}_3^{=}]$
12. $2\text{Cr}_7\text{C}_3 + 21\text{H}_2\text{O} \rightarrow 7\text{Cr}_2\text{O}_3 + 6\text{C} + 42\text{H}^+ + 42\text{e}^-$
 $E = -0.489 - 0.0591 \text{ pH}$
13. $2\text{Cr}_7\text{C}_3 + 39\text{H}_2\text{O} \rightarrow 7\text{Cr}_2\text{O}_3 + 6\text{H}_2\text{CO}_3 + 66\text{H}^+ + 66\text{e}^-$
 $E = -0.228 - 0.0591 \text{ pH} + 0.0054 \log [\text{H}_2\text{CO}_3]$
14. $2\text{Cr}_7\text{C}_3 + 39\text{H}_2\text{O} \rightarrow 7\text{Cr}_2\text{O}_3 + 6\text{HCO}_3^- + 72\text{H}^+ + 66\text{e}^-$
 $E = -0.194 - 0.0645 \text{ pH} + 0.0054 \log [\text{HCO}_3^-]$
15. $2\text{Cr}_7\text{C}_3 + 39\text{H}_2\text{O} \rightarrow 7\text{Cr}_2\text{O}_3 + 6\text{CO}_3^{=} + 78\text{H}^+ + 66\text{e}^-$
 $E = -0.138 - 0.0698 \text{ pH} + 0.0054 \log [\text{CO}_3^{=}]$
16. $\text{Cr}_7\text{C}_3 + 23\text{H}_2\text{O} \rightarrow 7\text{CrO}_2^- + 3\text{CO}_3^{=} + 46\text{H}^+ + 33\text{e}^-$
 $E = 0.095 - 0.824 \text{ pH} + 0.0054 \log [\text{CO}_2^{=}] + 0.0125 \log [\text{CrO}_2^-]$
17. $\text{Cr}_7\text{C}_3 + 14\text{H}_2\text{O} \rightarrow 7\text{CrO}_2^- + 3\text{C} + 28\text{H}^+ + 21\text{e}^-$
 $E = -0.122 - 0.0788 \text{ pH} + 0.0197 \log [\text{CrO}_2^-]$
18. $\text{Cr}_7\text{C}_3 + 30\text{H}_2\text{O} \rightarrow 7\text{CrO}^{\equiv} + 3\text{CO}_2^{=} + 60\text{H}^+ + 33\text{e}^-$
 $E = 0.468 - 0.1075 \text{ pH} + 0.0125 \log [\text{CrO}_3^{\equiv}] + 0.0054 \log [\text{CO}_3^{=}]$
19. $\text{Cr}_7\text{C}_3 + 21\text{H}_2\text{O} \rightarrow 7\text{CrO}_3^{\equiv} + 3\text{C} + 42\text{H}^+ + 21\text{e}^-$
 $E = 0.464 - 0.1182 \text{ pH} + 0.0197 \log [\text{Cr}_2\text{O}^{\equiv}]$
20. $\text{Cr}_7\text{C}_3 + 7\text{H}_2\text{O} \rightarrow 7\text{CrO} + 3\text{C} + 14\text{H}^+ + 14\text{e}^-$
 $E = -0.452 - 0.0591 \text{ pH}$

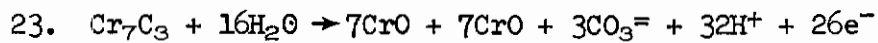
Table XII - (Continued)



$$E = -0.138 - 0.0591 \text{ pH} + 0.0068 \log [\text{H}_2\text{CO}_3]$$



$$E = -0.0946 - 0.0659 \text{ pH} + 0.0068 \log [\text{HCO}_3^-]$$



$$E = -0.024 - 0.0727 \text{ pH} + 0.0068 \log [\text{CO}_3^{=}]$$

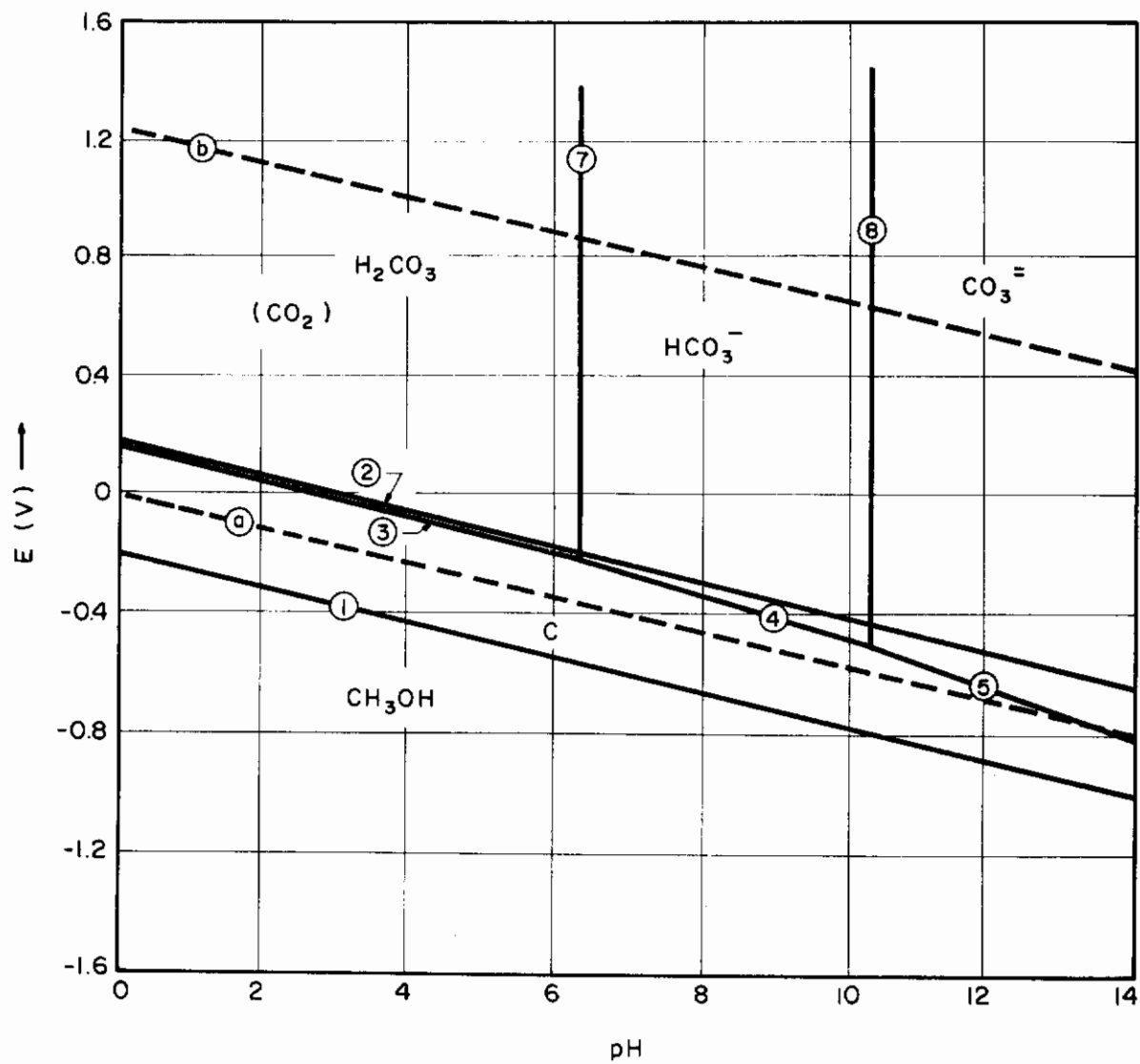


Fig. 86 - Potential-pH Diagram for the Carbon-Water System at 25°C

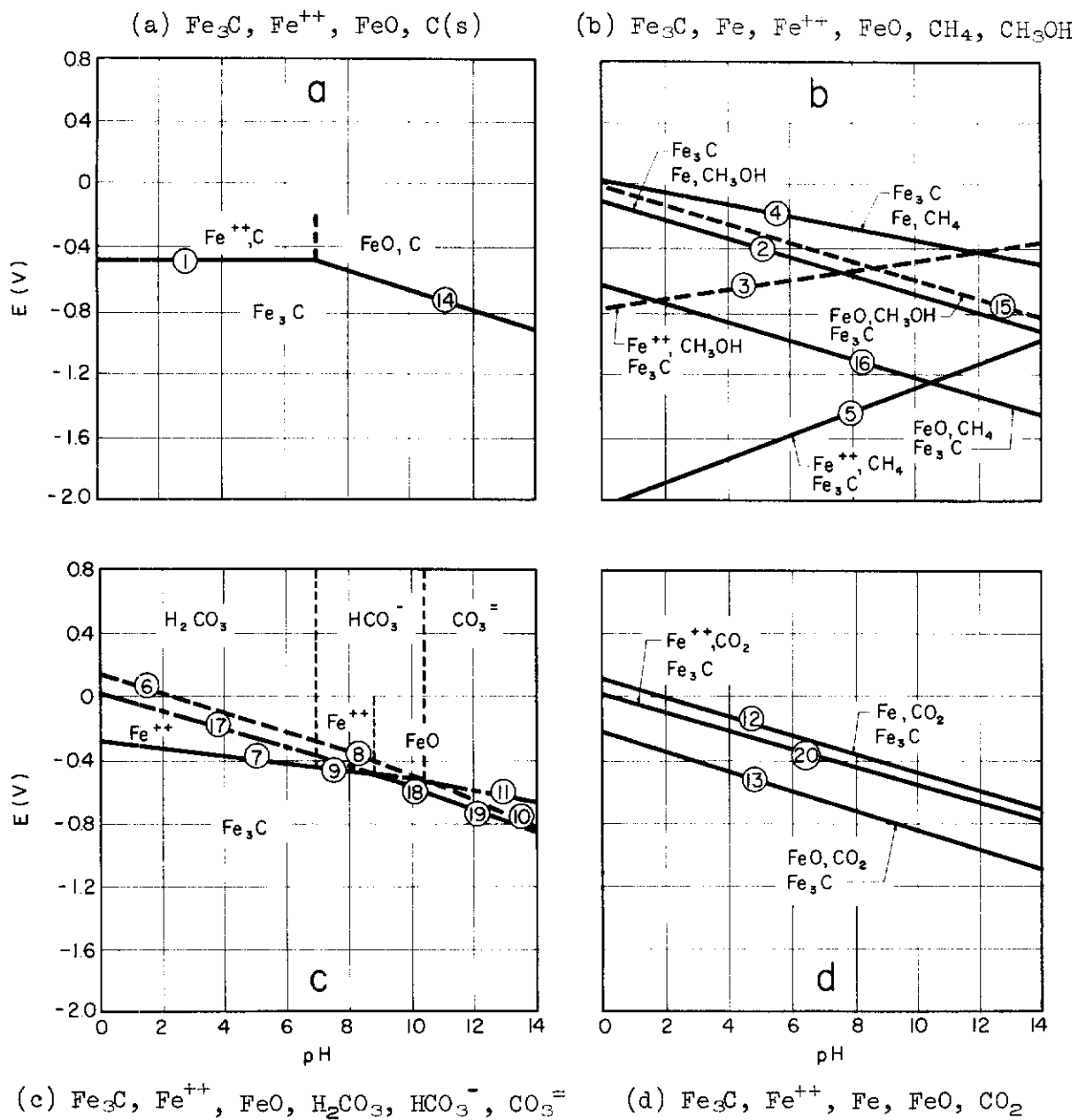


Fig. 87 - Potential-pH Diagrams for Fe_3C in H_2O Considering Species Shown

the potential required to reduce Fe_3C to methanol and methane, respectively. The iron carbide is less stable with respect to methane. The oxidation of iron carbide to carbonic acid, bicarbonate ion, and carbonate ion is considered in Fig. 87c. The dashed lines are metastable with respect to solid lines 7, 9, 18, and 19. Figure 87d shows lines for oxidation of Fe_3C to carbon dioxide

(4) Chromium Carbide (Cr_7C_3) Stability

The stability of chromium carbide is of interest because of its presence in any alloy of practical significance. Sensitization of stainless steels is but one example in which the electrochemical behavior of chromium carbide is important. Figure 88(a-d) shows plots of the equilibria considered. The equilibria are listed in Table XII. The species considered are Cr_7C_3 , Cr^{++} , Cr_2O_3 , CrO_2^- , CrO_3^{--} , CrO (hydr), C , CH_3OH , CH_4 , H_2CO_3 , HCO_3^- , and $\text{CO}_3^{=}$.

Figure 88a is the potential-pH diagram for the chromium-water system. Chromium, like iron, corrodes in acid solutions and passivates as pH increases. The chromium passive region is larger than that of iron.

(5) Complex Species Solubility

The formation of complexes between ions in solution may affect the kinetics of dissolution. If a soluble complex is stable, the dissolution kinetics can be accelerated. Conversely, if an insoluble compound is stable, the dissolution kinetics can be retarded. It is thought that the presence of complexes will prove to be the reason for the different behavior observed in the presence of different anions. A study has thus been undertaken to define the region of stability of the various complexes which are possible in an iron-water-carbon system. Some of the results of this study are given below.

(a). Iron Carbonate (FeCO_3). The solubility product for this complex as given by Latimer as 2.11×10^{-11} . Whenever the product of ferrous ion concentration and carbonate ion exceeds 10^{-11} ferrous carbonate will be precipitated. Higher ferrous ion concentration is favored by low pH whereas higher carbonate ion concentration is favored by

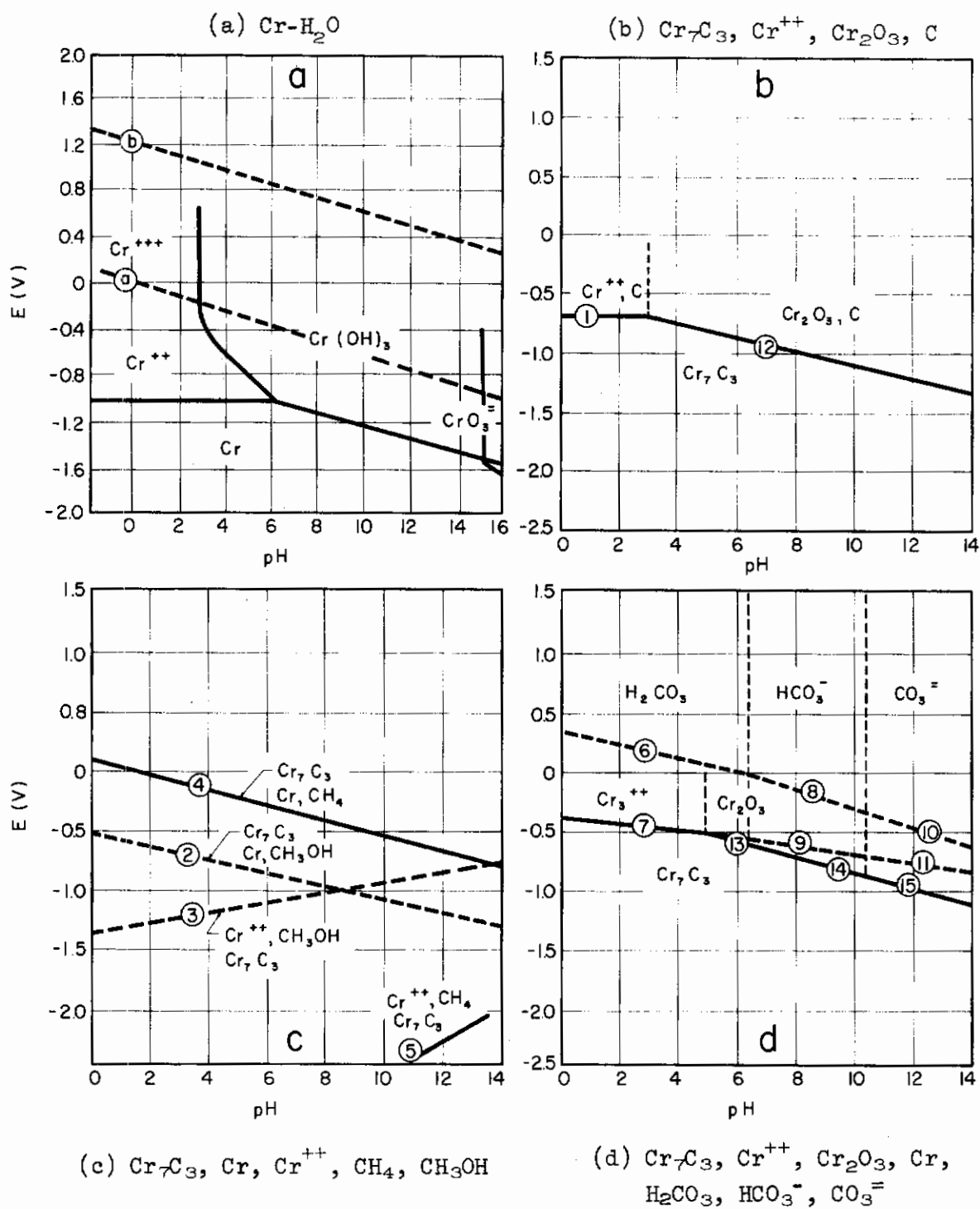


Fig. 88 - Potential-pH Diagrams for Cr_7C_3 Considering Species Shown

high pH. The carbonate ion concentration falls off much more rapidly than the ferrous ion concentration increases as pH is lowered. Thus, precipitation of iron carbonate is favored by high pH.

(b). Carbon Tetrachloride (CCl_4). In solutions containing chloride ions, carbon tetrachloride could be present. The free energy of formation of CCl_4 is small and hence the reaction, $\text{C} + 4\text{Cl}^- \rightleftharpoons \text{CCl}_4 + 4\text{e}^-$, has a high reversible potential ($E^\circ = 1.18$). The tendency to form CCl_4 is small.

(c). Ferric Tartrate - $\text{Fe}_2(\text{C}_4\text{H}_4\text{O}_6)_3$. The pH 4 buffer solution contained 0.1M $\text{KHC}_8\text{H}_4\text{O}_4$. Ferric tartrate is a soluble complex and may possibly explain why the specimens at +800 mV in the pH 4 buffer solution exhibited very rapid matrix attack (see Figs. 79 and 84).

4. Discussion

The significance of the above results is still not completely clear but a number of important ideas should be emphasized as follows:

(a). The behavior of ferrite and iron carbide varies drastically over the range of potential and pH.

(b). The effect of the anion present is substantial in some instances.

(c). The consideration of complexes formed in the system is of great importance and further work in this area should prove fruitful.

(d). In several cases, the carbide-ferrite interface was attacked more vigorously than the rest of the specimen. It is that this is the result of segregation of other elements to this interface. Manganese is suspected because it would be rejected from the carbide during carbide growth and it accelerates the anodic dissolution kinetics of iron.

(e). The dissolution of carbides and slight attack of the matrix at -1000 mV in the pH 4 HCl solution is unexpected but is in accord with the prediction of Fig. 87b.

F. DISSOLUTION KINETICS OF IRON CARBIDE, GRAPHITE (J. Payer)

1. Objectives and Background

Iron carbide and alloy carbides are important constituents of high-strength steels. The purpose of this investigation is to define the dissolution and reduction kinetics of these carbides. An understanding of these processes will be used to determine in what way and to what extent carbides take part in the stress-corrosion cracking of high-strength steels.

The study involves two types of investigations. The first is an investigation of the dissolution of thin foils of pure iron-carbon alloys using electron microscopy. The progress of this study is described in Section III E of this report. The second is an investigation of the dissolution and reduction kinetics of iron carbide using electrochemical techniques. The specific aspects of the experimental work will determine the reaction scheme for carbon oxidation and reduction while in the carbide lattice. The work will identify reaction products and rates.

2. Preparation of Iron Carbide

An essential problem which slows progress in the preparation of iron carbide is its thermodynamic instability. Efforts to procure iron carbide commercially have been unsuccessful. The aim of experimental work to produce iron carbide has been to optimize on reducing the degree of metastability and to increase the rate of carbide formation.

A schematic diagram of the equipment being used for preparation of iron carbide is shown in Fig. 89. A diagram of the furnace tube is shown in Fig. 90. A Marshall Products tube furnace in conjunction with a Barber-Coleman time-proportioning controller allows temperature control within $\pm 1^\circ\text{C}$. The atmosphere of the furnace can be regulated to any desired ratio of hydrogen and methane. This is accomplished by adjusting the flow rates through a series of manometers. By controlling the amount of methane in the gas mixture, the carburizing potential of the atmosphere can be regulated.

A series of runs has been systematically varying the temperature and carburizing potential. Thus far, only moderate success has been realized. Samples containing roughly 30 volume per cent carbide have been produced. Figure 91 shows a typical photomicrograph of a specimen with a high carbide concentration. Further runs are planned in an attempt to obtain a material with a greater content of iron carbide. In addition, three Fe-C alloys have been cast; i.e., 0.8% C (eutectoid) alloy, a 2.0% C alloy, and a 4.3% (eutectic) alloy.

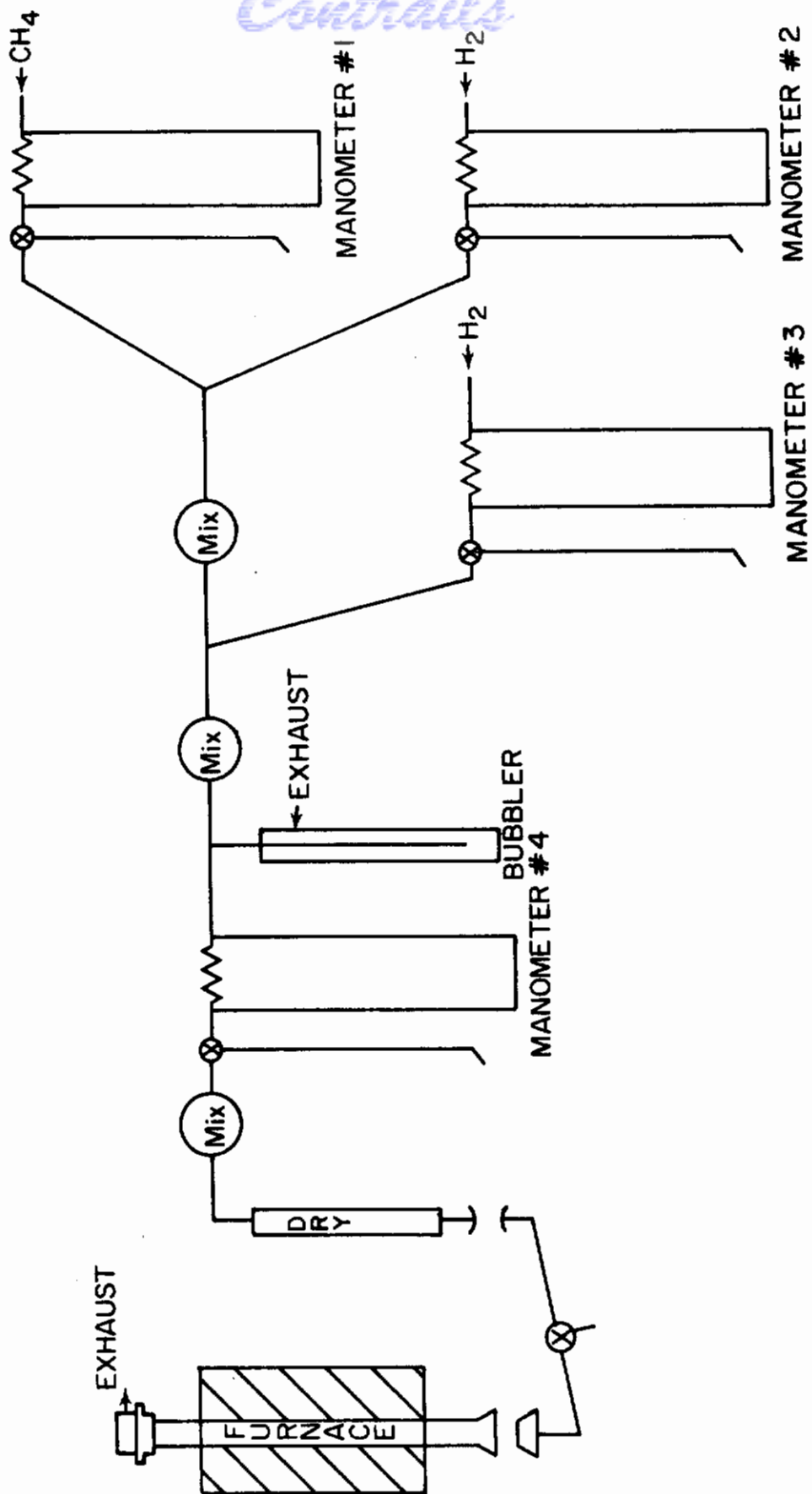


Fig. 89 - Schematic Arrangement of Furnace for Producing Fe₃C Using H₂-SO₄ Mixtures

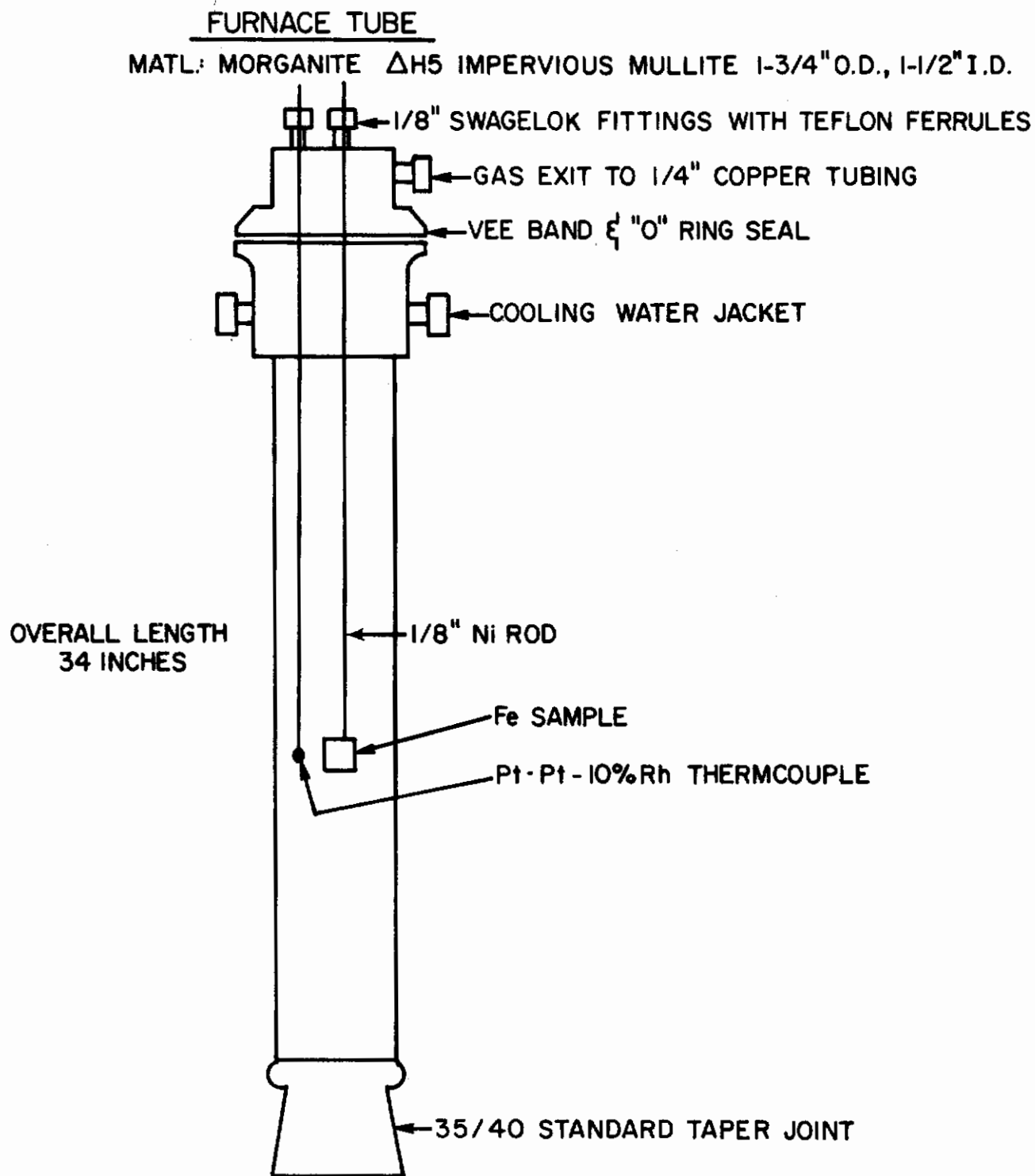


Fig. 90 - Schematic Arrangement of Furnace Tube



Fig. 91 - Photomicrograph of Specimen Containing Fe_3C

3. Work on Carbon Dissolution Kinetics

The dissolution and reduction kinetics of the iron electrode have been well documented, but this is not the case for the carbon electrode. One of the main reasons for the paucity of electrochemical work on graphite is the difficulty of preparing reproducible surfaces for investigation. A study carried out on graphite specimens showed the kinetics of oxidation and reduction to be extremely slow. The reason for the retardation of the kinetics is the difficulty of breaking the very strong carbon-carbon bond in graphite. It is thought that the carbon in the carbide lattice can react more readily because less energy is needed than is required to dissociate the carbon-carbon bond.

Since it is likely that a pure specimen of bulk iron carbide will never be obtained, the experimental determination of electrode kinetics of the carbon in iron carbide will be pursued as follows. Since the carbon is virtually all tied up in the Fe_3C , then all the reaction products can be assumed to originate from the source. By quantitative metallography it is possible to specify the relative area of the iron carbide. By holding at a series of potentials for protracted times the current-time behavior can be obtained. The solutions will be analyzed to determine both the amount of carbon reacted and the identity of the product species. The oxidation of the iron in the iron carbide can be studied in a similar way since the oxidation kinetics of pure iron can be readily obtained and the contribution of the iron in the iron carbide can be derived.

G. KINETICS OF GROWTH OF PASSIVE FILMS (K. N. Goswami)

1. Objectives and Background

The objective of this study is to determine the kinetics of growth of passive films on iron alloy surfaces. This work is directly relevant to the state of affairs immediately following the formation of fresh surfaces at a crack tip. The rate of formation of passive films affects the quantity of ions going into solution and also provides a barrier to the subsequent entry of hydrogen into the metal.

2. Experimental

The theory of ellipsometric measurements of kinetics of growth of passive films and a detailed experimental arrangement is reported in Technical Report AFML-69-16. For the results described herein, a deaerated solution of sodium borate and boric acid of pH 8.41 was used for both the anodic passivation and the cathodic reduction. The solution was kept under a stream of purified nitrogen.

The specimens of Fe, Fe-10Cr, Fe-10Ni, and Fe-10Cr-10Ni were mechanically polished (final polish with 1μ diamond abrasive) and finally washed in spectrographic grade methanol, dried quickly by adsorbing the methanol with lens paper, and placed in the cell. The oxide films formed on the specimen surfaces by existing air were reduced galvanostatically at $10\text{--}20\ \mu\text{A}/\text{cm}^2$ cathodic current. After cathodic reduction, the solution was completely replaced by fresh solution, with the metal surface maintained at the reduction potential. When the surface was so reduced, optical readings were made, and by using the potentiostat the surface was then brought rapidly to an anodic potential where films start to form. The film formation was carried out in the potential region $-400\ \text{mV}(\text{SCE})$ to $-800\ \text{mV}(\text{SCE})$. Before anodic polarization at each potential, the specimen was freshly polished and reduced. Throughout the experiment purified nitrogen was bubbled in the cell.

The optical constants and thicknesses of passive films of Fe, Fe-10Ni, Fe-10Cr, and Fe-10Cr-10Ni alloys were calculated by using the McCracking³⁴ programing for analysis of ellipsometer measurements from the electronic computer. The optical constants of the bare substrate and passive films are shown in Table XIII.

3. Results and Discussion

It has been found that our data fit equally well either the logarithmic (d vs. $\ln t$) and inverse logarithmic ($1/d$ vs. $\ln t$) rate laws. Kruger and Calvert³⁵ have also reported similar results for pure iron studied in solutions of pH 8.4. A logarithmic growth law has also been reported by Nagayama and Cohen³⁶ for film formation of iron in borate-boric acid solutions pH 8.41. The plots of growth rates

Table XIII - Comparison of the Complex Refractive Indices, $\eta(1-ki)$ of iron and iron base alloys and their anodic oxide films for $\lambda = 5461 \text{ \AA}$

	Substrate		Anodic Oxide Film	
	n	k	n	k
Fe	2.833	1.190	2.480	0.11
Fe-10Ni	2.875	1.255	2.300	0.12
Fe-10Cr	2.727	1.307	2.300	0.100
Fe-10Cr-10Ni	2.757	1.343	2.300	0.12

(logarithmic and inverse logarithmic) are shown in Figs. 92-99. It has been found that the direct logarithmic rate is independent of potentials (approximately parallel lines for different potential), but the intercept varies with potential. Sato and Cohen³⁷ have also observed the logarithmic growth law for iron in sodium borate and boric acid solutions of pH 8.41. They proposed a "place-exchange" mechanism for oxidation of iron. This mechanism involves film growth by the simultaneous exchange of positions between oxygen and iron ions for all layers of these two species forming the films.

We will now consider the other way of looking at the data which, as has been shown in the Figs. 96-99, fit an inverse logarithmic growth equally well. When this type of growth rate is observed, we can consider the rate to be controlled by the escape of ions from metal lattice over an activation barrier. For such a process the plot of the reciprocal of the film thickness vs. the log of time should yield a straight line. This is a well-known theory of growth of thin films proposed by Cabrera and Mott.³⁸

Linear relations between potentials and film thicknesses for an hour of polarization of iron and iron base alloys are shown in Fig. 100. A deviation from the linearity at lower potential may be interpreted in a term as film dissolution. Similar relations between potential vs. amount of charge are reported by Nagayama and Cohen³⁶ in their coulometric study of passive film on iron in solutions of pH 8.41. They have also found deviation from linearity below 0 mV(SCE). Kruger and Calvert³⁵ have also found the linear relation between potential and film thickness.

In Table XIV a comparison of film growth of Fe, Fe-10Ni, Fe-10Cr, and Fe-10Cr-10Ni alloys is given for the complete passivation range. From Table XIV it could be seen that the film thickness decreases as iron is alloyed with Ni, Cr, and Cr-Ni.

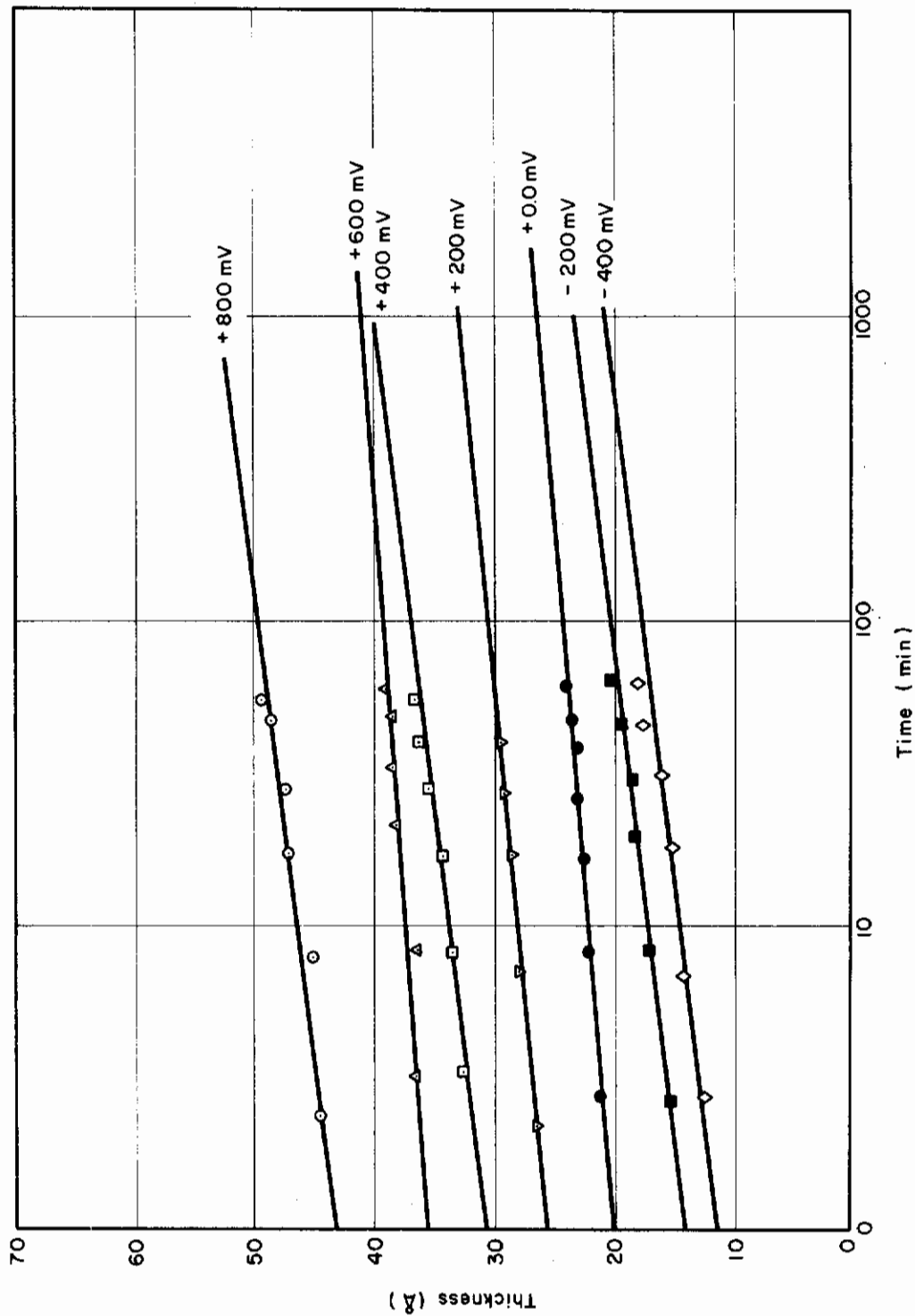


Fig. 92 - Growth of Passive Film on Fe in Solution of pH 8.41

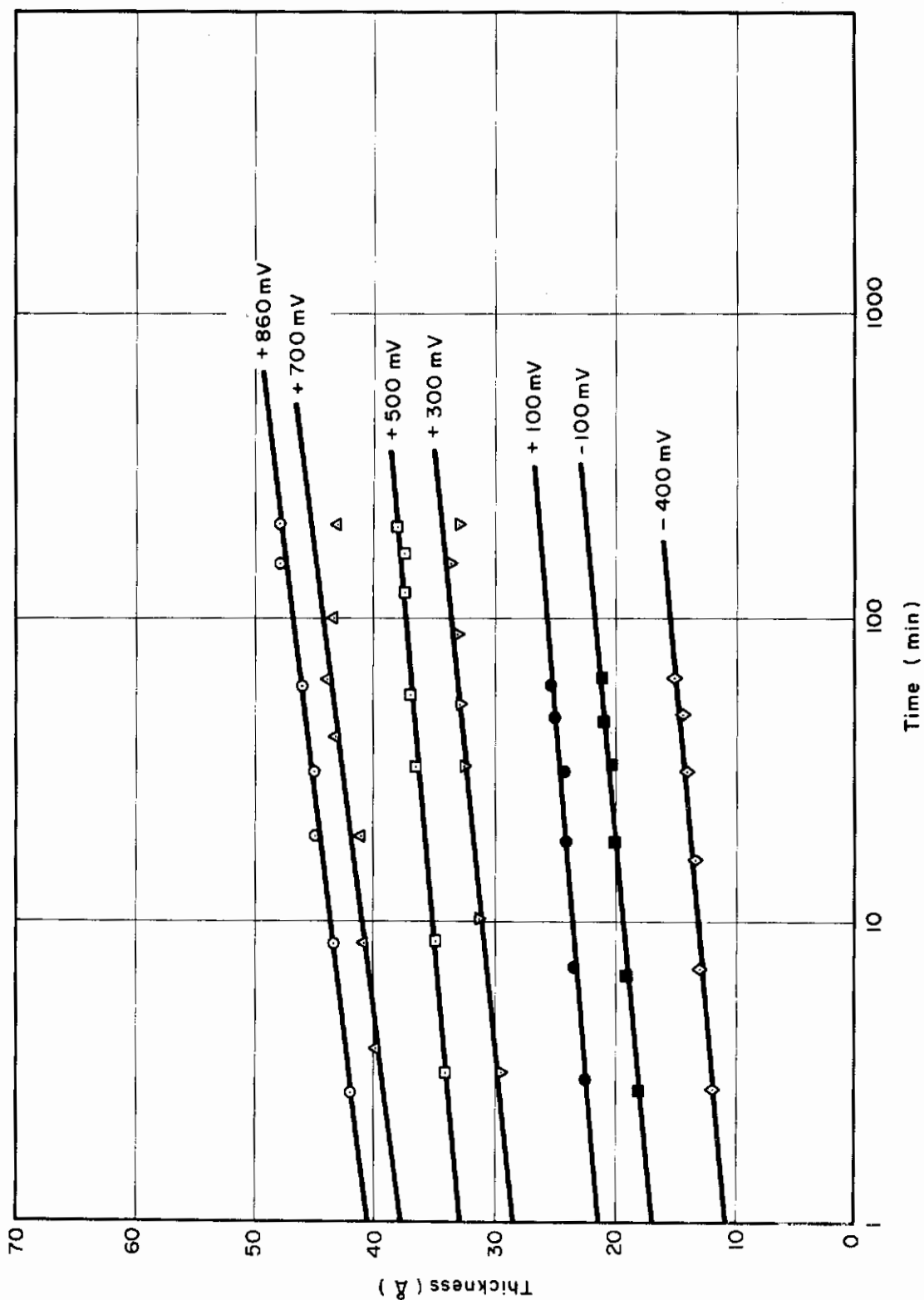


Fig. 93 - Growth of Passive Film on Fe-10Ni in Solution of pH 8.41

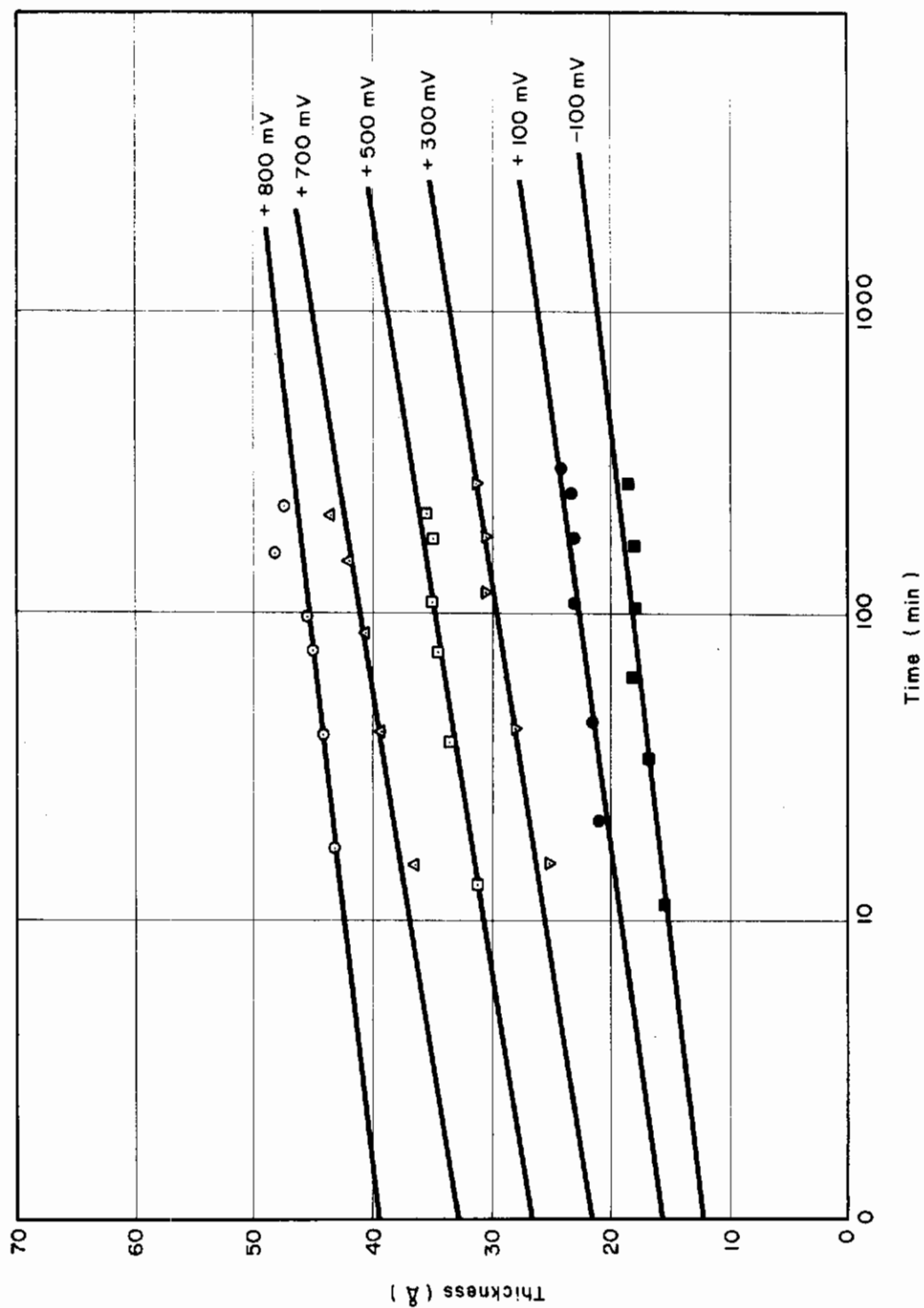


Fig. 94 - Growth of Passive Film on Fe-10 Cr in Solution of pH 8.41

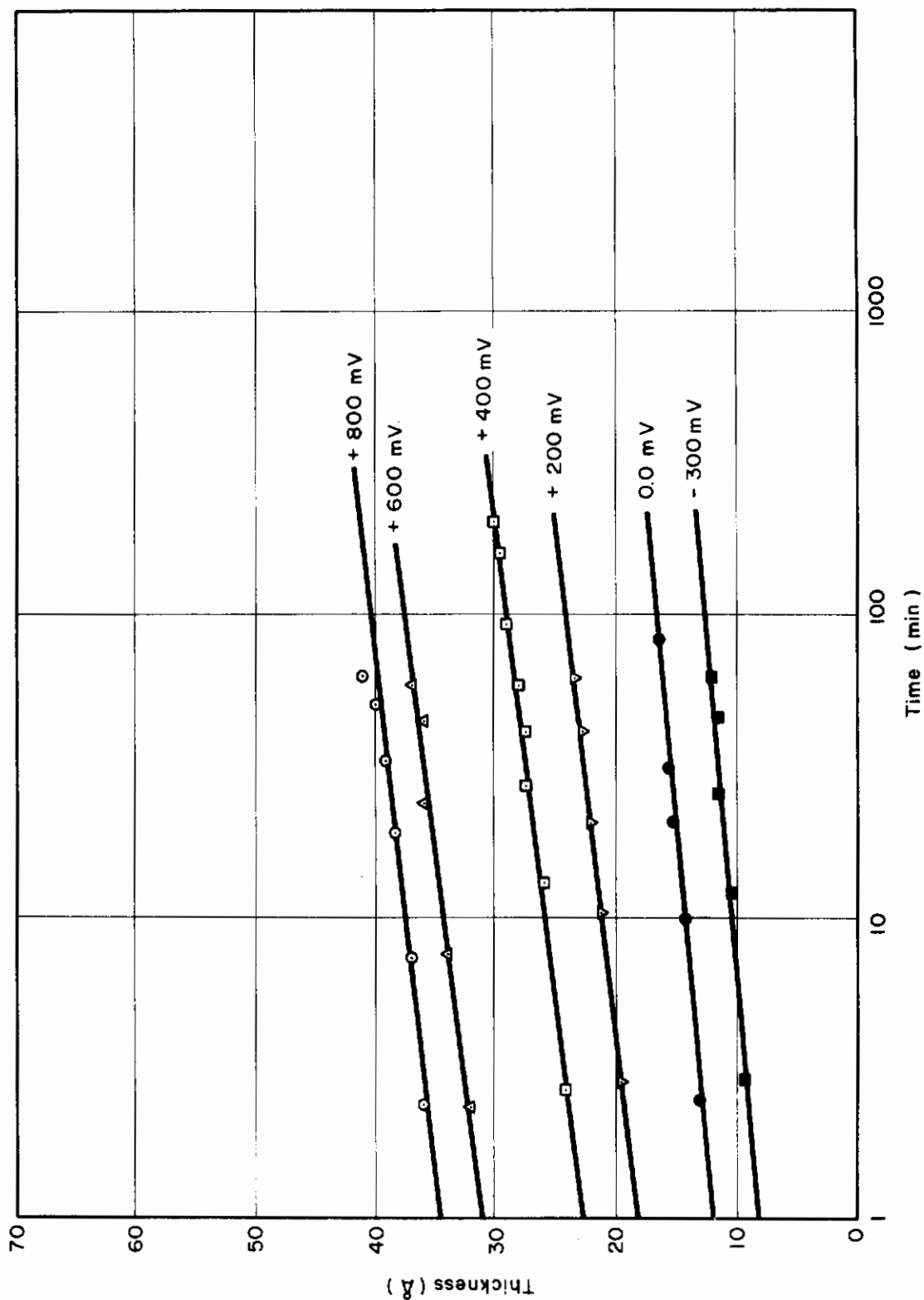


Fig. 95 - Growth of Passive Film on Fe-10 Cr in Solution of pH 8.41

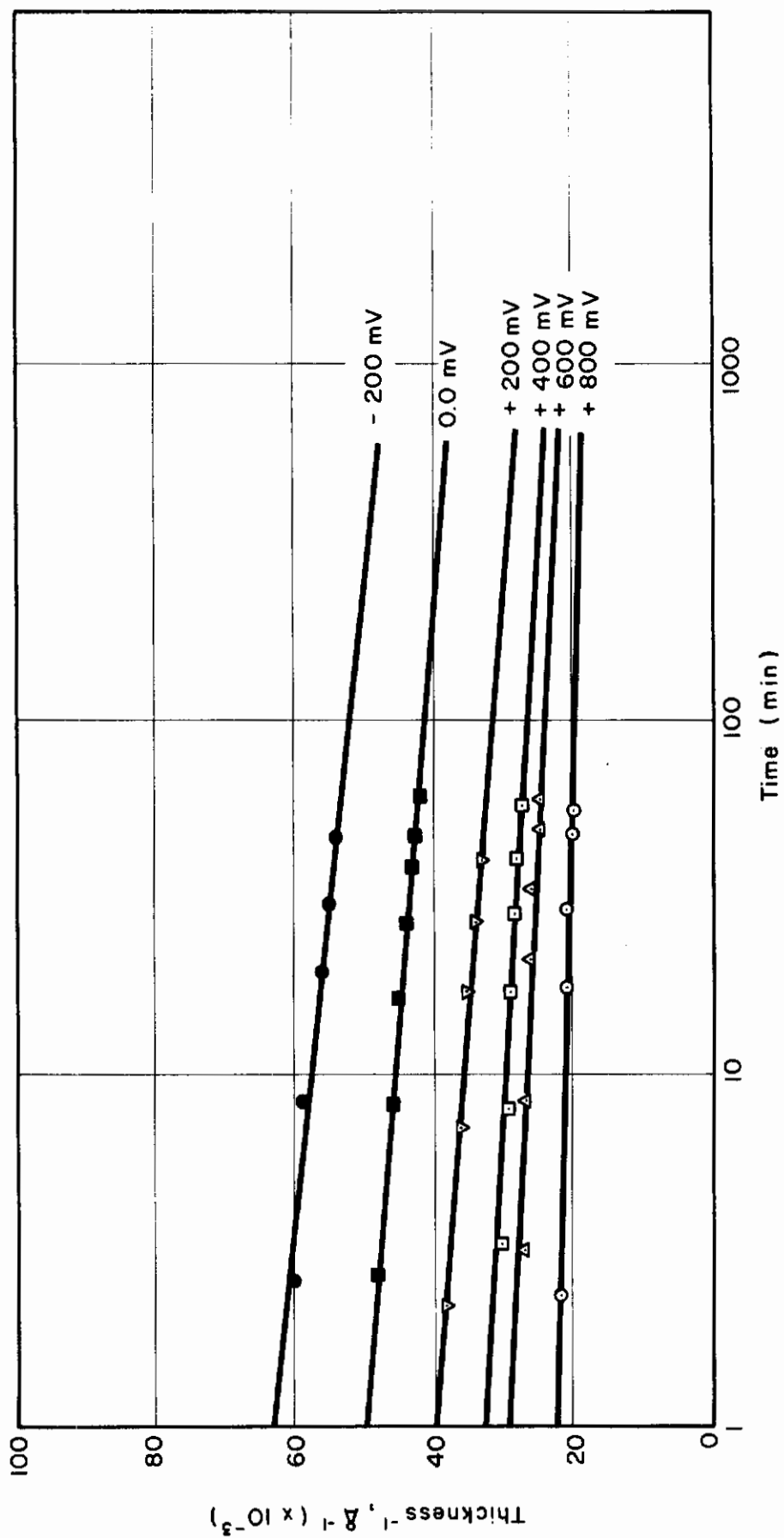


Fig. 96 - Plot of Reciprocal of Film Thickness vs. Time for Fe in Solution pH 8.41

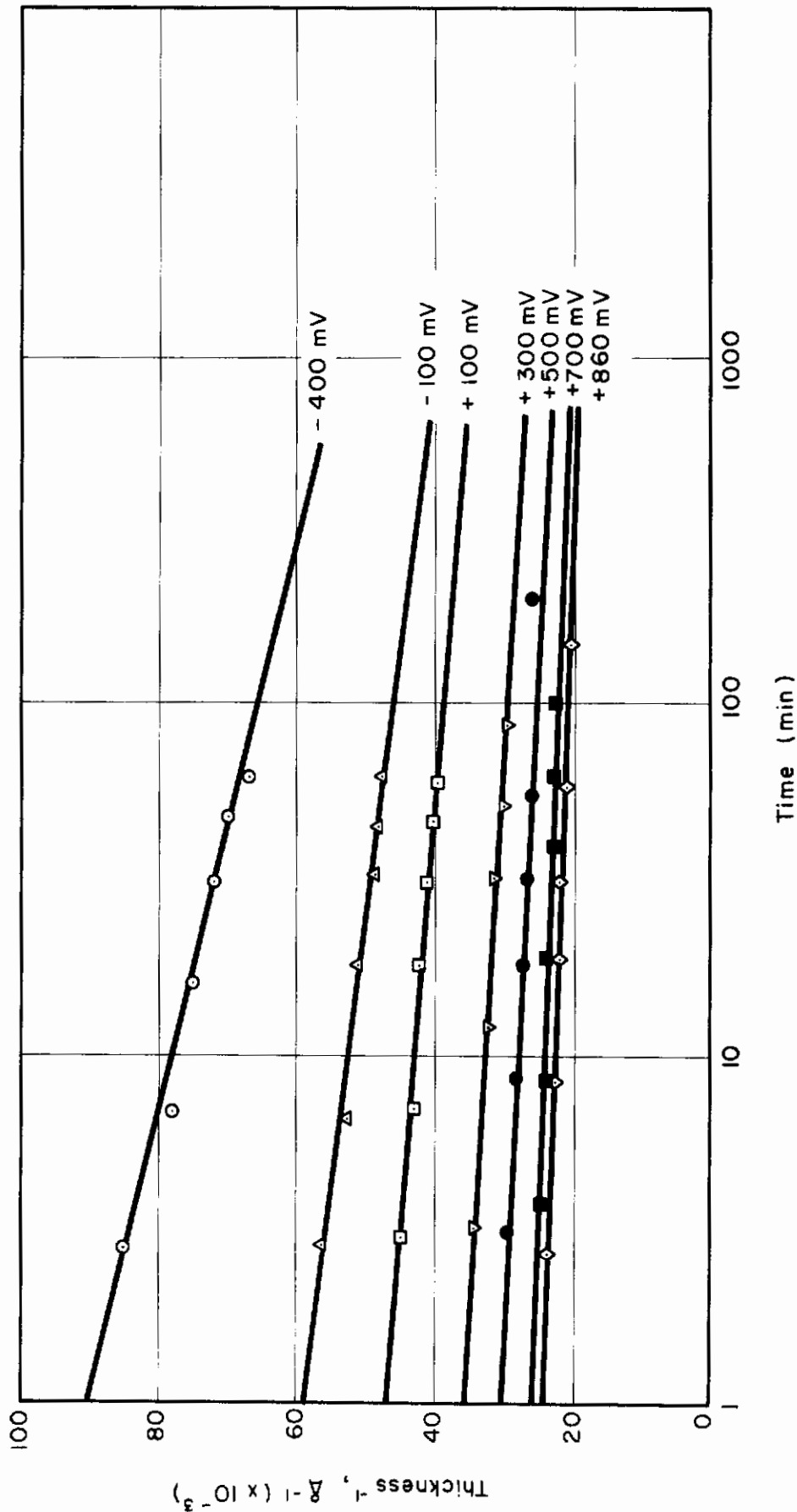


Fig. 97 - Plot of Reciprocal of Film Thickness vs. Log Time for Fe-10 Cr in Solution of pH 8.41

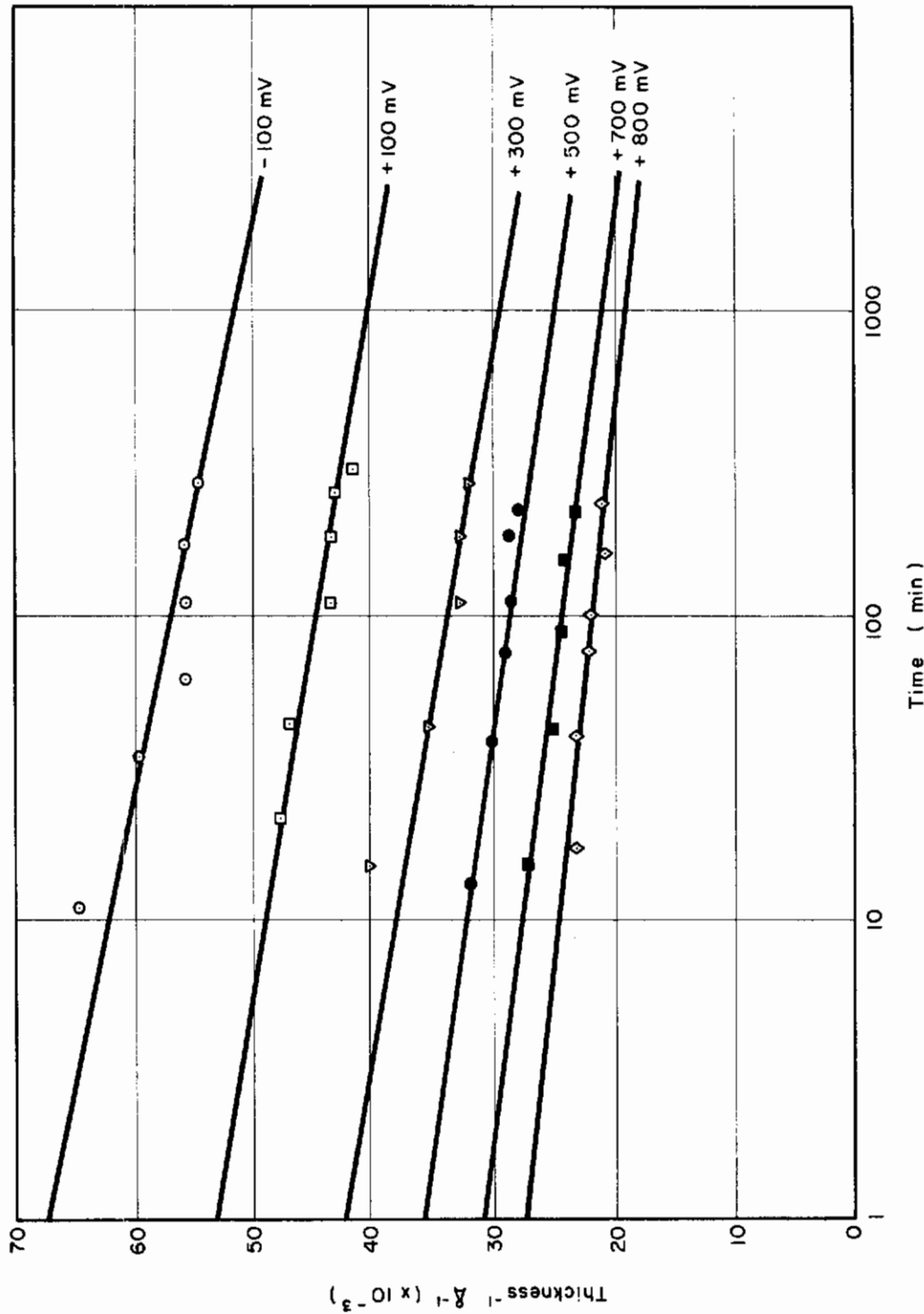


Fig. 98 - Plot of Reciprocal of Film Thickness vs. Log Time for Fe-10 Cr in Solution of pH 8.41

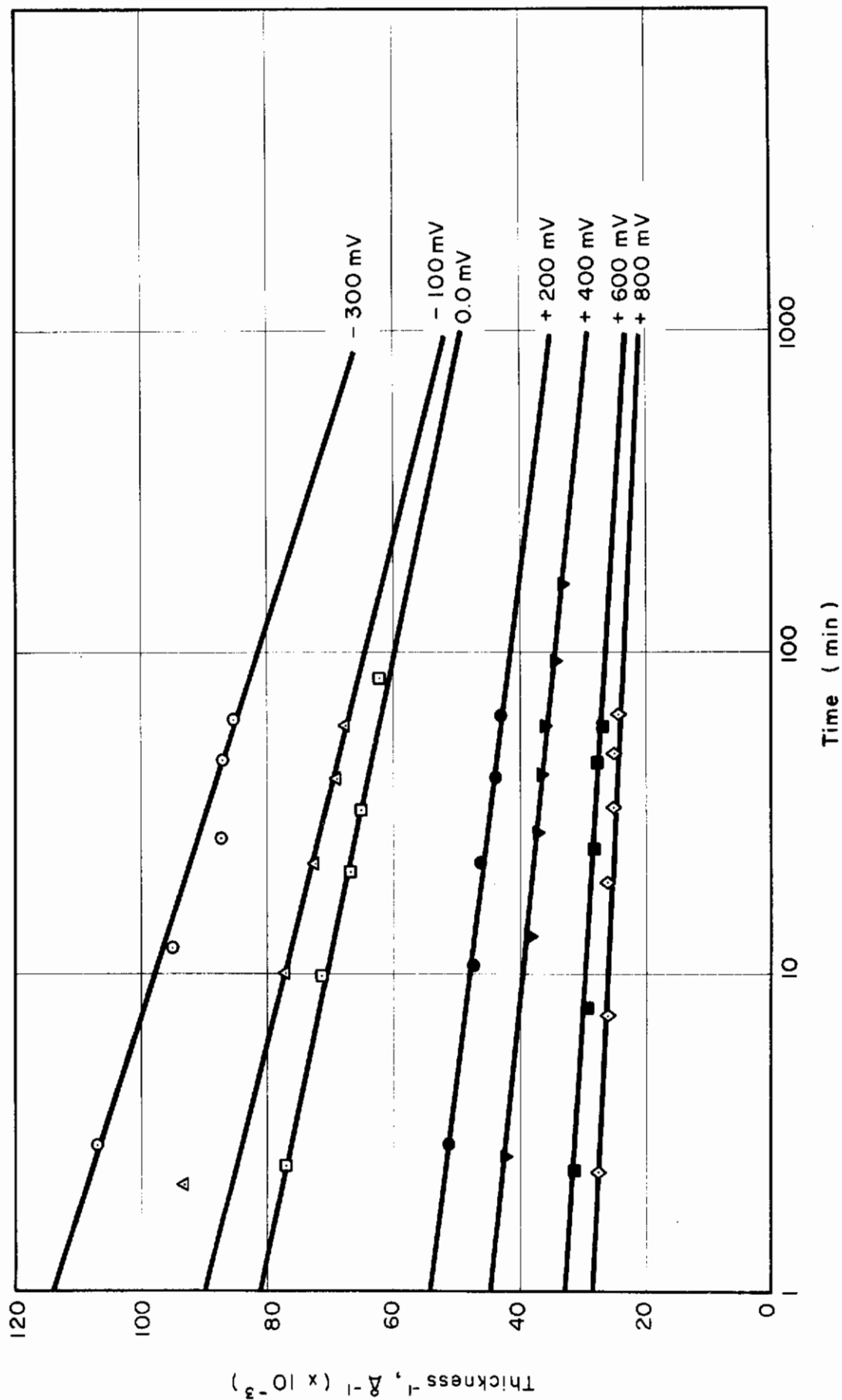


Fig. 99 - Plot of Reciprocal Film Thickness vs. Log Time for Fe-10 Cr-10 Ni in Solution of pH 8.41

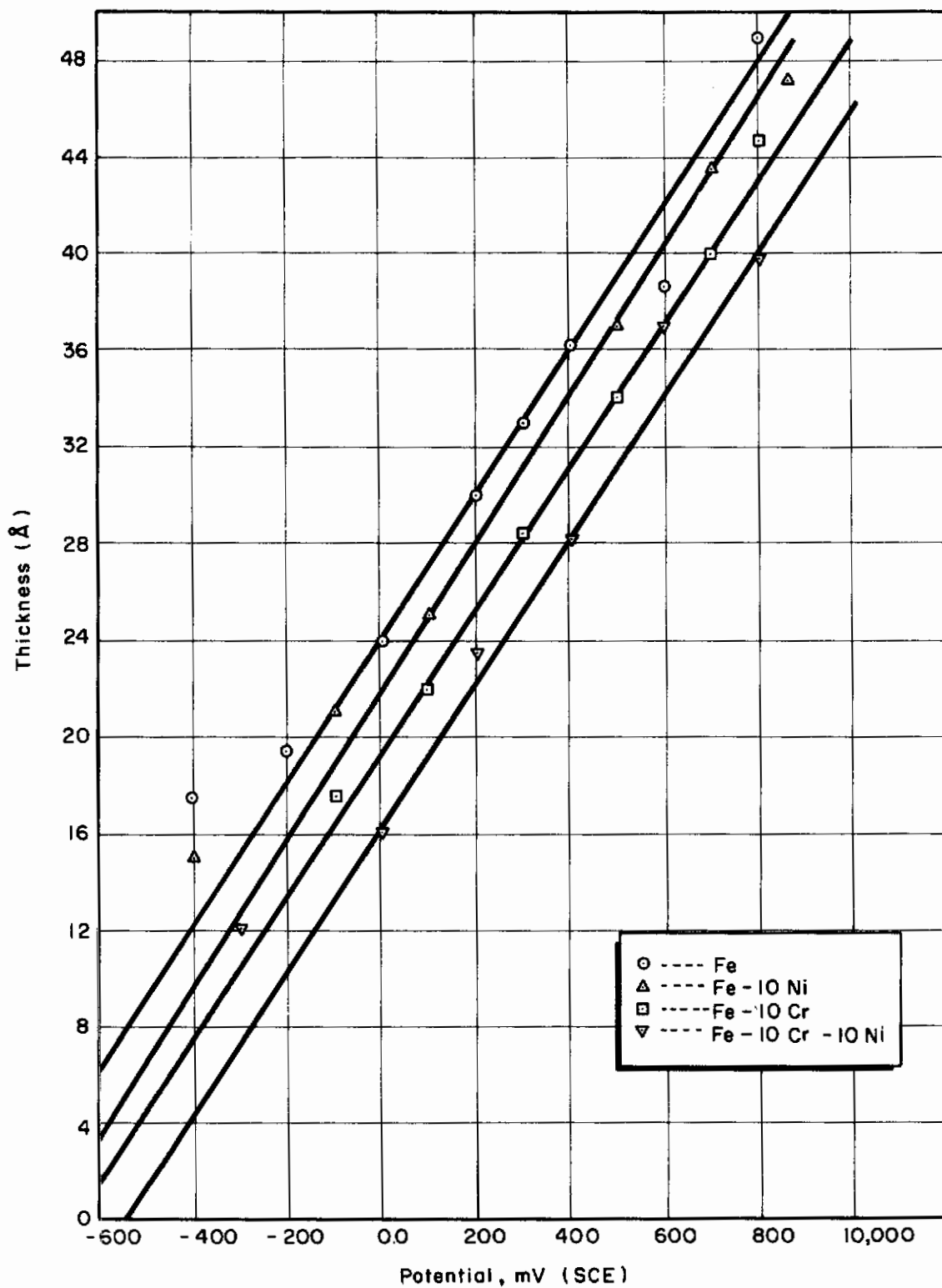


Fig. 100 - Film Thickness vs. Potential for One Hour Polarization

Table XIV - Comparison of the Change of Film Thickness of Fe, Fe-10Ni, Fe-10Cr, and Fe-10Cr-10Ni Alloys for one Hour of Polarization

Potential [mV(SCE)]	Fe	Thickness (Å)		
		Fe-10Ni	Fe-10Cr	Fe-10Cr-10Ni
-200	18.30	15.90	13.60	10.40
0.00	24.20	22.0	19.50	16.30
200	30.20	28.20	25.40	22.30
400	36.10	34.30	31.30	28.20
600	42.00	40.40	37.20	34.20
800	48.00	46.50	43.10	40.10

H. ELECTROCHEMICAL PROCESSES ABOVE 25°C (R. Cowan)

1. Background and Objectives of Current Work

The purpose of this work is to develop and apply techniques for measuring electrochemical kinetic properties at temperatures above 25°C in aqueous solutions. In addition, theoretical calculations of the ranges of thermodynamic stability of elements and their compounds as a function of temperature, pH, and electrochemical potential are being made. These calculations will then in turn be used to interpret the kinetic data.

The present scope of this research is to determine the temperature dependence of the kinetic behavior of Ni 270 (99.93%) in the acid range of pH. Emphasis is being placed on understanding changes in cathodic reduction kinetics and the breakdown of passivity at elevated temperatures.

2. Thermodynamic Stability

A series of recent papers³⁹⁻⁴¹ by Cobble et al. has shown a method for determining the Gibbs free-energy change as a function of temperature for reactions with ionic species included in the reactant and/or products. This type of calculation has been impossible for most types of electrochemical reactions because there are no data available for the heat capacity of most ionic species. Recently Townsend⁴² has used their method to calculate potential-pH diagrams of ions in the 25°C to 200°C range.

The free-energy change of a reaction at temperature, T, can be related to a reference temperature (i.e., 298°C) by

Table XV - Summary of Entropy Constants for Eq. (6) (in cal mole⁻¹deg⁻¹)

t°C	Simple Cations		Simple Anions and OH ⁻		Oxy Anions, XO _n ^{-m}		Acid Oxy Anions, XO _n (OH) _i ^{-m}		Std. State (entropy of H ⁺ (aq))
	a(i)	b(i)	a(i)	b(i)	a(i)	b(i)	a(i)	b(i)	
25	0	1.000	0	1.000	0	1.000	0	1.000	-5.0
80	3.9	0.955	-5.1	0.969	-14.0	1.217	-13.5	1.380	-2.5
100	10.3	0.876	-13.0	1.000	-31.0	1.476	-30.3	1.894	2.0
150	16.2	0.792	-21.3	0.989	-46.4	1.687	-50.0	2.381	6.5
200	23.3	0.711	30.2	0.981	-67.0	2.020	-70.0	2.960	11.1
200	23.3	0.630	-30.2	0.981	-67.0	2.020	-70.0	2.960	11.1
250	29.9	0.548	-38.7	0.978	-86.5	2.320	-90.0	3.530	16.1
300	36.6		-49.2	0.972	-106	2.618			20.7

$$\Delta F_{T_2}^O - \Delta F_{T_1}^O = \Delta H_{T_2}^O - T_2 \Delta S_{T_2}^O - \Delta H_{T_1}^O + T_1 \Delta S_{T_1}^O, \quad (4)$$

$$\Delta F_{T_2}^O - \Delta F_{T_1}^O = \Delta H_{T_1}^O + \int_{T_1}^{T_2} \Delta C_p dT - T_2 \Delta S_{T_1}^O - T_2 \int_{T_1}^{T_2} \frac{\Delta C_p}{T} dT - \Delta H_{T_1}^O + T_1 \Delta S_{T_1}^O, \text{ and} \quad (5)$$

$$\Delta F_{T_2}^O = \Delta F_{T_1}^O - (T_2 - T_1) \Delta S_{T_1}^O + \int_{T_1}^{T_2} \Delta C_p dT - T_2 \int_{T_1}^{T_2} \frac{\Delta C_p}{T} dT, \quad (6)$$

where

$$\Delta C_p = \sum_{\text{products}} \nu_i C_{pi} - \sum_{\text{reactants}} \nu_i C_{ri}.$$

One can define the average value of the heat capacity over a temperature range as

$$\bar{C}_p \Big|_{T_1}^{T_2} = \frac{\int_{T_1}^{T_2} C_p dT}{\int_{T_1}^{T_2} dT} \cong \frac{\int_{T_1}^{T_2} C_p d \ln T}{\int_{T_1}^{T_2} d \ln T} \quad (7)$$

The far right-hand side of Eq. (7) is an approximation that is valid within experimental error over temperature ranges of 175°C. Substituting the above equation into Eq. (6) we obtain this result:

$$\Delta F_{T_2}^O = \Delta F_{T_1}^O - \Delta T \Delta S_{T_1}^O + \Delta C_p \Big|_{T_1}^{T_2} \left[\bar{T} - T_2 \ln \frac{T_2}{T_1} \right], \quad (8)$$

where

$$\Delta C_p \Big|_{T_1}^{T_2} = \sum_{\text{products}} \nu_i C_{pi} \Big|_{T_1}^{T_2} - \sum_{\text{reactants}} \nu_i C_{ri} \Big|_{T_1}^{T_2}.$$

For most condensed liquid and gaseous phases the heat capacity and entropy data are readily available in thermochemical handbooks. However, for ionic species the only available data is S_{298}^O . It is Criss and

Cobble's^{40,41} unique method of determining $S_{T_2}^O$ and $\bar{C}_p \Big|_{T_1}^{T_2}$ that makes calculation of Eq. (8) possible.

Criss and Cobble have determined a correspondence principle between the entropy of an ion at 25°C and the entropy of the same ion at an elevated temperature that follows the relation

$$S_{T_2}^{\circ} = a_{T_2} + b_{T_2} \bar{S}^{\circ}(25)_{\text{abs. scale}} \quad (9)$$

In electrochemistry the entropy of hydrogen is artificially assigned an entropy of $S_{H^+}^{\circ} \equiv 0$. Chris and Cobble have determined the absolute entropy of H^+ as $S_{\text{abs}}^{\circ}(H^+) = -5.0$ at 25°C . By trial and error they have found values of $S_{\text{abs}}^{\circ}(H^+)$ at elevated temperatures that make all ions of a certain class give a linear dependence to their entropies at 25°C . In this manner the constants a_{T_2} and b_{T_2} have been determined for each class of ion for different temperatures. In order to use Eq. (9) the entropies from the literature must be put on the absolute scale by the following equation:

$$S_{\text{abs}}^{\circ}(25) = S^{\circ}(25) - 5Z, \quad (10)$$

where Z is the ionic charge. Thus, with the correspondence method it is possible to determine the entropy of any ion at the temperature of interest if the entropy is accurately known at 25°C . A listing of the a and b coefficients is shown in Table XV.

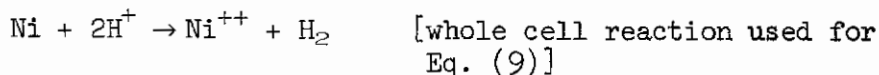
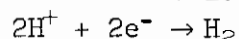
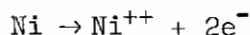
To evaluate Eq. (9) it is also necessary to know the average value of the heat capacity of the ions in question over the range of temperature in question, $\bar{C}_p|_{T_1}^{T_2}$. This is easily calculated for the temperature range 25°C to 200°C by the following equation:

$$\bar{C}_p|_{25}^{T_2} = \frac{\bar{S}^{\circ}(+2) - S^{\circ}(25)}{\ln T_2/298}$$

For temperatures greater than 200°C , Eq. (9) is evaluated for each temperature increment of 50°C using 200°C as T_1 , etc.

Using this method of calculation, we are determining the potential-pH diagrams of the Ni- H_2O system at temperatures to 300°C . Unfortunately, there are no $S^{\circ}(25)$ or C_p data available for Ni_2O_3 , Ni_3O_4 , or NiO_2 , which are stable only in aqueous solutions. However, data are available for Co_2O_3 , Fe_3O_4 , and MnO_2 . Since these compounds have the same crystal structure as the corresponding Ni oxides and because Co, Fe, and Mn are close to Ni in the periodic table, the $S^{\circ}(25)$ and C_p values of these compounds will be assigned to the corresponding NiO. Preliminary calculations show that there is a marked temperature dependence of the potential-pH diagram of Ni.

It should be noted that when calculating free energies from Eq. (8), the whole cell reaction should be used with $2H^+ + 2e^- \rightarrow H_2$ as the oxidation half-cell reaction. For an example we can use the Ni/ Ni^{++} equilibrium.



In this manner, the reference reaction at each temperature is the standard hydrogen electrode with $E^{\circ} = 0.000$ at every temperature. The standard free-energy charges are determined and potential-pH diagrams are constructed in the usual manner.

3. Kinetic Experiments

The experimental apparatus for the potentiostatic and potentiokinetic polarization experiments on Ni 270 was described in the previous report of this series. The apparatus is working nicely and experimentation on the electrode kinetics of Ni 270 is well under way.

The polarization behavior of Ni 270 is being studied in three different acidic pH's over the temperature range 25°C to 300°C. The environmental solutions are made of triple-distilled water, reagent grade H_2SO_4 , and reagent grade K_2SO_4 and has an ionic strength of 0.1N. Their compositions are

pH 1.3	0.05N H_2SO_4	0.05N K_2SO_4
pH 3.4	0.001N H_2SO_4	0.099N K_2SO_4
pH 6.4	---	0.1N K_2SO_4

Before testing the Ni samples are degreased and ground successively with 240-, 400-, and 600-grit abrasive paper. After the specimen is introduced into the autoclave, the solution is deaerated and saturated with hydrogen by bubbling for 12 hours. Tests are then made after the cell has reached the test temperature for one hour. The hydrogen redox potential, corrosion potential, and cell pressure are recorded before and at pertinent times during the test. The temperature inside the cell is monitored continuously. A test at a given temperature consists of three potentiostatic scans at a rate of 2000 mV/hr in the following order:

1. Measurement of $E(\text{H}^{+}/\text{H}_2)$ and E_{corr}
2. Noble-to-active anodic scan from $E_{\text{corr}} + 2000$ mV to E
3. One half-hour pause, then measurements of $E(\text{H}^{+}/\text{H}_2)$ and E_{corr}
4. Cathodic scan from E_{corr} to $E_{\text{corr}} - 600$ mV
5. One half-hour pause, the measurements of $E(\text{H}^{+}/\text{H}_2)$ and E_{corr}

6. Active-to-noble anodic scan from E_{corr} to +2000 mV
7. Measurement of $E(\text{H}^+/\text{H}_2)$

A new sample is used for each test at each pH and temperature combination.

In Fig. 101 is a comparison of an active-to-noble scan determined in a glass cell and the autoclave at 25°C on two different samples. The agreement is well within reproducibility limits on an overpotential basis. However, on the absolute potential scale as plotted in Fig. 101, it can be seen that the autoclave curve is shifted slightly in the noble direction. This phenomenon is due to streaming or membrane potentials produced in the salt bridge caused by the overpressure of nitrogen in the autoclave. This overpressure is required at low temperature to wet the salt bridge. This effect will be studied in the near future so that measured potentials can be adjusted to their real values. In Fig. 102, the cathodic reduction kinetics at pH 1.3 are plotted. The hydrogen reaction shows activation (Tafel) behavior followed by diffusion effects at temperatures to 100°C. Above this temperature the reaction shows a predominance of diffusion and possible resistance polarization. In Fig. 103 the noble-to-active scans are shown for pH 1.3. The salient feature of these curves is the absence of passivity at temperature above 100°C. These curves can be contrasted with Figs. 104 and 105 in which the noble-to-active scans for pH 1.3 from 25°C to 300°C are shown. Again, passivity is absent above 100°C. At 300°C the curve shows a behavior that indicates some new reaction is occurring that was absent at low temperatures. In Figs. 106 and 107 the cathodic reduction curves for pH 3.4 are presented. They are interesting in the fact that two separate reduction reactions take place at 200°C. Above this temperature the reactions are masked by apparent diffusion control. In Figs 108 and 109 the noble-to-active anodic scans are shown for pH 3.4. At this pH remnants of passivity are seen at 150°C. Again at 300°C at noble potentials some sort of reaction is taking place that is different from that at the lower temperature. The active-to-noble scans at pH 3.4 in Figs. 110 and 111 again show passivity absent at temperatures above 100°C as did the corresponding curves for pH 1.3. In addition, the reaction kinetics reach a maximum at 200°C.

No attempt has yet been made to analyze in detail the data in Figs. 102-111, nor will it be made until the data from pH 6.4 are completed and the potential-pH diagrams are determined for the temperatures of interest. In addition, an examination of streaming potential and membrane potential will be made to incorporate their effects into the data. In Fig. 112 a plot of measured $E(\text{H}^+/\text{H}_2)$ and E_{corr} for both pH's as a function of temperature is shown. The saw-tooth nature of these curves indicates that there is probably much uncertainty in the relative behavior of the measured potential and the actual potential due to membrane, streaming, and thermal potentials. Figure 113 is an Arrhenius type plot of critical current and minimum passive current density at the two pH's

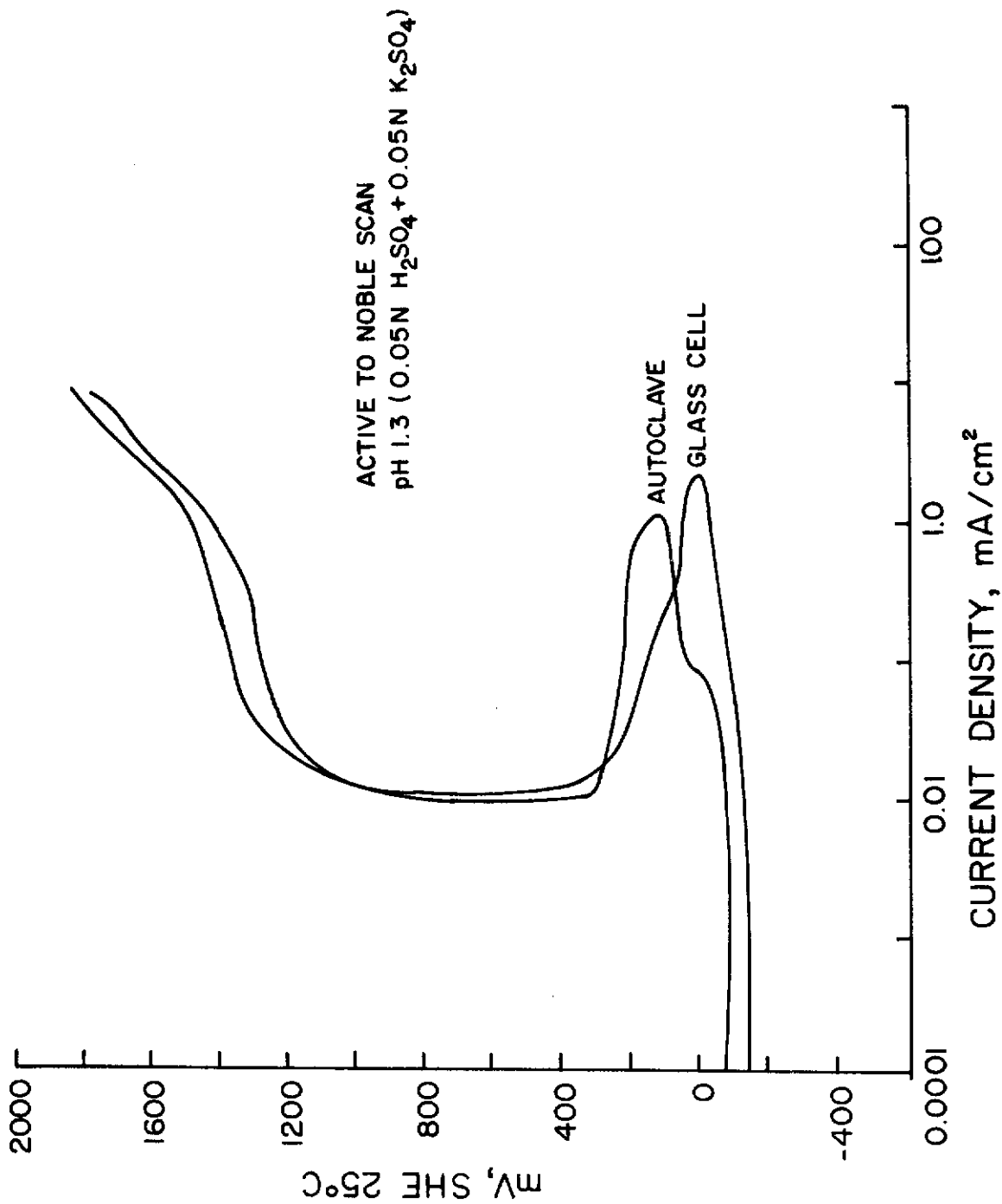


Fig. 101 - A Comparison of the Anodic Curve for Ni 270 at pH 1.3 Determined in a Standard Glass Polarization Cell and the Autoclave Cell at 25°C

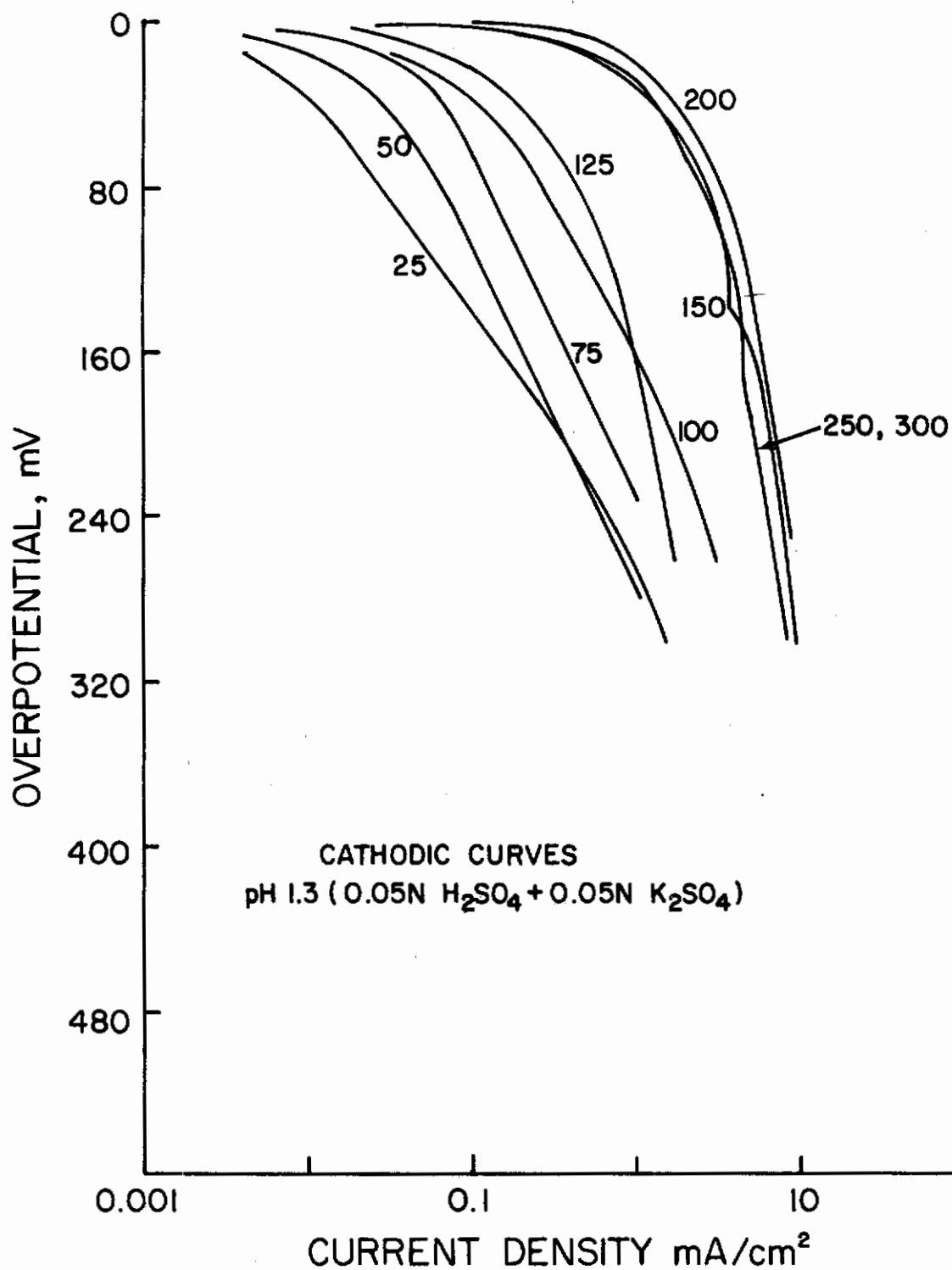


Fig. 102 - The Cathodic Reduction Curves of Ni 270 at pH 1.3 from 25°C to 300°C

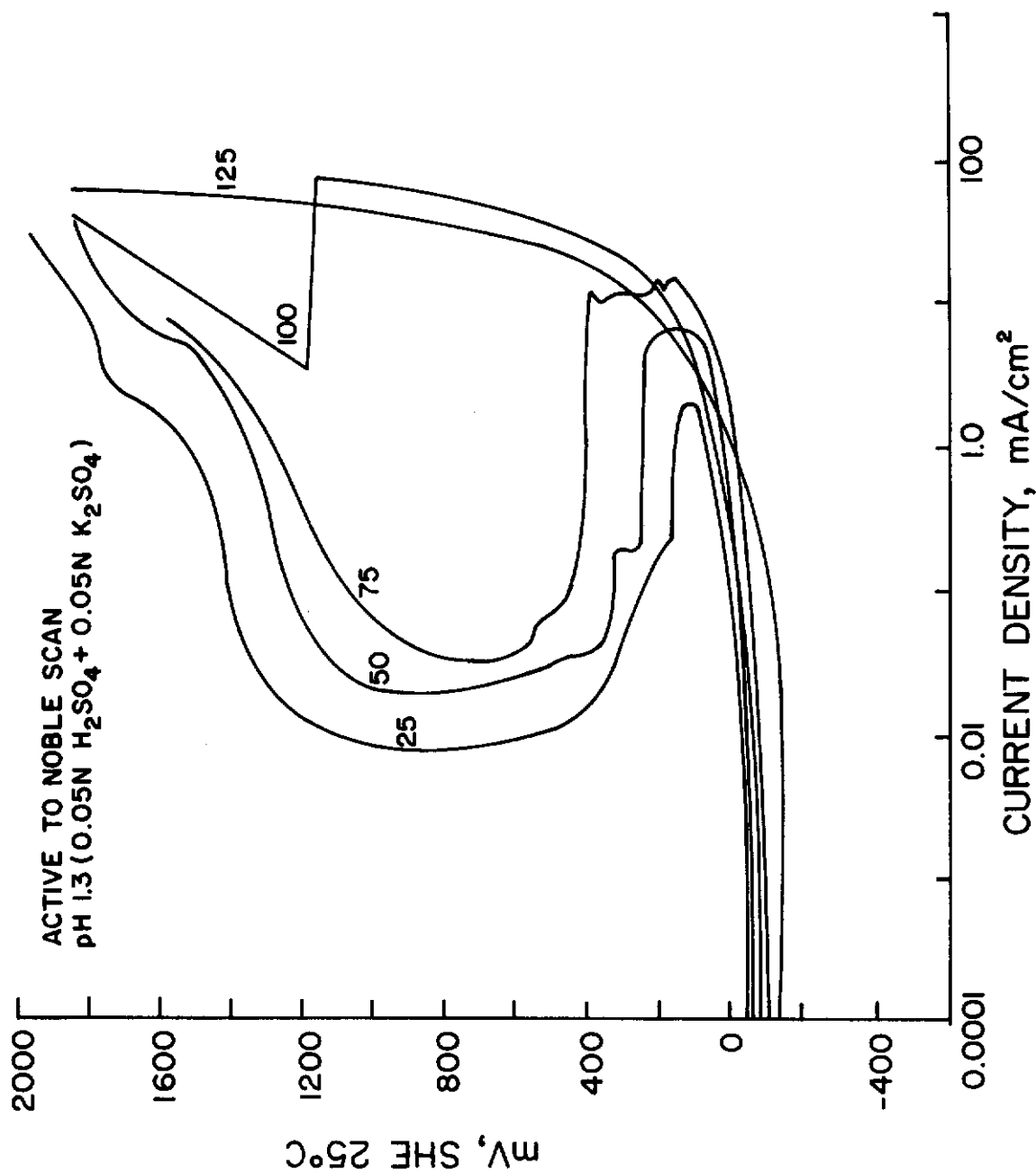


Fig. 103 - The Anodic Dissolution Curves for Ni 270 at pH 1.3 from 25°C to 125°C in the Active to Noble Scan Mode

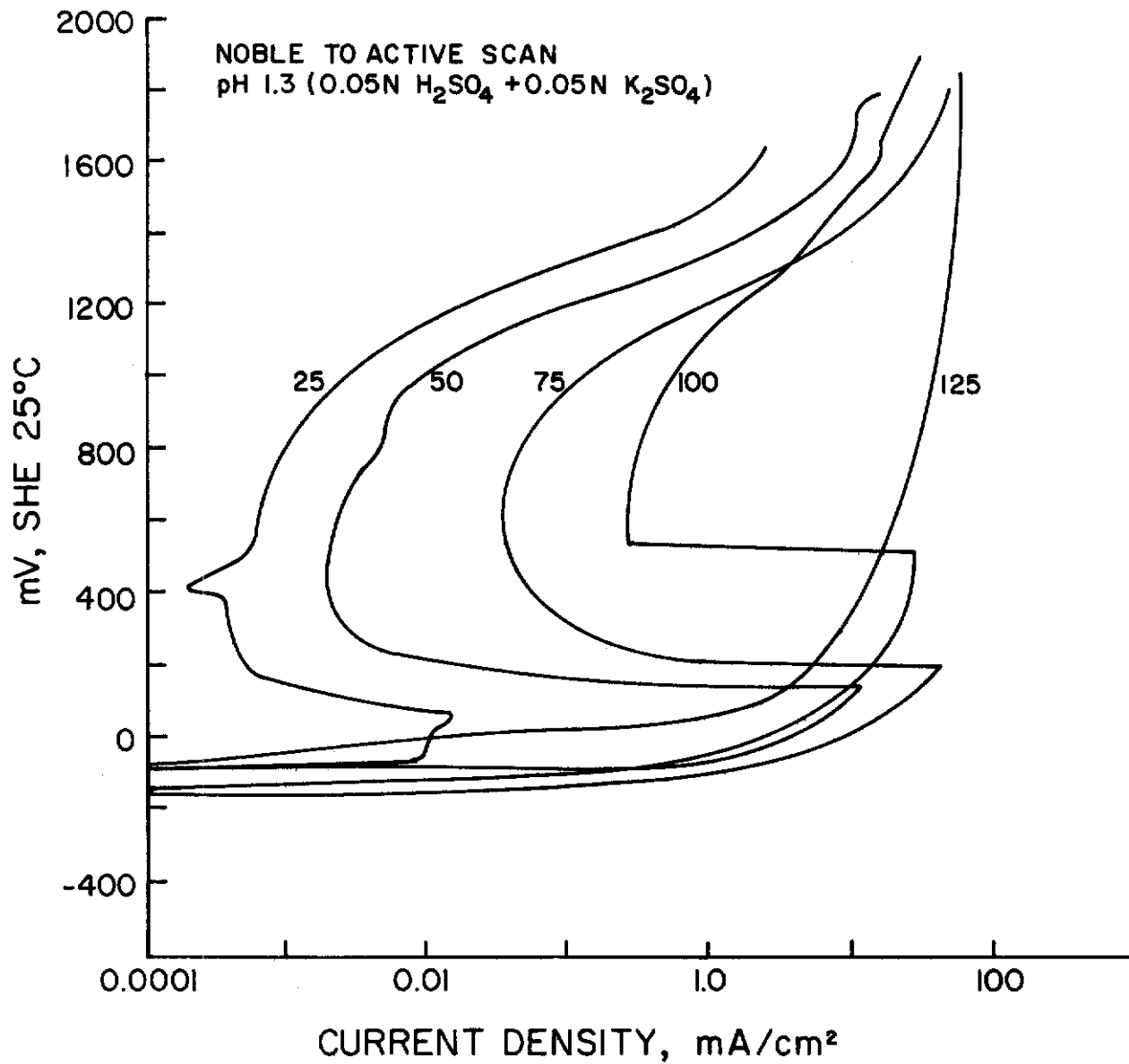


Fig. 104 - The Anodic Dissolution Curves for Ni 270 at pH 1.3 from 125°C to 300°C in the Active to Noble Scan Mode

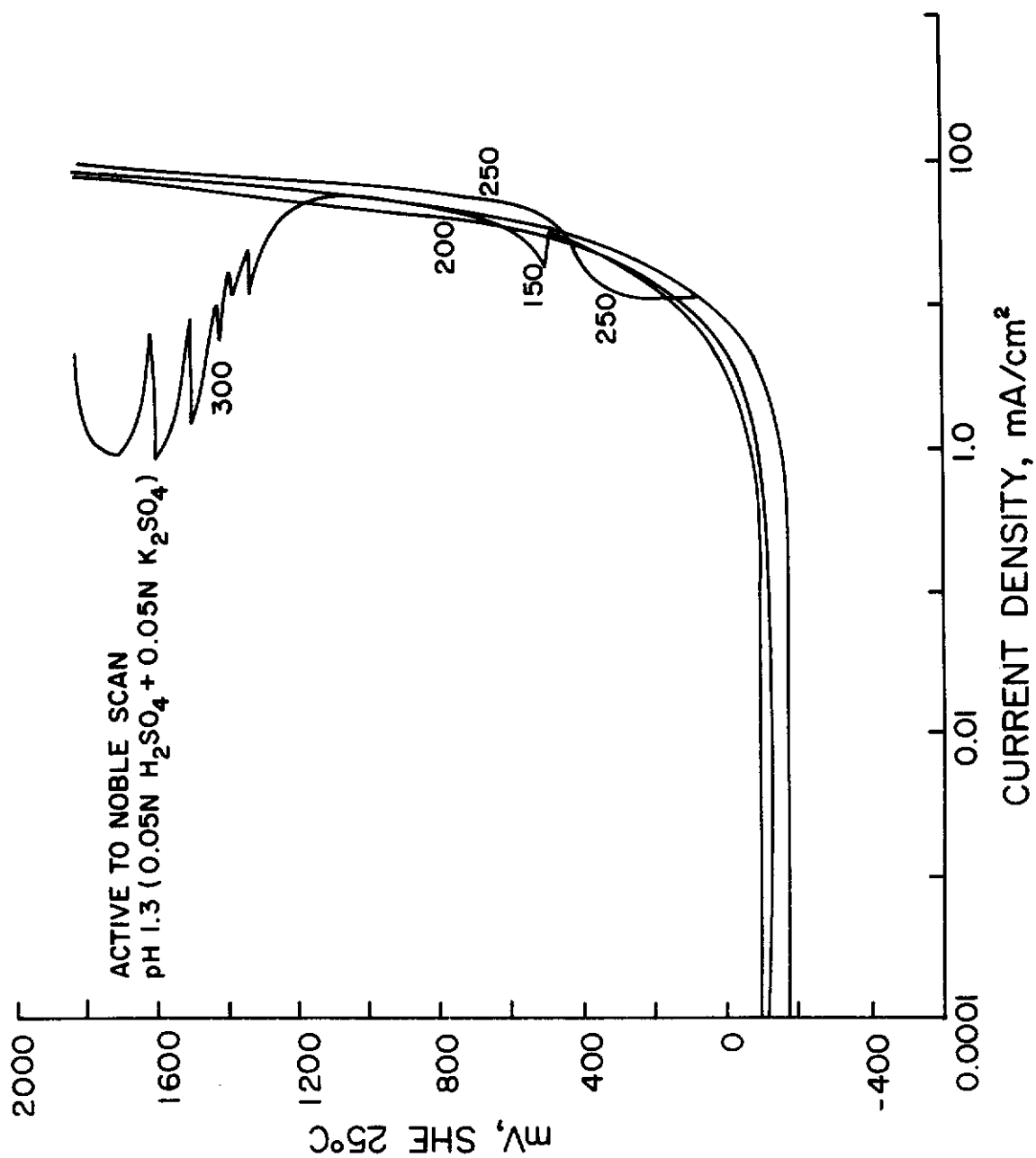


Fig. 105 - The Anodic Dissolution Curves for Ni 270 at pH 1.3 from 150°C to 300°C in the Active to Noble Scan Mode

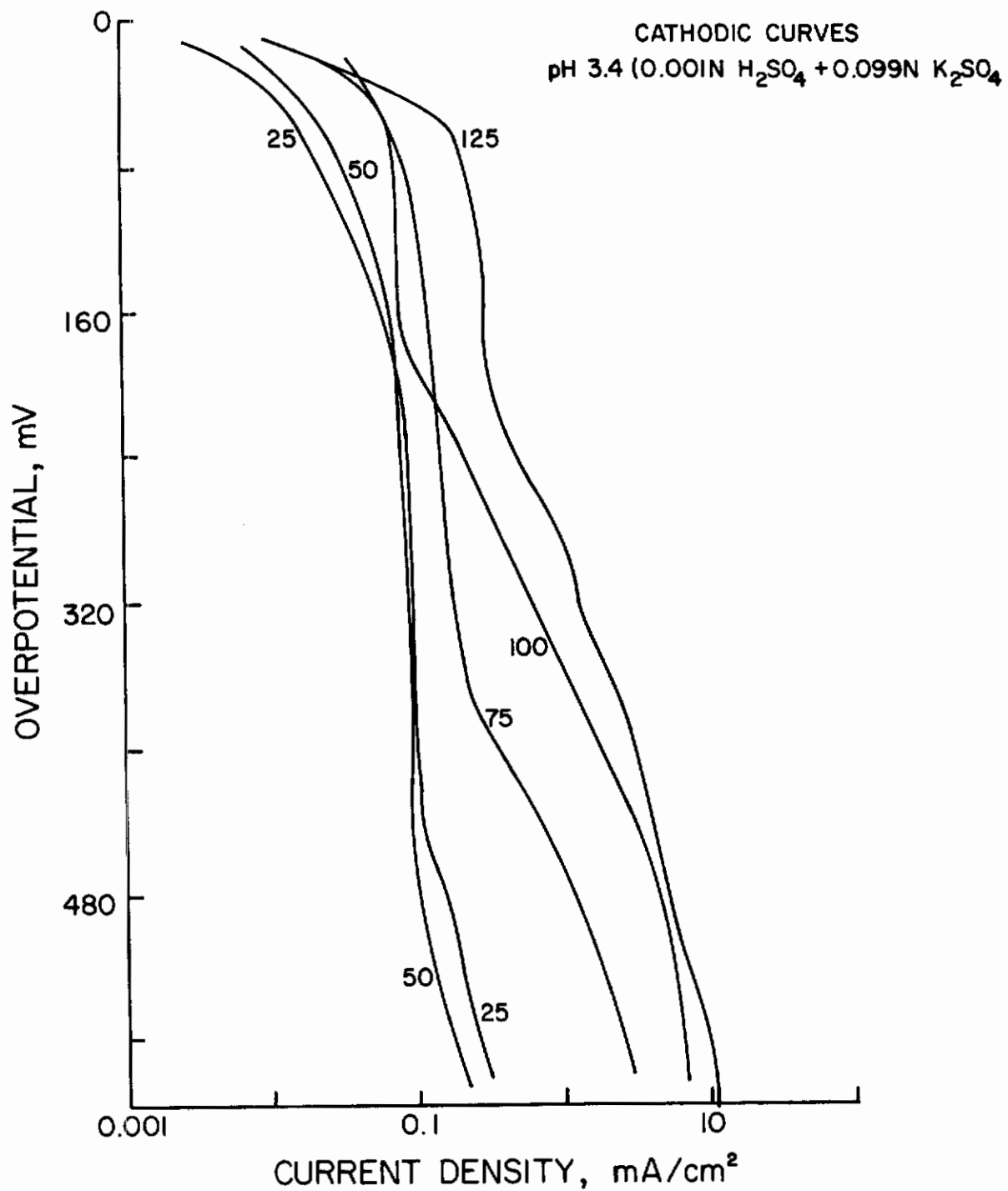


Fig. 106 - Cathodic Reduction Curves for Ni 270 at pH 3.4 from 25°C to 125°C

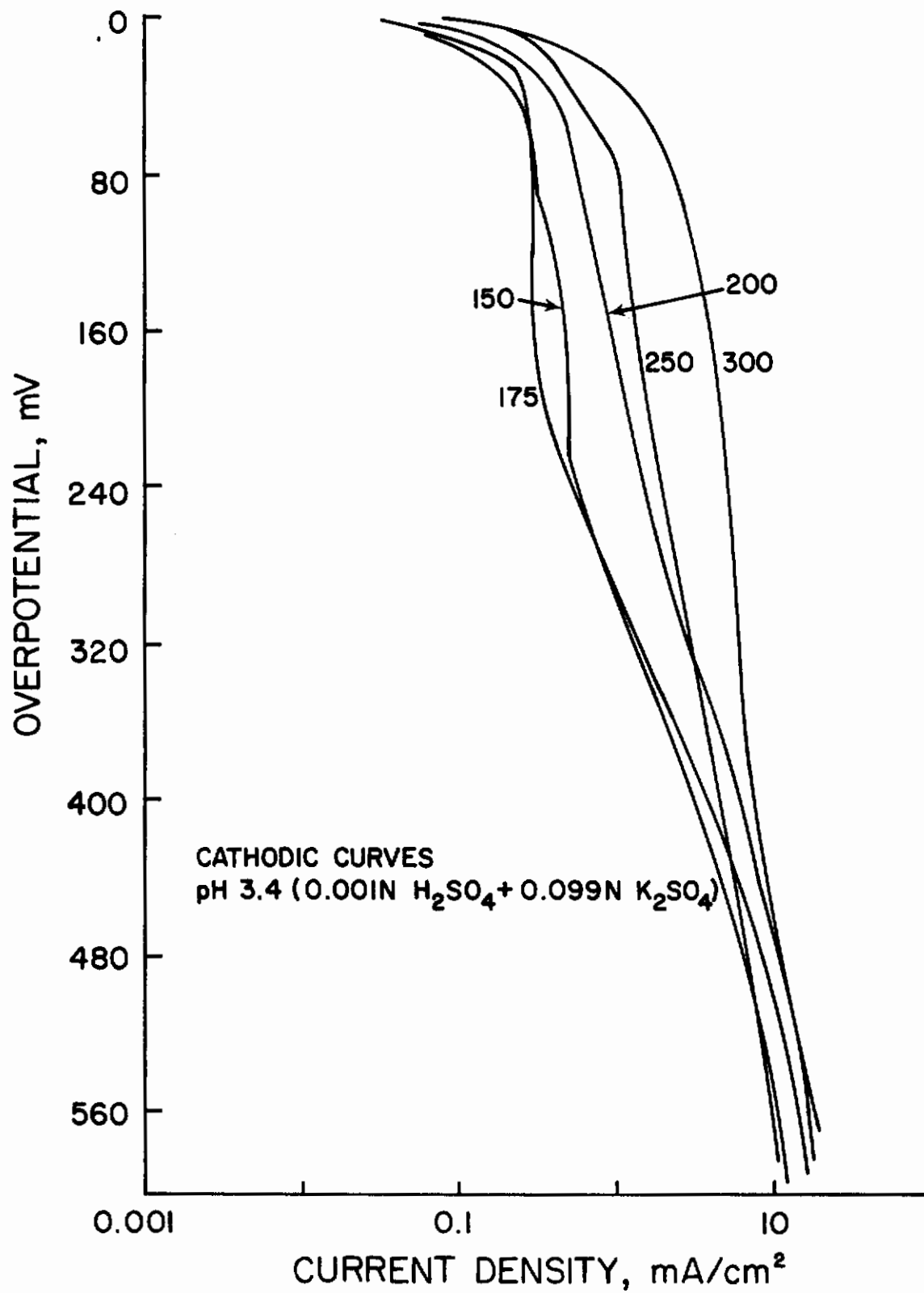


Fig. 107 - Cathodic Reduction Curves for Ni 270 at pH 3.4 from 150°C to 300°C

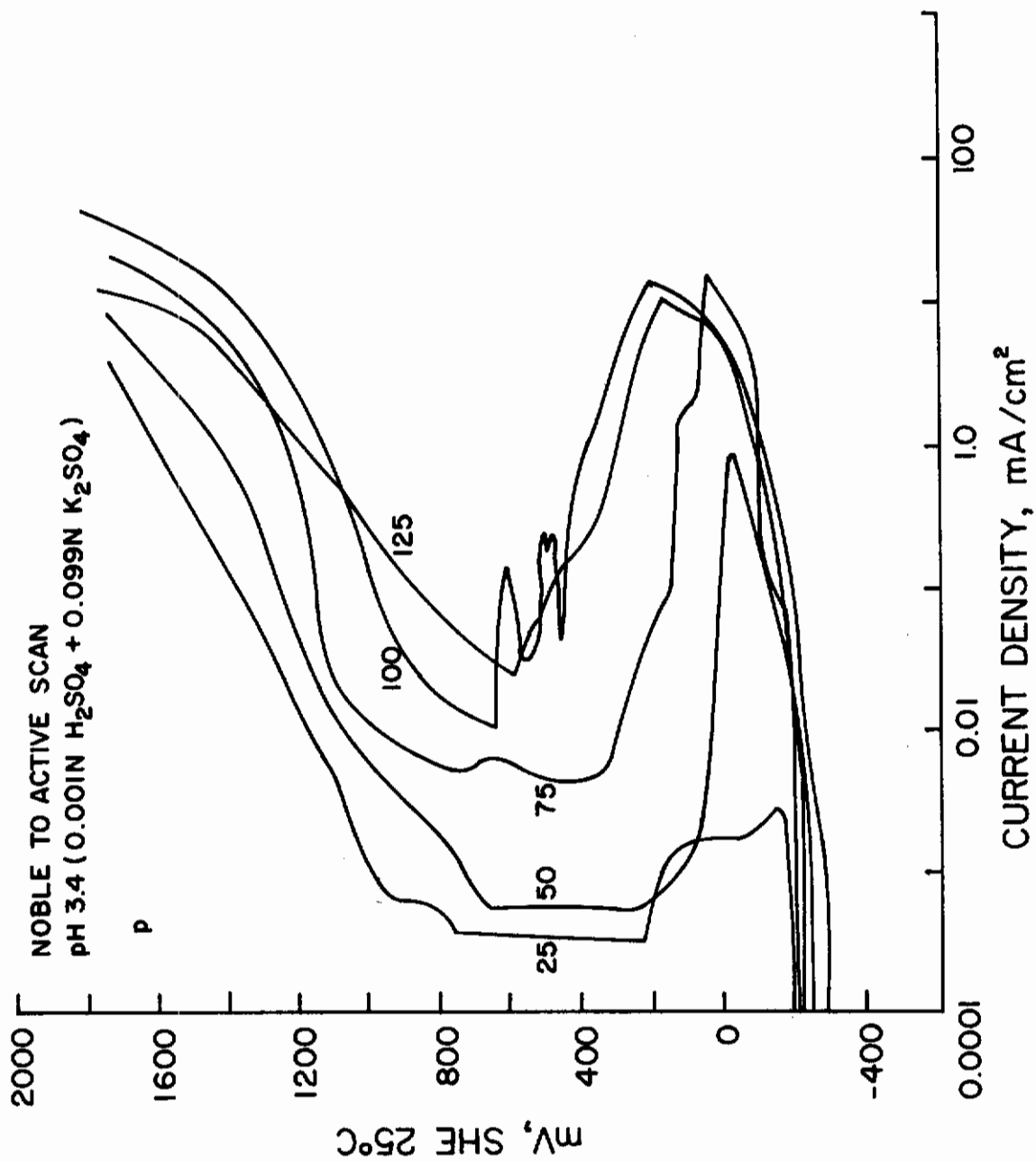


Fig. 108 - The Anodic Dissolution Curves for Ni 270 at pH 3.4 from 25°C to 125°C in the Noble to Active Scan Mode

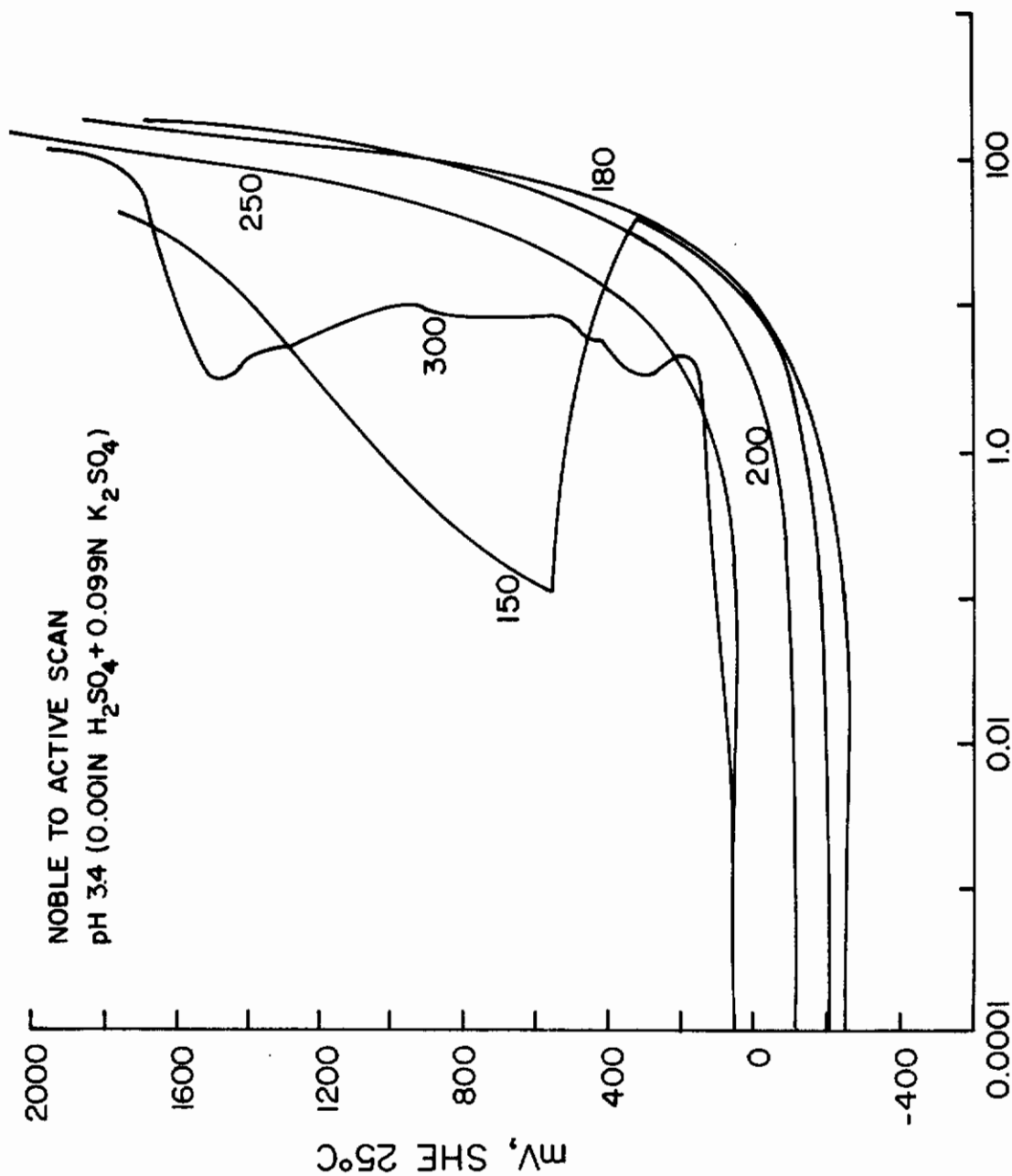


Fig. 109 - The Anodic Dissolution Curves for Ni 270 at pH 3.4 from 150°C to 300°C in the Noble to Active Scan Mode

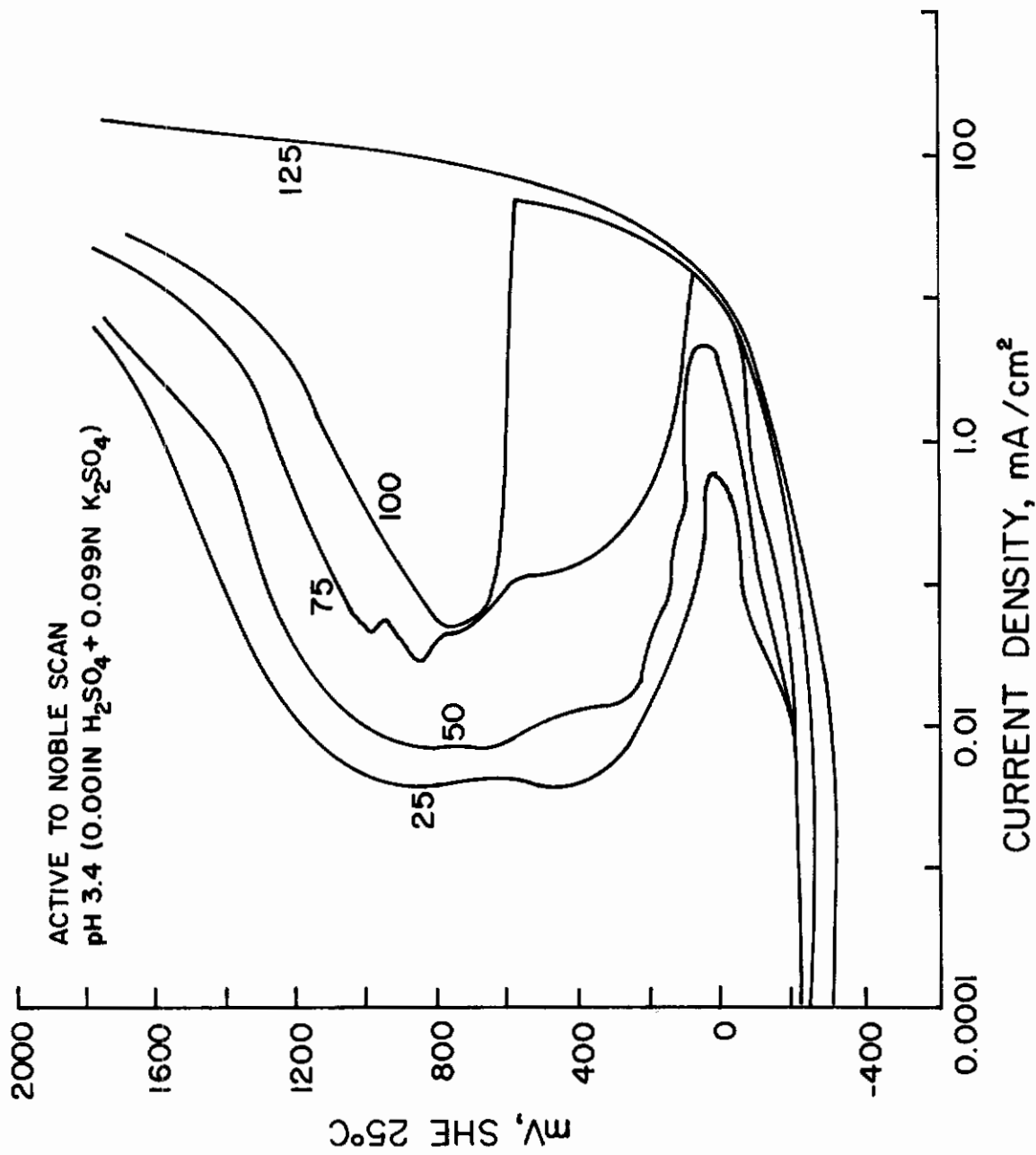


Fig. 110 - The Anodic Dissolution Curves for Ni 270 at pH 3.4 from 25°C to 125°C in the Noble to Active Scan Mode

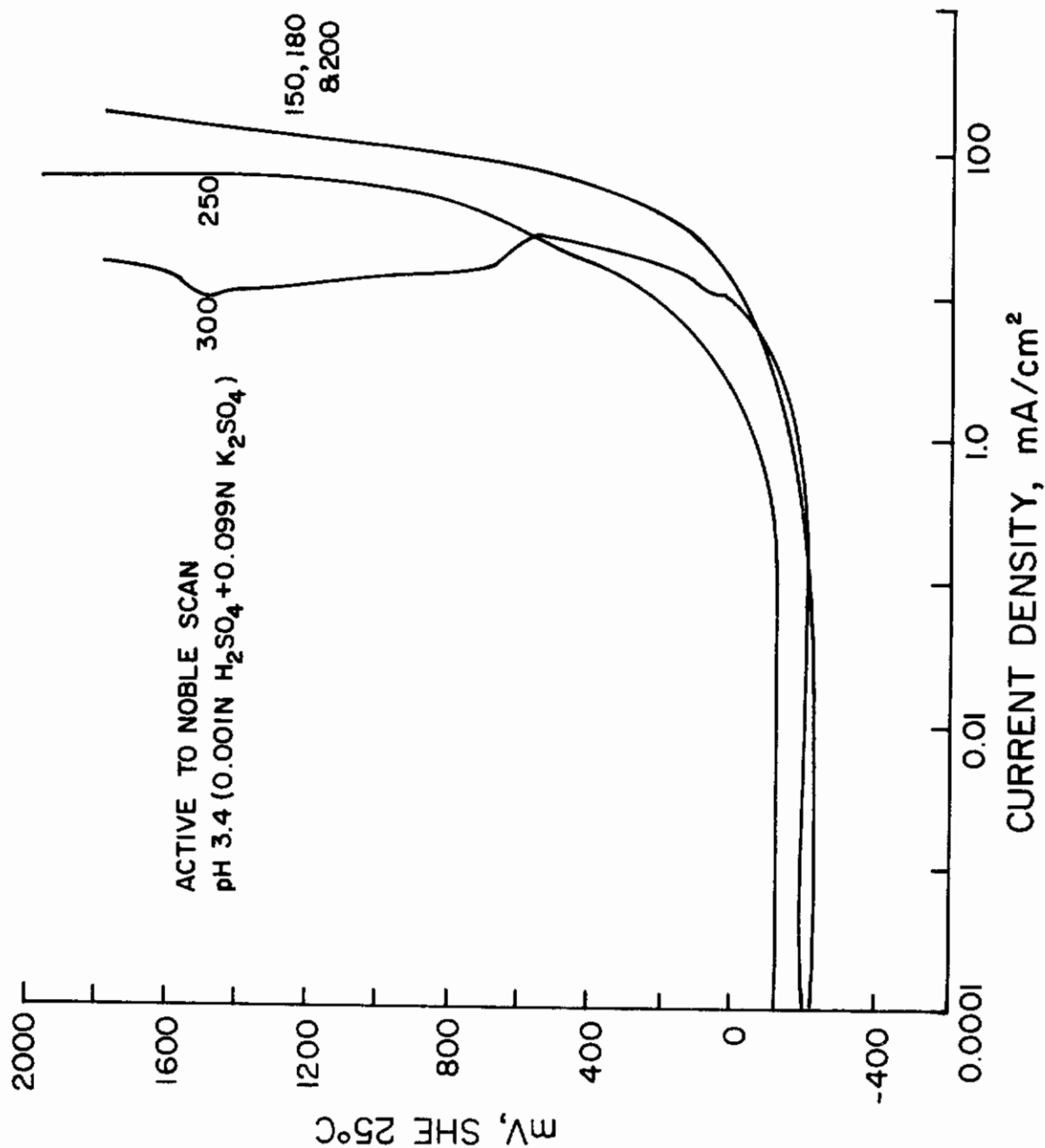


Fig. 111 - The Anodic Dissolution Curves of Ni 270 at pH 3.4 from 150°C to 300°C in the Active to Noble Scan Mode

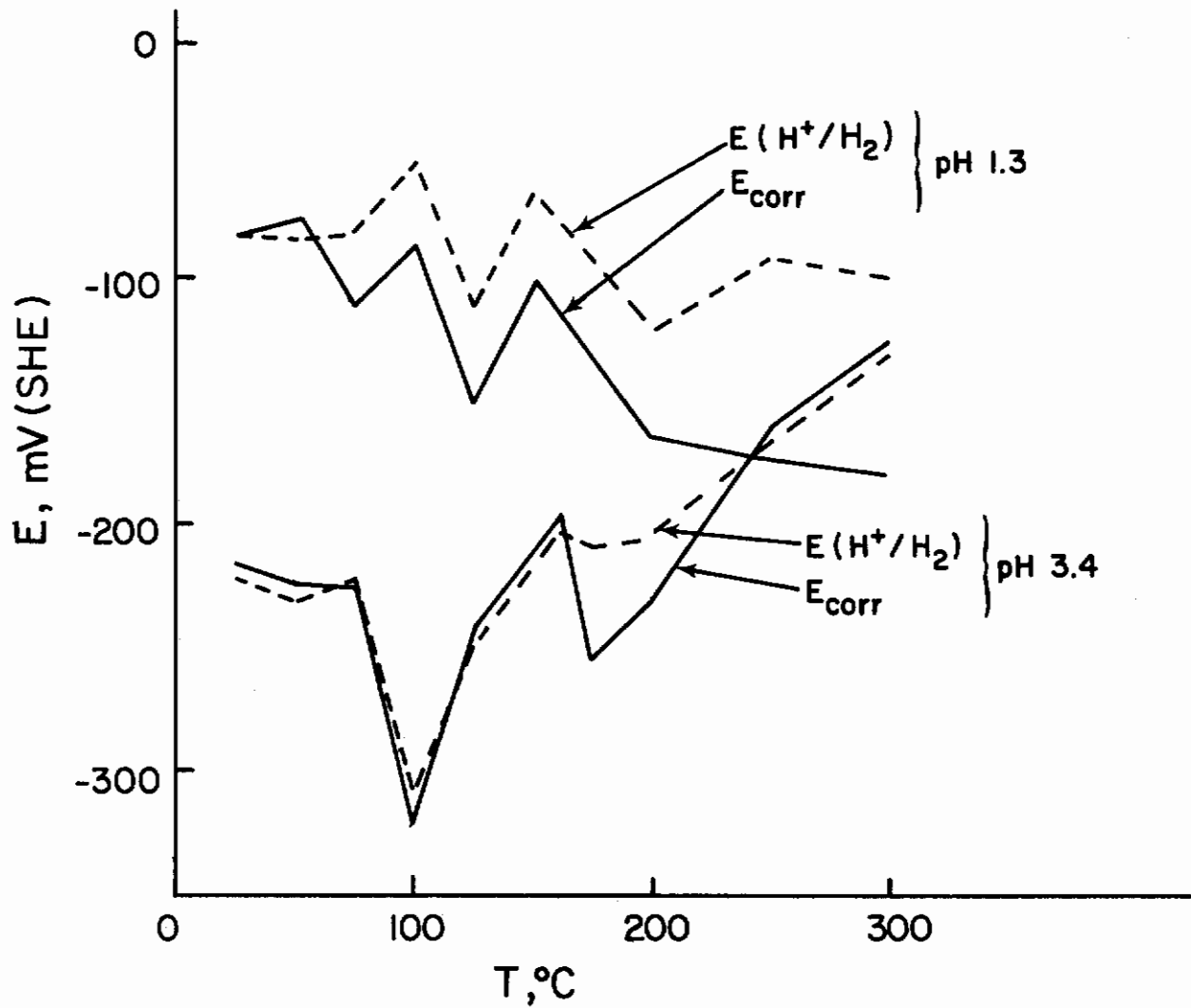


Fig. 112 - Variation of the Measured Hydrogen Redox Potential, $E(\text{H}^+/\text{H}_2)$ and the Corrosion Potential, E_{corr} with Temperature at pH 1.3 and pH 3.4

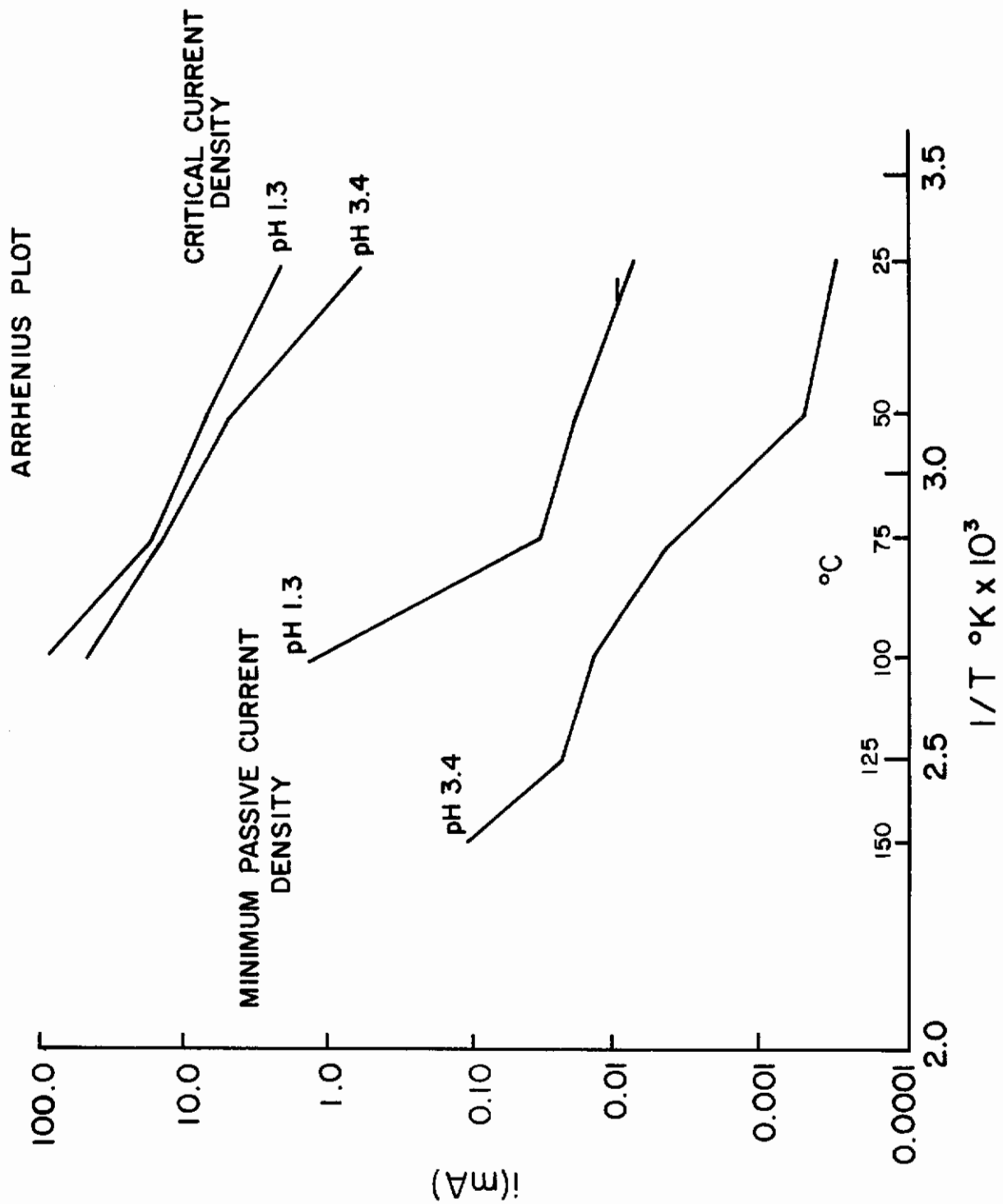


Fig. 113 - Arrhenius Plot of the Minimum Passive Current Density and the Critical Current Density at pH 1.3 and pH 3.4

SECTION IV

DELAYED FRACTURE OF HIGH STRENGTH STEELS
(G. Meyrick, J. P. Hirth and D. C. Langstaff)

A. INTRODUCTION

The furnace insert used for testing high-strength steel wires in a hydrogen atmosphere was modified because of the mechanical difficulties encountered in preliminary experiments. However, no delayed fractures were obtained in these experiments, so an alternative sample preparation technique, incorporating cathodic charging of the specimen with hydrogen and subsequent cadmium plating, has been developed and the requisite apparatus assembled. An apparatus for testing cathodically charged and cadmium-plated wires under ambient conditions has been designed, constructed, and tested.

B. EXPERIMENTAL

The first batch, (a), of AISI 4140 and HyTuff wire was received at the beginning of this investigation. An additional batch, (b), of AISI 4140 (2 lbs, 79 mil) and HyTuff (3 lbs, 80 mil) wires has been received since the February, 1969, management report. New 4140 wires of batch (b), which had the desired initial "patented" microstructure, with strength levels above 290 ksi have been drawn using a combination of selected cold reductions with the use of improved tempering and point-ing techniques. Commercially prepared AISI 4140 wires of various strength levels and diameters comprising batch (c) were received between June 27 and August 7, 1969. Metallography has been completed on all the as-received wire pieces in batches (b) and (c) and on wire cold-drawn to 93% reduction at Ohio State. In the latter photomicrographs were obtained for both as-drawn and tempered samples.

The specimens were prepared so as to provide a three-inch length free of macroscopic surface defects. This length was subsequently cathodically charged with hydrogen, cadmium-plated to retain the hydrogen, and baked at 300°F for one hour to homogenize the hydrogen distribution. It was thought that small defects within the wire would act as stress raisers and hence would produce stress gradients in the wire when it was uniaxially loaded in tension. The above conditions were expected to result in the delayed fracture of a susceptible material. Six stands, each using a horizontal beam for static loading, have been constructed and used to test these specimens under ambient conditions. A total of 20 tests has been completed on 21 mil, 250 ksi; 15.8 mil, 408 ksi; and 15.5 mil, 280 ksi wires. An improved furnace insert has been constructed for testing specimens under direct static load in a hydrogen atmosphere. A cam-type grip which can be used in all the testing equipment has been designed, constructed, and tested successfully.

A description of the furnace insert and grip was given in the "First Technical Management Report," dated June, 1969.

C. RESULTS AND DISCUSSION

The 21 mil, 250 ksi strength level 4140 wire (b) cold drawn at Ohio State was tested pending delivery of the commercially supplied wire (c). Upon receipt of the 15.8 mil, 408 ksi wire (c) static delayed fracture tests were initiated upon it. However no susceptibility was found for as-loaded specimens at stresses up to 95% of the yield strength, even though macroscopic specimens of 4140 are highly susceptible under similar testing. It was thought that the apparent lack of susceptibility was a grain size effect and that a wire having a larger grain size would be more susceptible. Tests were therefore initiated on the 280 ksi wire (c); no apparent susceptibility was observed in this case either. Furthermore, it became evident during the 20 tests that a proper loading technique was critical for reproducibility when loading to near the strength level of the material.

The delayed fracture tests either failed on loading or did not fail in 100 hours or more of testing. This result indicates that the conditions for delayed fracture are not being met. Three possible reasons are (1) that the defects are not acting as stress raisers, therefore the wire is uniformly and uniaxially stressed, (2) that not enough hydrogen is present in the sample; and (3) that heavily cold-worked AISI 4140 wires tested under the above conditions are not susceptible to delayed fracture because of association of hydrogen with the high density of dislocations in cell walls in the drawn wires. Because a notched geometry is not suitable for cylindrical specimens of 15 to 20 mils diameter and because the wire does not contain stress raisers effective when it is axially loaded, only reasons (2) and (3) will be studied subsequently.

The high reproducibility of Instron tensile test results obtained when using the cam-type grips indicates that they are more suitable for use in the delayed fracture tests than the serrated-face, wedge-type grips.

D. FUTURE WORK

The hydrogen content of some specimens will be determined by quantitative chemical analysis. Bend tests will be used as a qualitative measure of specimen embrittlement. These tests will be designed to reveal (1) whether or not hydrogen is entering the specimen initially, (2) whether or not hydrogen has entered escapes before the specimen can be cadmium plated, and (3) whether or not hydrogen is lost through the cadmium after plating. Specimens stressed to near their respective strength levels by bending will be cathodically charged in situ as a

qualitative measure of their susceptibility. If in situ charging proves more reliable than charging and cadmium plating, the test stands will be modified and delayed fracture testing continued using this technique.

SECTION V

COORDINATION AND BRIEFING
(Met.E.-OSU Staff)

Seminars and lectures were presented by the staff at the Air Force Materials Laboratory as follows:

<u>Date</u>		<u>Staff Member</u>
(1968) October 22	Plastic Instability and Its Role in Notch Ductility	J. W. Spretnak
November 19	Progress to Date in Investigating the Stress Corrosion of High-Strength Steels	R. W. Staehle
December 17	Progress to Date in Investigating the Stress-Corrosion Cracking of Titanium Alloys	F. H. Beck
(1969) January 21	Properties of Discontinuous Thin Films	R. Speiser
February 19	Some Applications of Field Ion Microscopy	G. Meyrick
April 22	Cyclic Stress-Strain Response of Materials as It Relates to Fatigue Failure	C. Laird
May 20	Recent Advances in High Temperature Oxidation	R. A. Rapp

SECTION VI

MISCELLANEOUS

Dr. C. M. Chen was transferred to AFML and is conducting his research there. Mr. E. J. Timmer received a Master's degree on this program. He left OSU because of the draft situation. Continuation of his work at AFML was dropped for the same reason. Robert L. Cowan received a Ph.D. on this program.

Contrails

REFERENCES

1. A. J. Sedricks, J. A. Green, and R. W. Slattery, "SCC and Corrosion Behavior of Ti and Ti-Al Alloys in Methanol Iodine Solutions," Corrosion, 24, No. 6, 1968, p. 172.
2. E. G. Haney, "Investigation of SCC of Ti Alloys," Mellon Institute, Semiannual Progress Report No. 1, November 30, 1966.
3. R. Wenk, Master's Thesis, The Ohio State University, 1968.
4. R. Cocks, J. Russo, and S. Brummer, "The Separation of Corrosion and Stress Effects in Stress Corrosion: Ti-Al-4V in Bromine-Methanol Solutions, J. Electrochem. Soc., May, 1968.
5. R. Cochran, Master's Thesis, The Ohio State University, 1966.
6. R. Green and J. Myers, "Effect of Grain Size on Incubation and Propagation of SCC in Type 302 Steel," Corrosion, 24, 5, 1968.
7. I. A. Menzies and A. F. Averill, "The Anodic Behavior of Ti in HCl-Methanol Solutions," Electrochimica Acta, 13, 801, 1968.
8. T. R. Beck, "SCC of Ti Alloys," Quarterly Progress Report, Boeing Corp., June 30, 1967.
9. W. D. France and N. D. Greene, "Passivation of Crevices during Anodic Protection," Corrosion, 24, No. 8, pp. 247-51, 1968.
10. Section II B of this report.
11. C. Edeleanu, Metallurgica, 50, 113 (1954).
12. J. D. Sudbury, O. L. Riggs, Jr., and D. A. Shock, Corrosion 16, 47t and 55t (1960).
13. O. L. Riggs, Jr., M. Hutchison, and N. L. Conger, Corrosion 16, 58t (1960).
14. A. O. Fisher and J. F. Bradly, Corrosion 19, 37t (1963).
15. M. G. Fontana and N. D. Greene, Corrosion Engineering, McGraw-Hill (1967).
16. M. N. Fokin and V. A. Timonin, Doklady Akademicheskikh Nauk SSSR 164, 50 (1965).
17. C. M. Chen, F. H. Beck, and M. G. Fontana, Corrosion (to be submitted for publication).

18. C. M. Chen, F. H. Beck, and M. G. Fontana, Corrosion (to be submitted for publication).
19. Section II A of this report.
20. E. G. Haney, G. Goldberg, R. E. Ernsberger and W. T. Brehm, Mellon Institute, Progress Report No. 2, NASA Research Grant NGR-39-008-014, May, 1967.
21. F. Whitmore, Organic Chemistry, Van Nostrand, New York, 1937.
22. G. A. Griffis, Ph.D. Dissertation, The Ohio State University, 1968.
23. M. Gensamer, "Strength of Metals under Combined Stress," American Society for Metals, 1940.
24. W. F. Brown Jr. and J. E. Srawley; "Plane Strain Crack Toughness Testing of High Strength Metallic Materials," ASTM Tech., Pub. No. 410, (1966), pages 33-38.
25. W. F. Brown Jr.; private communication with Brown.
26. L. E. Kinsler and A. R. Frey; "Fundamentals of Acoustics" John Wiley & Sons, New York (1962), 2nd Ed.
27. H. H. Johnson and G. G. Hancock; "Hydrogen, Oxygen, and Subcritical Crack Growth in High Strength Steel," Trans. AIME, Vol. 230, (April 1966), pages 513-516.
28. Technical Report AFML 69-16, (Feb. 1969).
29. J. O'M. Bockris and M. S. V. Devanathan; O.N.R. Report No. 551 (22), NR 036-028, (1961).
30. R. A. Oriani; "Hydrogen in Metals," SCC Conference, O.S.U., (Sept. 1967).
31. E. E. Fletcher and A. R. Elsea; "Hydrogen Movement in Steel Entry, Diffusion, and Elimination," IMIC Report 219, Battelle Memorial Institute, (June 30, 1965).m
32. M. A. V. Devanathan and Z. Stachurski, Proc. Royal Society (London) A 270, 90 (1962).
33. M. G. Fontana; "Corrosion Cracking of Metallic Materials," Technical Report AFML 69-16, (Feb. 1969).
34. A. Fortran Program for Analysis of Ellipsometer Measurements; Frank L. McCracken; NBS Technical Note 479, April 1969.

35. Kruger J. and Calvert J. P.; J. Electrochem. Soc.; 114 (1967), 43.
36. Nagayam and M. Cohen; J. Electrochem. Soc.; 109 (1962), 781.
37. N. Sato and M. Cohen; J. Electrochem. Soc.; 111 (1964), 512.
38. Cabrera and N. F. Mott; Rep. Prog. Phys. 12 (1949), 163.
39. C. M. Criss and J. W. Cobble; J. Am. Chem. Soc., 84, 5285-53901, (1964).
40. C. M. Criss and J. W. Cobble; J. Am. Chem. Soc., 84, 5390-5393.
41. J. W. Cobble; J. Am. Chem. Soc., 84, 5394-5401, (1964).
42. H. E. Townsend; to be published.

Contrails
DOCUMENT CONTROL DATA - R&D

(Security classification of title, body of abstract and indexing annotation must be entered when the overall report is classified)

1. ORIGINATING ACTIVITY (Corporate author) The Ohio State University Research Foundation 1314 Kinnear Rd. Columbus, Ohio		2a. REPORT SECURITY CLASSIFICATION Unclassified	
3. REPORT TITLE CORROSION CRACKING OF METALLIC MATERIALS		2b. GROUP N/A	
4. DESCRIPTIVE NOTES (Type of report and inclusive dates) Technical - December 15, 1968 - December 31, 1969			
5. AUTHOR(S) (Last name, first name, initial) Mars G. Fontana			
6. REPORT DATE January 1970		7a. TOTAL NO. OF PAGES 207	7b. NO. OF REFS 42
8a. CONTRACT OR GRANT NO. F33(615)-69-C-1258		9a. ORIGINATOR'S REPORT NUMBER(S)	
b. PROJECT NO.			
c.		9b. OTHER REPORT NO(S) (Any other numbers that may be assigned this report)	
d.		AFML-TR- 70 - 2	
10. AVAILABILITY/LIMITATION NOTICES This document is subject to special export controls and each transmittal to foreign governments or foreign nationals may be made only with prior approval of the Metals and Ceramics Division (MAM), Air Force Materials Laboratory, Wright-Patterson Air Force Base, Ohio 45433			
11. SUPPLEMENTARY NOTES		12. SPONSORING MILITARY ACTIVITY Air Force Materials Laboratory Wright-Patterson Air Force Base, Ohio 45433	
13. ABSTRACT Stress corrosion behavior of titanium alloys and high strength steels has been studied. In titanium alloys the initiation and propagation of cracks in aqueous and methanolic environments is being studied as a function of alloy composition, electrochemical control, and applied stress. Corrosion processes within crevices are being studied. Straining electrode studies are also reported. Crack initiation in Ti-6Al-4V specimens was observed at α - β interfaces and in β grains. Studies of crack velocity show it to depend on applied stress but not on potential. Crevice studies show corrosion to be accelerated when the IR drop is large. In high strength steels the processes of transient passivity, dissolution of carbides, crack propagation and hydrogen permeation are being studied. The kinetics of transient passivity on iron alloy surfaces shows good agreement with classic models for growth of thin films. Dissolution of iron carbides is shown to depend on pH, potential and anion. The action of cathodic poisons such as arsenic is shown to depend on co-deposition of the poison species. This document is subject to special export controls and each transmittal to foreign governments or foreign nationals may be made only with prior approval of the Metals & Ceramics Division (MAM), Air Force Materials Laboratory, Wright-Patterson Air Force Base, Ohio 45433			

Contrails

14. KEY WORDS	LINK A		LINK B		LINK C	
	ROLE	WT	ROLE	WT	ROLE	WT
stress corrosion cracking						
titanium						
high strength steels						
salt water						
methanol						
straining electrode						
crevices						
ellipsometry						
passivity						
iron carbide						
hydrogen permeation						
crack initiation						
crack propagation						
acoustic emission						

INSTRUCTIONS

1. **ORIGINATING ACTIVITY:** Enter the name and address of the contractor, subcontractor, grantee, Department of Defense activity or other organization (*corporate author*) issuing the report.
- 2a. **REPORT SECURITY CLASSIFICATION:** Enter the overall security classification of the report. Indicate whether "Restricted Data" is included. Marking is to be in accordance with appropriate security regulations.
- 2b. **GROUP:** Automatic downgrading is specified in DoD Directive 5200.10 and Armed Forces Industrial Manual. Enter the group number. Also, when applicable, show that optional markings have been used for Group 3 and Group 4 as authorized.
3. **REPORT TITLE:** Enter the complete report title in all capital letters. Titles in all cases should be unclassified. If a meaningful title cannot be selected without classification, show title classification in all capitals in parenthesis immediately following the title.
4. **DESCRIPTIVE NOTES:** If appropriate, enter the type of report, e.g., interim, progress, summary, annual, or final. Give the inclusive dates when a specific reporting period is covered.
5. **AUTHOR(S):** Enter the name(s) of author(s) as shown on or in the report. Enter last name, first name, middle initial. If military, show rank and branch of service. The name of the principal author is an absolute minimum requirement.
6. **REPORT DATE:** Enter the date of the report as day, month, year, or month, year. If more than one date appears on the report, use date of publication.
- 7a. **TOTAL NUMBER OF PAGES:** The total page count should follow normal pagination procedures, i.e., enter the number of pages containing information.
- 7b. **NUMBER OF REFERENCES:** Enter the total number of references cited in the report.
- 8a. **CONTRACT OR GRANT NUMBER:** If appropriate, enter the applicable number of the contract or grant under which the report was written.
- 8b, 8c, & 8d. **PROJECT NUMBER:** Enter the appropriate military department identification, such as project number, subproject number, system numbers, task number, etc.
- 9a. **ORIGINATOR'S REPORT NUMBER(S):** Enter the official report number by which the document will be identified and controlled by the originating activity. This number must be unique to this report.
- 9b. **OTHER REPORT NUMBER(S):** If the report has been assigned any other report numbers (*either by the originator or by the sponsor*), also enter this number(s).
10. **AVAILABILITY/LIMITATION NOTICES:** Enter any limitations on further dissemination of the report, other than those

imposed by security classification, using standard statements such as:

- (1) "Qualified requesters may obtain copies of this report from DDC."
- (2) "Foreign announcement and dissemination of this report by DDC is not authorized."
- (3) "U. S. Government agencies may obtain copies of this report directly from DDC. Other qualified DDC users shall request through _____."
- (4) "U. S. military agencies may obtain copies of this report directly from DDC. Other qualified users shall request through _____."
- (5) "All distribution of this report is controlled. Qualified DDC users shall request through _____."

If the report has been furnished to the Office of Technical Services, Department of Commerce, for sale to the public, indicate this fact and enter the price, if known.

11. **SUPPLEMENTARY NOTES:** Use for additional explanatory notes.

12. **SPONSORING MILITARY ACTIVITY:** Enter the name of the departmental project office or laboratory sponsoring (*paying for*) the research and development. Include address.

13. **ABSTRACT:** Enter an abstract giving a brief and factual summary of the document indicative of the report, even though it may also appear elsewhere in the body of the technical report. If additional space is required, a continuation sheet shall be attached.

It is highly desirable that the abstract of classified reports be unclassified. Each paragraph of the abstract shall end with an indication of the military security classification of the information in the paragraph, represented as (TS), (S), (C), or (U).

There is no limitation on the length of the abstract. However, the suggested length is from 150 to 225 words.

14. **KEY WORDS:** Key words are technically meaningful terms or short phrases that characterize a report and may be used as index entries for cataloging the report. Key words must be selected so that no security classification is required. Identifiers, such as equipment model designation, trade name, military project code name, geographic location, may be used as key words but will be followed by an indication of technical context. The assignment of links, rules, and weights is optional.